Hybrid-Mode-Locked Ce:LiCAF Lasers

By

Adam Oliver Sharp

A thesis submitted to Macquarie University
for the degree of Doctor of Philosophy
Department of Physics and Astronomy
March 2021

Typeset in LaTeX 2_ε.

Except where acknowledged in the customary manner, the material presented in this thesis is, to the best of my knowledge, original and has not been submitted in whole or part for a degree in any university.

Adam Oliver Sharp

Acknowledgements

This research project has demanded growth and effort from myself in many ways, nurtured by friends, family, mentors and colleagues all of whom were essential in guiding me to complete this chapter of my life, and I cannot adequately acknowledge everyone's contribution to helping me through this because almost everyone I encountered during this time was supportive in some way, so I mention the most significant.

Firstly, my superhero supervisors: David Coutts and David Spence. You have been aptly referred to as laser wizards by others, which I have found to be entirely accurate. Coutts, you were consistently encouraging, supporting, caring, and inspiring; your wisdom and joyfulness will continue to be an inspiration to me for years to come. Spence, you shared the same qualities; it was your grounded discipline that helped me stay on track.

Although technically not a supervisor, Alex Fuerbach may as well have been; you always had vital and friendly guidance. Your patience helped me to understand and visualise the mechanics of ultrafast lasers, and pushed me to achieve the best possible result. Another beacon of patience was Ondrej Kitzler; you always had time for a chat to discuss all kinds of imaginative designs and ideas. Of course, you are both also in the category of laser wizards.

Mum and Dad, you were pillars of strength that never failed to support and love me in whatever ways you thought would help. It both humbled and warmed me during the times I needed it most. To the rest of my family, you were there to provide whatever insight into life you could, showing me what the most important things in life are.

To my friends, you all brought me joy in some way or another, and helped me to want to become a better person in a number of ways. I will always be able to reminisce about our times together, whether or not you helped me through my studies or comforted me during hardships.

Lastly, to Ghazaleh, you were a constant source of happiness for me during the most crucial part of this project. You motivated me, inspired me, and cared for me. In a way, this is your third PhD, since it could not have happened without you.

Abstract

This research project entitled “cerium lasers: ultraviolet, ultrafast, and ultracool” was introduced at the MQ Photonics Research Centre in Macquarie University with the aim of advancing ultrafast ultraviolet lasers based on Ce:LiCAF. This resulted in a new mode-locking scheme for Ce:LiCAF lasers, a modified cross-correlation technique to measure the duration of the generated pulses, and characterisation of the spectral behaviour of the laser system.

Combining a synchronous pumping scheme with Kerr-lens mode-locking led to the first hybrid mode-locking scheme within a Ce:LiCAF laser. Compared with previous results, the addition of this latter mode-locking mechanism decreased the generated pulse duration by more than a factor of 60, from 6 ps to 91 fs. This duration was measured by modifying asynchronous cross-correlation with a simple microscope cover-slip time reference introduced into half of the reference beam profile, dubbed split-beam asynchronous cross-correlation. This new approach determines the measurement time-scale more quickly, on the order of 10^4, reducing uncertainty. The intra-cavity dispersion of the Ce:LiCAF laser was calculated, and measured experimentally, which enabled Kerr-lens mode-locking. The phenomenon of dispersion tuning was characterised and utilised to determine the amount of intra-cavity dispersion, and as a guide for identifying the zero point, at which there is minimal tuning. Additional dispersive elements were used to dispersion-tune over a range of more than 5 nm in the region of 290 nm.

The slope efficiency of the hybrid-mode-locked Ce:LiCAF laser was measured to be 9%, with a threshold of 1.0 W. A low-transmission plane output coupler was used to achieve this, which also consolidated the output power from the previous four beams, via a near-Brewster’s-angle plate output coupler, into a single beam for the first time. The low threshold achieved using this output coupler enabled the first demonstration of un-chopped operation from the mode-locked Ce:LiCAF laser.

Contents

1

Introduction

Since the first construction and operation of a laser in 1960, by Theodore H. Maiman at Hughes Research Laboratories [1], a myriad of gain media and techniques for manipulating laser light have been discovered and investigated. Over the last six decades manufacturing methods have improved via advances in numerous fields of science and technology. Consequentially, generation of almost any desired electromagnetic wave is technically acheivable, continuous-wave or pulsed. While this is a thrilling prospect, some spectral regions are still challenging to reach with established laser technologies, which may be restrictive due to cost, power efficiency, size, robustness, and simplicity. Improving any of these characteristics for any optical system makes it more accessible to researchers across the globe, potentially providing knock-on effects to countless fields of science and technology. Progress via nuance and detail will pave the way for major discoveries.

Besides power output, lasers can essentially be divided into two categories: those which generate a continuous-wave (CW) of radiation, and those which generate pulses. This thesis focusses on the latter, particularly pulses on the order of femtoseconds ($1\,\text{fs} = 10^{-15}\,\text{s}$). Femtosecond pulses, also known as ultrafast pulses, are immensely useful in many fields. These phenomenally brief bursts of light are generally useful for one of two reasons. Firstly, the narrow time window in which they interact with matter permits ultrafast temporal characterisation of the materials which they are made to illuminate. Secondly, the high peak power of femtosecond pulses, which can reach levels of $10\,\text{PW}$ ($10^{16}\,\text{W}$). The most popular and influential laser medium for generating these pulses is titanium-doped sapphire (Ti:sapphire). The success of Ti:sapphire can be attributed to the immense range of wavelengths that it

is capable of generating (bandwidth $\approx 650 - 1100$ nm) since a very broad bandwidth laser gain is required to directly generate femtosecond pulses. Ultrafast pulse generation outside this region of the spectrum, however, often requires expensive, complicated, and inefficient systems which are out of reach of many researchers. This is particularly true for shorter wavelengths, for which there are very few solid-state laser media that provide a cost-effective solution. Figure 1.1 indicates a variety of broad-bandwidth solid-state laser media, with their potential bandwidth-limited pulse duration. Note the top two, Ce:LiCAF and Ce:LiLuF, which are the two most prominent media for cerium lasers, which will now be discussed.

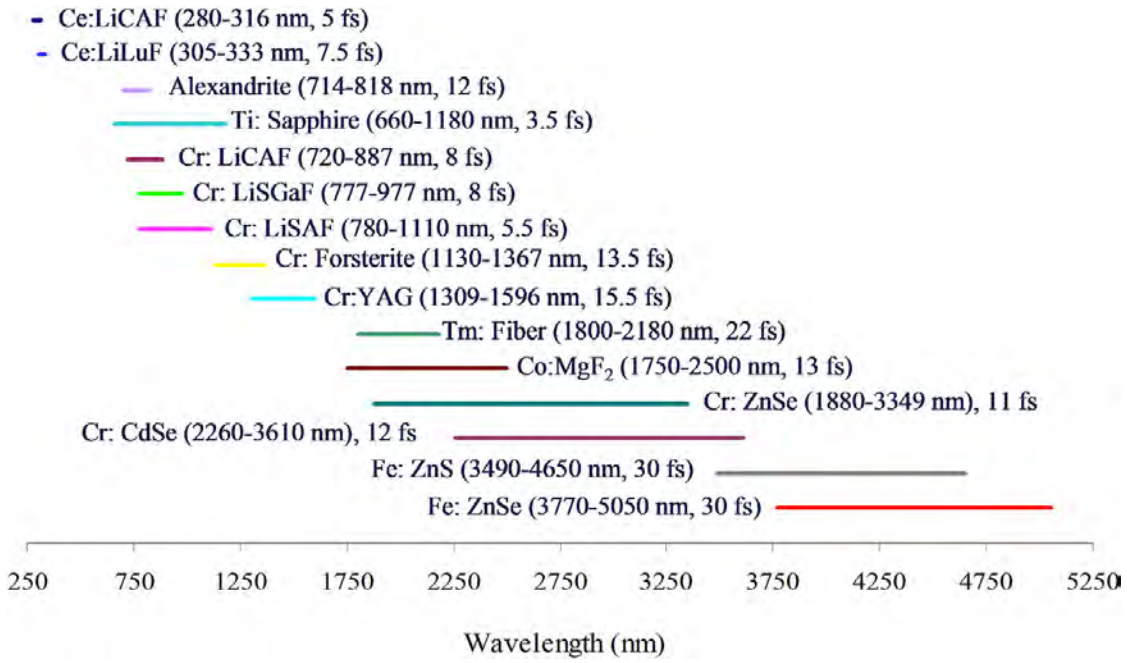

Figure 1.1: Comparison of ultrafast solid-state laser media, from [2]. Note the short 5 fs duration for Ce:LiCAF (determined using a narrower gain bandwidth than has been achieved).

Ultraviolet Cerium Lasers

The deep-ultraviolet (DUV) region is a prime example that is highly sought after, but in which it is difficult to produce ultrafast pulses. DUV light is valuable in numerous applications often because of its short wavelength, or interaction with transparent material, discussed in more detail in the following sections. Many of the methods of generating ultrafast pulses in this region actually begin from a Ti:sapphire laser, but there is a far simpler approach to accessing this region: cerium-doped fluoride lasers. They have been described as a Ti:sapphire in the UV [3] due to the comparable frequency bandwidth to Ti:sapphire and thus comparable bandwidth-limited pulse (figures 1.2 and 1.3). Cerium-doped fluoride has the advantage of a higher cross section, a lower quantum defect, and a shorter single cycle limit compared to Ti:sapphire in the IR, but it has a shorter upper-state lifetime, which is detrimental. The most prominent of the Ce-doped lasers is Ce:$LiCaAlF_6$ (Ce:LiCAF) due to its robustness, efficiency, and bandwidth; Ce:LiCAF has a maximum gain peak at 290 nm.

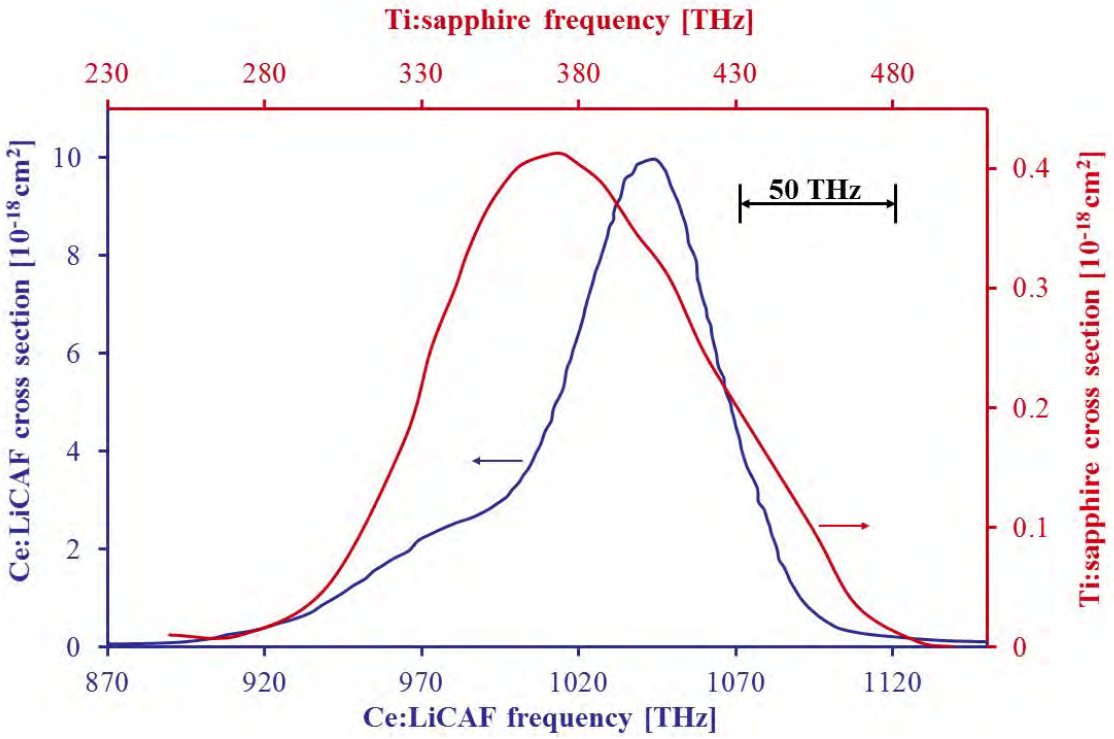

Figure 1.2: The bandwidth of Ce:LiCAF compared to Ti:sapphire from [4]. The cross sections have been translated to show relative bandwidth.

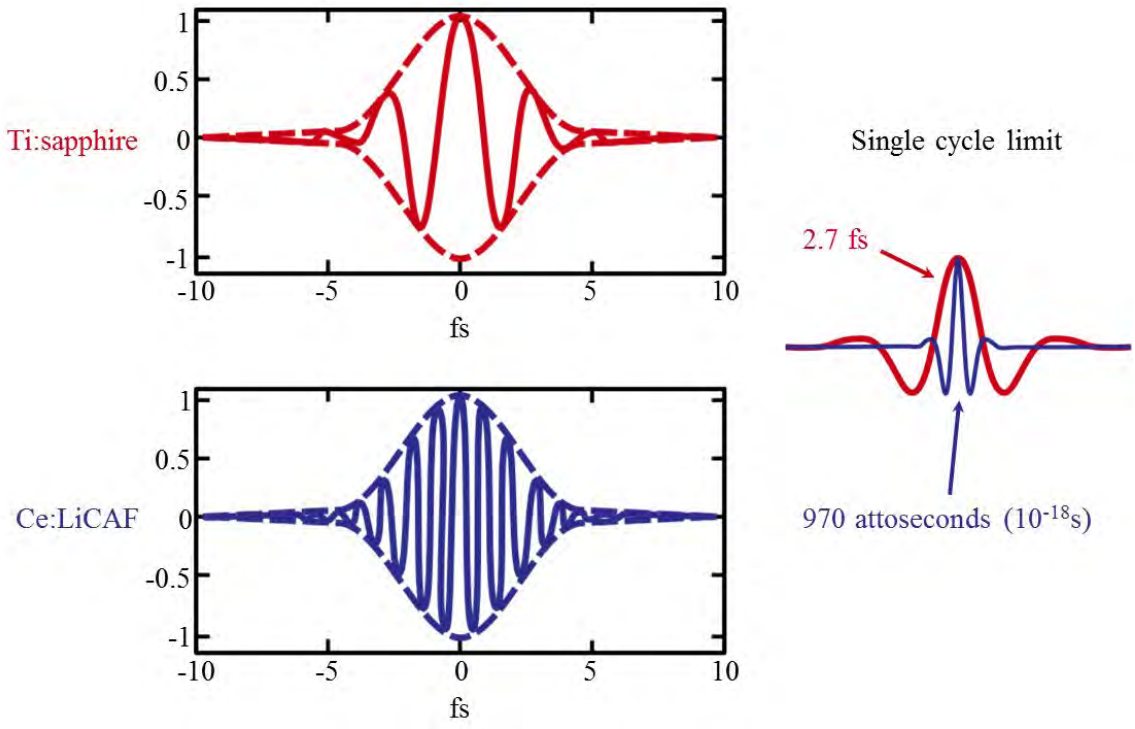

Figure 1.3: Comparison of theoretically achievable pulse durations of Ce:LiCAF and Ti:sapphire based on the full potential gain bandwidth, and the pulse duration if the pulses were to be subsequently compressed to their single cycle limits, from [4].

One of the most attractive traits of Ce:LiCAF lasers, their potential efficiency, is partly because they can be pumped by the frequency quadrupled output of Neodymium based lasers (discussed in chapter 3). Frequency conversion is significantly more simple and efficient to achieve using these fixed wavelength lasers, as opposed to a tunable laser such as Ti:sapphire. Neodymium based lasers are an industry standard for producing both ultrafast picosecond pulses and nanosecond pulses, since they are solid state, highly efficient, and easily pumped by laser diodes. However, they do not have the gain bandwidth required for generating femtosecond pulses or wavelength tuning over a wide range. Frequency conversion of Nd-lasers is therefore a simple and efficient route to generating ultrafast DUV pulses with high power. By using this powerful starting point to pump a Ce:LiCAF laser, wavelength tuning or shorter pulse durations can then be achieved. In summary, Ti:sapphire has been a monumentally influential laser medium for science and manufacturing. As a similarly robust medium, cerium-doped fluorides have the potential to make the UV region more accessible to researchers by simplifying the route to generating femtosecond pulses and/or tunable laser light in the UV.

1.1 Applications of Ultrafast UV pulses

Ultrafast UV pulses are required for many fields in science and industry, and sometimes desired but not utilised because of a greater cost and lack of reliability compared to their IR counterparts. These applications include, but are not limited to: machining, fabrication within transparent materials, pump-probe spectroscopy, laser-induced breakdown spectroscopy, coherent control, frequency combs, and high harmonic generation.

1.1.1 Materials Processing

Machining

UV pulses are commonly used to machine metals via ablation, as shorter wavelengths may be more tightly focussed for higher precision drilling and manufacturing on a smaller scale, compared with longer wavelengths. Additionally, the high energy of UV photons is well suited to metallic materials, which are more absorbant at these short wavelengths compared to their visible or infra-red counterparts. A particularly common wavelength to use for this task is 266 nm, generated by frequency quadrupled Neodymium-based solid-state lasers, using pulses on the order of nanoseconds. Generating ns pulses is simpler and cheaper than generating ultrafast pulses. However, using ultrafast pulses produces significantly higher quality cuts [5]. The higher intensity of ultrafast pulses reduces the threshold of laser fluence required for laser-induced breakdown [6]. Thus machining with femtosecond pulses, rather than with nanosecond ones, can be performed using a lower pulse energy. Additionally,

the femtosecond pulse duration is on a much shorter timescale than thermal diffusion of its absorbed energy; heating via a femtosecond pulse is well confined to the target region. This reduces collateral damage to surrounding areas for a more controlled cut; various differences between using long or short pulses are shown in figure 1.4.

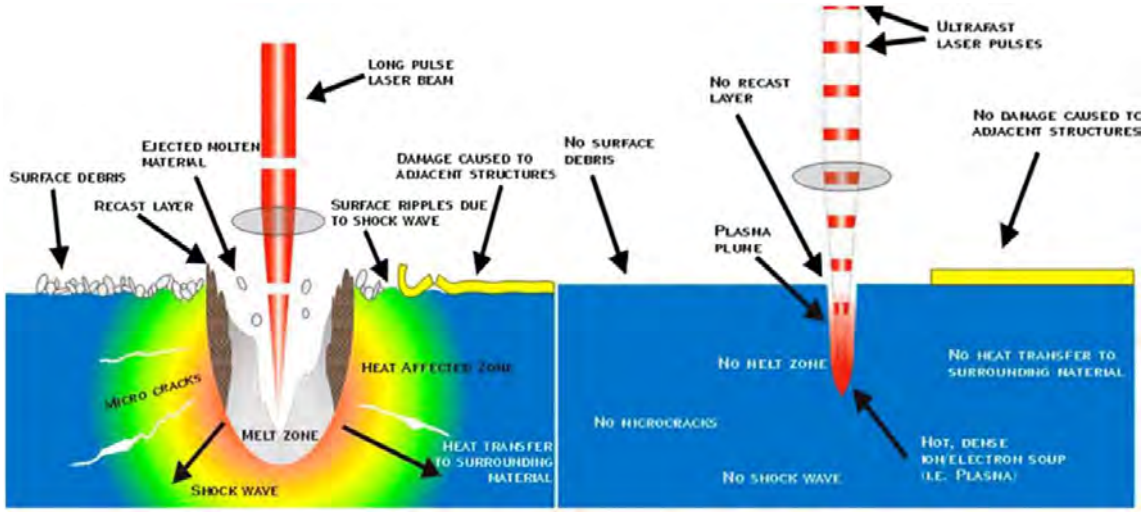

Figure 1.4: Comparison between two regimes of ablation, using ns pulses (left) and fs pulses (right). From [7], taken from [8, 9].

Machining techniques using ultrafast pulses continue to be refined. For example, bursts of ultrafast pulses with repetition rates over 1 GHz have been shown to have several significant advantages compared with using 1 kHz pulse trains [10]. This is largely because material removal and heat diffusion occurs on a nanosecond timescale [11]. A train of femtosecond laser pulses with a high repetition rate can ablate and eject material from a target region before the heat from previous pulses diffuses into the surrounding material. This approach is more precise compared with only using femtosecond pulses; it further minimises collateral damage because subsequent laser pulses may impart momentum unto the ablated material, thereby ejecting it from the target region. In addition to quality of cut, the threshold pulse energy is further reduced as well, as the target volume accumulates heat more quickly during a burst. Ultrafast Ce:LiCAF lasers have been operated at repetition rates of over 1 GHz [12], and can be amplified to high powers, making them a potentially suitable candidate for reliable and precise ultrafast machining.

Direct-write waveguides

Over two decades ago, femtosecond pulses were first used to write waveguides in glass, when they were strongly focussed into bulk materials that were transparent at the laser wavelength [13]. Since then, the physics behind fabrication within transparent materials has been studied and the direct-write technique is routinely performed by tightly focussed femtosecond pulses [14]. These are usually generated from a Ti:sapphire laser, at IR wavelengths. Fabrication

of Bragg gratings, and other geometrically complicated structures have also become well established by this technique, via careful control of the focussing geometry. The physical mechanisms of material modification are now well understood, as well as the effect of various pulse parameters including duration, repetition rate, and focussing. For example, using high repetition rates (MHz) utilises cumulative heating, whereas low repetition rates (kHz) are more reliant on stochastic processes. Much more recently, the effect of wavelength choice on refractive index modification has been studied. In bulk UV grade fused silica, which is transparent to both IR and UV pulses, it was found that the change in refractive index Δn was more significant when using UV pulses than IR ones; lower pulse energies at 343 nm were required to produce the same Δn compared to using pulses at 800 nm [15]. The authors later explored the physical mechanisms and found that the UV written waveguides could be less lossy because the various mechanisms for refractive index change (multi-photon ionisation, avalanche ionisation, tunnel ionisation, impact ionisation) are affected by the wavelength of radiation [16]. If using femtosecond pulses at a shorter wavelengths is a superior approach to direct-write waveguides, ultrafast Ce:LiCAF lasers could be the ideal tool to generate them.

1.1.2 Ultrafast Spectroscopy & Control

The UV region is home to a great number of spectral lines corresponding to electronic transitions in atoms and molecules. Ultrafast lasers have the capability to provide insight into (and control) extremely fast biological, chemical, and physical processes that involve these transitions. The aim of this section is not to elaborate on the plethora of methods and materials surrounding ultrafast spectroscopy and control, but to provide a brief glimpse into some of the processes that ultrafast lasers shed light on, and the tools that make this possible. One of the basic underlying concepts of ultrafast spectroscopy is pump-probe measurements; in which two temporally synchronised laser pulses are directed at a target, with a delay between their arrival times. The first pulse usually has a high energy compared to the second (pump) and is used to trigger the process that is to be characterised. The second pulse is used to probe the interaction as it unfolds, by varying the delay between the two pulses. Multiple probings are necessary to establish reliable results using this method, which is a core technique of ultrafast spectroscopy.

Biological Material

In regards to biology, the 200-300 nm region of the spectrum is readily absorbed by many aromatic molecules, and contains the peak absorption of DNA and RNA (260 nm) [17]. Absorption of DUV light by these molecules is particularly significant to photodamage. Studying the ultrafast dynamics of nucleic acids uracil and thymine (components of RNA and DNA, respectively) is therefore valuable to human health [18]. This has been performed using transient absorption spectroscopy; measurement of the shape and intensity of the

transient absorption spectrum is used to characterise the vibrational and electronic excited state dynamics of these nucleobases in aqueous solutions [19]. To conduct these experiments, one group used probe pulses of sub-9 fs duration in the spectral range 255-290 nm, generated by frequency converting a Ti:sapphire laser. This range partially overlaps with the tuning range of Ce:LiCAF, which could be used in its place.

Coherent Control

Over the last few decades, controlling extremely fast chemical, physical, and quantum processes using ultrafast pulses of light has become a reality via coherent control [20–23]. In the field of chemistry, this has been useful for improving the efficiency of synthesizing chemicals, and reducing undesirable by-products [24]. The overlaying concept is quite simple, for this application. Photochemical reactions are induced by ultrafast optical pulses, for which there is an optimal pulse(s) that will influence the reaction in a particular way. Parameters of the pulse include temporal shape, wavelength (e.g. UV), intensity, and number of pulses (i.e. pump-probe), each with different parameters. By tailoring the properties of these ultrafast pulses of light to a specific reaction, the possible pathways that the reaction could take (reaction channels) can be controlled. This process has been referred to as automated coherent control, because the optimal pulse parameters are not well-known, so the tailoring process requires a feedback loop for real-time optimisation. Experimental demonstrations of this technique have utilised powerful optical tools, aided by computers, to shape the temporal profile of regular optical pulses [25]. The basic layout for the pulse shaping process is shown below, in figure 1.5. A computer-controlled mask component with a fast response time (e.g. acousto-optic modulators, spatial light modulators, and phase modulators) is placed in the Fourier plane to manipulate the spectral components of the input pulse, which have been spatially dispersed by the grating.

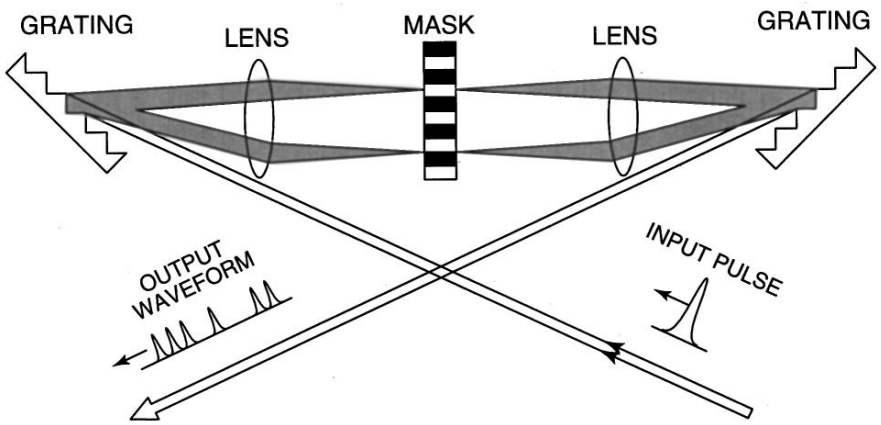

Figure 1.5: Basic layout of a Fourier transform femtosecond pulse shaping system, from [25].

The photochemical reactions to which the pulse is tailored are often optimal for short input pulse durations less than 100 fs; shorter pulses are also advantageous since they possess a broad spectral bandwidth, which allows for more flexibility in the shaping process. Since the shaping process only manipulates the input pulse, it is also necessary to begin with an ultrafast pulse that lies within the optimal wavelength range. In the UV, ultrafast cerium lasers could become the most convenient tool for coherent control, as they cover a range of over 50 nm (280 nm-333 nm) and have the potential to generate pulses of less than 10 fs.

Breakdown Spectroscopy

Femtosecond laser-induced breakdown spectroscopy is a destructive technique for analysing material composition. Femtosecond laser pulses with high energy are focussed onto the unknown material, which produce a plume of plasma via ablation. Inside the plasma, the atoms and molecules that comprise the unknown material are breaking apart, which emits light with corresponding spectral features that can be used to identify the composition of the material. This has significant real-world applications and is being developed for the process of recycling post-consumer plastics [26], which needs to be identified prior to being sorted. An optical solution in this area is ideal for time-efficiency, and this spectroscopic method has shown exceptional accuracy. As discussed in the previous section, UV lasers are well suited to the ablation processes that are utilised in this spectroscopic method, so there may be some benefit to using an ultrafast Ce:LiCAF laser over alternatives.

Frequency Combs

The spectral characteristics of any ultrafast laser (via mode-locking, discussed in detail 2) allow them to be used as optical frequency combs (OFCs). OFCs have been demonstrated over a wide range of the spectrum, from microwave radiation to the extreme-ultraviolet [27, 28], but some regions require more elaborate schemes to reach than others. The OFC is made up by the immense number of longitudinal modes (narrow spectral lines) that comprise the broad bandwidth output of these lasers. In the frequency domain, these spectral lines are equidistant, separated by the inverse of the round-trip time of the laser cavity (commonly 20 MHz-100 GHz). With stabilisation of the laser cavity, and therefore the longitudinal modes that comprise the OFC, the generated frequencies and their spacings can be used as a reference in a myriad of applications that require precise knowledge of time and/or frequency. These include all-optical atomic clocks, absolute optical frequency measurements, coherent control, chemical and gas sensing, metrology, instrument calibration, communication, ranging, and microwave generation [29]. Of these, coherent control and chemical and gas sensing may require UV wavelengths.

1.1.3 High Harmonic Generation

Harmonic generation in a gas or plasma is an effective method of producing light from extreme ultraviolet (XUV) to X-ray wavelengths (less than 10 nm) for many applications in science and industry [30–33]. Harmonic generation in gas was discovered less than a decade after the first laser, using a ruby laser to generate its third-harmonic at 231 nm [34]. The development of harmonic generation accelerated with the availability of short-pulse excimer lasers [35], since the process relies on exposing atoms or ions to an intense driving laser field. High harmonic generation (HHG) refers to harmonic generation of much higher orders, above the fifth harmonic. It was first observed in 1987 [36], using picosecond UV pulses from an excimer laser to generate harmonics with wavelengths as short as 14.6 nm. This corresponds to the seventeenth harmonic. The laser light was strongly focused into various gases: He, Ne, Ar, Kr, Xe, which are still in use today. HHG was shown to be highly promising for attosecond pulse generation in the 1990s [37, 38] which resulted in significant effort to improve methods of generation [39–42].

Both the efficiency and maximum photon energy of HHG are highly dependent on the wavelength of the driving laser field [43]. The intensity of HHG has been measured in several cases [31, 32] to be proportional to wavelength at about $I \propto \lambda^{-5}$ to λ^{-7}. Thus the efficiency is much higher for shorter wavelengths ie UV radiation. However, the maximum photon energy scales quadratically with the wavelength of the driving laser, given by $E_c \approx I_p + 3.17U_p$ where $U_p \propto I_L \lambda_L^2$ is the average quiver (ponderomotive) energy of an electron, for a driving laser of intensity I_L and wavelength λ_L [44]. Therefore, it was thought for a certain intensity, shorter driving wavelengths yield a lower maximum photon energy.

Recently, interest in using ultrafast UV lasers instead of mid-IR ones for HHG has once more been sparked when a comparison was made between a Ti:sapphire laser and its frequency converted output at shorter wavelengths [45]. As expected from previous research, the efficiency of HHG was much higher using the frequency converted intense UV pulses instead of near-IR. However, it was found that for UV pulses, the maximum photon energy can actually increase when using a multiply ionised plasma instead of a weakly ionised gas as the medium for HHG. This unexpected property is shown in figure 1.6, as dashed lines, with an increasing upconverted photon energy for shorter wavelengths.

Another aspect of performing HHG by using a short wavelength laser driving field, as opposed to a long wavelength one, is the bandwidth and chirp of the HHG output. Using UV pulses results in less bandwidth and chirp; although the bandwidth-limited pulse duration is longer via UV pulses, the reduced dispersion corresponds to less chirp and ultimately the pulse duration may in fact be shorter (without dispersion compensation). This can be seen as both an advantage and a disadvantage, since the limited bandwidth via the UV reduces the need for pulse compression, but also increases the compressible pulse duration. Pulse compression of XUV light in this region is still challenging and often greatly increases losses. There

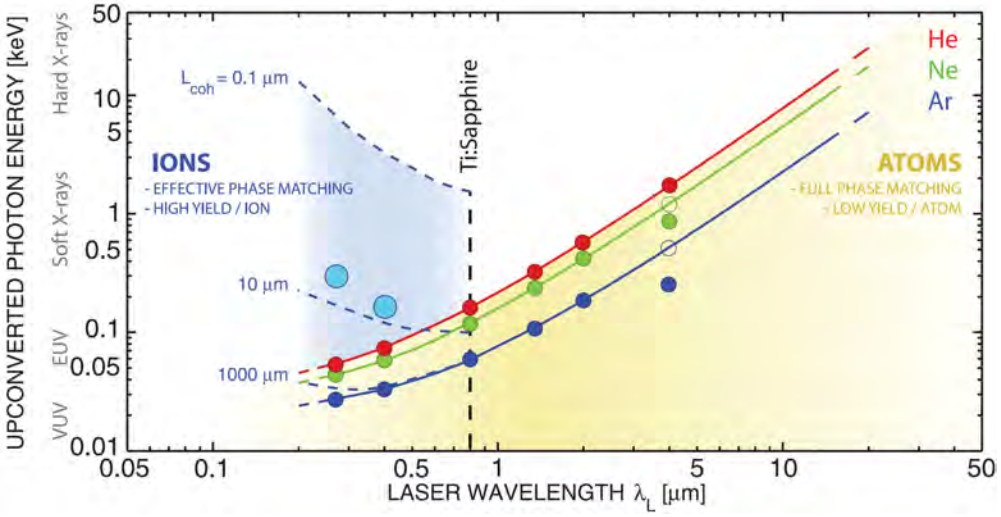

Figure 1.6: Increasing photon energy for shorter wavelengths (dashed lines) when using multiply ionised plasma (ions), taken from [45]. L_{coh} is the coherence length of the driving laser field, and the circles indicate experimental data.

are numerous methods in development, such as chirped mirrors, gratings, monochromators, transmission filters, and conical diffraction [46–51]. Therefore, it is less complex and more efficient to directly generate near bandwidth-limited pulses than it is to generate a chirped pulse that requires compression. Using short wavelengths for HHG may potentially negate the need for compression altogether, particularly if the system is in a vacuum.

Research surrounding HHG with UV driving lasers has only scratched the surface, as most groups choose to pursue longer wavelength driving lasers in the strive for higher energy photons. The high cost and complexity of generating intense UV pulses to drive HHG make the short wavelength side of HHG research impossible for many labs, and generally less desirable. This has resulted in significantly limited research using shorter wavelengths for HHG, rather than longer ones [52]. As a result of using less efficient IR radiation for HHG, the driving pulses are necessarily more energetic. Hence, generation of the IR driving pulses requires a significant amplification stage, such as a regenerative amplifier; the pulse repetition frequency (PRF) of these systems is often much lower than that of the seed laser being amplified (of order 10 Hz-1 kHz compared to 80 MHz). Using low PRFs for the driving pulses restricts the PRF of the high-harmonic pulses that are generated and limits the amount of data that can be collected from attosecond experiments. On the other end of the spectrum, using a driving pulse with a short wavelength (e.g. UV) enables more efficient HHG which can be performed with lower pulse energies, permitting the use of higher PRFs and simpler amplification stages. Cerium lasers have the potential to generate intense pulses and high PRFs in the UV (which can be subsequently amplified) with simplicity and efficiency over current popular methods. Directly generating the necessary driving pulses with ultrafast Ce:LiCAF lasers, which has the shortest wavelength of today's optically pumped solid-state laser media, may spark new and improved methods of HHG.

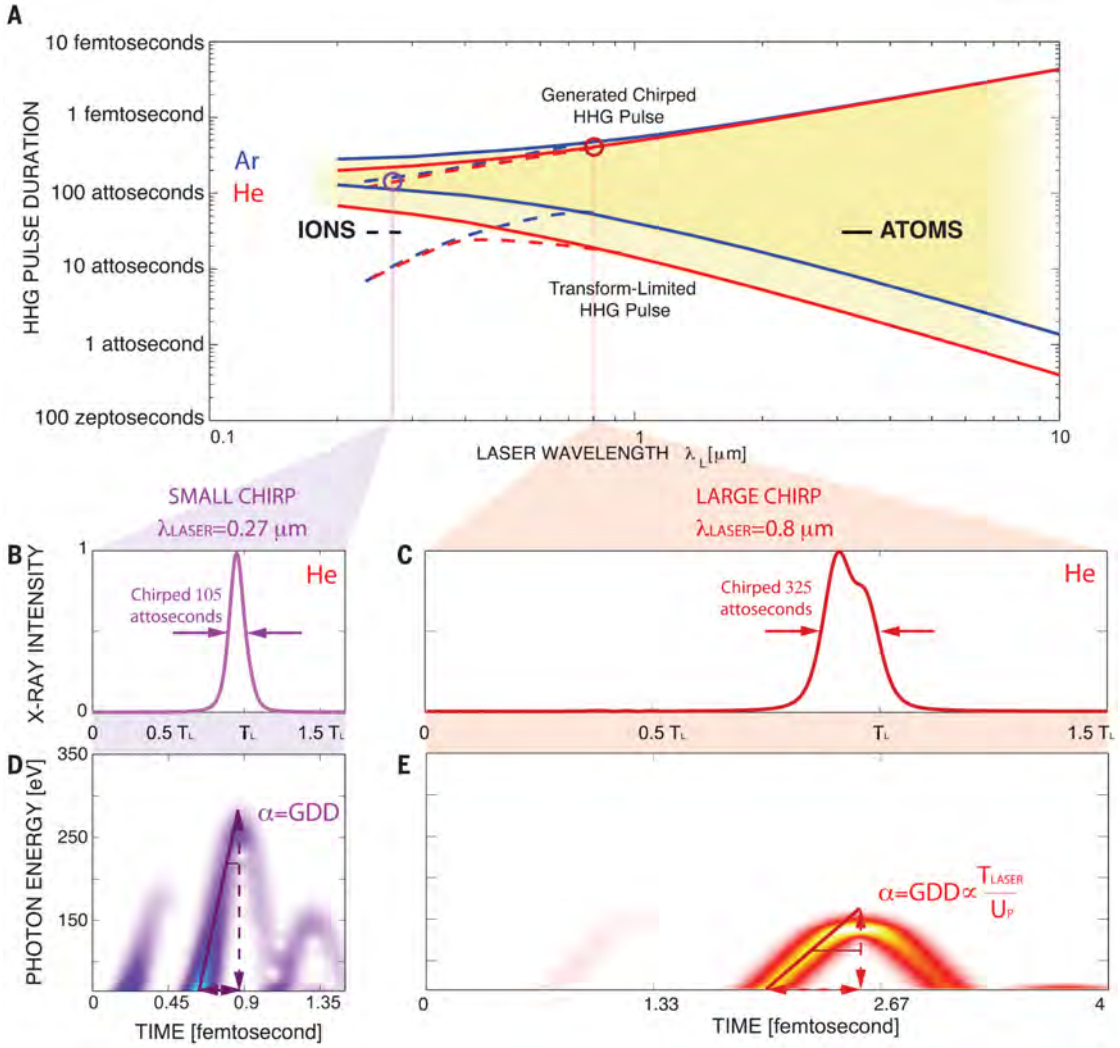

Figure 1.7: Wavelength dependence of pulse duration and transform limit for HHG, from [45]. A: comparison of generated pulse duration (upper lines) and transform-limited pulse duration (lower lines). B: temporal pulse profile of HHG using UV and IR driving lasers. C: pulse duration and depiction of chirp.

1.2 Structure of this Thesis

In the following chapters of this thesis, the theory and history that contributed to the development of the first hybrid mode-locked Ce:LiCAF laser is documented. In chapter 2, the theory surrounding active and passive mode-locking mechanisms in ultrafast lasers that utilise dispersion compensation and pulse compression is detailed. Additionally, the challenges and drawbacks of measurement techniques that seek to characterise these pulses are examined, particularly for UV wavelengths. In chapter 3, various techniques for obtaining ultrafast UV pulses are compared, and the challenges and aspects of frequency conversion in non-linear crystals is discussed. A history of cerium lasers is also presented, with a focus on Ce:LiCAF lasers, which delves into previously achieved results of active mode-locking and CW operation. Chapter 4 includes the design and tools of operation for the experimental Ce:LiCAF laser system. The primary results are presented there, with a broad view of the hybrid mode-locked Ce:LiCAF laser's operating characteristics. Chapter 5 details the spectral output of the Ce:LiCAF laser, and the tools and techniques that were used to manage the chromatic dispersion within the cavity. Chapter 6 presents a modified characterisation technique, an altered form of asynchronous cross-correlation, which was used to measure the pulse duration of the Ce:LiCAF laser and characterise stability. To conclude, chapter 7 summarises the most significant findings presented within this thesis, the implications for them are analysed, and the future of research in the field of ultrafast Ce:LiCAF lasers is discussed.

2

Pulsed Lasers

There are a variety of mechanisms to force a laser cavity to generate a pulse of light, rather than a continuous stream of photons. These can essentially be divided into two different categories for initiating a pulse: switching, and mode-locking. Switching is generally slower and used to produce relatively long pulses with a duration from several hundred picoseconds up to microseconds, with repetition rates up to 100 kHz. Mode-locking can yield much shorter pulses from several femtoseconds to tens of picoseconds, usually having a cavity much longer than a switched laser (e.g. of order 1 m versus several centimetres). The repetition rate of mode-locked lasers can range between tens of kHz using extremely long fiber lasers, to hundreds of GHz by resonating multiple pulses. Combining one of these fundamental pulsing schemes with external amplifiers can yield extremely high peak powers and pulse energies.

2.1 Q-Switching & Gain Switching

Rapid switching of laser operation can be performed by either modulating the power input to the gain medium (gain-switching) or modulating the loss of the cavity (Q-switching). The term Q-switching arises from the quality factor (Q-factor) of an oscillator/resonator, which represents the level of damping present within the system. A high Q-factor equates to low damping, and thus low losses. These two means of switching are basically direct opposites, the more prevalent of the two being Q-switching since it typically produces higher energy pulses with greater control. However, the similarity of the pulse output between these two

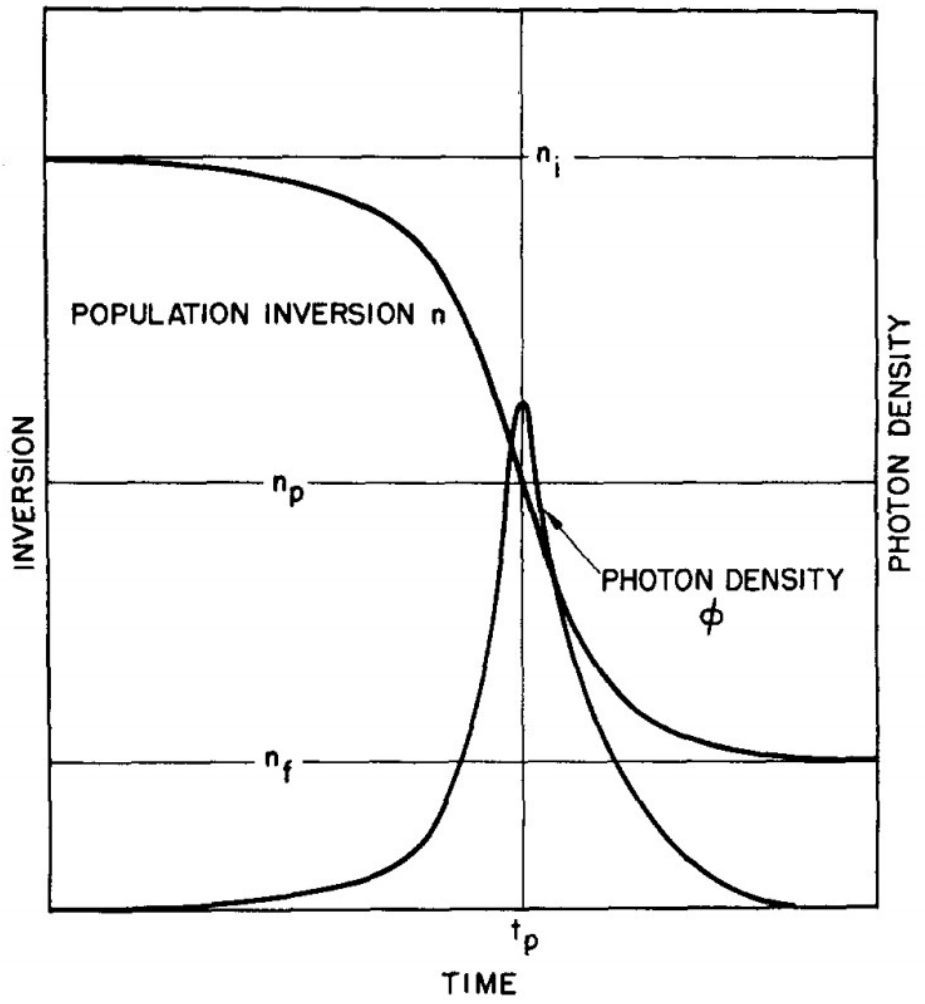

Figure 2.1: Gain depletion and pulse formation in a Q-switched laser [53].

lasers (high pulse energy and low repetition rate) makes Q-switched lasers an ideal optical pump for a gain-switched laser. The main advantage of using a Q-switched laser as a pump is that the Q-switched pulse is typically shorter than the upper level lifetime of the gain switched laser medium.

The principle of Q-switching is to pump the gain medium while there is an attenuator present in the cavity, minimally to achieve population inversion or maximally to saturate absorption entirely; approaching 100% inversion. When the cavity is in a high loss configuration (low-Q) and round-trip gain < 1, spontaneous emission occurs according to the upper-state lifetime of the material but the lasing threshold is not surpassed; there is insufficient feedback from the laser cavity because stimulated emission is supressed by resonator loss. Once the cavity is switched to a low loss configuration (high-Q) and round-trip gain > 1, the cavity mode builds up from spontaneous emission. The power within the cavity begins to increase exponentially via stimulated emission, until the gain approaches saturation after which the remaining gain is depleted. This results in a pulse on the order of a few hundred picoseconds to microseconds.

Q-switching can be performed passively or actively. Passive methods require a saturable absorber that provides sufficient loss to prevent laser operation while the population inversion increases via continuous pumping. The upper-state population then surpasses a threshold (gain>1) at which there is sufficient lasing to saturate the absorber, and the cavity mode builds up to deplete the gain. The saturable absorber then recovers, and the process is repeated. An example saturable absorber used for this type of laser is Cr:YAG, within 1064 nm lasers. The advantage of passive Q-switching is simplicity, no external controller is required. The disadvantage is that the pulse duration and energy are practically fixed; increasing the pump power merely increases the repetition rate as the threshold is overcome more quickly and the pulse forms faster. It is therefore imporant to consider the response time, recovery time, and absorption of the saturable absorber when constructing passively Q-switched lasers.

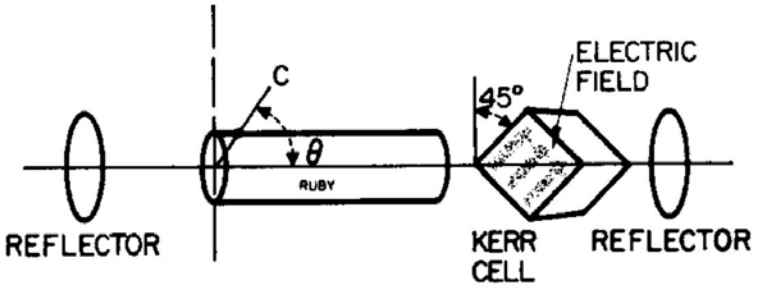

Figure 2.2: The first Q-switched laser created in 1961 [54].

Active Q-switching is often achieved using either an acousto-optic or electro-optic modulator. The first Q-switched laser utilised a Kerr cell in a ruby laser to rotate the polarisation by 90 degrees to quench laser action. This is shown in figure 2.2. Another example, a well known electro-optic modulator, the Pockels cell, will also act as a wave plate in the presence of an electric field. Placing this within a laser cavity, and combining it with a polariser is a sufficient Q-switch. The cavity has a high Q-factor when the Pockels cell is deactivated, since it does not alter polarisation. When the Pockels cell is activated, a double-pass through the cell rotates polarisation by 90°, so that light passing through the polariser is attenuated after a round-trip. By modulating the Pockels cell at a few kHz, Q-switching is achieved. The acousto-optic modulator functions very similarly, by deflecting the luminescence to prevent lasing. A popular example is a piezo-electric crystal that is subject to a modulated voltage, which forms a diffraction grating and deflects the beam. When there is no voltage present, the luminescence transmits and the laser mode builds up.

The pulse duration of Q-switched and gain switched lasers is highly dependent on the cavity round-trip time, and the upper-state population provided by pumping. Shorter cavities and upper-state lifetimes result in a faster build-up of the cavity mode, which depletes the gain more quickly so the generated pulse has a shorter duration. Cavities with a length on the order of 100 µm can yield pulse durations as short as tens of picoseconds [55]. To generate shorter pulses than these requires different techniques altogether.

2.2 Mode-Locking

Pulses from switched lasers are akin to a burst of amplified spontaneous emission, the longitudinal modes of Q-switched lasers therefore have a random phase relationship. When the longitudinal modes of a laser resonate with a fixed phase relationship, an ultrashort pulse may form within the cavity. This can be visualised as a beat frequency between different frequencies of light, as the superposition of modes forms a pulse of light. Figure 2.3 taken from [56] shows this visualisation using just three different frequencies ω_q, ω_{q+1}, and ω_{q+2} that are equally spaced in the frequency domain, as the modes of a laser cavity would be. The superposition of these three frequencies, the equivalent of the combined electric field, and their carrier envelope is also plotted. They are in phase at $t = 0$, for which there is a noticeable peak in the carrier envelope of the superimposed electric field. This is the mechanism under which ultrashort pulses form.

In reality, there are usually far more than three modes within a cavity. The mode spacing of a laser cavity is $\Delta\nu = c/2L$, so for N modes, the bandwidth is $N\Delta\nu$. For a cavity that is 2 m long with a gain bandwidth of 1 nm at 1064 nm, there are approximately 3500 available modes. Additionally, the amplitude of the modes are seldom equal. Figure 2.4 shows several examples of carrier envelopes as the phases and amplitudes of the locked frequencies are altered.

Random phases produce a periodic signal but there is no significant peak that equates to a single pulse. Using random amplitudes that are in phase produces a discernible pulse, albeit with additional features corresponding to subsidiary peaks. Increasing the number of modes decreases the presence of the subsidiary peaks, resulting in a smoother primary pulse. Applying a Gaussian envelope to the amplitudes of the modes results in the smoothest temporal profile for the pulse envelope. In reality, this tends to happen anyway as a result of a non-uniform gain profile. Therefore the gain bandwidth is often quoted at its full width half maximum (FWHM), as is the pulse duration. Modelling the gain profile as a Gaussian also simplifies the mathematics of calculations, for example, Fourier analysis to convert between frequency-time domains.

Increasing the frequency range over which the modes oscillate may also decrease the temporal duration of the pulse. Indeed, the minimum pulse duration (FWHM) of a mode-locked laser τ_p is inversely proportional to the bandwidth [57]:

$$\tau_p = \frac{0.441}{N\Delta\nu} \tag{2.1}$$

assuming the temporal profile of the pulse is Gaussian. For a soliton pulse, the numerator becomes 0.315 relating to a sech^2 temporal shape. For the previous example of a gain bandwidth of 1 nm at 1064 nm, this equates to a minimum pulse duration $\tau_p \approx 1.7$ ps. This assumes perfect phase between the modes, which is generally not the case since dispersion shifts the phase of each mode differently. This is discussed in more detail in section 2.3.

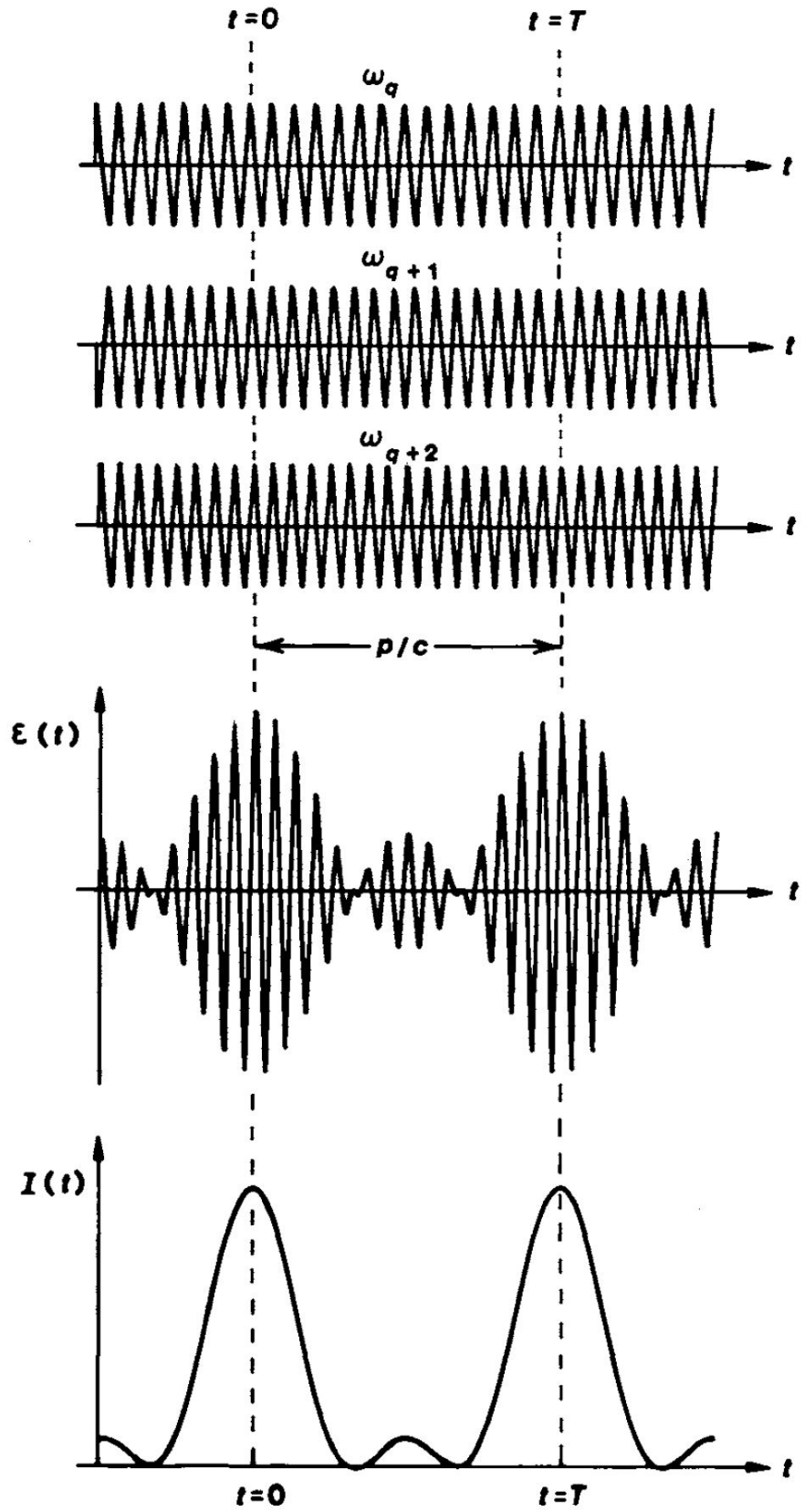

Figure 2.3: Mode-locking of three equally spaced frequencies, in phase at $t = 0$, from [56].

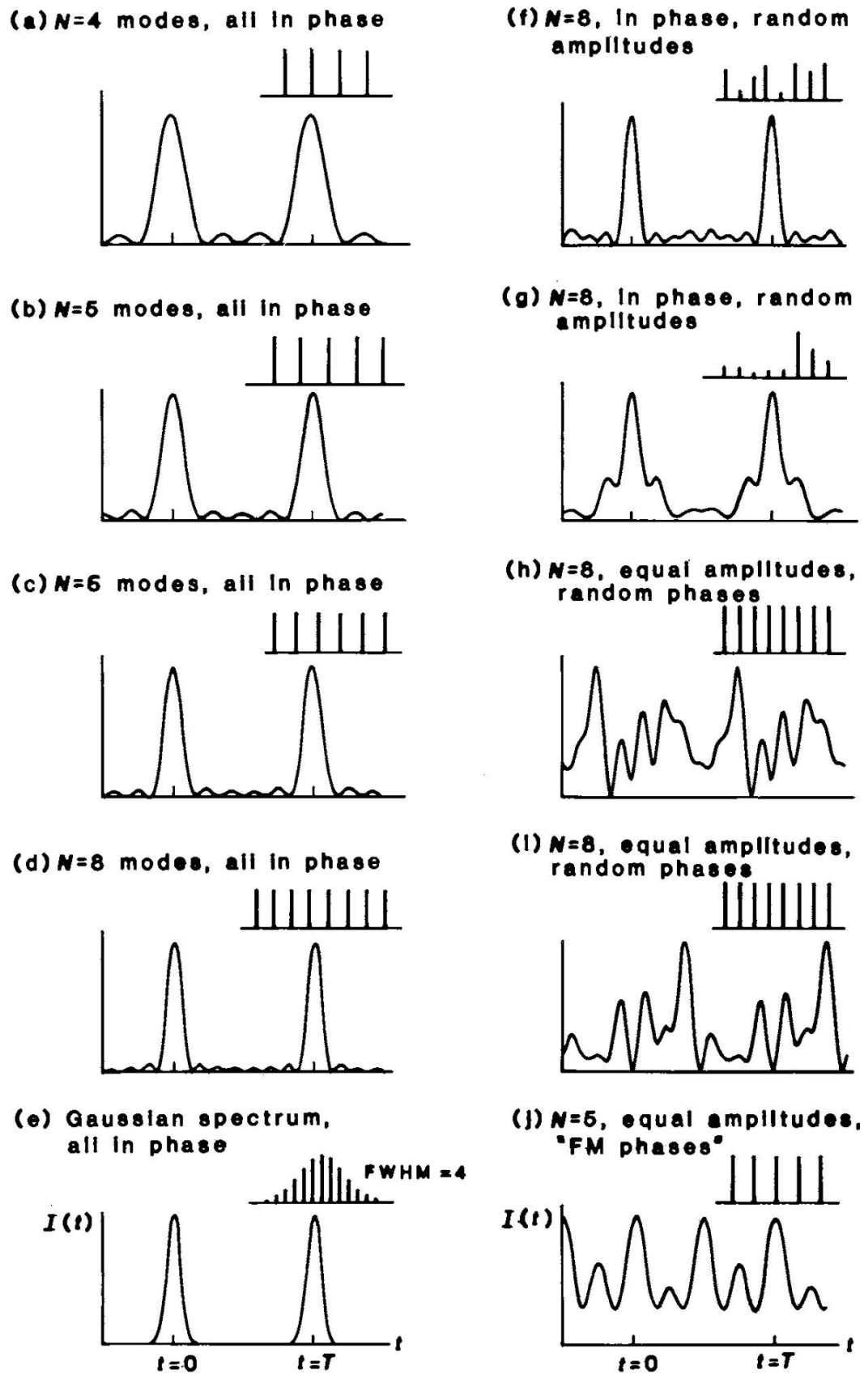

Figure 2.4: Various mode-locking of equally spaced frequencies, from [56].

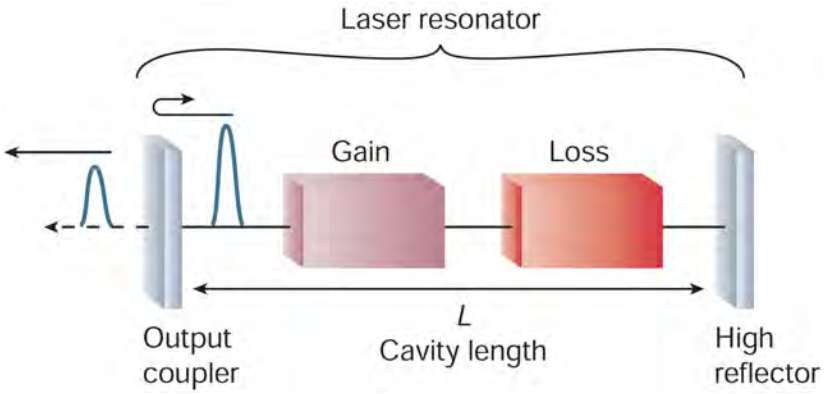

Figure 2.5: The essential elements of a mode-locked laser resonator [58].

Initiating mode-locking in a laser requires modulation of gain or loss shown in figure 2.5, similar to Q-switching, but usually significantly faster. The various mechanisms of modulation are categorised as being passive or active, and are detailed below. The length of the cavity also tends to be much longer than Q-switched lasers, since the pulse repetition frequency (PRF) of a mode-locked laser depends on the round-trip time of the cavity, based on group velocity v_g (PRF = $v_g/2L$). The PRF of mode-locked lasers is often on the order of 100 MHz, with cavity lengths of 1-2 m. This requires modulation that also occurs on these time scales.

Using a cavity dumping mechanism will decrease the overall repetition rate of the output, but generally increases the pulse energy. The principle is to let a mode-locked pulse form in a resonator with a switchable output coupler. The pulse increases in energy until the roundtrip losses outweigh the gain, after which the switch is activated and the pulse is emitted. It was utilised in the 1970s to increase the pulse energy of dye lasers [59].

Passive Mode-Locking

There are two primary means of mode-locking a laser resonator: passively, or actively. Passive techniques utilise a saturable absorber (or a mechanism for saturable loss) within a laser cavity that increases loss for low intensity light (sometimes decreases gain). Saturable absorber dyes were first researched and developed in the mid-1960s [60]. The first demonstrations of mode-locking did not yield a pulse train of stable amplitude. In fact, the envelope of the mode-locked pulse train was modulated on the timescale of a Q-switched laser. As the mechanism responsible was indeed Q-switching, the phenomenon was referred to as Q-switched mode-locking. Mode-locking with a stable pulse train was subsequently referred to as mode-locked CW.

The saturable absorber is a passive element, that exhibits lower losses for high intensity incident light. This has the effect of suppressing CW operation of a laser cavity, while promoting more intense pulses to resonate. The relaxation time of the saturable absorber is a factor, but mode-locking is achievable whether they are fast or slow [61, 62].

The passive mode-locking process generally produces the shortest pulses since the response time of the switch, such as a saturable absorber, can be rapid. Figure 2.6 depicts how the loss decreases rapidly for an ultrashort pulse, which corresponds to increased gain for the high intensity pulse. The initiation of the mode-locking itself occurs due to noise fluctuations, the most intense of which is then amplified to become the dominant resonating pulse.

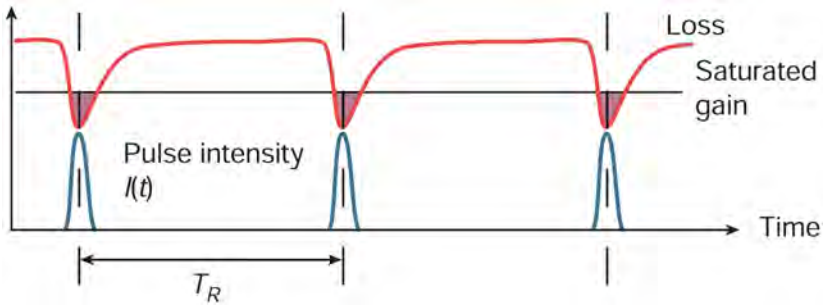

Figure 2.6: Passive mode-locking invoked via a saturable absorber [58].

Nowadays, a common saturable absorber for passively mode-locking lasers is the semiconductor saturable absorber mirror (SESAM). Invented in the 1990s [63], SESAMs are an effective and simple saturable absorber that require little maintenance, and are easily replaced. They are often used in neodymium lasers, such as mode-locking Nd:YVO_4 or Q-switching Nd:YAG. The former of these gain media has a larger bandwidth, capable of generating pulses as short as 5-10 ps, and is therefore more suited to mode-locked operation whereas the latter is commonly used for Q-switched operation.

Kerr-lens mode-locking (KLM) is an elegant passive technique that exploits the non-linear Kerr effect. This is an effect that relies on a high peak power pulse, in a Gaussian transverse mode, which self focuses due to a non-linear refractive index change $\Delta n = n_2 I$ (where I is the optical intensity). It is highly suited to ultrafast lasers with large gain bandwidths such as Ti:sapphire, or Ce:LiCAF, which are capable of easily generating pulses with durations of less than 100 fs.

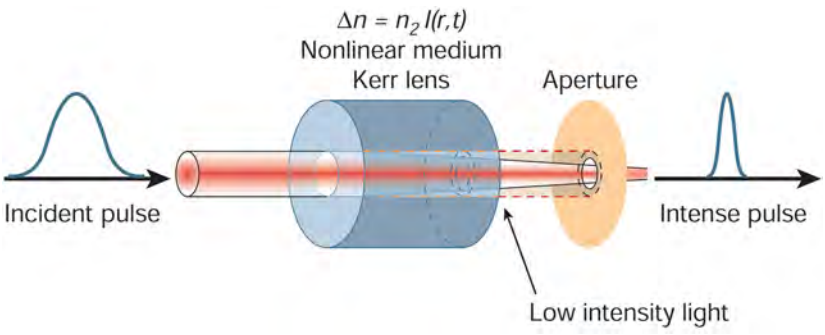

Figure 2.7: A Kerr-lens with a hard aperture that transmits intense pulses while increasing loss for low intensity light [58].

To create a saturable absorber using KLM requires a hard or soft aperture, to respectively reduce the loss or increase the gain provided to a resonating pulse compared to continuous-wave. Simple examples of this are a pinhole (hard), or a smaller pump focus (soft) that matches the KLM cavity mode better compared with the CW mode. Figure 2.7 depicts a hard aperture adjacent to the Kerr-lens, which exhibits almost no losses for an intense pulse while blocking a fraction of the low intensity light. Inside a laser cavity, the Kerr-lens would ideally also be the gain medium, particularly given that there is usually a small waist in the gain medium, thereby maximising the Kerr effect. Although the optical Kerr effect predates KLM by several decades [64], KLM was dubbed magic mode-locking as it was not thoroughly understood to be the mechanism of self mode-locking in Ti:sapphire lasers [65]. However, it was later explained and techniques for engineering KLM lasers began to improve [66, 67].

The aforementioned techniques can be used simultaneously within a laser resonator without disrupting each other. For example, a SESAM and KLM; The SESAM provides more reliable self-starting operation, while KLM improves ultrashort pulse generation by producing shorter pulses. Increasing the power output from such a laser can be done simply and effectively without modifying a laser resonator, using extra-cavity amplifiers, which often require the pulses to be stretched in time prior to amplification to reduce intensity and avoid damage to optics [68].

Active Mode-Locking

Active mode-locking techniques require modulation of the gain or loss, and tend to result in longer pulse durations than passive techniques. This is because, as shown in 2.8, the modulation originates from an external modulator which is often driven by a sinusoidal waveform. Unlike passive modulators, the modulation does not depend on the laser pulse, so there is no mechanism to produce pulses that are significantly shorter than the window of modulation. The frequency of modulation must also be matched to the round-trip time of the cavity for stable operation, unlike passive mode-locking which needs no external control. Devices such as acousto-optic and electro-optic modulators can be used to actively mode-lock lasers by modulating the loss of the laser resonator at a frequency matched to the round trip time (or a rational harmonic) of the resonating pulse.

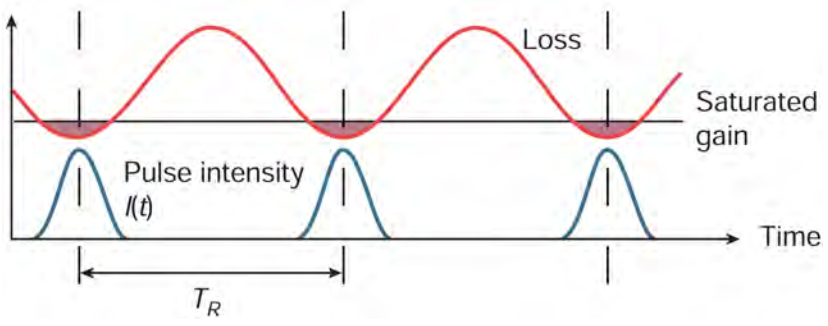

Figure 2.8: Active mode-locking caused by modulation of loss [58].

Active Mode-Locking by Synchronous Pumping

Synchronous pumping is a means of achieving active mode-locking, that does not necessarily require electronic controllers, initiated by modulation of the gain. It was introduced in dye lasers of the 1970s [69] and developed theoretically and experimentally well into the 1980s [70, 71]. It provides a simple mechanism for mode-locking and potentially increases efficiency, if the gain decays quickly over time, since the resonating pulse is driven towards maximal gain.

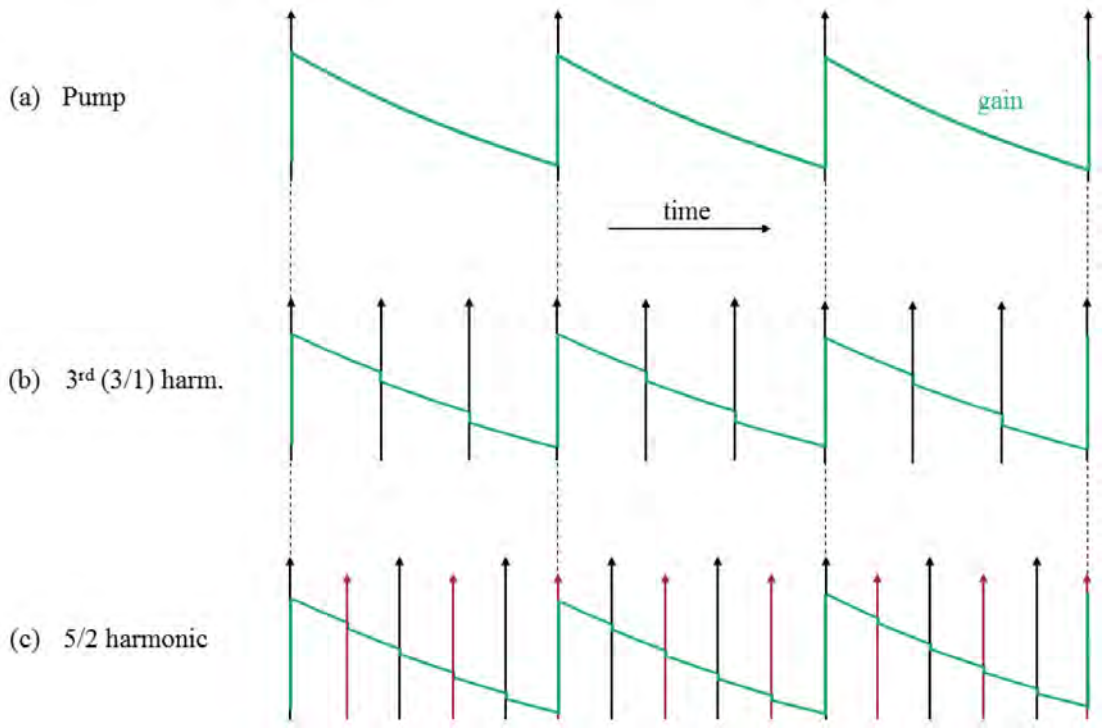

Figure 2.9: Synchronously pumped gain variation, from [12]. The arrows represent the resonating pulse inside a laser cavity being pumped; the red arrows indicate a second pulse.

When a mode-locked laser is used as a pump laser, the output of the laser being pumped will be mode-locked if the ratio of the two lasers' cavity length is a rational number, as shown in figure 2.9. Choosing a cavity length that is a particular rational harmonic of the synchronous pump laser is an effective method of increasing the PRF of the laser being pumped. For example, the 3rd harmonic is arranged by setting the laser cavity length to be one third of the pump laser's; a single pulse is resonating but the output PRF is triple that of the pump laser. While fundamental mode-locking refers to the case of a single pulse resonating within a laser cavity, harmonic mode-locking is a phenomenon whereby multiple pulses resonate within a laser cavity, effectively increasing its repetition rate. For example, the 5/2 harmonic is arranged for a cavity length that is 0.4 times the length of the pump laser, which causes two pulses to resonate for an output PRF that is five times that of the pump laser. Of course, the pulse energy in this arrangement is lower for fixed average power, and the average gain:loss ratio is lower.

In the past, both dye lasers and Ti:sapphire lasers have been mode-locked by synchonous pumping, each with a different level of sensitivity to variations in cavity length. This was attributed to the upper-state lifetime of the gain medium, which differs by orders of magnitude (Ti:sapphire ~3.2 µs, dye laser ~3 ns) and influences the amplitude of the gain modulation. One author described the effect of synchronously pumping a Ti:sapphire laser as filtering the gain spikes of pump pulses [72], resulting in very little modulation of the gain. For a dye laser, the gain may decay entirely in between pump pulses, resulting in a more stringent requirement for matching the cavity length of the dye laser to its synchronous pump laser.

Drift instability of synchronously pumped mode-locked dye lasers was studied extensively, with detrimental effects surrounding cavity length jitter on the order of 1 µm [73]. This limited their operational stability due to cavity length fluctuation from environmental vibrations. This sensitivity was so severe, that a number of groups worked to stabilise the output using active and passive techniques. Active techniques were often implemented by maintaining maximum power, minimum pulse duration, or a fixed oscillation wavelength [74–76]. Passive techniques often relied on forcing a low energy satellite pulse to resonate within the cavity just ahead of the main pulse (e.g. by using a coupled cavity of slightly shorter length [77, 78], or a modified end-mirror [79]) to overpower the effect of spontaneous emission and provide gain to the leading edge of the main pulse. While these techniques are useful, they inevitably add complexity to the system.

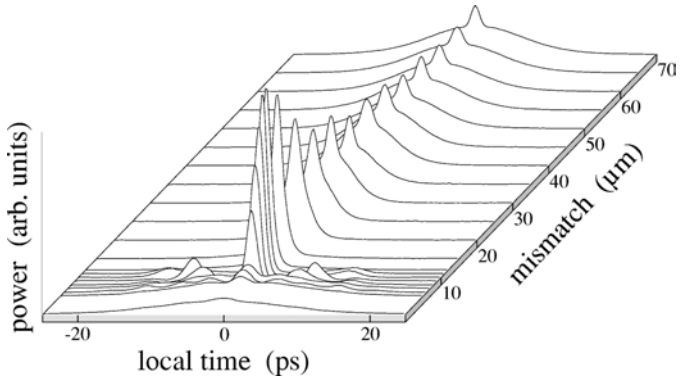

Figure 2.10: Drift instabilities of a synchronously pumped dye laser, from [73].

The detuning effect is not symmetrical; a positive cavity length mismatch has a greater range of stability [70]. This is due to the asymmetry of the gain profile, for which there is a steep incline created by the arrival of a pump pulse, followed by a relatively gradual decline that results from relaxation. Figure 2.10 indicates how this affects mode-locking. Shortening the cavity from synchronism to the pump rapidly disturbs the otherwise short pulses and causes multi-pulsing or much longer pulses. This is due to the resonating pulse being forced towards the steep gain incline, which results in a large gain differential over the length of the pulse. Increasing the cavity length results in a more gradual reduction of peak power as the gain declines more gradually after the arrival of a pump pulse. Relatively small

cavity length mismatches cause the resonating pulse to reformat on each round trip. If the cavity is too short, the tail end of the pulse is amplified more than the front; conversely, if the cavity is too long, the front end is amplified more than the tail. For example, a +70 µm cavity length mismatch requires the peak of the resonating pulse to shift by 0.23 ps to maintain synchronicity. Since the gain modulation is small for positive mismatch, the pulse must be relatively long compared to this shift.

Hybrid Mode-Locking

Active and passive techniques of mode-locking can be implemented simultaneously, which is referred to as hybrid mode-locking. For example, synchronous pumping may be used in conjunction with KLM. In this case, mode-locking is initiated by gain modulation from the synchronous pump, and ultrashort pulses are maintained by the non-linear effect of Kerr-lensing, combined with a hard or soft aperture. While it is advantageous to have self-starting mode-locking by synchronous pumping, detuning the cavity length from synchronicity may still have a detrimental effect on the nature of mode-locking. The modulation strength of the gain (or loss) plays a significant role, determined by the upper-state lifetime of the gain medium, in the case of synchronous pumping. For example, early researchers of hybrid-mode-locked Ti:sapphire lasers (which has weak modulation) could significantly mismatch the cavity length (1.5 mm) without losing hybrid mode-locking [72]. Another group found that the synchronicity between the pump laser and Ti:sapphire laser ceased when an absorbed pump power threshold of 2.5 W was surpassed [80]. The maximum allowable detuning of cavity length was also found to increase with pump power, as the passive mode-locking effects of KLM take hold: self-phase modulation in conjuction with net anomalous intra-cavity dispersion promote a single intense pulse via gain guiding or implementation of a hard aperture.

More recent studies into the behaviour of hybrid-mode-locked lasers as they are subject to detuning have revealed several states of mode-locking [81]. Indeed, in the case of weak modulation, there is a particularly stable asynchronous mode-locking (ASM) state that exists for significant detuning. In ASM, mode-locking is initiated by the modulation introduced by an active mechanism (such as synchronous pumping) but it is the saturable loss of the passive mechanism (such as KLM) that maintains it and permits an increased level of detuning, as was found with Ti:sapphire lasers. For increased modulation strength, the permissible range of cavity lengths for ASM diminishes. This is shown in figure 2.11. The synchronous states of mode-locking shown here (short, short with oscillation, and long with high chirp) take over from ASM, for increased modulation strength.

The short state represents minimal detuning, where the PRF of the laser closely matches the modulation frequency. In this case, the resonating pulse reforms (shifts slightly) each round trip to maintain synchronicity, but it is relatively stable. Likewise, the long pulse

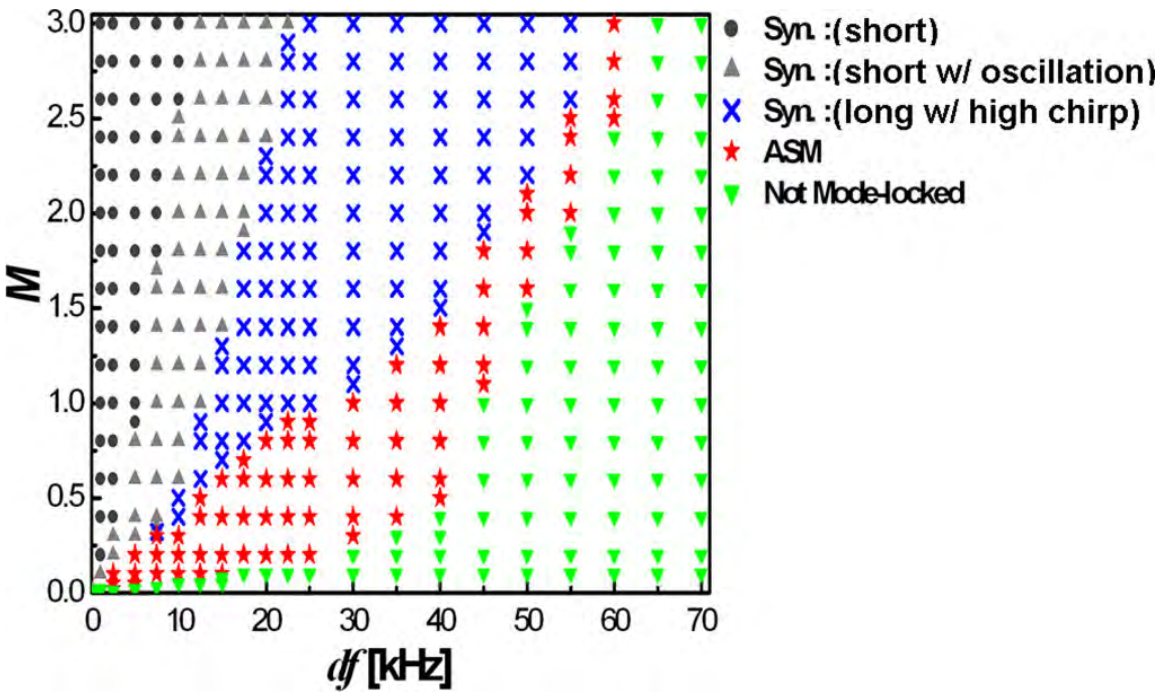

Figure 2.11: Hybrid mode-locking states for various modulation strength M (modulation of gain or loss) and detuning df (from synchronicity to round trip time) from [81].

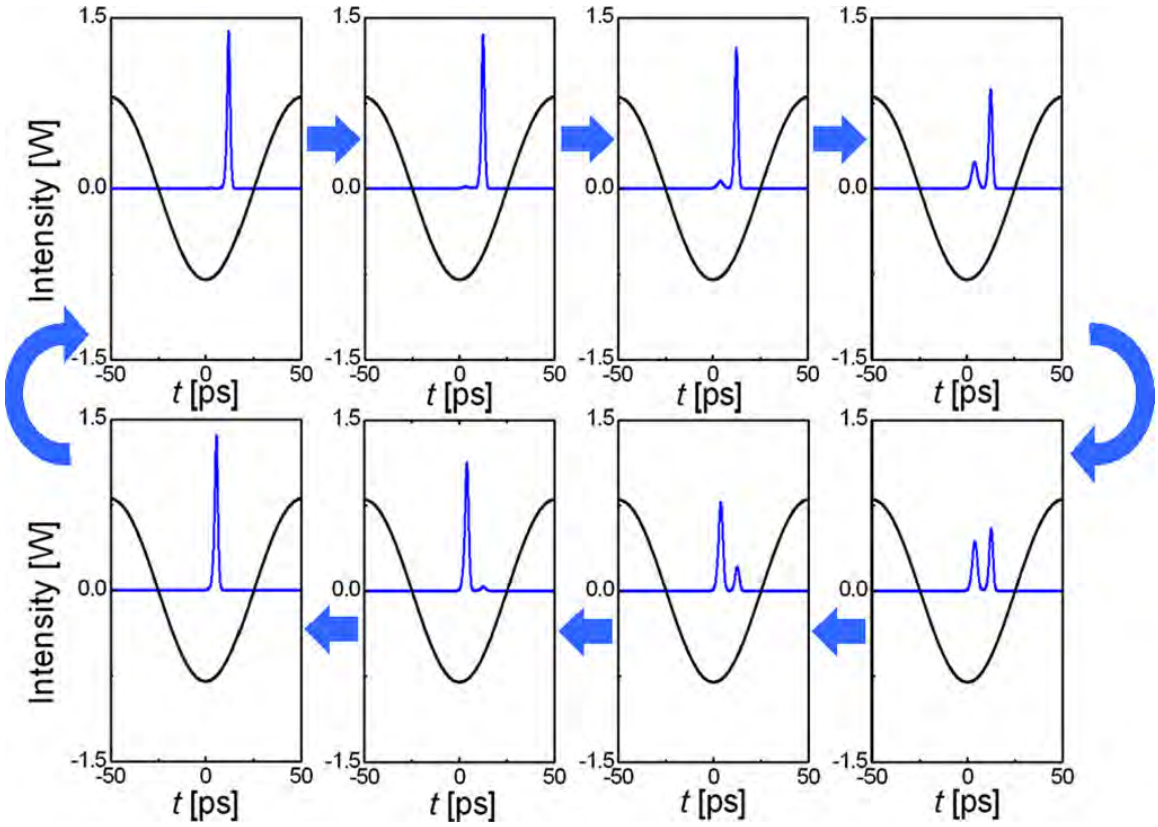

Figure 2.12: Ultrashort pulses with oscillation via hybrid mode-locking due to a cavity length mismatch , from [81]. Each stage corresponds to approximately 100 additional round-trips.

state is relatively stable, and less affected by the passive KLM mechanism. On the other hand, the short pulse state with oscillation exists between the two of these, and is depicted in figure 2.12. The black line depicts the modulation of loss used in some active mode-locking schemes. The blue line depicts the ultrashort pulse formed by hybrid mode-locking, which encounters more loss as it drifts further from synchronicity. In this case, the dominant pulse drifts away from synchronicity faster than it can reform, and is superceded by a pulse with closer temporal overlap to gain modulation. This state, and indeed the transition between each of the mode-locking states, is to be considered unstable.

While detuning an actively mode-locked laser from synchronicity to the mode-locking mechanism may potentially be useful as a tool to control the output pulse duration, it is an extra complexity that can introduce undesirable instability, particularly on the transition between each of the mode-locking states. For a hybrid mode-locked laser, such as the cerium laser that this thesis focuses on, the short pulse regime and the transition to a state of oscillation is of particular importance. Oscillation can arise simply from detuning of the cavity length, causing the resonating pulse to decline and a new pulse to form; this complicates aspects of laser operation such as efficiency, non-linear effects, characterisation of pulse duration, and the potential for synchronisation to another laser.

2.3 Dispersion Management

In a medium with a high refractive index, light effectively travels more slowly due to phase delays caused by atoms and molecules. Chromatic dispersion is a well known phenomenon in which the phase velocity of light in a medium is dependent on the light's wavelength, along with the refractive index n. Mathematically, that is to say that $n = n(\lambda)$. Notation using angular frequency $\omega = 2\pi\nu$ and wavenumber $k = 2\pi n/\lambda$ simplifies mathematics, $k = k(\omega)$. Note that λ here is the vacuum wavelength of light. The Taylor series expansion of k is given by equation 2.2. The first term is simply a common phase shift so does not affect the pulse shape. The second term is a time delay that also does not affect pulse shape, but contains the inverse group velocity. The third term contains the inverse group velocity dispersion (GVD), which is the greatest contributor to dispersion.

$$k(\omega) = k_0 + \frac{\partial k}{\partial \omega}(\omega - \omega_0) + \frac{1}{2} \cdot \frac{\partial^2 k}{\partial \omega^2}(\omega - \omega_0)^2 + \frac{1}{6} \cdot \frac{\partial^3 k}{\partial \omega^3}(\omega - \omega_0)^3 + \ldots \tag{2.2}$$

where ω_0 is the central angular frequency

GVD and third order GVD (TOGVD) of a known material may be calculated simply by using the material's Sellmeier equations (to calculate $n(\lambda)$) and equation 2.3 and 2.4.

$$\mathrm{GVD}(\omega_0) = \left(\frac{\partial^2 k}{\partial \omega^2}\right)_{\omega=\omega_0} = \frac{2}{c}\left(\frac{\partial n}{\partial \omega}\right)_{\omega=\omega_0} + \frac{\omega_0}{c}\left(\frac{\partial^2 n}{\partial \omega^2}\right)_{\omega=\omega_0} \quad (2.3)$$

$$\mathrm{TOD}(\omega_0) = \left(\frac{\partial^3 k}{\partial \omega^3}\right)_{\omega=\omega_0} = \frac{3}{c}\left(\frac{\partial^2 n}{\partial \omega^2}\right)_{\omega=\omega_0} + \frac{\omega_0}{c}\left(\frac{\partial^3 n}{\partial \omega^3}\right)_{\omega=\omega_0} \quad (2.4)$$

where c is the speed of light.

A pulse of light that propagates through a dispersive medium will broaden in time as the frequencies that comprise it effectively travel slower or faster than the central frequency. This produces a frequency dependent phase delay across the spectrum of the pulse, and results in a chirped pulse, shown in figure 2.13. The level of chirp is reasonably predictable when propagating through a known distance of a known material. Group delay dispersion (GDD) is the term that describes the dispersive effect, and is simply the GVD of the material multiplied by distance of propagation.

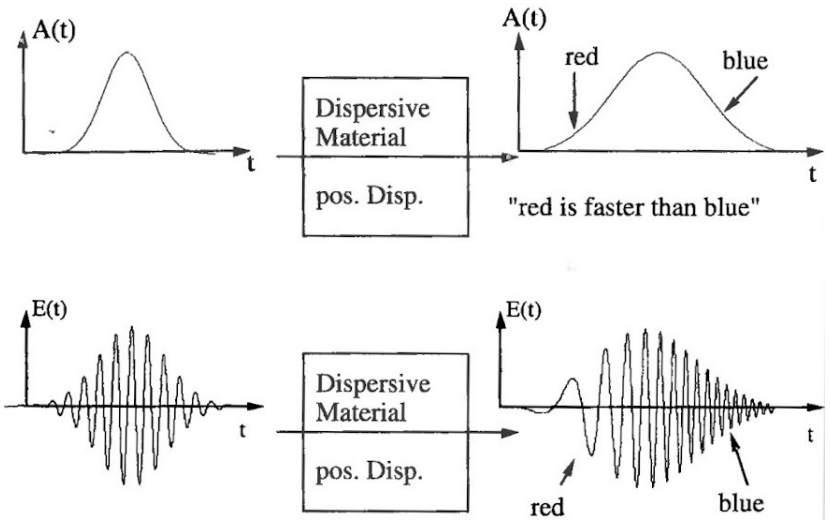

Figure 2.13: The amplitude envelope and electric field of a chirped optical pulse formed by positive material dispersion [82].

In relation to laser cavities, especially mode-locked ones which are affected by the phase relationship between longitudinal modes, chromatic dispersion plays an important role; it can be a hindrance to generating ultrashort pulses, but sometimes a useful mechanism as well. It is more often a hinderance since mode-locked lasers are usually desired for their ultrashort pulse capabilities and chromatic dispersion that is not compensated for causes pulses to temporally broaden, and become chirped. A chirped pulse of light can be engineered using dispersion to be positively or negatively chirped, or to be unchirped (bandwidth-limited). To produce a relatively unchirped pulse, the overall GDD affecting the pulse during its generation must be balanced to be zero. Higher orders of dispersion, the next most significant being third-order dispersion (TOD, which is to TOGVD as GDD is to GVD), are more challenging to compensate for whilst balancing GDD. Common methods of pulse compression include

prism or grating pairs, and chirped mirrors, all of which are capable of balancing GDD and TOD at certain wavelengths. However, grating pairs and chirped mirrors introduce high losses for some regions, such as the UV, so may not be useable for intra-cavity pulse compression. Dispersion management inside a laser cavity is vital for generating the shortest possible pulses using KLM, which requires high peak powers and relies on a delicate balance between spectral broadening via self-phase modulation (which introduces a chirp onto the resonating pulse) and dispersion compensation which in-turn affects Kerr-lensing. A small amount of anomalous dispersion is necessary to balance these effectively.

Prism pairs were first used to compensate dispersion in 1984 [83], and rapidly studied and utilised thereafter [84, 85]. While the prism material itself introduces normal (positive) dispersion, a pair of prisms can result in net anomalous (negative) dispersion by causing different wavlengths of light to pass through different amounts of material in the second prism. Normally, shorter wavelengths refract more than longer wavelengths, causing them to propagate through less material in the second prism. Hence, shorter wavelengths encounter less material dispersion than longer ones, which can be visualised by them traversing the prism pair arrangement more quickly than longer wavelengths. Normally, material dispersion causese longer wavelengths to propagate more quickly, so the prism pair can be used to compensate for dispersion from various sources i.e. the optical components of a laser cavity.

During the 1990s, prism pairs were crucial to the rapid inception of Ti:sapphire as the dominant ultrafast laser [65, 66]. They were widely used for intra-cavity dispersion compensation, reducing pulse durations and increasing intensity to the point that enabled KLM. The standard configuration for a general prism pair within a laser cavity is shown in figure 2.14 (adapted from [86]) which is followed by a plane mirror as a retro-reflector. While this is for a general case, the cut angle α can be fixed for a Brewster's-cut pair, and the prisms set to the angle of minimum deviation whereby $\theta_0 = \theta_3$.

When adjusting an intra-cavity prism pair, the two most significant variables are usually the separation and insertion. With respect to the above notation, the geometry of a particular prism pair arrangement can be summarised by equations 2.5 and 2.6. The term L is the prism separation (the distance between faces) and L_g describes the propagation distance through the prism material (which is akin to insertion).

$$L = \frac{s}{\cos\theta_3} \tag{2.5}$$

$$L_g = (t - s\tan\theta_3)\,\frac{\sin\alpha}{\cos\theta_1} \tag{2.6}$$

The GDD of a single pass through this general prism pair, using the variables depicted in figure 2.14, is given by equation 2.7, derived in [86] using finite ray-tracing. The first and third terms govern how the GDD is affected by material dispersion. The middle term represents

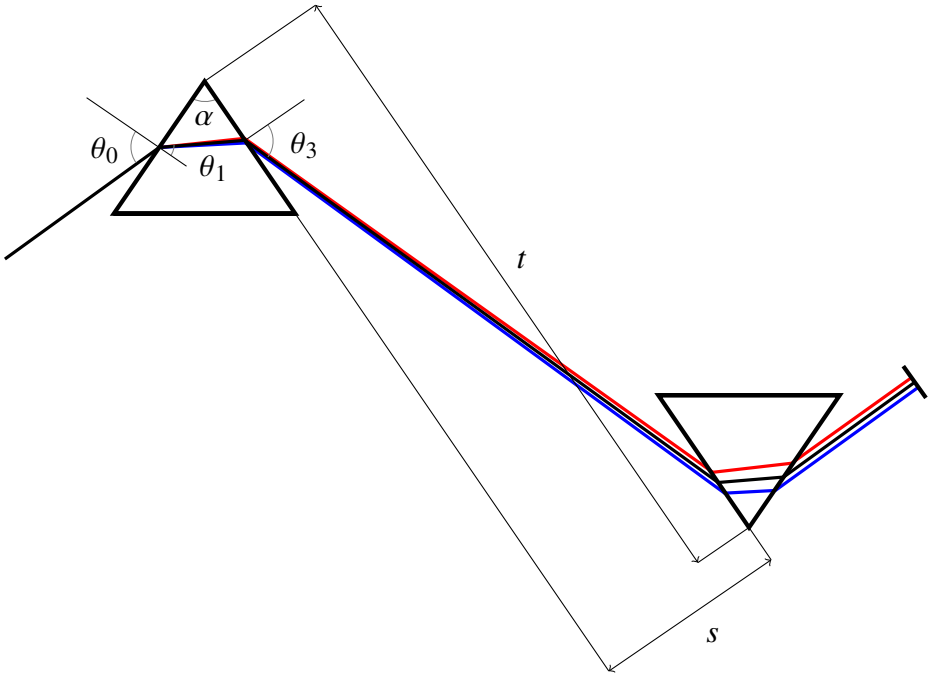

Figure 2.14: A simplified diagram of a prism pair in parallel face configuration used for intra-cavity dispersion control, adapted from [86].

how separation between the prisms governs GDD, and it is strictly negative; for prisms with normal material dispersion, increasing their separation will strictly increase the anomalous dispersion that they introduce into a propagating pulse. The derivative of the GDD term, with respect to ω, is the TOD that is introduced by the pair, and shown in equation 2.8. These analytical expressions can be used to accurately and precisely calculate the GDD and TOD of a prism pair with any prism angle α and any incident angle θ_0 in a parallel configuration.

In the UV, prism pairs cut at Brewster's angle exhibit very low losses compared to chirped mirrors, which are currently limited to a reflectivity of 92% [87]. Brewster's-cut prisms are therefore the ideal starting point for intra-cavity dispersion mangement inside a UV laser. Hence, these equations are utilised in chapter 5 for a cerium laser in order to invoke KLM.

$$\left.\frac{\mathrm{d}^2\Psi}{\mathrm{d}\omega^2}\right|_{\omega_0} = \left[-\frac{n\omega_0}{c}L_g\left(\frac{\mathrm{d}\theta_1}{\mathrm{d}\omega}\right)^2 - \frac{\omega_0}{c}\left(\frac{s}{\cos\theta_3}\right)\left(\frac{\mathrm{d}\theta_3}{\mathrm{d}\omega}\right)^2 + \frac{L_g}{c}\left(2\frac{\mathrm{d}n}{\mathrm{d}\omega} + \omega_0\frac{\mathrm{d}^2n}{\mathrm{d}\omega^2}\right)\right]\Bigg|_{\omega_0} \tag{2.7}$$

$$\begin{aligned}\left.\frac{\mathrm{d}^3\Psi}{\mathrm{d}\omega^3}\right|_{\omega_0} = {} & \frac{\omega_0}{c}\frac{\mathrm{d}^2n}{\mathrm{d}\omega^2}\frac{\mathrm{d}L_g}{\mathrm{d}\omega} + \frac{1}{\omega_0}\left(\frac{\mathrm{d}^2\Psi}{\mathrm{d}\omega^2} - \frac{2L_g}{c}\frac{\mathrm{d}n}{\mathrm{d}\omega}\right) + \frac{2}{c}\frac{\mathrm{d}n}{\mathrm{d}\omega}\frac{\mathrm{d}L_g}{\mathrm{d}\omega} + \frac{2L_g}{c}\frac{\mathrm{d}^2n}{\mathrm{d}\omega^2} \\ & + \frac{L_g\omega_0}{c}\frac{\mathrm{d}^3n}{\mathrm{d}\omega^3} - \frac{\omega_0}{c}\frac{s}{\cos^2\theta_3}\sin\theta_3\left(\frac{\mathrm{d}\theta_3}{\mathrm{d}\omega}\right)^3 - \left(\frac{2\omega_0 s}{c\cos\theta_3}\right)\left(\frac{\mathrm{d}\theta_3}{\mathrm{d}\omega}\frac{\mathrm{d}^2\theta_3}{\mathrm{d}\omega^2}\right) \\ & - \left(\frac{\omega_0}{c}\frac{\mathrm{d}n}{\mathrm{d}\omega}L_g + \frac{n\omega_0}{c}\frac{\mathrm{d}L_g}{\mathrm{d}\omega}\right)\left(\frac{\mathrm{d}\theta_1}{\mathrm{d}\omega}\right)^2 - \frac{n\omega_0}{c}L_g\left(2\frac{\mathrm{d}\theta_1}{\mathrm{d}\omega}\frac{\mathrm{d}^2\theta_1}{\mathrm{d}\omega^2}\right)\end{aligned} \tag{2.8}$$

where

$$L = \frac{s}{\cos\theta_3} \tag{2.9}$$

$$L_g = (t - s\tan\theta_3)\,\frac{\sin\alpha}{\cos\theta_1} \tag{2.10}$$

$$\frac{\mathrm{d}L}{\mathrm{d}\omega} = \frac{s\tan\theta_3}{\cos\theta_3}\frac{\mathrm{d}\theta_3}{\mathrm{d}\omega} \tag{2.11}$$

$$\frac{\mathrm{d}L_g}{\mathrm{d}\omega} = L_g\tan\theta_1\frac{\mathrm{d}\theta_1}{\mathrm{d}\omega} - \frac{s}{\cos^2\theta_3}\frac{\sin\alpha}{\cos\theta_1}\frac{\mathrm{d}\theta_3}{\mathrm{d}\omega} \tag{2.12}$$

$$\frac{\mathrm{d}\theta_1}{\mathrm{d}\omega} = -\frac{\tan\theta_1}{n}\frac{\mathrm{d}n}{\mathrm{d}\omega} \tag{2.13}$$

$$\frac{\mathrm{d}^2\theta_1}{\mathrm{d}\omega^2} = -\frac{1}{n\cos^2\theta_1}\frac{\mathrm{d}\theta_1}{\mathrm{d}\omega}\frac{\mathrm{d}n}{\mathrm{d}\omega} + \frac{\tan\theta_1}{n^2}\left(\frac{\mathrm{d}n}{\mathrm{d}\omega}\right)^2 - \frac{\tan\theta_1}{n}\frac{\mathrm{d}^2n}{\mathrm{d}\omega^2} \tag{2.14}$$

$$\frac{\mathrm{d}\theta_3}{\mathrm{d}\omega} = \frac{\sin\alpha}{\cos\theta_1\cos\theta_3}\frac{\mathrm{d}n}{\mathrm{d}\omega} \tag{2.15}$$

$$\frac{\mathrm{d}^2\theta_3}{\mathrm{d}\omega^2} = \frac{\sin\alpha}{\cos\theta_1\cos\theta_3}\frac{\mathrm{d}^2n}{\mathrm{d}\omega^2} + \frac{\sin\alpha\tan\theta_1}{\cos\theta_1\cos\theta_3}\frac{\mathrm{d}\theta_1}{\mathrm{d}\omega}\frac{\mathrm{d}n}{\mathrm{d}\omega} + \frac{\sin\alpha\tan\theta_3}{\cos\theta_1\cos\theta_3}\frac{\mathrm{d}\theta_3}{\mathrm{d}\omega}\frac{\mathrm{d}n}{\mathrm{d}\omega} \tag{2.16}$$

2.4 Ultrashort Pulse Characterisation

To measure the duration of ultrashort pulses on this timescale (femtoseconds or picoseconds) usually requires a probe that is equally as short, or ideally shorter than the pulse. Often, the pulse itself is used as such a probe, which is referred to as autocorrelation. This involves splitting the laser beam into two arms, and then recombining them, usually by focussing them to a common spot inside a medium with a non-linear response, with a detector behind it (e.g. photodiode or power meter). One of the arms has a mechanical delay line that is used to sweep the pulse from one arm through the pulse from the other arm. When the pulses overlap, the non-linear response of the medium is at its maximum, and there is a peak (or trough) in the detected signal. The An example of a non-linear reponse is two-photon absorption (TPA) which is present in many materials [88]; overlapped pulses increase absorption, thereby creating a trough in the signal as the delay line sweeps the pulses through one another. If the shape of the pulse is known (e.g. sech^2 or Gaussian) and the pulses are stable and consistent, then the pulse duration can be determined from the autocorrelation trace. The trace itself represents the convolution of the test pulse with the reference pulse, which in this case is the same thing. To retrieve a pulse duration under these circumstances, one must simply perform a deconvolution based on an assumed pulse shape.

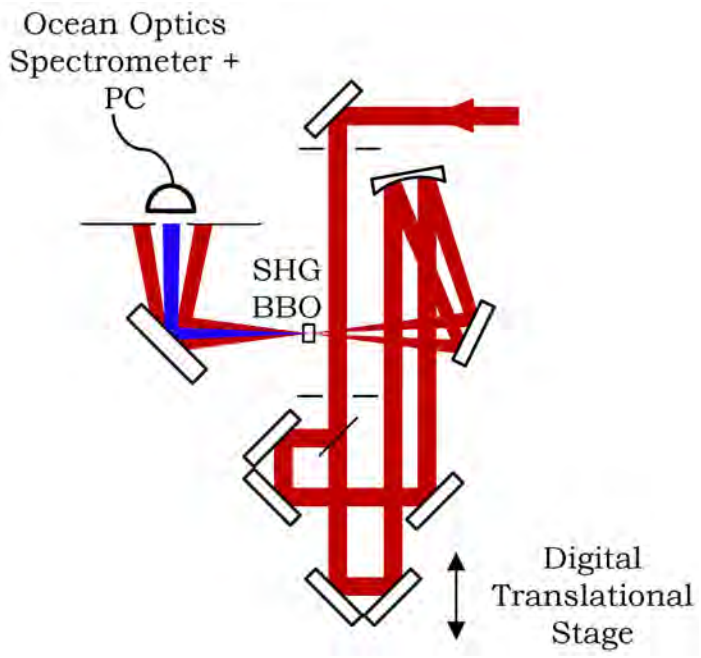

Figure 2.15: Optical layout of MesaPhotonics FROG system, from [89].

While autocorrelation provides the pulse duration and some (but not all) information regarding the temporal shape of the pulse, it does not retrieve the spectral phase; in other words, it alone cannot be used to determine the chirp of a pulse. This capability divides ultrashort pulse characterisation into two distinct groups: those with no phase retrieval, and those that provide information about the spectral phase. Ascertaining the phase relationship of the pulse bandwidth is useful in determining the compressibility of an ultrashort pulse by providing a time-bandwidth product as a measure of how close the pulse is to being transform-limited. Perhaps the most popular technique to do this is frequency resolved optical gating (FROG); a well established method of retrieving the phase of ultrashort pulses since 1991 [90, 91]. It has been used to characterise pulses with a duration of less than 5 fs [92]. FROG is almost as simple as a standard autocorrelation and commercial FROG system are readily available; for example in this thesis FROG systems from MesaPhotonics have been used: the FROG layout shown in figure 2.15. As with autocorrelation, a digital translation stage is used as an optical delay line for the two pulse trains. In this type of FROG system, the non-linear response medium is a phase-matching crystal used for second-harmonic generation (SHG). The primary difference between this technique and autocorrelation using TPA is that both signal and detector contain spectral information that is used to determine the level of chirp.

In some cases, for which the pulse energy is too low, or there are no non-linear media available for autocorrelation, cross-correlation can be performed using a synchronised auxiliary probe laser. The most similar form of cross-correlation compared to the aforementioned techniques is cross-correlation frequency resolved optical gating (X-FROG) [93]. An example of the X-FROG layout is shown in figure 2.16. This method requires a train of reference laser pulses to be synchronised to the test pulses, and frequency mixed (sum or

difference) to generate a signal. In many cases, synchronisation is automatic because both sets of pulses originate from the same laser cavity, and merely have different temporal and spectral properties; it is therefore useful if the spectral region of the test pulses preclude simpler techniques. Compared with SHG FROG, X-FROG also has the advantageous capability of maximising the signal, using high-energy reference pulses in the frequency mixing stage to maximise depletion of the test pulse energy. For sufficently high test pulse energies, $\chi^{(3)}$ methods of gating can also be used in FROG, other than frequency mixing, such as polarisation (PG-FROG) or self-diffraction.

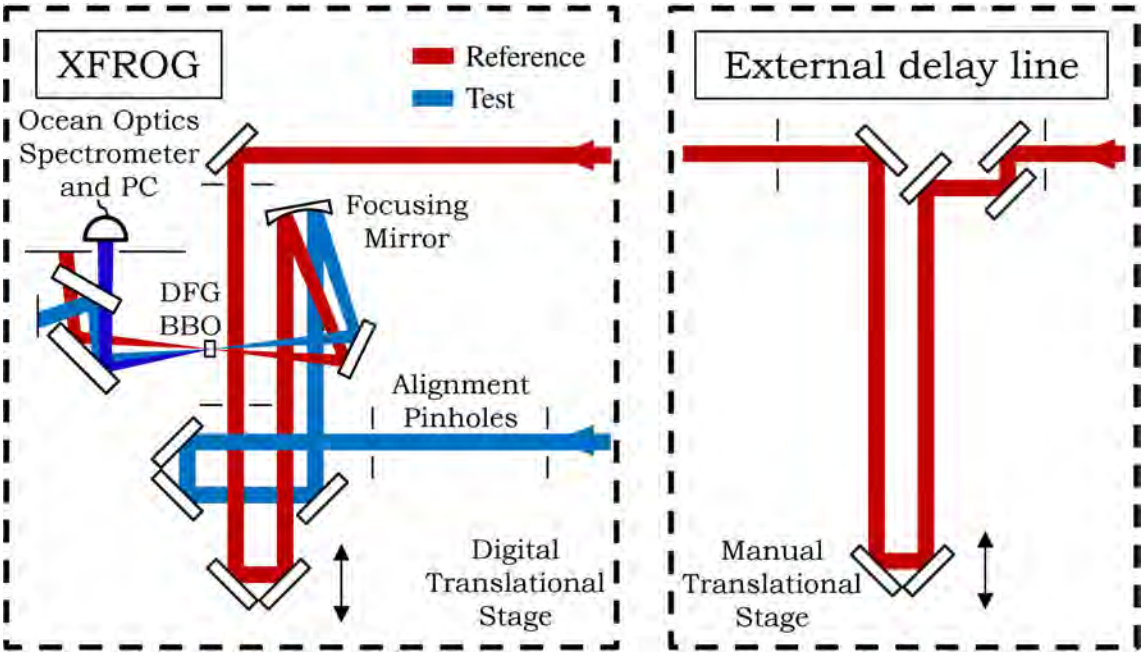

Figure 2.16: Optical layout of MesaPhotonics XFROG system, from [89].

The data that is retrieved from FROG techniques using a spectrometer is in the form of a spectrogram, which is a three dimensional array of time, frequency (wavelength), and intensity. This is shown in figure 2.17 for three examples of simple pulse chirp; indicating the effect of GDD (b) and TOD (c) on a transform-limited pulse. While an autocorrelation would only retrieve a symmetrical result for the temporal intensity, more advanced FROG techniques can retrieve a more accurate result of temporal intensity, in addition to the spectral intensity and phase.

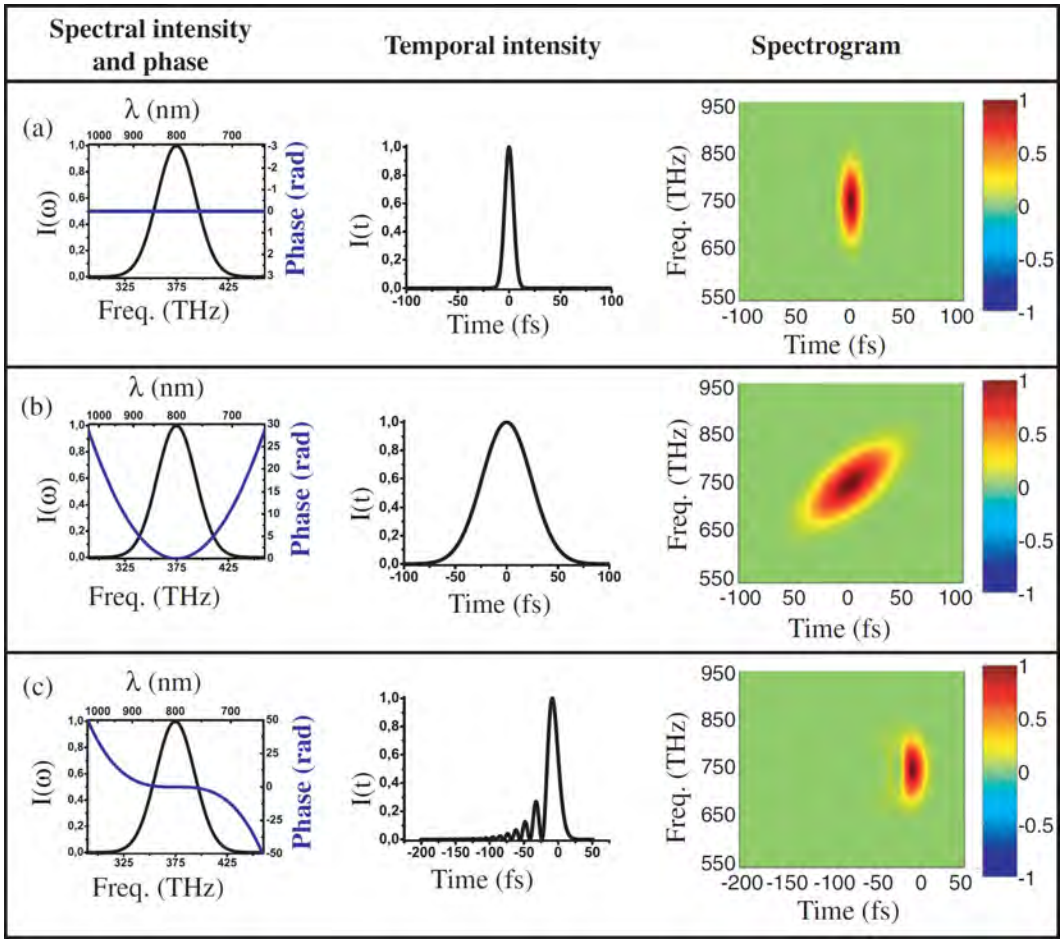

Figure 2.17: Examples of temporal pulse profiles and their corresponding spectral phase profile for: (a) flat phase; (b) quadratic phase; (c) cubic phase, adapted from [94].

Aside from FROG, interferometric techniques can also be used for phase retrieval; a popular method in this group is spectral phase interferometry for direct electric field reconstruction (SPIDER). The basic principle relies on non-linear phase-matching the test pulse and a time-delayed duplicate with a highly chirped pulse (usually produced using another copy of the test pulse) [94]. Each test pulse undergoes frequency mixing with the chirped pulse to generate two pulses with different spectra; once these are filtered and received by a spectrometer, an interferogram is received. A reconstruction algorithm is then used to retrieve the spectral phase. A few examples of interferograms using SPIDER (simulated) are shown in figure 2.18 alongside equivalent SHG FROG spectrograms.

Unfortunately, the common characterisation techniques discussed above are blind to unstable or multiple pulsing [95]. The nonrandom pulse train in figure 2.18 shows the expected results of characterising a highly stable mode-locked laser (nonrandom train) in terms of intensity and phase in the temporal and spectral domains. Unfortunately, when attempting to characterise random trains of pulses, SPIDER and SHG FROG fail to resolve the detailed structure of the pulse train. In particular, SPIDER retrieves almost no information about the intensity or spectral phase of the random pulse trains, whilst FROG may at least indicate the test pulse is unstable. As a comparison, the results from two variants of FROG (PG-FROG and X-FROG) are shown in figure 2.19 using the same random pulse trains. Clearly, these methods retrieve significantly more detail regarding intensity and phase, with results that match the actual pulses more closely. This is primarily the result of using a separate reference pulse, that is stable, to probe the test pulse. In many circumstances, these more advanced FROG variants provide ample information in order to stabilise a laser pulse train. However, in some cases, the reference pulses must come from an auxiliary reference laser that is synchronised with the test laser's pulse train. Synchronising an external laser to a random train of pulses, which exhibit instability or multi-pulsing, is often impossible; techniques that are simpler and less demanding are to be desired.

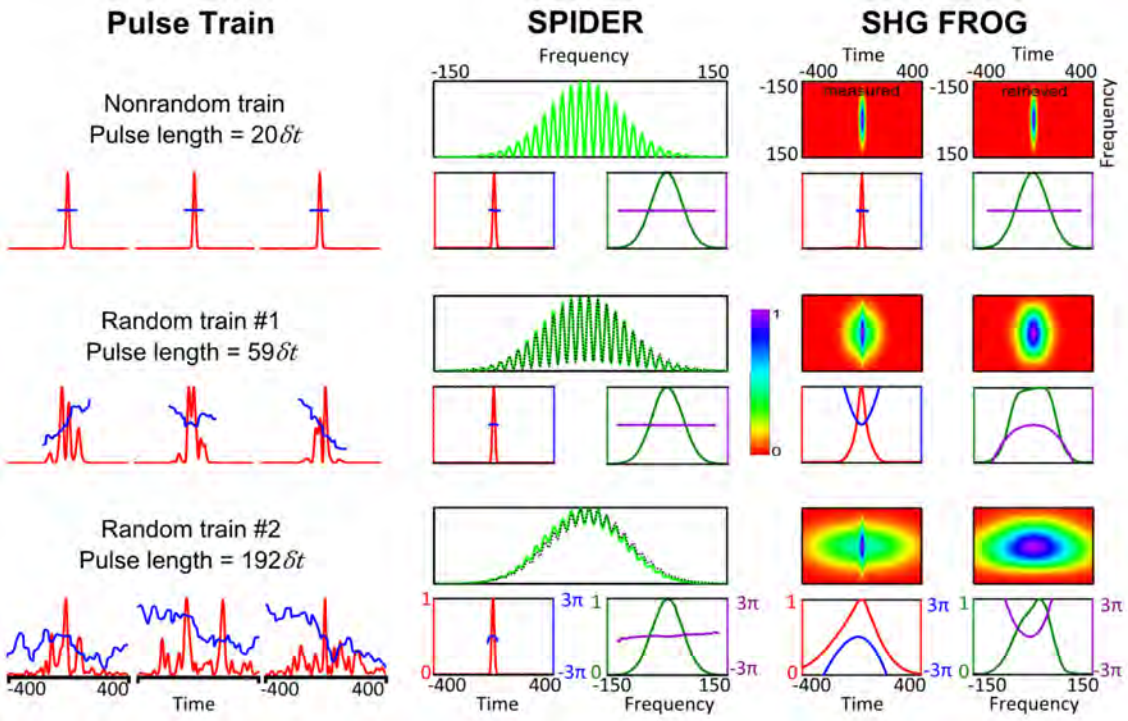

Figure 2.18: Simulated measurement of pulse duration for decreasingly stable pulse trains, using multi-shot techniques SPIDER and SHG FROG, from [96]. Red curves indicate intensity, blue is phase, green is spectrum, purple is spectral phase.

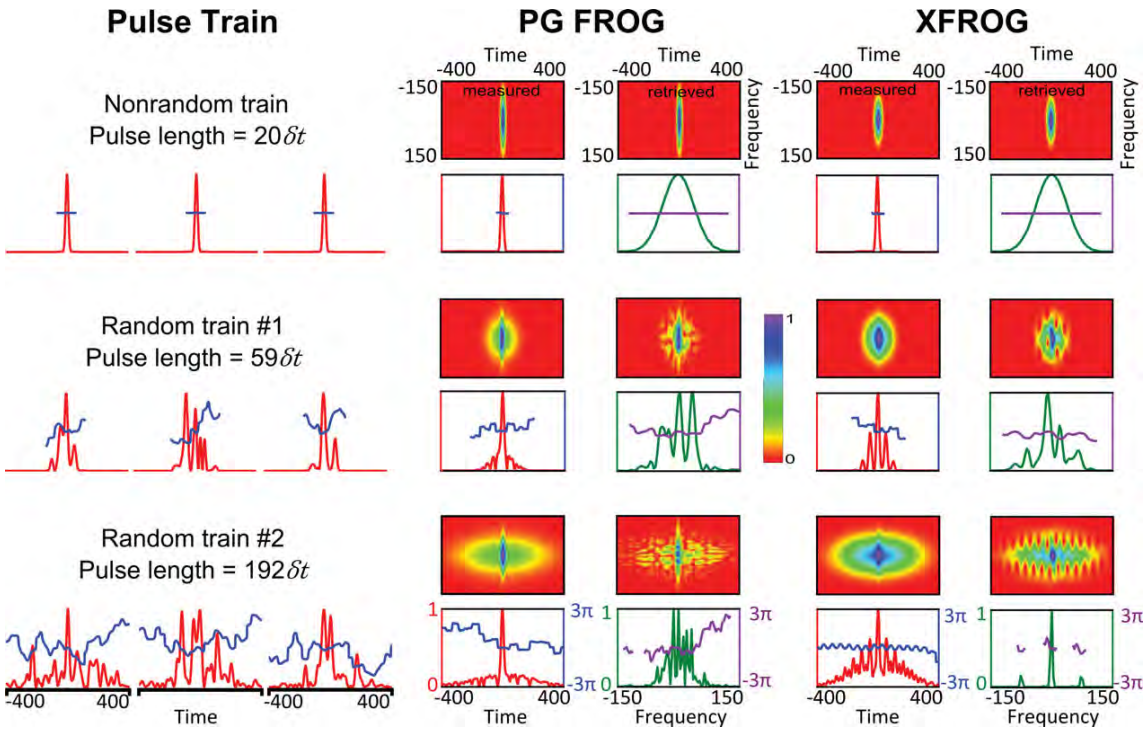

Figure 2.19: Simulated measurement of pulse duration for decreasingly stable pulse trains, using multi-shot techniques PG-FROG and X-FROG, from [96]. The same random trains were used as in figure 2.18. Red curves indicate intensity, blue is phase, green is spectrum, purple is spectral phase.

The characterisation technique that this thesis focuses on is asynchronous cross-correlation; it is presented in detail in chapter 6. This technique was refined to measure shorter pulse durations than previously, and does not require a synchronised reference laser. It is therefore ideal method for characterising the mode-locking stability of an experimental laser system, such as our cerium laser. In comparison, X-FROG would require careful control and knowledge of the relative timing between the cerium laser pulse and the reference laser pulse.

3

Ultraviolet Pulse Generation

Possibly the most well-known direct generated ultraviolet (UV) pulses are from excimer lasers, also called exciplex lasers. These are gas lasers that can produce powerful pulses with joule-level energies. They are arguably the most historically important UV lasers ever, being an effective driver of change on this planet by improving the semiconductor manufacturing industry and thus catalysing the most recent wide-scale revolution in the history of our species: computers. Their utilisation for this task was dicussed in the early 1980s [97] using XeCl and KrF, operating at 308 nm and 248 nm respectively. Their efficacy for lithography was due to their short wavelength and power output. These lasers eventually achieved pulse durations as short as 300 fs, limited by their bandwidth, and are still in use today. However, they are also limited by their size, cost, and robustness.

Today, there are numerous methods of generating UV pulses, each with their distinct advantages and disadvantages that restrict the range of applications for which they can be utilised. This chapter will discuss the most robust solid-state methods of generating high repetition rate, tunable deep-UV (DUV) pulses and CW radiation. These methods can be separated into two different categories: frequency conversion, and direct generation. The efficiency of these two approaches for accessing the DUV varies depending on the desired pulse characterstics. There are always trade-offs, particularly pulse duration, efficiency, tunability, and complexity. It will be shown that cerium based lasers have the potential to be the ideal tool for accessing the DUV region since they deal with all of these issues.

3.1 Non-Linear Frequency Conversion

Ultraviolet laser light was first generated in 1961 [98], almost immediately after the first laser was demonstrated. This was done by frequency doubling a ruby laser in quartz; frequency doubling is still among the most prominent methods of UV pulse generation to this day. Non-linear frequency conversion is the general term for this process, utilised to generate different wavelengths of light from the original laser beam, or beams. This encapsulates frequency doubling, sum frequency mixing (SFM) and difference frequency mixing (DFM). This is a particularly useful technique for accessing regions of the electro-magnetic spectrum for which there are no available laser gain media. The most common form of non-linear frequency conversion is harmonic generation, which is widely used to produce photons that are the sum of the frequency of the original photons i.e. two photons are annihilated in the creation of a new photon with their combined energy. This method requires a birefringent non-linear crystal, such as beta barium borate (BBO) or lithium triborate (LBO). While propagating in the crystal, orthogonally polarised beams (ie ordinary and extraordinary polarisation relative to the optical axis) can have equal refractive indices. Thus the input and output radiation are made to have closely matched, or equal, refractive indices. This process is generally tuned for optimal frequency conversion via crystal angle and/or temperature. Frequency doubling, also known as second harmonic generation, is generally the most simple and efficient type of harmonic generation because it requires a single input laser beam, that does not need to be overlapped with another.

Dye Lasers

In the 1970s, research based on ultrafast dye lasers rose to prominence; they are an important historical stepping stone in the story of ultrafast lasers. A great number of different dyes were discovered, and found to lase directly (with appropriate pumping) from the UV to the near infra-red (NIR) [99]. The primary advantage of dye lasers is their broad bandwidth, for tunability and femtosecond pulse generation. Direct laser action as low as 311 nm was achieved via tuning, from a 2,2"-dimethyl-p-terphenyl dye laser, which was pumped by a 248 nm KrF excimer laser. However, generation of shorter wavelengths (such as those at which Ce:LiCAF operates) required frequency doubling [100]. This was often performed intra-cavity, making use of the high power that is favoured by this non-linear process [101]. While they cover a wide range of wavelengths, the most detrimental aspects of dye lasers are their operating complexity, toxic materials, and degradation. These often necessitate careful protective equipment, a steady flow of dye solution (to allow recovery from triplet states), and regular replacement of the dye. Hence, dye lasers have been mostly superceded by solid-state lasers.

Neodymium Lasers

Infrared lasers that operate around wavelengths of 1 μm can easily be frequency doubled twice (fourth harmonic) as a simple and robust means of producing high power UV light. Neodymium-based diode-pumped solid-state (DPSS) lasers are effective for this task, as they can easily produce average powers of over 100 W, and be passively mode-locked simply using a SESAM. Q-switched Nd:YAG is often doubled twice, first in LBO and then BBO $1064 \rightarrow 532 \rightarrow 266$ nm for high energy nanosecond pulses. YVO_4 is the preferred laser host medium for mode-locked Nd lasers as this material has slightly more bandwidth and can therefore be modelocked to generate 10 ps pulses at 266 nm. These lasers are commercially available for scientific and industrial applications, even at high repetition rates. For example, Photonics Industries International, INC. now offer a DPSS laser system that produces a 3 W average power, 15 ps, 80 MHz pulse train at 266 nm. This is capable of pumping a Ce:LiCAF laser, in fact its output is almost identical to the fourth harmonic stage that is used in this thesis. These Nd-based DPSS lasers are robust, but their bandwidth-limited pulse duration of 5 ps is restrictive, and it is seldom reached.

Fibre Lasers

Fibre lasers also offer a robust means of generating ultrafast IR pulse trains [102] that can be frequency quadrupled to produce average powers over 1 W in the ultraviolet [103, 104]. Recently a fibre laser system was demonstrated, achieving 4.6 W of average power at 258 nm. The laser was operated at 796 kHz, generating 150 fs pulses that could potentially be compressed to 40 fs [105]. The fiber laser itself was chirped-pulse amplified, operating at a centre wavelength of 1032 nm. The frequency quadrupling step to 258 nm was performed in a 0.1 mm long BBO crystal, which had water-cooled sapphire windows bonded to both faces. Despite the additional thermal management, the authors reported significantly reduced beam quality for higher average powers due to thermal effects.

Non-Linear Phase-Matching Crystals

Non-linear optical crystals for frequency doubling to UV $532 \rightarrow 266$ nm at high average powers vary primarily in terms of their efficiency, and robustness. There is a set of crystals that can operate with high efficiency (over 70%), which include ADP, KDP, and DKDP, that are desirable for inertial confinement fusion [106, 107]. The system design using these crystals is of a signficantly greater scale and much lower repetition rate than common mode-locked lasers, usually only of order several pulses per day. They are generally only suitable for high peak powers at low average powers, and as such will not be extensively discussed here. Instead, we discuss borate crystals that are efficient for different reasons, particularly their non-linear coefficient d_{eff} [pm/V] and high average power operation.

Frequency conversion from 532 nm to 266 nm and similar regions is still challenging at high average powers as each non-linear crystal comes with its own set of issues. The choice is therefore heavily dependent on the intended application, by assessing the trade-off of issues for the required optical output, which is generally the desired power. The crystals that are most effective at high-power frequency conversion have practical issues that must be considered, which includes beam walk-off, thermal effects, and hygroscopy. Beam walk-off refers to the angle difference (poynting vector) between the input and generated beams, which can reduce beam quality and conversion efficiency. A summary of some noteable non-linear crystals is shown in table 3.1, including somewhat newer ones.

Table 3.1: The type 1 phase-matching parameters for frequency doubling 532 → 266 nm from [108, 109]; d_{eff} is the non-linear coefficient; α_{UV} is the absorption at 266 nm; ρ is the walk-off angle; acceptance refers to the angular tolerance of phase-matching.

Crystal	Cutoff [nm]	d_{eff} [pm/V]	α_{UV} [cm^{-1}]	ρ [mrad]	Acceptance [mrad·cm]
BBO	180	1.75	<0.17	85	0.19
CLBO	180	0.76	-	33	0.47
KABO	180	0.26	0.10	50.5	0.3
KBBF	160	0.39	0.11	52.8	0.3
RBBF	170	0.34	0.62	56.5	0.28

The most efficient high power crystal with the highest d_{eff} is BBO, despite the large walk-off that it exhibits, which can be dealt with by using a line focus. As much as 14 W of 266 nm light has been generated in BBO, but with moderate PRFs of 100 kHz using 10 ns long pulses [110]. At high PRFs of 80 MHz, 2.9 W of 266 nm light has been generated in BBO [108]. It is only slightly hygroscopic, so it can be used at room temperature or slightly heated to negate the degradation due to humidity. However, thermal effects inhibit the generation of higher powers for high PRF. This is due to absorption and colour centre formation leading to thermal lensing and thus beam degradation. However, the primary limiter of high power generation is thermal dephasing which reduces the efficiency of frequency conversion. Higher PRFs exacerbate thermal effects, because the pulse repetition period is less than the timescale on which heat diffusion occurs. Non-linear absorption of the second and fourth harmonic generation (532 nm and 266 nm) is the most significant contributor to heat deposition. Non-linear absorption can be reduced by heating the BBO crystal to 100-200°C thereby reducing thermal issues for high power generation at higher PRFs or CW operation [108, 111, 112]. A method of countering thermal effects is to use a tight focussing geometry perpendicular to the walk-off plane, such that the generated 266 nm light quickly shifts away from the 532 nm pump to distribute heat accumulation [113]. Heat management and higher quality BBO manufacturing, including fluxless growth, is still underway to take this all-round efficient crystal to higher power for high PRFs [105].

CLBO is a viable alternative, as it exhibits very little absorption and thus fewer thermal

issues. The walk off angle is small, and it has a wide acceptance angle. As much as 28.4 W of 266 nm light has been generated using CLBO using a PRF of 10 kHz [114]. It is almost an ideal solution to high power 266 nm generation. However, it is highly hygroscopic, and as such requires additional engineering effort to prevent it from rapidly deteriorating. It is therefore seldom used in commercial systems but is sufficient for impermanent use, in research for example, and may simply require an elegantly engineered approach for industrial applications.

The several other non-linear crystals mentioned above are relatively new, being recently discovered and researched. They are therefore more scarce, but have shown to be effective at high power generation without hygroscopic effects. For example, $NaSr_3Be_3B_3O_9F_4$ (NSBBF) was recently discovered in 2017 [115] and shown to be efficient at 10 Hz. The development of nonlinear crystals for frequency conversion into the UV is important for many industrial manufacturing and commercially available scientific tools. Due to such high demand, it is a world-wide effort and is likely to significantly improve over the coming decades. This overview is therefore nowhere near exaustive as there are numerous other developments in growing crystals [116, 117].

Ultrafast Non-Linear Frequency Conversion

Tunable and ultrashort pulses are desirable in the UV, as described in the introduction. This is achievable by frequency converting a broad-bandwidth tunable IR source. For example, Ti:sapphire lasers are routinely used to generate few femtosecond pulses, and are converted to the UV using a frequency tripling stage - sum frequency of the fundamental and second harmonic. The acceptance bandwidth of the nonlinear crystal (e.g. in table 3.1) becomes significantly more important for this process, since the phase matching limits the conversion process. Efficient frequency conversion of femtosecond pulses becomes more complex when dealing with the very broad bandwidths that are necessary to support pulse durations of several femtoseconds, such as with Ti:sapphire lasers [118]. This can be done by spatial dispersion (spatial chirp) of the input pulse prior to frequency conversion, so that the phase matching is more closely satsified. This essentially increases the acceptance bandwidth by a factor of 10-100.

For example, a prism pair can spatially separate the wavelengths/frequencies of a pulse prior to frequency conversion. The pulse frequencies are then ideally at the precise angle at which they would be phase matched in a narrow bandwidth scenario. This process is referred to as achromatic phase matching [119, 120] and is shown in figure 3.1. This is one stage of the harmonic frequency conversion process, since for Ti:sapphire pulses frequency tripling is required.

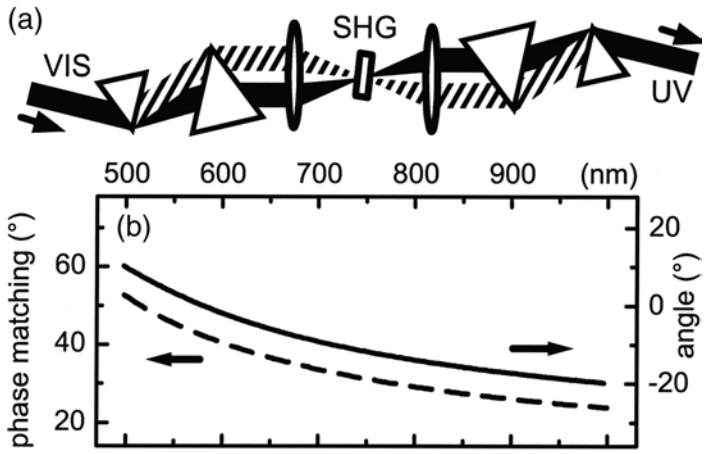

Figure 3.1: Taken from [121]. (a) Phase matching scheme for efficient broad bandwidth second harmonic generation by increasing the acceptance bandwidth. Fused silica prisms are used to spatially disperse visible light, which is frequency converted in BBO, after which the spatial dispersion is compensated for by CaF_2 prisms. (b) Wavelength dependent internal crystal angle for phase matching (dashed line) and the effective angular dispersion that the scheme achieves inside the BBO crystal (solid line).

Achromatic phase matching is efficient enough such that a broad bandwidth, and thus femtosecond pulse duration, can be maintained during conversion into the UV region. Efficiencies can reach 20%, and tuning from 275 to 335 nm has been demonstrated for pulses shorter than 10 fs [121]. However, the optical system required to achieve this was significantly more complex than the single achromatic frequency conversion stage depicted in figure 3.1. Firstly, a non-collinear optical parametric amplifier (NOPA) was used prior to SHG, pumped by a kilohertz chirped-pulse regenerative amplifier Ti:sapphire system, to generate visible pulses. This is a system that is, itself, quite complex. Secondly, achromatic phase matching for higher orders of dispersion was managed using a deformable mirror and required digital computer control to achieve the aforementioned pulse durations. After all this, albeit for an impressive result, additional optics are still necessary for reducing pulse durations by compensating for higher orders of dispersion affecting the UV output pulses.

Non-Linear Frequency Conversion in Gas

Harmonic generation in gas has been useful in generating ultrashort pulses, discussed in the introduction under high harmonic generation. Since only odd harmonics are achievable with this method, frequency tripling of Ti:sapphire is suitable. A new record ultrashort pulse duration of 1.9 fs has been achieved recently, with a bandwidth spanning the deep UV from 210 to 340 nm [122]. A laser-microfabricated gas cell with a variable gas pressure was used, for optimising the efficiency. This process still has the need for dispersion management as the impressive result was obtained with the optical system in vacuum to avoid UV pulse dispersion, for which compensation would be required for simply propagating in air. The pulse energy was 150 nJ, but the repetition rate is not mentioned; this process exhibits issues

for MHz level PRFs.

Similarly, gas-filled fibres have been used for frequency conversion from high intensity NIR pulses to DUV light. Optical fibres offer a robust solution and the strong and extended confinement of high intensity pulses can be subject to soliton dynamics, which can be used to obtain widely tunable DUV pulses via supercontinuum generation. Nearly a decade ago, a hollow-core argon-filled photonic crystal fibre (PCF) was used to produce tunable output from 200-320 nm [123]. The conversion efficiency was no more than 8%, but others theorised that conversion efficiencies of up to 20% could be possible at vacuum UV (VUV) wavelengths [124]. Further research into the interaction of intense optical pulses in hollow-core PCFs led to the development of wide ranging physical processes including: soliton compression down to few-cycle pulses, tunability over the DUV region, soliton-plasma interactions, and Raman frequency combs [125]. Most recently, large hollow core fibres without microstructures were used for frequency conversion, generating pulses in a wide region from 100 to 400 nm, with high energies of up to 16 µJ by injection of 400 µJ, 26 fs pulses from a Ti:sapphire laser system [126]. While these systems utilise the elegance of an optical fibre, they still require a gas cell with variable pressure, and a high power laser system as a starting point.

Cerium Lasers: an Alternative Strategy Based on Nonlinear Frequency Conversion of a Pump Laser followed by direct generation in the UV

The simple solution to generating ultrashort and/or tunable pulses in a region such as the UV is to generate it via a laser that operates at a broad bandwidth directly in that region. Cerium lasers can perform this task exceptionally well in the UV and will be discussed in detail in the following sections. They offer highly efficient laser action over a broad bandwidth, and come with all the advantages that solid-state laser systems offer. This includes long material lifetimes, simple construction, and compactness, whilst operating directly in the UV to avoid complex and less efficient frequency conversion schemes.

Although the fourth-harmonic of neodymium lasers is a convenient pumping tool for a cerium laser, the simplest and thus most desirable approach may be to generate pump light directly from a diode laser. Since 2009, blue and green diode lasers such as gallium nitride (GaN) have been used to directly pump Ti:sapphire thus eliminating the need for a frequency doubled Nd-based laser for small Ti:sapphire systems [127–132]. Shorter wavelengths are more challenging to generate using diode technology, although the 315–400 nm region has been reached. Most recently, a DUV laser diode operating at a record short wavelength of 271.8 nm has been successfully demonstrated using aluminium gallium nitride (AlGaN) [133]. Pulse durations of 50 ns at a repetition frequency of 2 kHz were produced, with a bandwidth of about 0.4 nm. It is shown in the next section that this wavelength is well suited for pumping the Ce:LiCAF gain medium. This advancement is highly promising for the future of Ce:LiCAF lasers, if the power output of this new class of laser diode increases in

the same manner as blue-green diodes did.

The route to tunable UV light using frequency tripled Ti:sapphire versus a Ce:LiCAF laser is visualised in figure 3.2. The choice of starting from near-IR diode lasers is a common preference because of their high power and efficiency, despite the increased complexity. This is advantageous because of the remarkable maturity of DPSS lasers in the 1.06 µm region. Indeed, Nd-based DPSS laser systems which contain additional optics for 2nd or 4th harmonic frequency conversion are commercially available at high power and repetition rates (e.g. 266 nm, 3 W, 100 MHz - Photonics Industries). The comparison between Ti:sapphire and Ce:LiCAF then differs by the number of frequency conversion stages that require active adjustment when wavelength tuning is necessary. In the Ce:LiCAF approach, tuning the wavelength output is performed at the last stage of generation, and thus only the laser requires active adjustment. This differs from wavelength tuning in a frequency tripled Ti:sapphire system, for which two additional adjustments are necessary; the 2nd and 3rd harmonic frequency conversion stages of the Ti:sapphire approach also need to be tuned, in addition to the laser itself.

In addition to the simplified system arrangement, the efficiency of the Ce:LiCAF approaches in figure 3.2 is also significant. Not only are there are fewer conversion stages required, which would otherwise reduce the system's overall efficiency, but the quantum effeciency of Ce:LiCAF is also higher. The quantum efficiency of Ce:LiCAF is > 90% [134], while for Ti:sapphire it is approximately 70% [135].

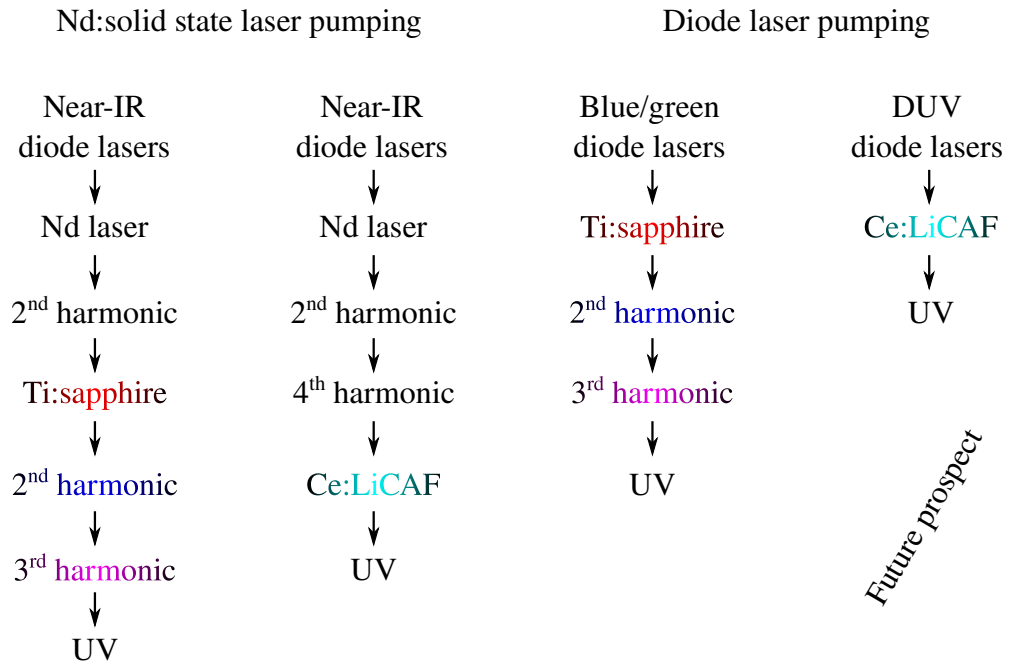

Figure 3.2: The route to tunable UV laser light, inspired by [4]. The coloured text represents a stage which requires active adjustment to wavelength tune the UV output.

3.2 Cerium Lasers

Cerium doping for potential ultraviolet laser gain media based on the 5d → 4f transition was first published by Elias *et al.* over 45 years ago [136]. A host of LaF_3 was doped with trivalent cerium ions Ce^{3+} with conncentrations from 0.01% to 100%. Fluorescence was observed over a wide range between 270 - 450 nm for 100% doping, when pumped with a 250 nm light source via synchrontron radiation. Although laser action was not immediately demonstrated, the discovery of fluorescence in this desirable region led to the development of cerium doped scintillators [137–139]. It was clear that this broad bandwidth of optical emission was promising for potential directly-emitting ultraviolet lasers, as discussed by Elias *et al.* in the 1973 report. This sparked numerous studies and the search for appropriate doping concentrations into suitable host materials began [140].

Fluorescence at shorter wavelengths of 172 nm was also observed in 1976 using neodymium as a dopant, which seemed promising [141, 142]. Lasing was reported in two highly cited reports, but not repeated since [143, 144]. The role of excited state absorption (ESA) was found to prevent lasing [145]. The effort to develop potential VUV solid-state sources continues with studies conducting into the viability of Nd-doping in LiCAF and LiSAF [146, 147]. The search and refinement of prospective hosts for Ce^{3+} was also hindered by ESA, which prevented laser action in many cases such as Ce:YAG. The formation of colour centres (CC), also known as photochromic centres or solarization, was the other significant factor in preventing lasing [148]. These two factors were the most prevalent inhibitors in the search for better Ce^{3+} gain media.

The laser action of Ce^{3+} doped gain media in fluoride hosts, which are the most practical host materials reported to date, is based on the 5d-4f transitions and shown in figure 3.3, for Ce^{3+} ions inside a host material. The free-ion spectrum was studied extensively by Lang in 1936 [149]. The ground configuration of Ce^{3+} consists of a xenon-like core of 54 electrons, over which a valence shell contains one 4f electron. The 4f level is split by the spin orbit interaction into $^2F_{7/2}$ and $^2F_{5/2}$ levels, which are separated by 2,253 cm^{-1}. The 5d energy level is also split by spin orbit interactions into $^2D_{3/2}$ and $^2D_{5/2}$, energy levels at 49,737 and 52,226 cm^{-1}, while the 6s level is located at 86,600 cm^{-1}. The large spatial extent of the 5d wavefunction results in domination of the crystal field interaction, over the spin orbit interaction. This splits the 5d configuration into 4 or 5 broad Stark levels, which are each separated by 5,000 cm^{-1}. The laser transition, 5d → 4f, exhibits a large energy level difference of between 20,000 and 30,000 cm^{-1}. This results in high quantum efficiences of over 90% [134], which arise from a low probablity of non-radiative decay via multi-phonon emission [150].

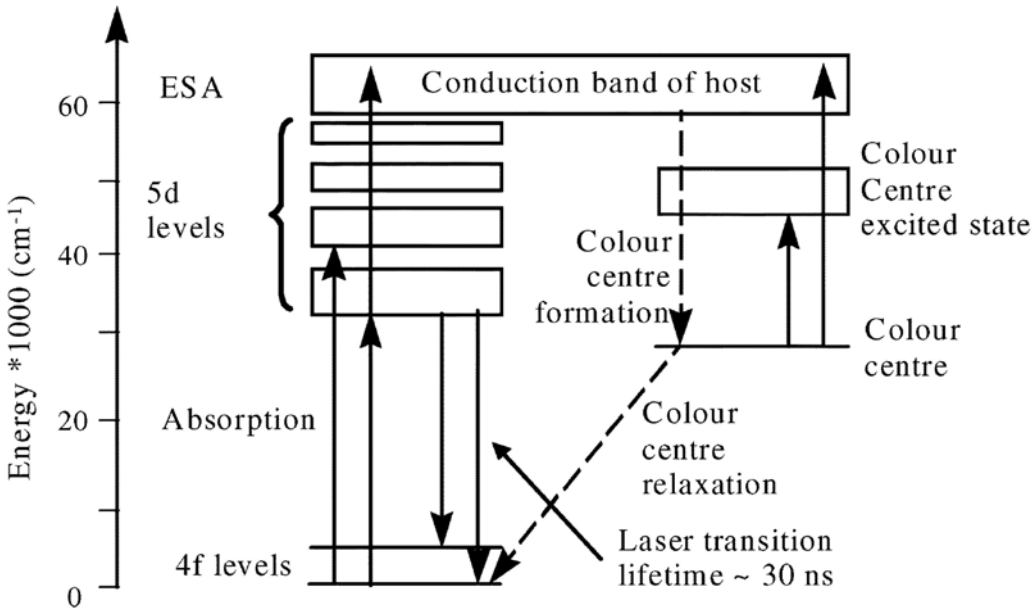

Figure 3.3: Typical energy level structure of cerium doped fluorides from [151].

Figure 3.3 shows the two primary loss mechanisms of cerium-doped fluorides, which are excited state absorption (ESA) and colour centre formation (CC), solarization. ESA describes the transition of an electron into the conduction band by excitation, which in the case of optical pumping is typically a second photon interacting quickly after an initial excitation photon. The formation of a CC may occur when the relaxation of an electron from the conduction band results in it being trapped at a lattice defect or impurity site [151]. The CC may then be excited back into the conduction band, or return to the ground level after relaxation. These mechanisms divert the pump or laser photons away from potential laser transitions to undesirable lattice interactions, and thus reduce the available gain or increase loss. While ESA is difficult to avoid in some materials, CC lifetimes depend on impurity trap depth and temperature, so they may be thermally deactivated. Alternative approaches to reducing the formation of CCs in some host materials include codoping with a charge compensating ions [152] or via bleaching using an antisolarant pump beam at a longer wavelength [153].

Despite the problematic loss mechanisms mentioned above, the first demonstration of laser action using a cerium ion was achieved less than a decade after it was considered, in 1979 by Ehrlich *et al.* [154]. This established a new record for the shortest wavelength generated by an optically pumped solid-state laser. The authors used $LiYF_4$ (YLF) as the host medium to produce 325.5 nm radiation, pumped by a 249 nm KrF excimer laser. This record was quickly surpassed in 1980 by the same group [155], generating 286 nm radiation with a LaF_3 host, and the same pump source. This was a considerable milestone, but the performance of these lasers was limited by both ESA and solarization which resulted in efficiencies of less than 1%. With the search for more suitable host crystals underway, Owen *et al.* [156] established selection criteria for potential hosts for trivalent lanthanide ions:

> (1) Excited-state absorption is likely to occur if the sum of the energy of the probe beam and the energy of the zero phonon fluorescence level is equal to the energy of a normal absorption band. Thus, in order to avoid excited-state absorption, twice the expected laser frequency should correspond to an energy for which there is no normal absorption. (2) Host materials should be selected with large band gaps, and the impurity ion groundstate energy should be low relative to the conduction band energy. This restricts consideration to fluorides and possibly some oxides and chlorides. (3) Many electron atoms ought to be avoided since the abundance of excited states increases the possibility of absorption compared to that of an ion with a single electron outside the core.

For over a decade, numerous studies to counter ESA and CC losses were conducted, and new host media investigated, but there were was no significant improvement in the efficiency of cerium gain media [157–162]. In the late 1980s and early 1990s, two new host materials were developed that found huge success in generating near-IR light with Cr^{3+} chromium-doping [163–165]. These are lithium strontium hexafluoroaluminate ($LiSrAlF_6$ shortened to LiSAF), and lithium calcium hexafluoroaluminate ($LiCaAlF_6$ shortened to LiCAF). These lasers have improved significantly over the last 30 years to become efficient and reliable sources of femtosecond pulses in the near-IR [166–168]. They were shown to be successful Kerr-lens mode-locked (KLM) lasers [169]. Soon after they were initially developed, the host media were tested with Ce^{3+} ions [134] which sparked a resurgence of interest UV solid-state lasers. A flurry of research and new host materials subsequently arose over the next few years, as efficient cerium lasers were finally developed.

The first demonstration of a Ce:LiCAF laser was by Dubinskii *et al.* in 1993 [170]. A high quality crystal was used, grown using the Bridgman-Stockbarger technique, a technique that is still in use for refining the quality of Ce:LiCAF for high efficiency operation [171]. A Ce:LiSAF laser was also demonstrated in 1994 by Marshall *et al.* [172], which was slightly favoured as the manufacturing processes was more established at the time. Within a year, a more efficient room-temperature Ce:YLF laser was demonstrated [173], and the Dubinskii group also demonstrated a Ce:$LiLuF_4$ (LiLuF) laser [174].

This first demonstration of Ce:LiCAF showed promise with low ESA and an almost non-existent presence of solarization. The absorption peak of Ce:LiCAF (as well as Ce:LiSAF) between 260-270 nm was of particular importance, as it corresponds to the fourth-harmonic of Nd lasers which had become widely available over the last decade. The pump sources for cerium lasers became more refined between 1995 and 2005. The development of efficient, robust, and tunable UV sources was driven by the desire for atmospheric sensing, specifically laser radar systems for ozone detection [175, 176]. The use of these new media for pulse amplification became highly attractive and well established over this time. The use of Ce:LiCAF for pulse amplification will be discussed in detail in section 3.3.2.

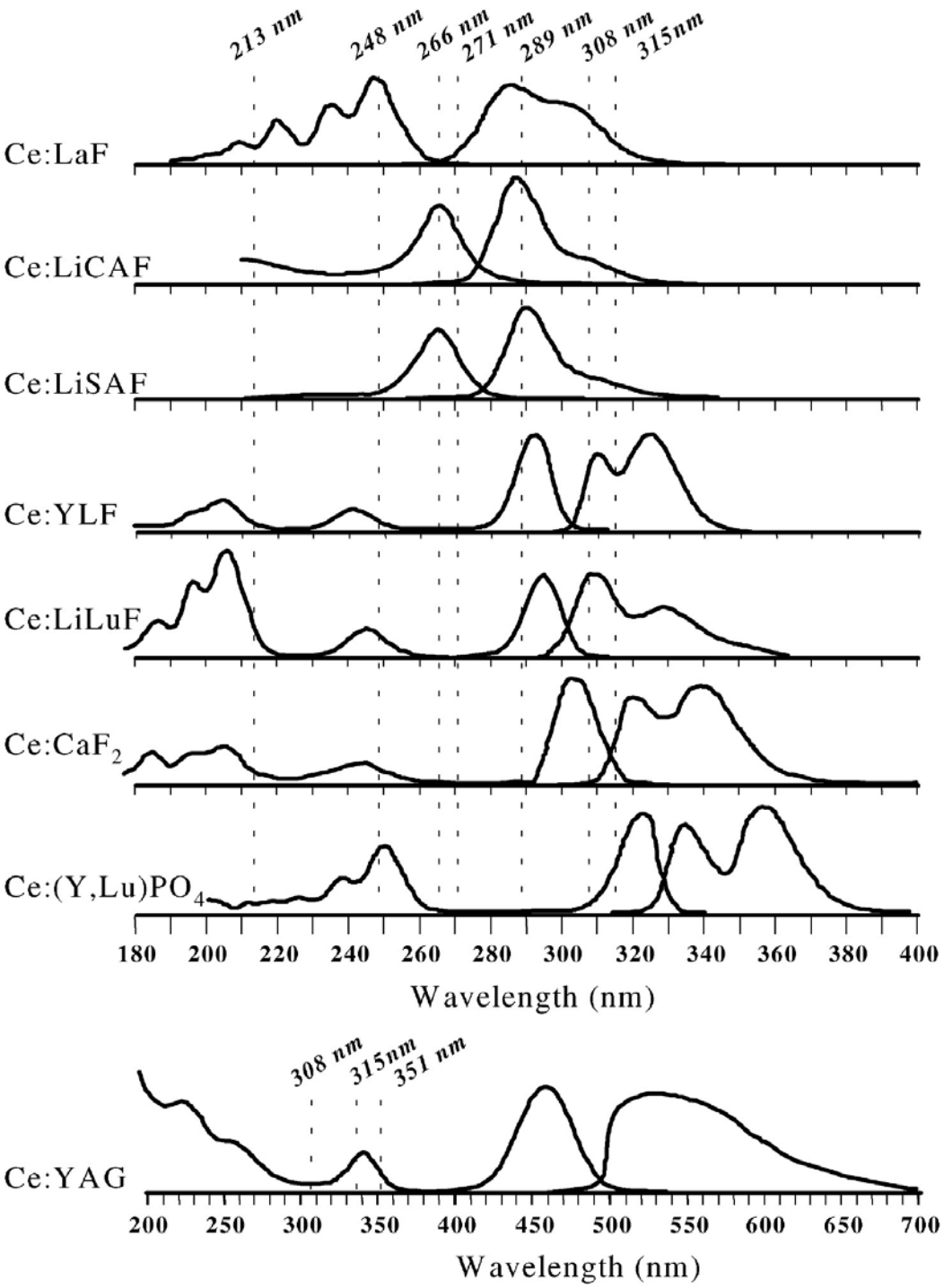

Figure 3.4: Absorption and emission spectra (left and right, respectively) comparison of cerium doped materials, and potential pumping wavelengths, from [151].

Of all the potential Ce^{3+} gain media in figure 3.4, there are three that stand above the rest when it comes to efficient operation: LiCAF, LiSAF, and LiLuF. The third of these, LiLuF, operates at significantly higher efficiency than its isomorph, YLF, as it has roughly twice the quantum yield. It is also in a different spectral region from the first two, LiCAF and LiSAF. These two hosts exhibit remarkably similar absorption and emission peaks when doped with Ce^{3+} ions, and are both well suited to frequency-quadrupled Nd lasers. A significant review

of prospective cerium-doped media was published in 2004 [151] that noted that the three aformentioned hosts are effectively the only viable successors for the future of cerium lasers and amplifiers. Figure 3.5 shows the power output of these three fluoride host media: LiLuF, LiSAF, and LiCAF, over a significant portion of their potential tuning range [177, 178].

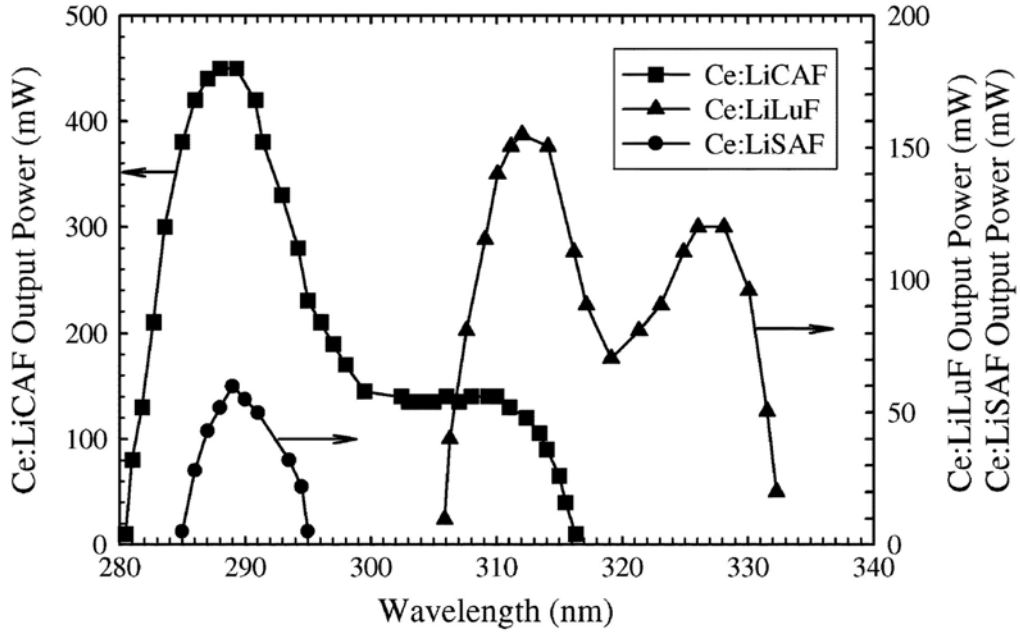

Figure 3.5: Tuning ranges achieved for Ce:LiCAF, Ce:LiLuF, and Ce:LiSAF under ns pulse pumping at kHz pulse repetition frequencies, from [151].

The tuning range of LiSAF in figure 3.5 is a very small portion of its potential. Its range of fluorescence (283-313 nm) is almost as wide as LiCAF (280-316 nm). This reduced range in figure 3.5 is partly due to poor efficiency from higher ESA in Ce:LiSAF. However, solarization was shown to be the most significant factor in reduced efficiency for LiSAF. This has been approached with an anti solarant pump beam (e.g. pumping at 532 nm in addition to the 266 nm pump) to annihilate colour centres in Ce:LiSAF. Slope efficiency was increased from 30% to 47% with an additional 532 nm anti-solarant pump laser to bleach colour centres [153, 179], at the cost of of complexity.

Co-doping has also been a successful approach to reducing solarization. The beneficial effects of Yb^{3+} and Lu^{3+} ions on the broad-band properties and gain from cerium doped $YLuPO_4$ and its isomorph $LiYLuF_4$ have been shown [180]. In Ce:LiSAF, co-doping 2% Na^+ led to an increase of slope efficiency from 17% to 33%. Similarly, in Ce:LiLuF, co-doping with 1% Yb^{3+} increased slope efficiency from approximately 50% to 62% [152, 181]. Co-doping of 2% Yb^{3+} in Ce:KY_3F_{10} even enabled the first reported case of laser action using this gain medium, with an output observed at 362 nm [182].

Mixed crystal structures have been useful to improve growing methods or optical properties of fluoride laser crystals like Ce:LiLuF and Ce:LiCAF. For example, mixing LiCAF and LiSAF for the mixed crystal Ce:$LiSr_{0.8}Ca_{0.2}AlF_6$ (Ce:LiSCAF) was developed to harness

the faster growth of LiSAF without significantly compromising the advantageous optical and thermal properties that LiCAF affords [183]. The elemental mixture was varied to optimise these crystals' characteristics, arriving at the 80:20 ratio. Conveniently, Ce:LiSCAF also possess a higher absorption coefficient than Ce:LiCAF or Ce:LiSAF, including at 266 nm. Theoretically, it also spans a greater wavelength tuning range [184]. However, to date, laser operation has not been experimentally demonstrated.

The prospect of upconversion pumping to obtain UV luminescence from the $5d-4f$ transition in rare earth ions (such as cerium) has been considered for multiple host media. Techniques to achieve this include ESA, TPA, and stepwise sensitisation. For cerium-doped media, the most successful of these is stepwise sensitisation, enabled via co-doping Ce:$LiY_{0.3}Lu_{0.7}F_4$ with Pr^{3+} ions [185], and pumping with two different wavelengths of radiation. The energy of each wavelength is absorbed by Pr^{3+} ions in a stepwise manner, which then transfers to a nearby Ce^{3+} ion, which allows stimulated emission to occur on the $5d-4f$ transition of Ce^{3+}. In 2016, gain was observed using upconversion pumping in Ce:$LiY_{0.3}Lu_{0.7}F_4$ [186], which has a less convenient pump wavelength compared with Ce:LiCAF, generally requiring either another cerium laser or a Raman frequency converter for pumping. However, the upconversion pumping scheme used by the authors still required frequency conversion from 1064 nm to 266 nm and an additional dye laser operating at 595 nm (pumped at 532 nm) to pump the Pr^{3+} ions at 266 nm and 595 nm. On the other hand, a major benefit of upconversion pumping is reduced ESA, since the excitation of Ce^{3+} ions by 266 nm radiation is negligible in this particular host medium, but the gain remains low due to excited-state photoionisation by Pr^{3+} ions, which makes lasing a challenge. A more direct approach to pumping, starting with industry-standard IR laser diodes, has also been considered [187]. In 2013, the BaY_2F_8 host and dopants Yb^{3+} + Pr^{3+} + Ce^{3+} was shown to luminesce in the 250 – 550 nm region. It was pumped by three different laser diodes operating at 808 nm, 840 nm, and 960 nm with a combined power of 5 W [188]. The authors posulated that efficiency can be improved with futher investigation of the excitation dynamics. In time, advances in the field of upconversion pumping by optimisation of ion content and pumping parameters may yield a slightly more convenient and effective approach to UV lasers, if lasing is possible using a simplified pumping scheme.

In recent years, the electronic band structures of LiCAF and LiSAF were compared via ab initio calculations; density functional theory, and local density approximation using optimised lattice constants [189]. When compared with LiCAF, it was determined that ESA and solarization are more pronounced in LiSAF because of the shorter 5d conduction band distance, combined with the difficulty of growing high-purity crystals. In contrast, Ce:LiCAF crystals can be grown with high purity and physical size, which exhibit nearly no photoinduced degradation of laser function, and have a high saturation fluence [3]. The damage threshold of Ce:LiCAF is also likely higher, as it is with Cr:LiCAF, in terms of both fluence and irradiance for high powers and ultrashort pulses [190]. The non-linear Kerr refractive index

of LiCAF is modest in the IR and changes positively, which is a necessary feature for KLM; it is expected to be considerably higher in the UV over the bandwidth of Ce:LiCAF [191, 192]. All of this makes Ce:LiCAF the superior gain medium in the 290 nm region. It is currently the most practical avenue for experimental ultrafast and CW UV laser development, and the ideal candidate for an all-solid-state high power femtosecond UV MOPA.

3.3 Ce:LiCAF Lasers

3.3.1 Gain Switched

As mentioned in the previous section, the first Ce:LiCAF laser was demonstrated by Dubinskii *et al.* in 1993 [170]. The all-solid-state system was composed of a frequency quadrupled neodymium pump laser and a relatively long gain-switched Ce:LiCAF cavity that allowed for the pump light to be inserted into the gain medium quasi-longitudinally. The Ce:LiCAF laser cavity was comprised of two curved mirrors with a radius of curvature of 30 cm, separated by 21 cm, for non-selective experiments. They had high reflectance between 280-300 nm, and about 0.4% transmittance. The group used a 4 mm long crystal with a diameter of 5 mm doped with 0.6 at.% Ce^{3+}, and were able to grow a 20 mm long, 6 mm diameter cylindrical boule with 0.9 at.% Ce^{3+} ion doping by the Bridgman-Stockbarger technique. Due to optical quality considerations of early growth technology, the active medium was set at an arbitrary angle relative to the crystallographic axes of LiCAF. This was compensated for by rotating the polarisation of the pump beam for maximum absorption, but hindered the system's efficiency. The 266 nm pump pulses, doubled from 532 nm using DKDP, provided pulse energies of up to 3 mJ with a FWHM of 16 ns at a PRF of 12.5 Hz. Using this, the Ce:LiCAF laser produced 0.15 mJ, 10 ns pulses with a slope efficiency of 8.7% at 288 nm, using an output coupler mirror with 68% transmission. Tuning between in the range 281-297 nm was achieved using an intracavity prism, and plane parallel cavity mirrors. The group observed no evidence of colour centre formation, and demonstrated Ce:LiCAF to be a robust and efficient gain medium despite the limitations imposed by the manufacturing quality of crystals and UV mirrors at the time.

The unpolarised spectroscopic characteristics of Ce:LiCAF are shown in figure 3.6 which shows two of the common absorption peaks that are shared by Ce^{3+} doped colquiriites (near 190 nm and 270 nm). The other commonality between the spectra for these media is the two-peaked emission spectrum, which occurs due to the split ground state ($^2F_{7/2}$ and $^2F_{5/2}$) at which the 5d-4f transitions terminate. This presents differently for fluorescence and gain, as the figure shows. The gain bandwidth closely matches the 280-316 nm tuning range that is achieved by future laser results, but the fluorescence is much broader and extends to longer wavelengths. While these unpolarised data are useful, the birefringent aspect of LiCAF (which is uniaxial) lends it to different behaviour for polarised radiation.

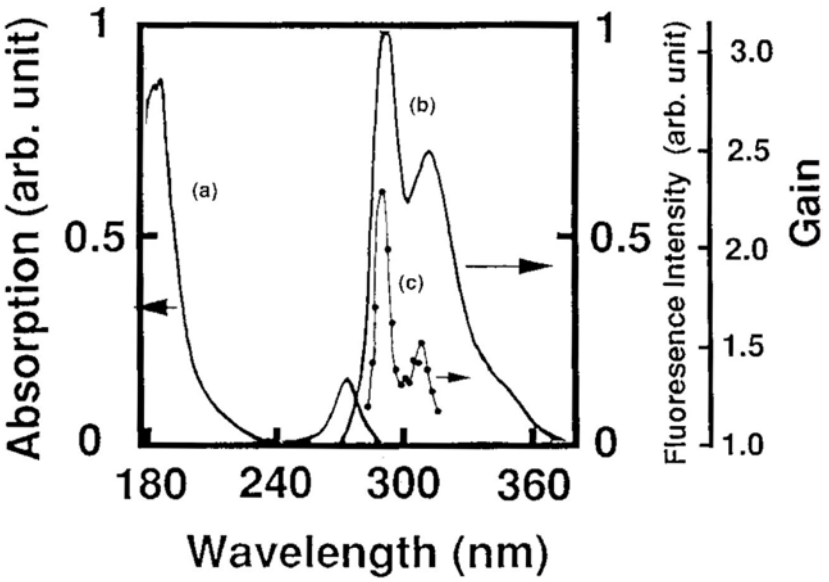

Figure 3.6: (a) The nonpolarised absorption spectrum of 2.3 mm Ce:LiCAF sample with doping concentration of 0.1% (b) the nonpolarized fluorescence spectrum of Ce:LiCAF (C = 0.9 at.%); (c) single-pass small-signal gain dependence of the probe-beam wavelength for a Ce:LiCAF sample (0.9 at.%, the thickness is 2.3 mm). From [193].

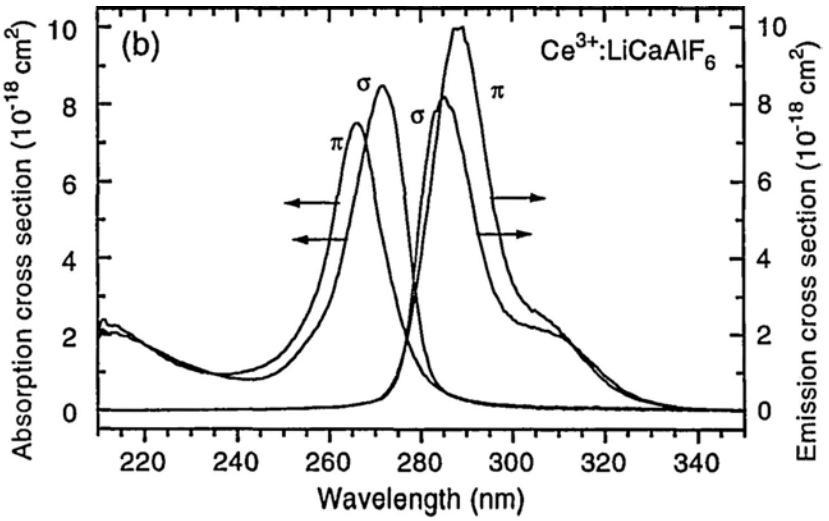

Figure 3.7: Absorption and emission spectra of Ce:LiCAF for π and σ polarisations from [172].

The polarised spectroscopic properties of Ce:LiCAF (shown in figure 3.7, note that the extent and profile of these spectra are affected by doping concentration and impurities, hence often differ in some way) were measured and studied by Marshall *et al.* using high quality crystals grown by the Czochralski technique [172]. The group cut a range of high quality samples from the initial 20 mm length and 10 mm of large boules (100 mm long with a 20 mm diameter) with cerium concentrations of 0.5 to 1 mol.%, and demonstrated record efficiency. Using a two-mirror cavity each with a 10 mm radius of curvature (ROC), a 50% transmissive output coupler was used to generate slope efficiencies of up to 21% at a similarly low PRF

of 10 Hz. The short upper state lifetime of 25 ± 2 ns was measured, which is comparable to a dye laser. The small signal gain was also investigated for π and σ polarisation of the pump and probe beams, from which the absorption and emission cross sections were determined. Although the absorption cross section for a σ polarised pump is higher, it was found that ESA is less pronounced for π polarised light, since higher gain was achieved when using pump-probe beams that were both π polarised. The various cross-sections that were determined by the group are shown in table 3.2

Table 3.2: Cross-sections of Ce:LiCAF, from [172].

	266 nm Wavelength		290 nm Wavelength	
Parameter	π Polarised	σ Polarised	π Polarised	σ Polarised
Absorption, σ_{ABS} (10^{-18} cm^2)	7.5	5.8	–	–
Emission, σ_{EM} (10^{-18} cm^2)	–	–	9.6	6.2
ESA, σ_{ESA} (10^{-18} cm^2)	5.5	9.9	3.6	2.2
Gain, $\sigma_{EM} - \sigma_{ESA}$ (10^{-18} cm^2)	–	–	6.0	4.0

Shortly after the spectroscopic insight provided by Marshall's group, Pinto *et al.* demonstrated improved laser cavity designs that favoured π polarisation by utilising Ce:LiCAF crystals cut at Brewster's angle for π polarised radiation. The cavity was composed of a plane output coupler with high transmittance of 85% separated by 7 cm from the HR back mirror with a 2 m ROC, to achieve slope efficiencies up to 39% and pulse energies over 10 mJ. The laser was also prism tuned over a wide range of 281-315 nm, but still operated at a PRF of 10 Hz.

The drive for a higher repetition rate from gain-switched Ce:LiCAF lasers was pushed partly by the desire for increased data acquisition in atmospheric monitoring applications, such as laser induced fluorescence monitoring of OH radicals in the troposphere [194]. Petersen *et al.* made significant progress in this regard, by using a 10 kHz Nd:YVO_4 laser to longitudinally pump a Ce:LiCAF cavity that was composed of two 10 cm ROC mirrors to form a 6 cm long cavity; one an HR mirror, and the other an output coupler. The group achieved a 350 mW power output, slope efficiency of 28%, and tuning range of 289-312 nm with a Brewster's angle prism. They also found that the high repetition rate did not affect colour centre formation.

Shortly after the first high PRF gain-switched Ce:LiCAF lasers, a different pump source was utilised by McGonigle *et al.* [178], in the form of a copper vapour laser (CVL). Like the previous neodymium pump lasers, CVLs are capable of PRFs on the order of kHz, with high average powers on the order of tens of Watts. The CVL fundamental lines are 511 and 578 nm; using sum frequency generation (SFG) or frequency doubling yields three possible wavelengths: 255, 271, and 289 nm. The latter two of these are well suited to the absorption of the most prominent cerium gain media, specifically Ce:LiCAF/LiCAF and Ce:LiLuF

respectively. As shown in figure 3.8, the authors used SFG to convert the 25 mm diameter output beam from a 1 m long CVL laser to 271 nm, and then quasi-longitudinally pump a Ce:LiCAF laser cavity that was composed of a 9 mm long crystal, a flat output coupler, and an HR mirror with ROC 250 mm. This system operated at a PRF of 7 kHz and a central wavelength of 288.5 nm, achieving a slope efficiency of 32% and maximum output power of 530 mW (limited by the available pump power), and a wide tuning range of 280.5-316 nm. The pulse duration was also measured to be 2.9 ns.

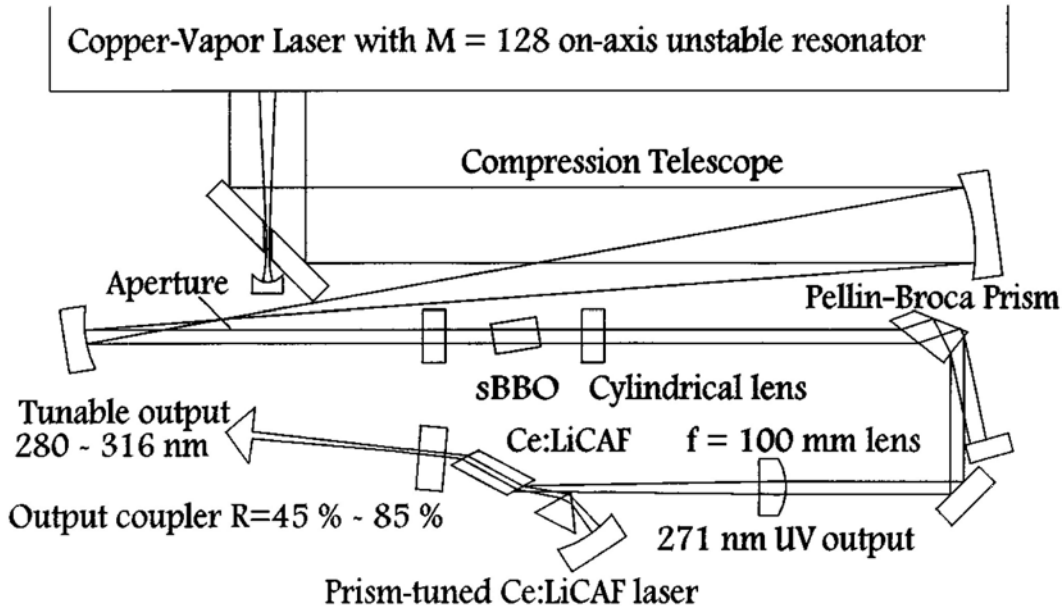

Figure 3.8: Copper-vapour laser pumped Ce:LiCAF laser optical arrangement, from [178]. The arrangment for sum-frequency mixing the 511 nm and 578 nm outputs of a copper vapour to generate the 271 nm pump wavelength is also included.

Shorter pulse durations from gain-switched Ce:LiCAF lasers were achieved by Liu *et al.* [193], by using short cavities with a low-Q, and self-injection seeding. The authors demonstrated 600 ps pulses with a 1.5 cm long cavity composed of plane mirrors, one of which was an 80% transmissive output coupler; the system was pumped by 10 ns long pulses. The group later reduced the pulse duration to 150 ps by using shorter pump pulses that were 75 ps long, and a 70% transmissive output coupler [195]. This was measured using a streak camera, shown in figure 3.9, which stood as the shortest recorded pulse from a Ce:LiCAF laser for 10 years.

More recently, through theoretical evaluation, shorter pulse durations from gain-switched Ce:LiCAF lasers have been found to be achievable using even shorter cavities of only 2 mm in length [196]. This was determined via the rate equations for gain-switched operation, comparing different geometries and pump fluences, and their effect on the output pulse properties. The authors determined pulse durations as low as 31.5 ps could potentially be generated from a 2 mm long Fabry-Perot cavity with a 70% transmissive output coupler containing a 1 mm long Ce:LiCAF crystal.

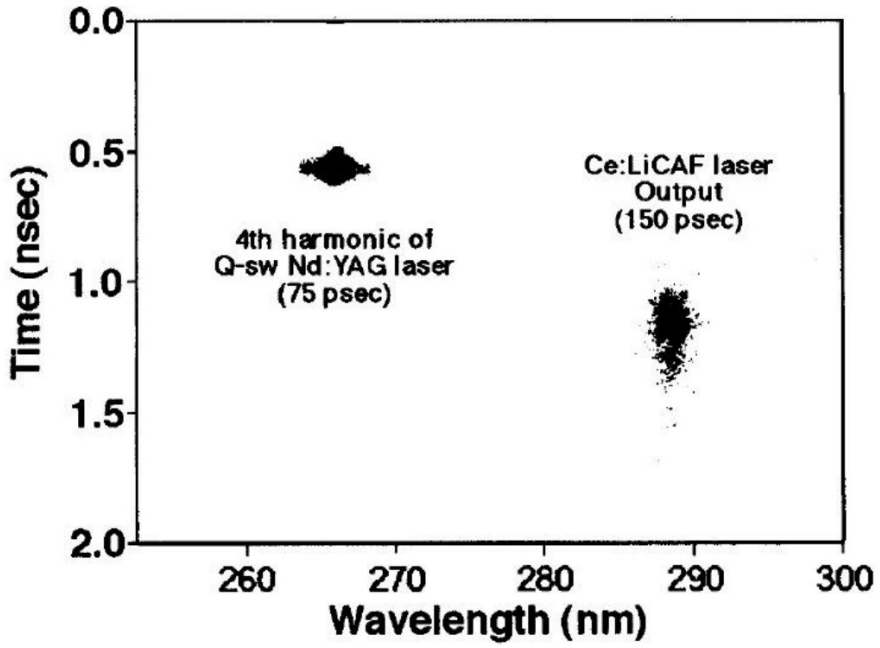

Figure 3.9: Streak camera image of the long-held record-breaking 150 ps long Ce:LiCAF laser pulse from [195], achieved using a 70% transmissive output coupler and 75 ps long pump pulses.

After the experimental advances around pulse duration, power, and PRF, research into Ce:LiCAF lasers turned to the miniaturisation of the optical system, as a whole, that was required for generating Ce:LiCAF laser light. Neodymium lasers are compact compared to excimer and copper-vapour lasers, even with an external non-linear frequency quadrupling stage; one approach to reducing the footprint of this system was achieved through a novel method of frequency doubling from 532 nm to 266 nm inside the laser cavity itself [197]. This method involved the usual two mirror cavity, longitudinally pumped, with a BBO crystal positioned between the input coupler and Ce:LiCAF crystal, thereby avoiding multiple additional lenses and mirrors that are usually required for prior frequency quadrupling. As a side note, a Ce:LiLuF laser was constructed in a similar fashion, pumped by an intra-cavity Ce:LiCAF crystal [198]. Aside from this novel approach, passively Q-switched neodymium lasers based on microchips enabled significant minimisation, as they were merged with frequency doubling to directly generate 532 nm radiation [199, 200]. This resultsed in a more compact pump system overall, shown in figure 3.10, as only the second frequency doubling stage (using CLBO) needed to be constructed.

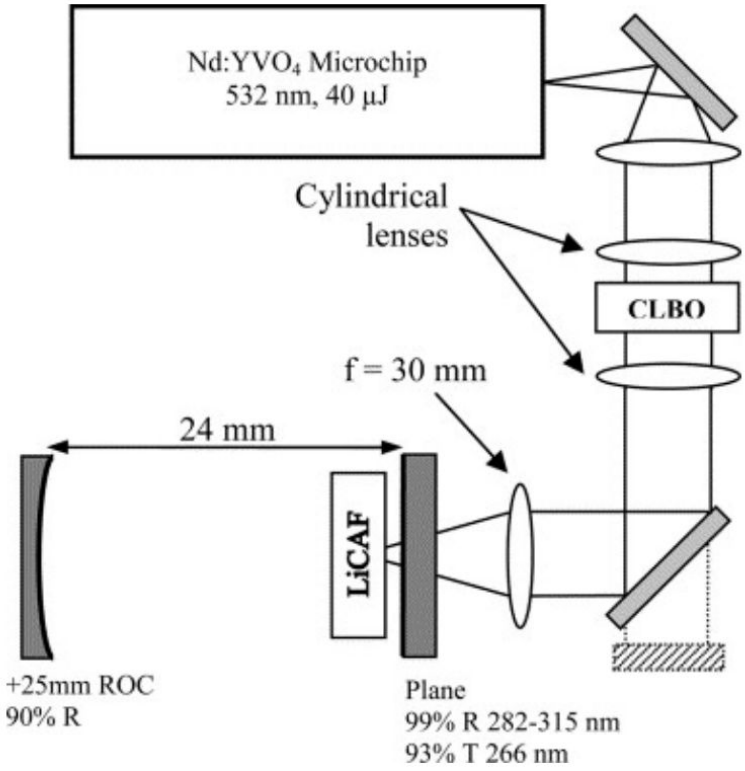

Figure 3.10: Miniature pump and Ce:LiCAF laser, from [200].

In 2012, Le *et al.* published the results of a Ce:LiCAF whispering gallery mode resonator; a 4µ m thick disk of 2-3 mm diameter pumped via the top face [201]. The schematic, which used a prism as an output coupler, and the spectral output is shown in figure 3.11. The group reported an approximate pump threshold of only 1.6µJ and an effective slope efficiency of 25%, for a broad bandwidth over 280-330 nm. However, such a broad bandwidth that extends past the previously measured gain profile is questionable for a laser that has no mode-locking mechanism in a spectral region that is prone to increased scattering losses. The reported lasing may therefore simply be fluorescence; no additional results have been published to date.

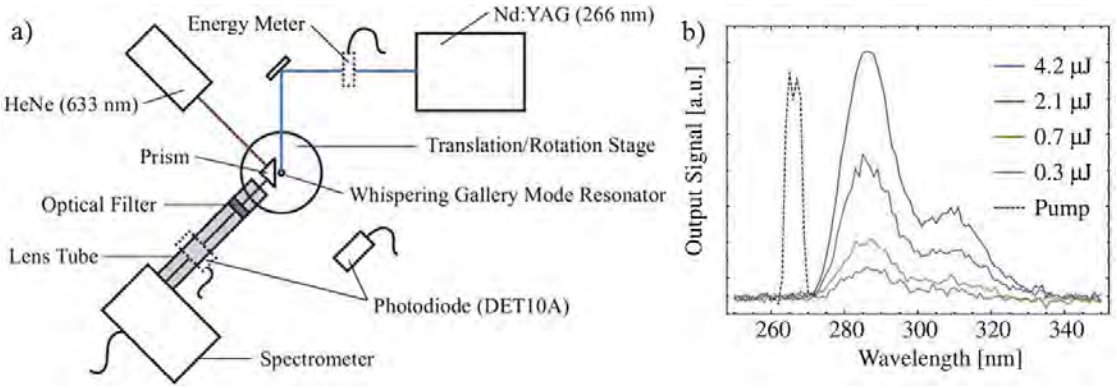

Figure 3.11: Whispering-gallery-mode Ce:LiCAF laser a) schematic, b) spectral characterisation for a range of pump energies, from [201].

Most recently, a Littrow grating has been used, replacing one of two cavity mirrors, as the tuning mechanism in place of the more commonly used Brewster's angle prism [202]. The quasi-longitudinally pumped laser cavity is shown in figure 3.12, which generated pulses as short as 450 ps without the grating. With the grating in place, wavelength tuning from 281 nm to 299 nm was demonstrated with spectral linewidths as narrow as 0.17 nm. With efficiencies of 8-10%, this simple configuration is well-suited to remote sensing applications.

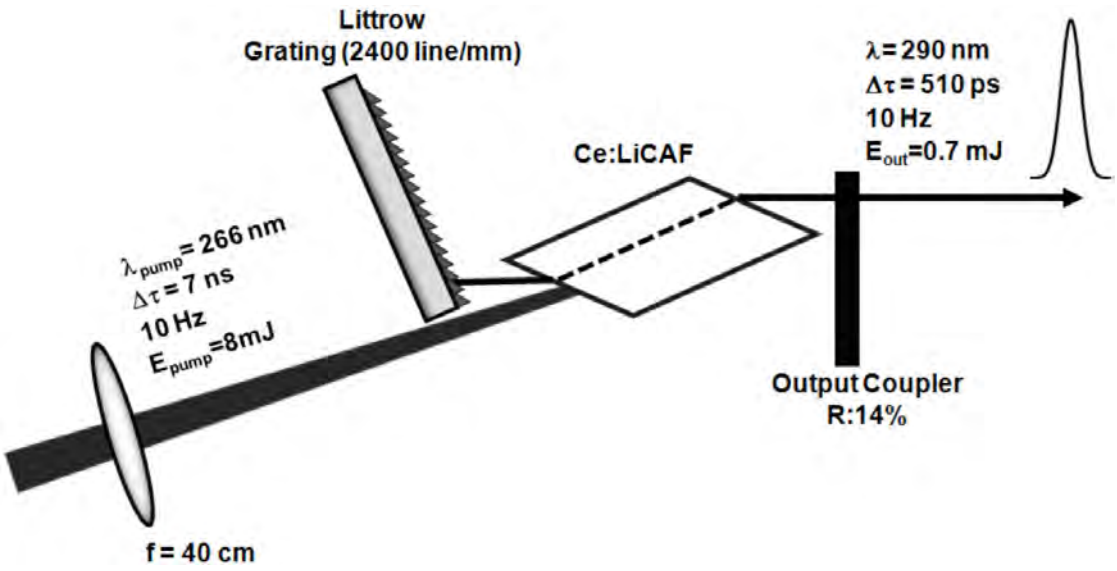

Figure 3.12: Grating tuned Ce:LiCAF laser from [202], which achieved tuning from 281 nm to 299 nm and a linewidth as narrow as 0.17 nm, and efficiencies of 8-10%.

3.3.2 Pulse Amplification

Cerium gain media are ideal for amplification of UV pulses; in particular, Ce:LiCAF is well-suited to this role due to its high damage threshold, saturation fluence, and gain cross section. There are several prominent publications that experimentally demonstrate its capability for this task, published in the late 1990s and early 2000s [203, 204]. The experimental multi-pass amplification systems were capable of amplifying nanosecond pulses, generated directly from a gain-switched Ce:LiCAF laser, as well as femtosecond pulses (frequency tripled Ti:sapphire) that were temporally broadened via chirped pulse amplification. Unfortunately, the regenerative amplifier arrangement that is often used for Ti:sapphire systems is not well suited to Ce:LiCAF, due to the short upper-state lifetime which results in a rapid decay of gain, hence the use of a multi-pass design that quickly consumes the available gain before it decays.

Figure 3.13 shows a nanosecond pulsed system; a Ce:LiCAF master oscillator power amplifier (MOPA) developed by Liu *et al.* in 1998 [203]. A frequency-quadrupled Q-switched Nd:YAG pump laser delievered 10 ns pulses at 266 nm of up to 15 mJ energy to a 1.5 cm long Ce:LiCAF cavity (same as in previous section) that was composed of a plane

HR mirror and an 80% transmissive plane output coupler. This generated 1 mJ pulses that were 600 ps in duration, used as seed pulses for a double-pass amplifier at a PRF of 1 Hz. The seed pulses were amplified to 4 mJ in the double-pass amplifier, with a minimum pulse duration of 0.9 ns. A tuning range of 282-314 nm was achieved from the MOPA, which was also extended further into the DUV region via sum frequency mixing with the 1064 nm fundamental of the Nd:YAG pump laser. The extended range covered 223-232 nm, yielding 0.5 mJ pulses that were 1.0 ns long.

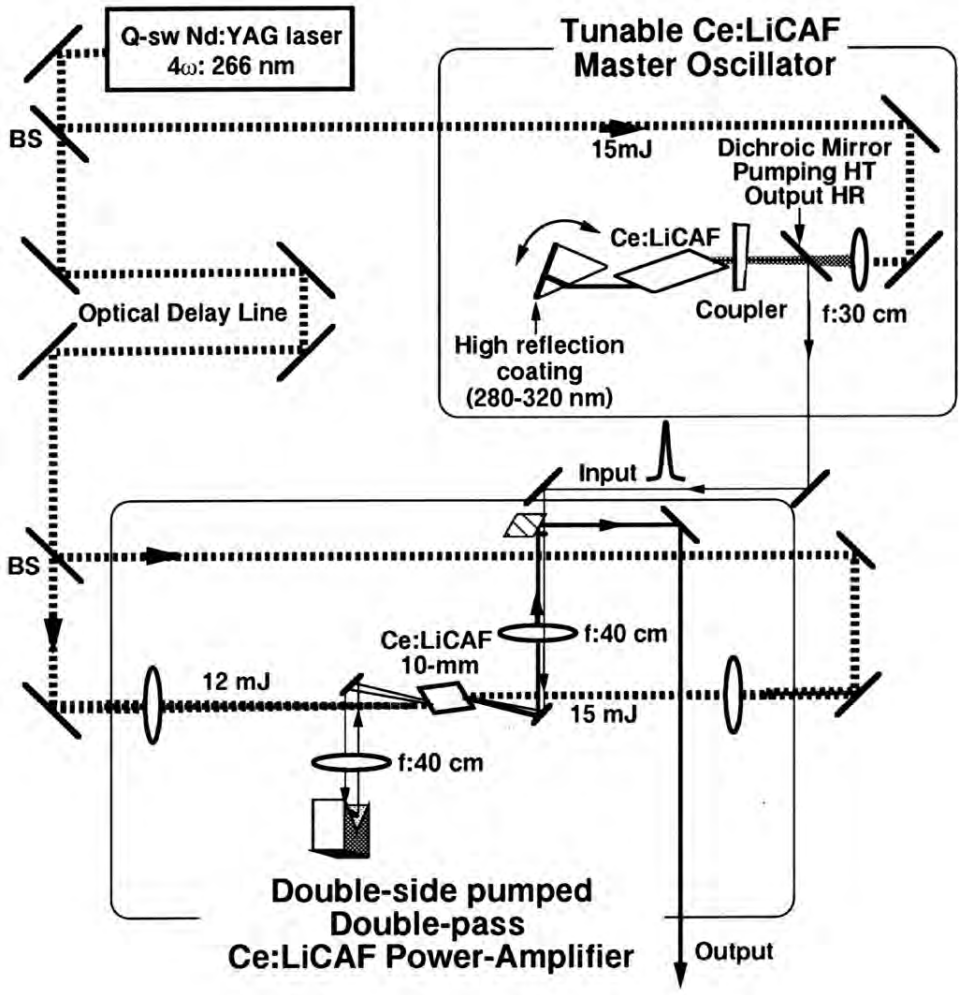

Figure 3.13: A Ce:LiCAF master oscillator pulse amplifier (MOPA) from [203].

To better accomodate the geometry of multi-pass and multi-pump-beam amplifier designs, larger Ce:LiCAF (as well as Ce:LiSCAF) crystals were grown using the Czochralski technique [205–208]. The size of Ce:LiCAF boules increased over several years, with a particular focus on minimising defects to improve yield, from useable crystals that were 15 mm in diameter and 10 mm length to Brewster-cut crystals with dimensions $1 \times 2 \times 2\,\mathrm{cm}^3$ [3]. This crystal size was used in the amplifier stage of a MOPA which took advantage of the large aperture of the crystal by utilising four pump beams, shown in figure 3.14. Pulses that were 3 ns long were amplified from 13 mJ to 98 mJ via the bow-tie double-pass arrangment.

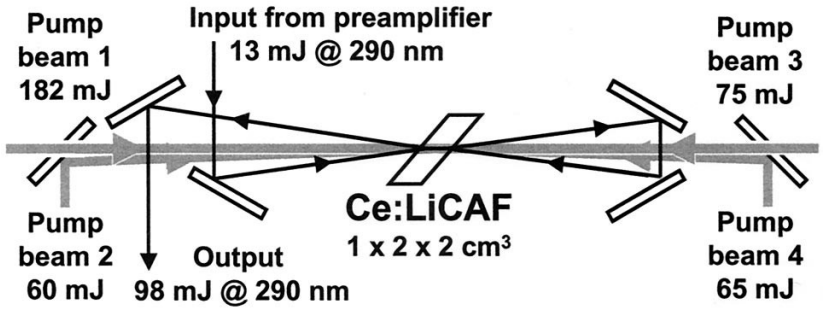

Figure 3.14: A high pulse energy MOPA using a large Ce:LiCAF crystal, from [3].

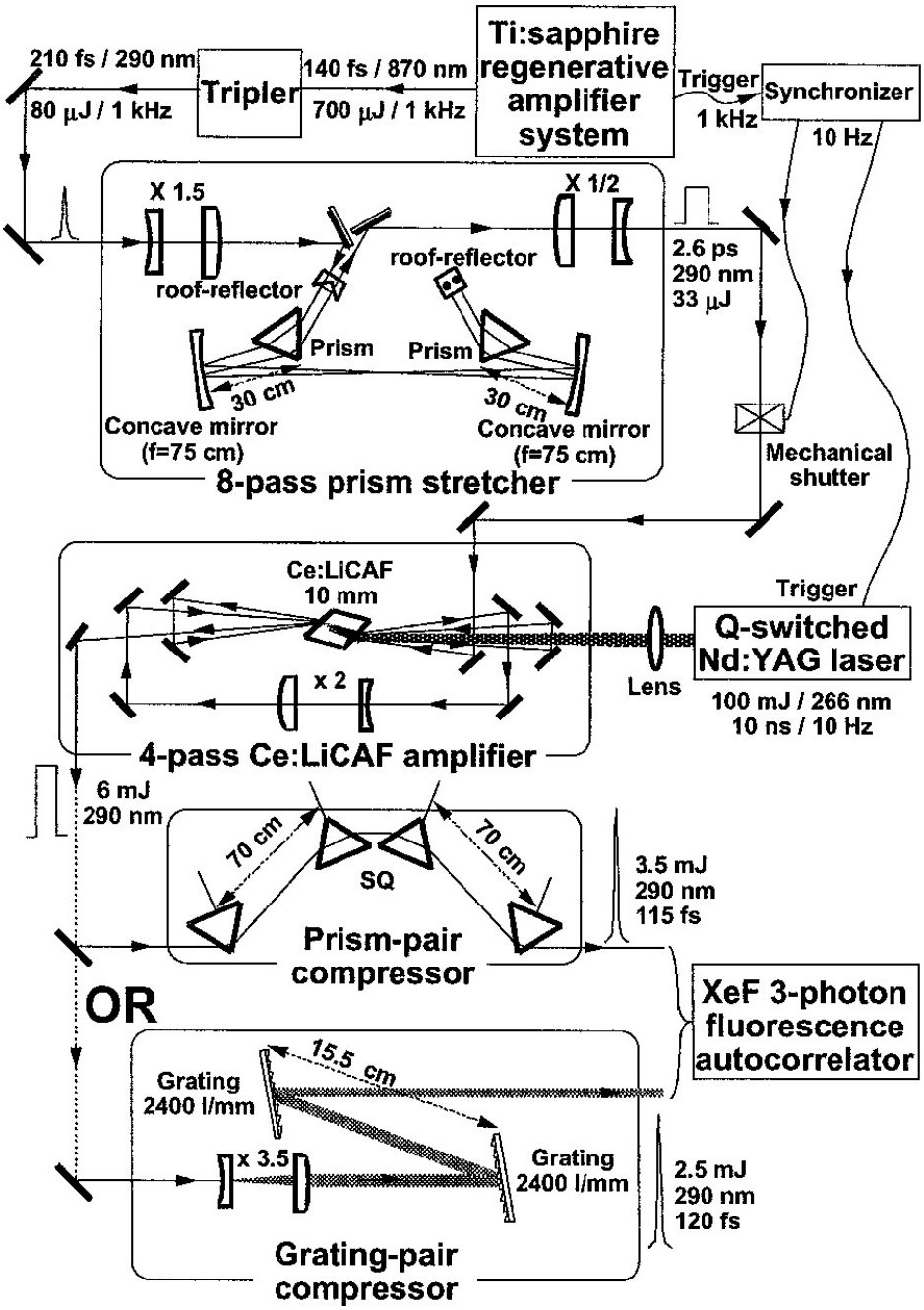

Figure 3.15: A chirped-pulse amplifier using Ce:LiCAF to amplify Ti:sapphire frequency-converted pulses, from [204].

In addition to MOPAs, chirped pulse amplification (CPA) using Ce:LiCAF was demonstrated in 2001 by Liu *et al.* [204, 209], using the arrangement shown in figure 3.15. The authors injected the frequency tripled output a 1 kHz Ti:sapphire regenerative amplifier system into an 8-pass prism stretcher to increase the pulse duration by over an order of magnitude, from 210 fs to 2.6 ps. This 1 kHz system was then reduced to 10 Hz via a pulse-picking shutter, so as to be synchronised with the four-pass amplification stage, which was pumped at 10 Hz. A gain of 370 was achieved, increasing the energy of the 290 nm pulses from 33 µJ to 6 mJ. After a compression stage to reduce the pulse duration to as low as 115 fs, the pulses retained up to 3.5 mJ of their energy. This amplifier was pumped using 100 mJ 266 nm pulses. Without CPA, the authors achieved a 60 dB gain by seeding the 4-pass amplifier with 200 fs pulses, increasing their energy from 200 pJ to 54 µJ; a pump pulse energy of 15 mJ was used to achieve this.

More recently, a different growth method was used for manufacturing Ce:LiCAF crystals intended for amplification. The micro-pulling-down method is significantly faster and more cost-effective than the aforementioned Czochralski and Bridgman-Stockbarger techniques [210]. Its applicability was demonstrated in a femtosecond pulse amplification without any prior chirping. Figure 3.16a shows a cross-section of the side-pumping arrangement that uses a cylindrically-cut crystal of length 30 mm and diameter 2 mm. This crystal geometry effectively utilises the shape of crystal growth, while the use of side-pumping redistributes fluence to minimise pump-induced damage. The authors achieved a net gain of 4, increasing the energy of 40 µJ, 150 fs long pulses to 160 µJ that were 180 fs long. Further research into the efficiency of Ce:LiCAF amplification is still being conducted, via creative methods of maximising pump energy absorbed by the crystal [211]. The arrangement of 3.16b is particularly elegant for use in a two-pump system, using a Ce:LiCAF crystal that is cut for total internal reflection (TIR) of the pump beams.

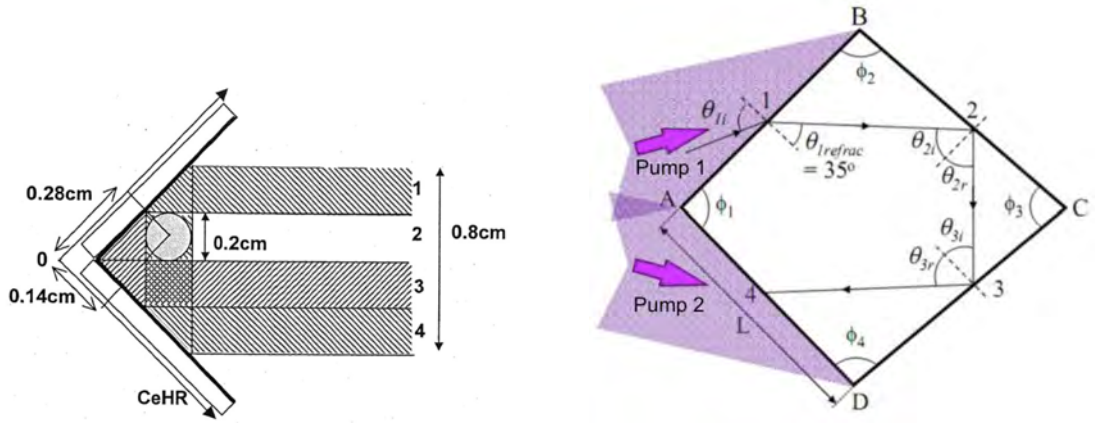

(a) Four-beam pumping.

(b) Two-beam TIR pumping.

Figure 3.16: Optimised side-pumping configurations for a Ce:LiCAF amplifier, from [211].

3.3.3 Mode-Locked & CW

The first demonstration of mode-locked and CW output from a Ce:LiCAF laser came in 2009, by Granados Mateo *et. al.* [212, 213] using the same cavity for both modes of operation. Mode-locking was achieved actively by synchronous pumping, while CW operation was set up by significant detuning away from synchronicity to the pump laser. This resulted in slightly modulated output due to the pulsed pump source. Their experimental setup is shown in figure 3.17, which used an external frequency quadrupling stage to convert the 1064 nm pulse train of a mode-locked pump laser to 266 nm; this was injected into the cavity through a dichroic mirror (transmissive at 266 nm, and HR at 290 nm) to longitudinally pump a short Brewster-cut Ce:LiCAF crystal that was located between two curved mirrors. The three-mirror cavity was composed of two curved mirrors, M1 and M2, with ROC 10 cm and 5 cm, respectively, and a plane mirror M3 that could easily be translated to maintain synchronicity to the pump. The three miror cavity allowed for two aspects of operation. Firstly, the short cavity arm resulted in a small mode size within the crystal; this effectively increased the pump intensity hence population inversion, thereby countering high losses from fluorsence. Secondly, the Brewster-cut crystal reduced round-trip losses, but introduced astigmatism in the cavity mode; the folded cavity arrangement compensates for astigmatism to achieve a stable cavity. This is presented in more detail in the next chapter.

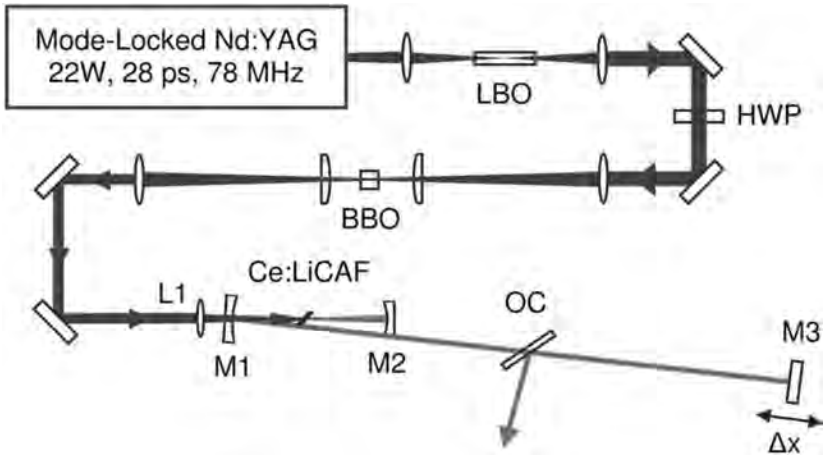

Figure 3.17: First mode-locked Ce:LiCAF laser, from [212], which uses three high reflectivity cavity mirrors (M1, M2, M3) and a near-Brewster's angle output coupler (OC). Included in the diagram is the frequency-quadrupling stage of the synchronous pump laser.

Using a near-Brewster's angle output coupler (OC), the authors generated up to 52 mW of average power during mode-locked operation, contained in the four-beam output of the plate; the corresponding slope efficiency was 13%. Upon detuning of the cavity length, the power decreased gradually down to approximately half the maximum for a detuning of more than 0.5 mm; this is shown in figure 3.18. Note the asymmetry around $\Delta x = 0$ mm, caused by temporally asymmetric gain as a result of synchronous pumping. This gain profile is also presented in more detail in the next chapter.

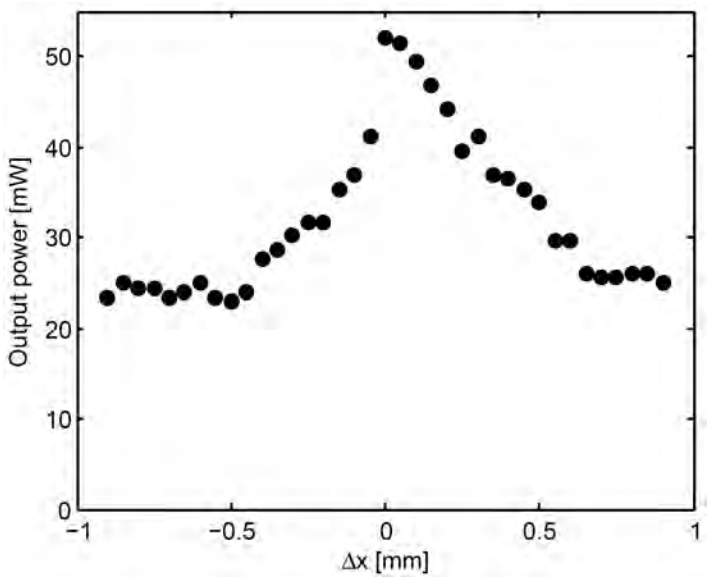

Figure 3.18: Power output of Ce:LiCAF laser versus cavity length detuning from synchronicity to the pump laser, from [213].

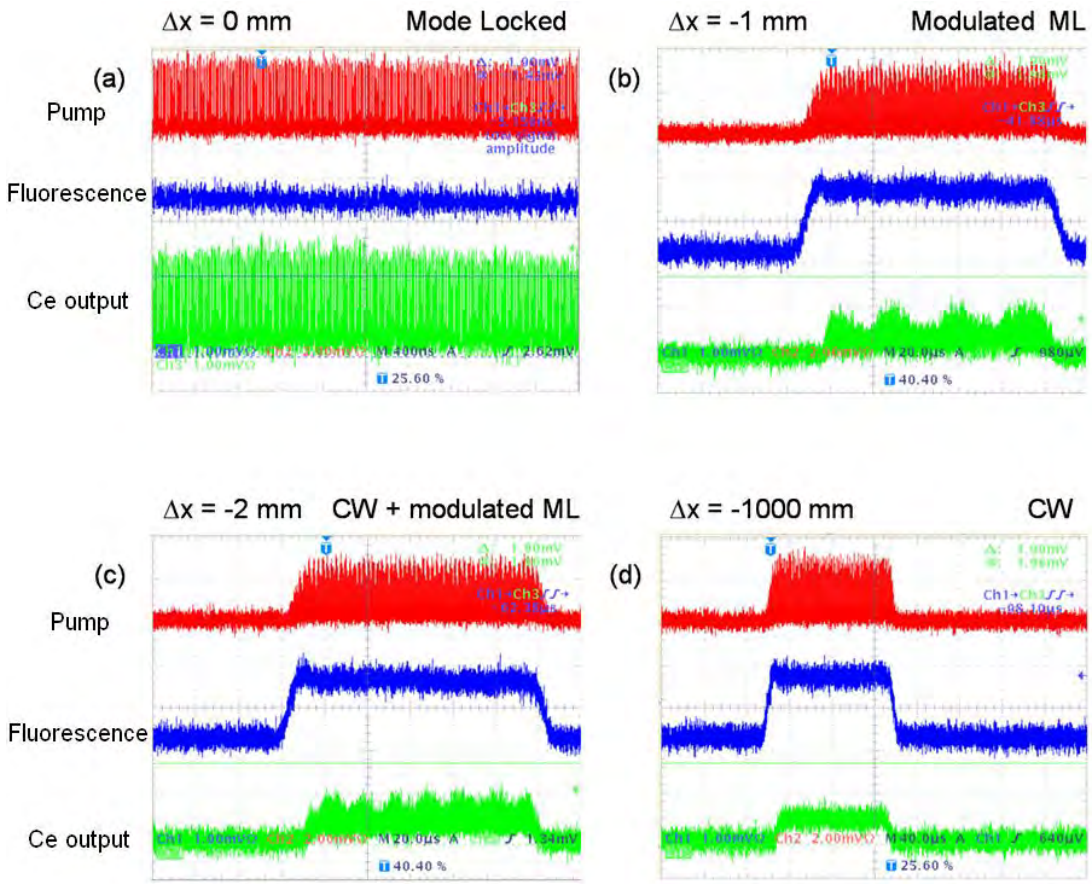

Figure 3.19: Mode-locking and CW output characteristics, affected by cavity length detuning from the first harmonic, from [213]. Note that the pump pulse train was chopped to produce a burst of approximately 100 µs.

While the output power for moderate detuning (±1 mm) is equivalent to that achieved for CW operation, the laser itself is still mode-locked, albeit less stable. The stability for several cavity lengths is shown in figure 3.19; note that the top-hat profile arises from the use of a chopper acting upon the pump laser to reduce thermal effects, the open cycle of this is shown. The mode-locked pulses of the pump and Ce:LiCAF laser were recorded on a photodiode, as well as fluorescence from the crystal. As the laser is detuned the envelope of pulses becomes modulated on the order of tens of kHz. For significant detuning, the mode-locked pulses subside as CW operation (with slight modulation) dominates.

For zero detuning, the shortest pulse duration that was measured was 6 ps, via asynchronous cross-correlation (see chapter 6). The chirp of these pulses was not determined from this method, but the cross-correlation trace of the intensity of the pulse is shown in figure 3.20a. The time-averaged spectrum that was recorded for this duration of pulse (figure 3.20b) had a bandwidth of over 2 nm, which is sufficient to support sub-100 fs pulse durations for a carrier wavelength of 290 nm. The authors summised that this pulse was therefore far from being transform-limited.

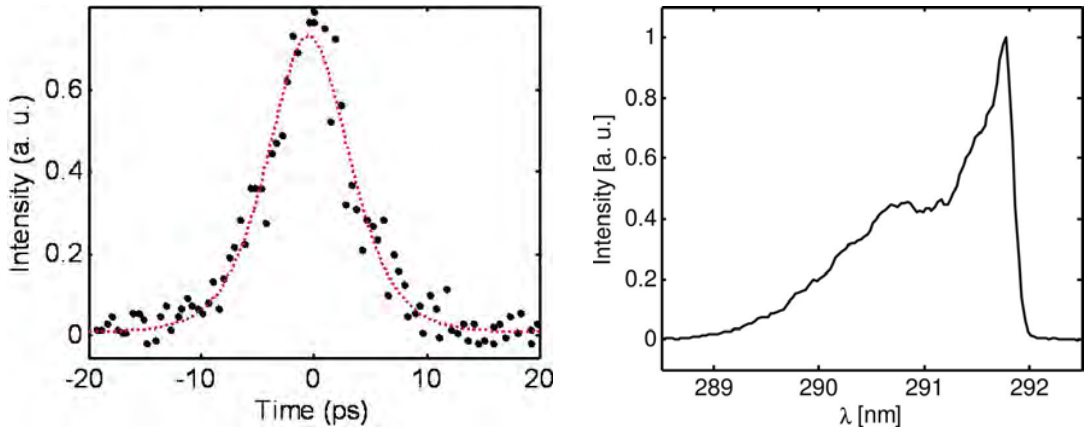

(a) Measurement of a 6 ps pulse from the first mode-locked Ce:LiCAF laser, from [214].

(b) Spectrum (time-averaged) of the first mode-locked Ce:LiCAF laser, from [212].

Figure 3.20: Pulse duration measurement by asynchronous cross-correlation with a Ti:sapphire reference laser, and output spectrum of the first mode-locked Ce:LiCAF laser developed by Granados Mateo *et al* [212].

Pulse broadening and sensitive variation of the output spectrum due to cavity length detuning was observed during the initial characterisation of a mode-locked Ce:LiCAF laser, shown in figures 3.21 and 3.22. The variation of spectrum has been identified as dispersion tuning, which is discussed in detail for this laser in chapter 5. The efficiency of this laser has been significantly increased since these results were recorded, as well as the pump power used, so the spectral features presented later on differ in bandwidth and tuning range.

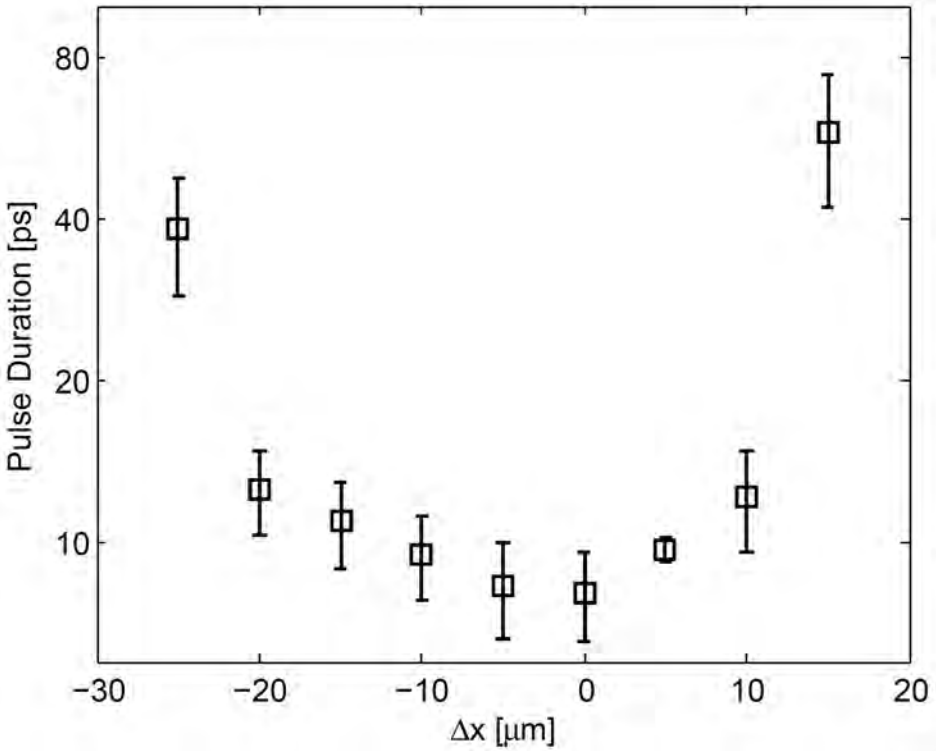

Figure 3.21: Sensitivity of mode-locked Ce:LiCAF laser output pulse duration with cavity length variation, from [213].

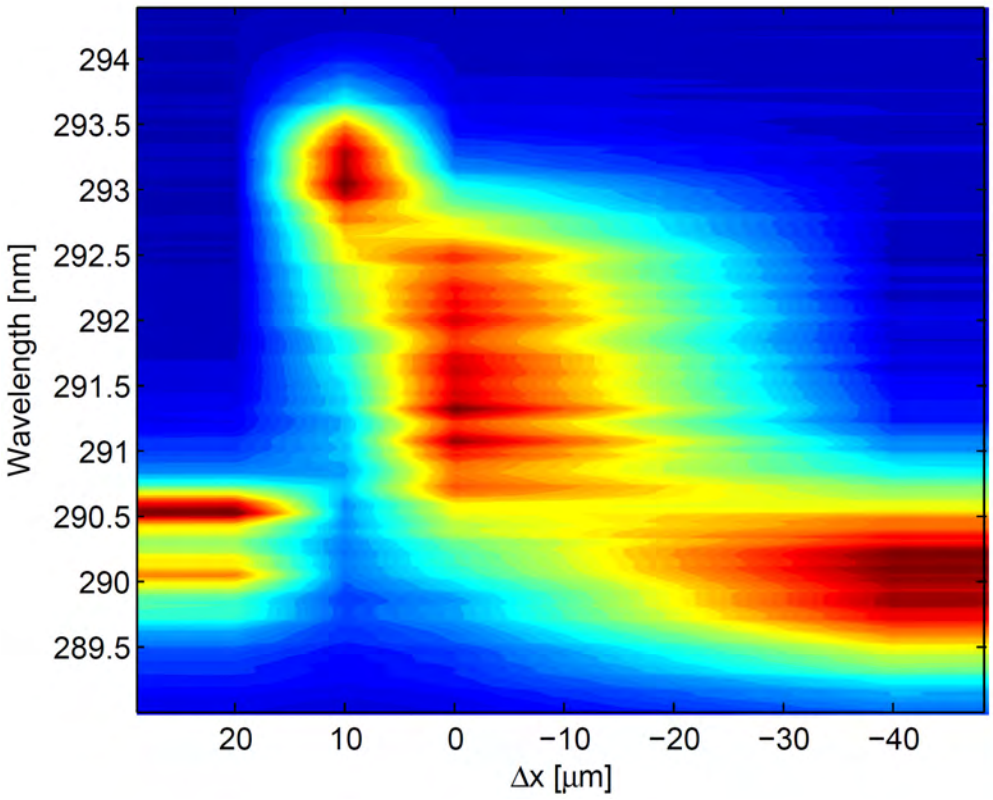

Figure 3.22: Variation of mode-locked Ce:LiCAF laser spectral output with cavity length detuning (Δx), from [213].

After the success of achieving the first demonstration of mode-locking and CW operation using Ce:LiCAF, Wellmann *et al.* made several improvments to the same optical system. The efficiency of the laser was improved by using higher quality mirrors, and optimised to reduce round-trip losses, including switching the input coupling mirror [4]. A slope efficiency of 20% with maximum output powers up to 384 mW were achieved by optimising the output coupling of the laser with a near-Brewster's angle fused-silica plate [4, 215]. Tuning was also demonstrated from 286 to 295 nm. The dynamics of the laser, subject to cavity length detuning, were also explored extensively [12], particularly for rational harmonics with the synchronous pump laser; for example, the second harmonic where the Ce:LiCAF laser is half the length of the pump laser, which doubles the effective PRF. Several rational harmonics were demonstrated, including the 14/5 harmonic; the Ce:LiCAF laser cavity length was set to 5/14 of the pump laser, which caused 14 pulses to resonate for an ultimate PRF of 1.1 GHz. This is the highest repetition rate ever achieved from a Ce:LiCAF laser.

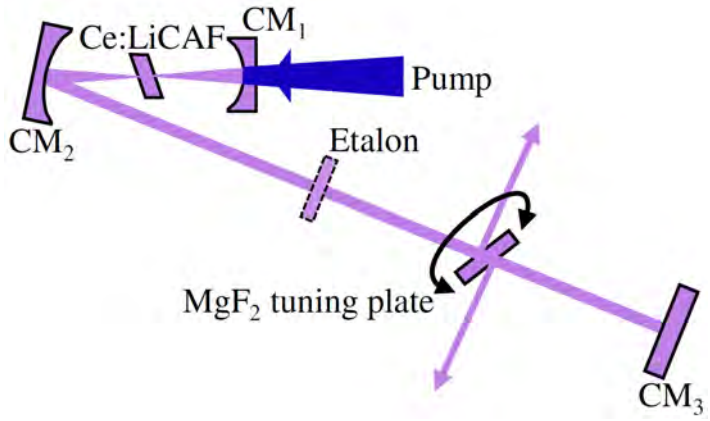

Figure 3.23: Linewidth-narrowed continuous-wave Ce:LiCAF laser, from [216]. A near-Brewster's angled rotated MgF_2 waveplate provided birefringent tuning and an additional etalon could be inserted for further linewidth narrowing.

In addition to rational harmonics, the avoidance of harmonics was also analysed, referred to as asynchronous pumping. In regards to the Ce:LiCAF laser, it was found that the optimal cavity length for CW operation under asynchronous pumping was 0.3964 that of the pump laser's cavity length. This resulted in minimal modulation of output power; less than 1% modulation was measured for frequencies below 1 GHz, and 4% on faster timescales. The linewidth of this laser was also narrowed using a 250 µm thick birefringent MgF_2 plate as a near-Brewster's angle output coupler [216], reducing the linewidth from 0.2 nm down to 14 pm, for a 13 nm tuning rage from 284.5 to 297.5 nm. A 3 mm etalon was then combined with a 6 mm MgF_2 tuning plate to reduce the linewidth further to only 0.75 pm, which corresponds to 13 longitudinal modes. The laser cavity for this arrangement is shown in figure 3.23. The measurement itself was potentially limited by the finesse of equipment, as a high finesse is challenging in the UV. However, it was noted that single longitudinal mode (SLM) operation is unlikely to become operational using a mode-locked pump source, due

to the modulation of gain that arises from pump pulses and the short upper-state lifetime of Ce:LiCAF.

Progress towards SLM in a CW Ce:LiCAF laser relies on having a CW pumping scheme that eliminates modulation of gain. Such a system has been demonstrated with moderate success [217]. The layout of the pump system and Ce:LiCAF laser is shown in figure 3.24. A commercial CW laser was used to inject 532 nm radiation into a home-built resonant doubling ring; frequency doubling to 266 nm was performed in a BBO crystal. This pump system was capable of generating up to 2 W of 266 nm radiation, limited by thermal effects in the BBO. The Ce:LiCAF laser was composed of the same 3-mirror cavity and Brewster-cut crystal that was previously used in the pulse-pumped variant, except that the Ce:LiCAF itself was used as an output coupler by rotating it away from Brewster's angle. A threshold of 1.5 W was measured, despite the theoretical value being closer to 1 W. For 1.9 W of pump power, a maximum output power of 6 mW was generated, at 289.9 nm with a linewidth of 0.1 nm; and several minutes of stable operation was achieved. It was concluded that thermal variations in the system were the primary limitation of stability. Although the stability was an issue, this was the first demonstration of CW-pumped Ce:LiCAF and CW Ce:LiCAF operation without the use of a chopper in the pump system, and is therefore a significant milestone that will contribute to future developments that work to stabilise the pump and laser system by managing thermal effects in both.

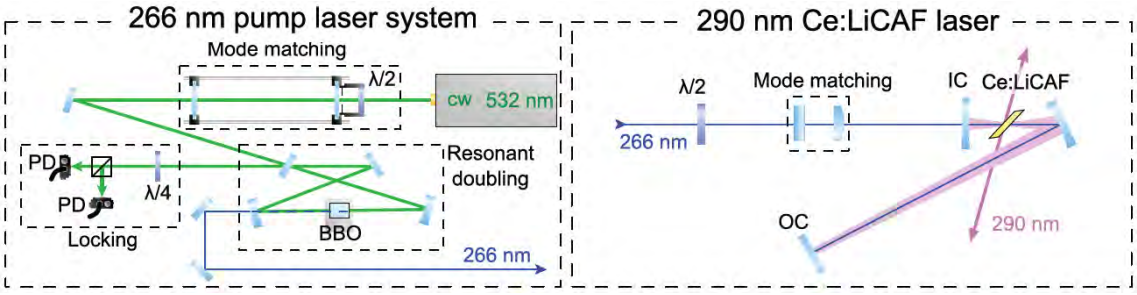

Figure 3.24: Pump layout (left) for CW-pumping a CW Ce:LiCAF laser (right) from [217]. The pump laser is composed of a CW laser operating at 532 nm that is frequency doubled inside a ring cavity to generate 266 nm radiation. This is injected through a dichroic into a three-mirror Ce:LiCAF laser cavity, which utilised the Brewster's cut Ce:LiCAF crystal as an output coupler via angle detuning.

4

Hybrid-Mode-Locked Ce:LiCAF Laser

The previous chapter introduced many aspects of the operation of cerium lasers, which have developed initially as gain-switched resonators; after three decades, they were actively mode-locked, and CW operation was also demonstrated [212, 213]. In this chapter, the Ce:LiCAF laser that was used in this thesis is presented in detail; its continued development is the primary aim of this research project. The cavity arrangement was introduced in the previous chapter as the first Ce:LiCAF laser to be mode-locked and operated CW. Mode-locking was achieved actively by using a synchronous pumping scheme, while CW operation (with slight modulation of power) was achieved via asynchronous pumping, by detuning the Ce:LiCAF laser cavity length sufficiently far away from synchronicity to the pump laser. The same synchronous pumping scheme was used again here as an active mode-locking mechanism, but various alterations and additions to the pump laser system and Ce:LiCAF laser cavity have improved its operation.

This chapter introduces the first demonstration of hybrid-mode-locking in our Ce:LiCAF laser, and covers several important aspects of its operation. The cavity design is presented first, followed by a detailed layout of the pumping scheme, characterisation of the various cavity elements, as well as the mode-locking characteristics and power output. Hybrid-mode-locking was established by the combination of the active and passive mode-locking mechanisms of synchronous pumping and Kerr-lens mode-locking (KLM), respectively. This scheme was used to generate the shortest pulses ever from a Ce:LiCAF laser, and still had the advantage of being self-starting, via synchronous pumping. In our laser, KLM was enabled via dispersion management of the laser cavity, performed using an intra-cavity prism

pair (details of dispersion are presented in chapter 5). The intra-cavity prism pair allowed the net chromatic dispersion within the cavity to be reduced to an anomalous value close to zero. By combining these prisms with an extra-cavity prism pair that compensated for dispersion outside the laser cavity, the pulse duration from the system was further reduced. We measured pulses with a duration of less than 100 fs (see chapter 6 for methodology and details of pulse duration) which is a 60-fold reduction from 6 ps that was achieved without this scheme of hybrid-mode-locking. Previously, experiments have also required the use of a chopper that reduces the pump laser system to short bursts ever few milliseconds, in order to minimise the detrimental thermal effects that are encountered whilst frequency doubling a high-powered laser beam in BBO. For the first time, our mode-locked Ce:LiCAF laser has been operated without the use of this chopper, owing to reduced losses within the laser cavity, and careful management of laser power within the frequency doubling BBO crystal. Previous experiments also utilised a near-Brewster's angle window as an output coupler (made of fused silica) which was replaced by a plane mirror. This consolidated the laser output into a single beam for the first time (previously four beams). It also removed the additional chromatic dispersion and resonator losses that were encountered by propagation through fused silica. Respectively, these are advantageous for ultrafast pulse generation, and lowering the threshold; minimising dispersion and losses was crucial for un-chopped operation of our hybrid-mode-locked Ce:LiCAF laser.

4.1 Cerium Laser Design

Our laser was initially designed for minimal round-trip losses [4], which has resulted in the use of a Ce:LiCAF crystal cut at Brewster's angle, and as few mirrors as possible. This also simplifies the design of the cavity geometry, but the Ce:LiCAF crystal geometry must be taken into consideration. Because of the obliqueness of the Brewster's angle cut, the laser cavity mode propagates differently when it enters the Ce:LiCAF crystal; the two transverse planes of the beam differ upon reaching the crystal, since they were circular and are being projected onto the crystal surface at an angle. In other words, the radius of a beam that is focussed into the crystal is different in the horizontal (tangential) and vertical (sagittal) plane once it enters the crystal. The altered beam size affects the focussing geometry, and causes one axis to reach a focus faster than the other, referred to as astigmatism, and can result in an unstable laser cavity. However, compensating for the astigmatism introduced by the crystal is quite simple. Compensating the astigmatism of Gaussian beams was first discussed in the late 60s [218]. For z-fold and 3-mirror cavities like ours, the astigmatism can be well compensated for at a specific location in the cavity via adjustment of the fold angle of a concave mirror [219], which is denoted by α.

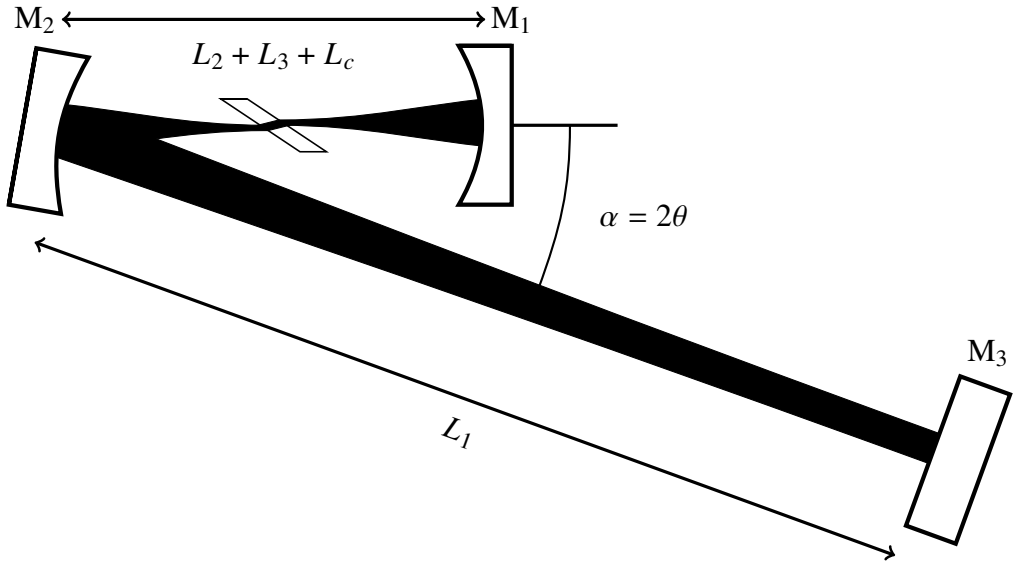

Figure 4.1: The free-running Ce:LiCAF laser cavity (not to scale).

The basic layout of the cavity is shown in figure 4.1, which includes a 1.4 mm long Ce:LiCAF crystal between the two curved cavity mirrors. This crystal was cut at Brewster's angle to minimise reflection losses. The c-axis was chosen to be in the horizontal (tangential) plane and perpendicular to the direction of propagation, to minimise ESA of the pump and maximise laser gain. The first mirror M_1 was a dichroic input coupler with T>90% at the 266 nm pump wavelength and R>99.5% at the 290 nm laser wavelength; it had a ROC of 50 mm. The second mirror M_2 was an HR (R≈99.8%) folding mirror with an ROC of 100 mm. For the end mirror M_3, we used two different plane mirrors for the experiments in this thesis; an HR mirror (R≈99.8%) and an OPC (T≈1.5%). The HR end mirror, as well as M_1 and M_2, were coated by Advanced Thin Films (ATF) while the OPC was coated by LAYERTEC. The HR variant of the end mirror was useful for initial alignment and when high intra-cavity powers were needed, such as the spectral characterisation in chapter 5. However, only the plane OPC was used for the results presented in this chapter.

Note that the reflectivities of the cavity mirrors and Ce:LiCAF crystal were measured previously, using the cavity-ringdown method. This involved an auxiliary gain-switched Ce:LiCAF laser that generated sub-nanosecond pulses at a relatively low repetition rate of 1 kHz. These pulses were coupled into the cavity of our mode-locked Ce:LiCAF laser setup with an additional HR mirror (whilst it was switched off) via the small transmissivity of the HR end mirror. The pulse then resonated within the well-aligned cavity and its energy decayed exponentially, according to the round-trip loss. Detection of the residual transmission loss from one of cavity elements, by directing a PMT toward the Ce:LiCAF crystal or a mirror, resulted in a direct measurement of exponential decay of the pulse energy. From this slope, the round-trip loss was determined, and the loss of each individual element was determined by comparing the round-trip loss of the cavity with and without the element.

Since our Ce:LiCAF laser cavity was synchronously pumped, the total cavity length

had to match a rational harmonic of the pump laser. For the majority of this work, the fundamental harmonic was chosen, requiring a total cavity length of approximately 1.90 m. This corresponds to a mode-locked train of pulses at a repetition rate of 78.8 MHz, for a cavity round-trip time of 12.7 ns. In order to match the cavity length of the Ce:LiCAF laser to that of the pump, the end mirror M_3 was placed on a high-precision translation stage.

To determine the appropriate folding angle, we used equation 4.1, which is adapted from [219]. The left-hand set of brackets describes the difference in path length through the Brewster's angle material (Ce:LiCAF crystal) in the two orthogonal planes, which is dependent on the length and refractive index of the material. The right-hand set of brackets describes the difference in focal length that arises due to reflection from the cavity mirror M_2, which is placed at an oblique fold angle. Note that the two terms in the first set of brackets are the effective propagation distance within the crystal in the sagittal and tangential planes, respectively. This effective distance is only related to the transverse spatial properties of the propagating Guassian beam; they are actually less than the crystal length itself. The coefficient (L_c) is the length of the crystal, measured perpendicular to the surfaces. This is the value used in equation 4.1, but differs from the physical distance that the laser beam traverses, subsequently referred to as $(L_{c,PL})$.

$$\left(L_c\sqrt{n^2+1}/n^2 - L_c\sqrt{n^2+1}/n^4\right) - (f/\cos\theta - f\cdot\cos\theta) = 0 \tag{4.1}$$

Equation 4.1 can be rearranged and solved for θ using the quadratic equation, shown in equation 4.2. We take the positive result $+\sqrt{}$ for calculating arccos, and this determines the folding angle $\alpha = 2\theta$ for which the astigmatism is compensated.

$$\theta = \arccos\left(\frac{-B \pm \sqrt{B^2+4}}{2}\right) \tag{4.2}$$
$$\text{where} \quad B = \frac{L_c}{f}\cdot\left(\frac{\sqrt{n^2+1}}{n^2} - \frac{\sqrt{n^2+1}}{n^4}\right)$$

For a crystal length $L_c = 1.4$ mm, and refractive index of LiCAF at 290 nm $n = 1.404$, the fold angle is $\alpha = 2\theta = 12.6°$. This result is used in aligning the laser cavity, as well as the forthcoming modelling, which utilised ray transfer matrices to calculate various parameters of the stable laser cavity mode.

Modelling the Gaussian cavity mode of our laser was performed simply, using standard ray transfer matrices (ABCD matrices) and the complex Gaussian beam parameter q. Ray transfer matrix analysis using ray transfer matrices is a well known method, used to determine how a Gaussian beam propagates through various optical elements. These are basic 2×2 matrices that represent common elements such as transparent plates and curved surfaces, lenses, curved mirrors, and propagation through free space. Propagation through multiple

elements can be represented by multiplying several ray transfer matrices, opposite to the order of propagation. Multiplication combines the matrices of all elements and reduces them to a 2×2 matrix; a procedure that is simpler to perform numerically. The matrices that correspond to a complete round trip for our laser cavity, in the sagittal and tangential plane, are shown in equations 4.3 and 4.4, starting with propagation towards the Ce:LiCAF crystal from M_2.

$$\begin{aligned} T_s = \begin{bmatrix} A_s & B_s \\ C_s & D_s \end{bmatrix} = &\begin{bmatrix} 1 & 0 \\ -\cos\theta/f_{\mathrm{M2}} & 1 \end{bmatrix} \begin{bmatrix} 1 & 2L_1 \\ 0 & 1 \end{bmatrix} \begin{bmatrix} 1 & 0 \\ -\cos\theta/f_{\mathrm{M2}} & 1 \end{bmatrix} \\ &\begin{bmatrix} 1 & L_2 + L_3 + L_c\sqrt{n^2+1}/n^2 \\ 0 & 1 \end{bmatrix} \begin{bmatrix} 1 & 0 \\ -1/f_{M1} & 1 \end{bmatrix} \begin{bmatrix} 1 & L_2 + L_3 + L_c\sqrt{n^2+1}/n^2 \\ 0 & 1 \end{bmatrix} \end{aligned} \tag{4.3}$$

$$\begin{aligned} T_t = \begin{bmatrix} A_t & B_t \\ C_t & D_t \end{bmatrix} = &\begin{bmatrix} 1 & 0 \\ -1/(f_{\mathrm{M2}}\cos\theta) & 1 \end{bmatrix} \begin{bmatrix} 1 & 2L_1 \\ 0 & 1 \end{bmatrix} \begin{bmatrix} 1 & 0 \\ -1/(f_{\mathrm{M2}}\cos\theta) & 1 \end{bmatrix} \\ &\begin{bmatrix} 1 & L_2 + L_3 + L_c\sqrt{n^2+1}/n^4 \\ 0 & 1 \end{bmatrix} \begin{bmatrix} 1 & 0 \\ -1/f_{M1} & 1 \end{bmatrix} \begin{bmatrix} 1 & L_2 + L_3 + L_c\sqrt{n^2+1}/n^4 \\ 0 & 1 \end{bmatrix} \end{aligned} \tag{4.4}$$

In the above equation, $f_{\mathrm{M1}} = 25\,\mathrm{mm}$ and $f_{\mathrm{M2}} = 50\,\mathrm{mm}$ refer to the focal lengths of the curved cavity mirrors M_1 and M_2, n refers to the refractive index of Ce:LiCAF, and L_c the length of the Ce:LiCAF crystal (measured perpendicular to surfaces). The length L_2 is the distance between M_2 and the crystal, while L_3 is the distance between M_1 and the crystal, and L_1 is the distance from M_2 to M_3. Note that synchronous pumping necessitates a total cavity length that matches the pump laser, as shown in equation 4.5, where $F \approx 78.8\,\mathrm{MHz}$. This ultimately results in a cavity length of approximately 1.9 m, of which the short arm is only 0.1 m.

$$L_{\mathrm{total}} \approx 2\left(L_1 + L_2 + L_3 + L_{c,PL}\right) \approx c/F \tag{4.5}$$

Now, we turn to introduce the complex q parameter, which is a complex term that is commonly used to describe the propagation of a Gaussian beam. As a function of propagation distance z, $q(z)$ can be written in terms of the radius of curvature $R(z)$ and waist size $w(z)$ of the Gaussian beam, shown in equation 4.6, where λ is the wavelength of radiation and n is the refractive index of the medium.

$$\frac{1}{q(z)} = \frac{1}{R(z)} - i\frac{\lambda}{\pi n\left(w(z)\right)^2} \tag{4.6}$$

Note that at the location of a beam waist, q will be purely imaginary since the radius of curvature is infinite ($R(0) = \infty$) and the real term is therefore zero. Thus the waist size of a beam propagating in free space can be determined using equation 4.7.

$$w_0 = \sqrt{\frac{\lambda_0 \cdot \mathrm{Im}(q)}{\pi}} \tag{4.7}$$

The q parameter is transformed by ray transfer matrices simply, according to equation 4.8.

$$q' = \frac{Aq + B}{Cq + D} \tag{4.8}$$

For the laser cavity to be stable, it must be the case that $q' = q$ after one complete round-trip. In other words, the Gaussian beam must remain unchanged after each round-trip. With this condition in mind, solving equation 4.8 for q yields equation 4.9, where we choose $+\sqrt{}$ for convenience. If this round-trip condition is not satisfied, then the laser cavity is therefore not stable.

$$q = \frac{1}{2}\left(\frac{A - D}{C} \pm \sqrt{\left(\frac{A - D}{C}\right)^2 + 4\frac{B}{C}}\right) \tag{4.9}$$

If the cavity is determined to be stable, then the waist size and radius of curvature of the Gaussian laser mode can be determined for any position in the cavity, by applying the ray transfer matrices of the appropriate optical elements to q. The real and imaginary components of q then provide the radius of curvature and waist size, respectively.

For the chosen mirrors and cavity geometry, which has a predetermined optimal folding angle due to astigmatism and a fixed cavity length due to synchronous pumping, there is only one variable parameter: the distance between the curved mirrors M_1 and M_2. Using this as the independent variable, there were only three dependent variables of interest for our laser cavity: the waist size at the focal position between the curved mirrors, its position relative to these mirrors, and finally the waist size at the end mirror M_3.

The purpose of folding the cavity is to ensure that the stability range of the sagittal and tangential planes overlap; so the cavity is stable in both planes. Figure 4.2 shows the calculated focal waist size between M_1 and M_2 for distances between M_1 and M_2 that result in a stable laser cavity, using the ray transfer matrices above. As the figure shows, stability overlap in both planes has been reasonably satisfied, hence astigmatism has been adeqately compensated. The distance between M_1 and M_2 should be set to approximately 101.5 mm, the centre of the stability range, to minimise the sensitivity of the cavity to slight changes in the $M_1 \leftrightarrow M_2$ distance. The centre of the stability range yields a waist size of approximately 8 µm (radius) in each plane and there is approximately 1.4 mm of leeway of $M_1 \leftrightarrow M_2$. For a waist size of at least 6 µm, there is only approximately 1 mm of leeway.

The focal position between M_1 and M_2 was also calculated, relative to the distance from M_1, and is shown in figure 4.3. For these calculations, it is assumed that the foci of the two planes are equidistant from the centre of the crystal, which is reasonable as the focal waist

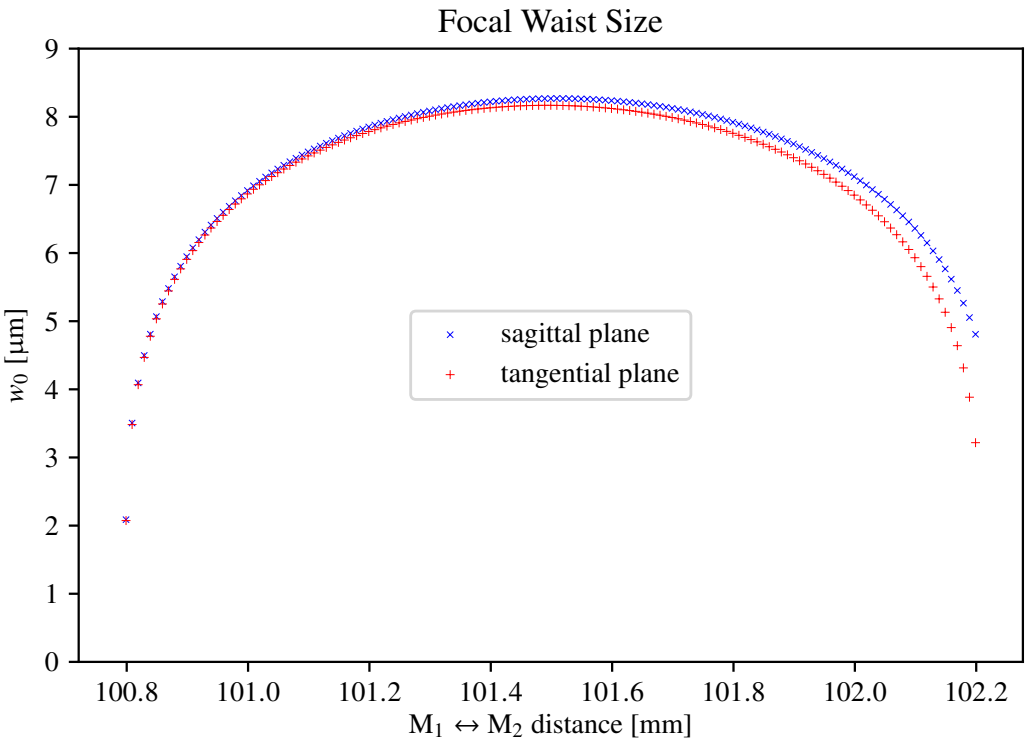

Figure 4.2: Calculated waist size of the waist located between M_1 and M_2 as a function of $M_1 \leftrightarrow M_2$ separation ($M_2 \leftrightarrow M_3$ distance was calculated from an overall cavity length of approximately 1.9 m). Note that the waist size is given as the equivalent waist in air.

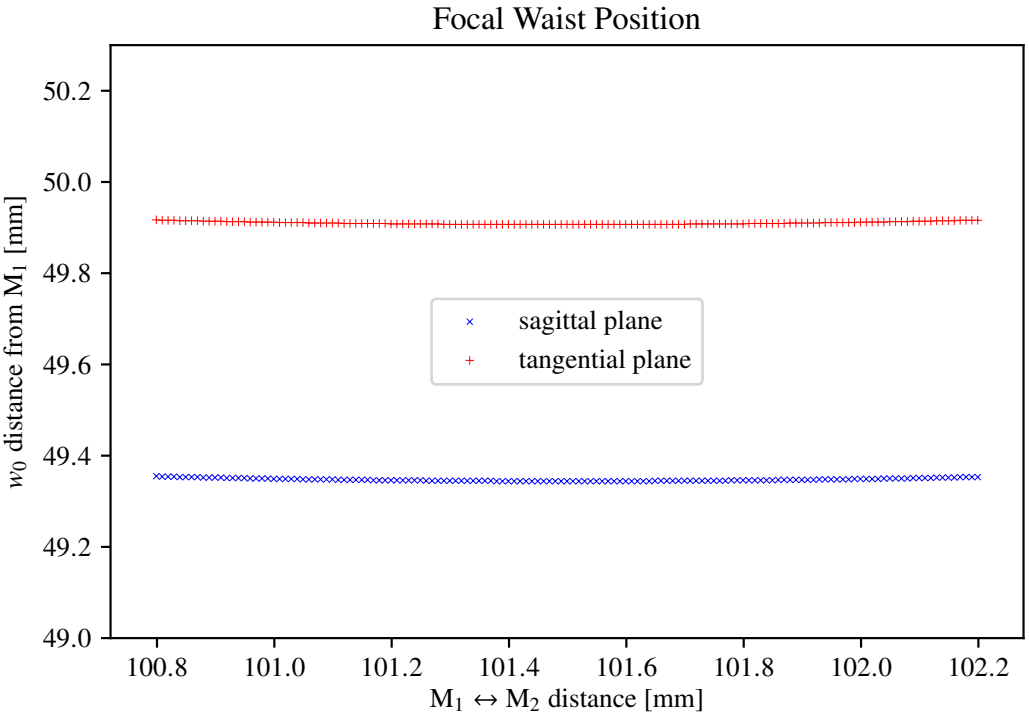

Figure 4.3: Calculated position of the waist between M_1 and M_2 as a function of $M_1 \leftrightarrow M_2$ separation, relative to the mirror M_1 ($M_2 \leftrightarrow M_3$ distance was calculated from an overall cavity length of approximately 1.9 m).

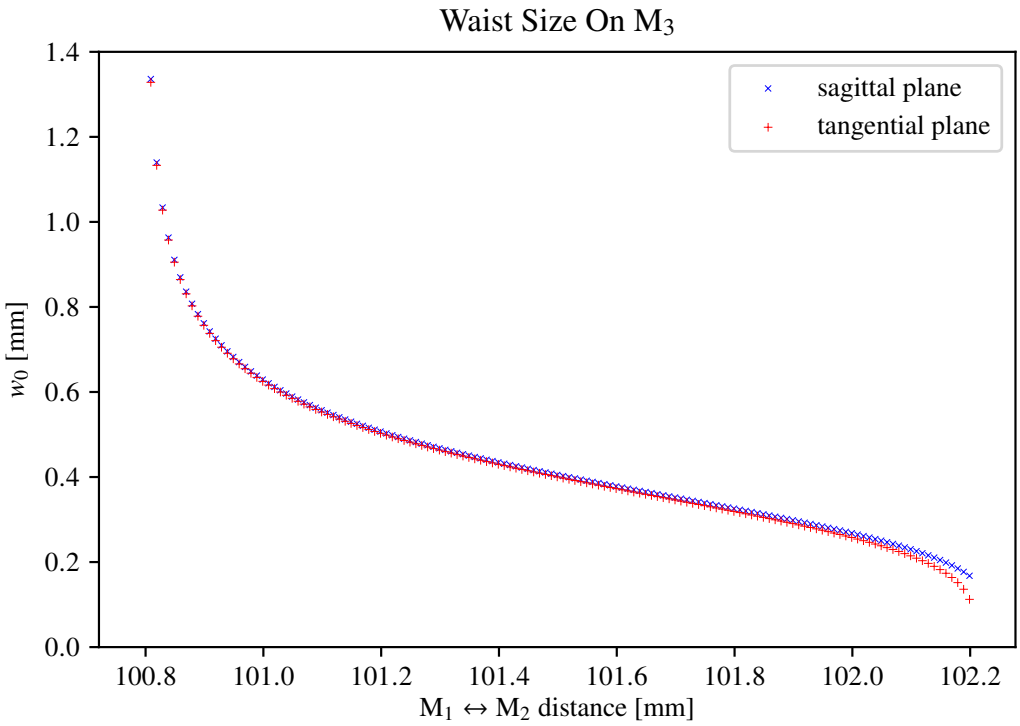

Figure 4.4: Calculated size of the waist located at M_3 as a function of $M_1 \leftrightarrow M_2$ separation.

should certainly be positioned to be within the Ce:LiCAF gain medium. The plot indicates that there is very little change in focal position as a function of $M_1 \leftrightarrow M_2$. Therefore, the Ce:LiCAF crystal is ideally placed approximately 49.6 mm from M_1, and the position of the pump focus should be adjusted to match it. Based on the insignificant variation of the distance between M_1 and the focal position, optimisation of $M_1 \leftrightarrow M_2$ should be performed by only adjusting the position of M_2, since the distance between M_1 and the Ce:LiCAF crystal is practically fixed. While the waist sizes for each plane are very similar, their locations unavoidably differ due to refraction as the beam enters the gain medium at Brewster's angle, since we used an asymmetric three mirror cavity. This would not be the case for the more usual four mirror cavity, which is symmetrical.

There is a second focus at the end mirror of our laser cavity, the size of which is shown in figure 4.4. Unlike the focus at the Ce:LiCAF crystal, between M_1 and M_2, the waist at M_3 varies more asymmetrically; it is smaller if the mirrors M_1 and M_2 are positioned further apart, and larger if they are closer together, eventually diverging as the edge of stability is reached. At the centre of the stability range, this waist size is approximately 0.4 mm; two orders of magnitude larger than the focal waist in the gain medium. Over the centre 1 mm of the stability range, this waist size varies by less than 0.2 mm.

4.2 Pump Source

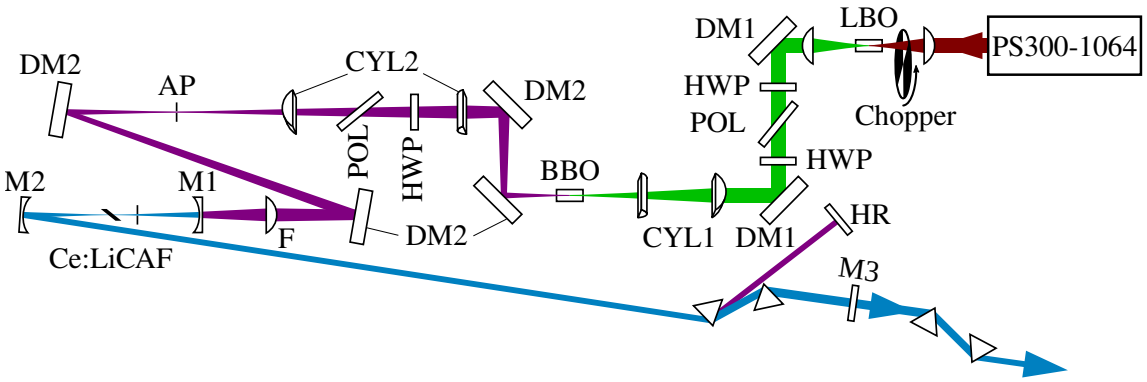

Figure 4.5: Schematic of frequency quadrupled pump laser and hybrid-mode-locked Ce:LiCAF laser. DM1: dichroic mirrors (HR/AR for 532/1064 nm). HWP: half-wave plate. POL: Brewster's angle thin film polariser. CYL1: focussing cylindrical lenses. DM2: dichroic mirrors (HR/AR for 266/532 nm). CYL2: collimating cylindrical lenses. AP: aperture. F: focussing lens.

The frequency quadrupled output of a mode-locked Nd:YVO_4 laser was used to pump our Ce:LiCAF laser, using a home-built frequency conversion stage to convert picosecond laser pulses from 1064 nm to 266 nm. The pump laser (Photonics Industries PS-1064-25) was a passively mode-locked MOPA capable of generating average powers of 25 W, composed of ultrafast pulses 20 ps long, at a PRF of approximately 78 MHz. Using a spherical plano-convex lens (f = 8 cm), the vertically polarised 1064 nm radiation was focused to a 60 µm waist in an LBO crystal, which was setup for type-I non-critical phase-matching. The crystal was inside a temperature controlled oven with 0.1 °C resolution; the oven was set to 152.4 °C, although the internal crystal temperature may differ due to poor thermal insulation.

Note that the 1064 nm beam was chopped using a 1:12 duty cycle at approximately 150 Hz, prior to entering the LBO crystal, to avoid thermal issues in the second frequency doubling stage. The optical power presented in this chapter refers to the average power during the burst, when the chopper was open.

After the LBO crystal, the second harmonic was collimated using an AR-coated spherical plano-convex lens (f = 8 cm). Dichroic mirrors (DM1) were used to separate the second harmonic from the fundamental wavelength. They had a combined transmittance of 99% for the 1064 nm radiation, and a combined reflectivity of 98% for the 532 nm radiation. An AR-coated half-wave plate (HWP) and Brewster's angle thin-film polariser (POL) were placed after the first dichroic mirror to be used as a variable attenuator for the 532 nm radiation. The second HWP, after POL, was used to rotate the polarisation of the 532 nm beam from horizontal to vertical for the frequency quadrupling stage. The LBO frequency doubling stage generated up to 16 W of 532 nm radiation, measured from the reflection off POL, which corresponds to a conversion efficiency of approximately 60%.

The 532 nm radiation was shaped using two AR-coated cylindrical lenses (CYL1), with focal lengths of 300 mm and 100 mm (in order of propagation) to produce an elliptical horizontal line focus that was approximately 180×12 µm in size. This focal shape was chosen to avoid poor beam quality associated with walk-off in the BBO crystal, which exhibits a high level of walk-off. This beam was frequency doubled inside a BBO crystal (NewlightPhotonics $5 \times 5 \times 7$ mm^3 AR-coated for 532&266 nm on both sides) for type-I critical phase-matching, which generated 266 nm, pulses approximately 13 ps in duration. The BBO crystal was held in a temperature controlled mount that was set to 90 °C to avoid hygroscopic effects. This high temperature was also used to slightly reduce TPA of the generated beam [108], which contributes to thermal dephasing and lensing effects under high power.

The generated 266 nm radiation was separated from the 532 nm using four dichroic mirrors (DM2) that transmitted the 532 nm beam and reflected the 266 nm. The combined reflectivity of the DM2 mirrors was <0.2% at 532 nm. The reflectivity at 266 nm degraded over several months, accompanied by observable coating damage to the front side surface. The power loss due to this was approximately 10-20% per degraded optical element. This was rectified by rotating each mirror to use an undamaged region of the HR coating.

After the BBO and the second DM2, two AR-coated cylindrical lenses (CYL2), with focal lengths 10 cm and 30 cm, were used to shape the cylindrical 266 nm beam to a circular focus at a beam-cleaning aperture (AP). This focussing geometry permitted control of the beam waist inside the Ce:LiCAF cavity simply by adjusting the distance between the last two DM2 mirrors. Another HWP-POL combination was placed between CYL2, where the beam diameter was still relatively large to minimise coating damage. This was used to rotate the polarisation of the 266 nm radiation from vertical to horizontal, and continuously vary the power of the 266 nm pump beam, which exceeded 5 W under optimal conditions. This corresponds to an infrared-to-UV conversion efficiency of approximately 20%. The stability of the 266 nm pulse train is shown in figure 4.6.

An AR-coated lens (F) with a focal length of 75.6 mm was used to focus the 266 nm beam into the laser cavity, through dichroic cavity mirror M1, which had a transmittance of >90%. The other two cavity mirrors (M2, M3) were an HR mirror and an OPC, respectively. The focal waist of the pump beam at the position of the Ce:LiCAF crystal was imaged (figure 4.7) using a plano-convex lens with a focal length of 35 mm and a charge-coupled device (CCD). This was done to optimise pumping efficiency, by matching the waist size of the pump focus to the Ce:LiCAF laser mode (mode-matching; calculations presented in the next section). The M-squared value of the 266 nm beam was estimated to be in the range of 2-10, based on a number of knife-edge measurements. Note that the prisms depicted in figure 4.5 were neglected in the previous simplified model, because they were placed close to M_3 where the beam is reasonably collimated and therefore have an insignificant effect on the alignment of the short arm of the cavity. After the first intra-cavity prism, angular dispersion separated the pump beam from the laser cavity mode, causing the pump beam to narrowly miss the

second prism and exit the cavity. A high reflector (HR) was placed in the path of the pump to recycle it back into the Ce:LiCAF crystal, thereby increasing the absorption of the average power from the pump beam from approximately 70% to 90%.

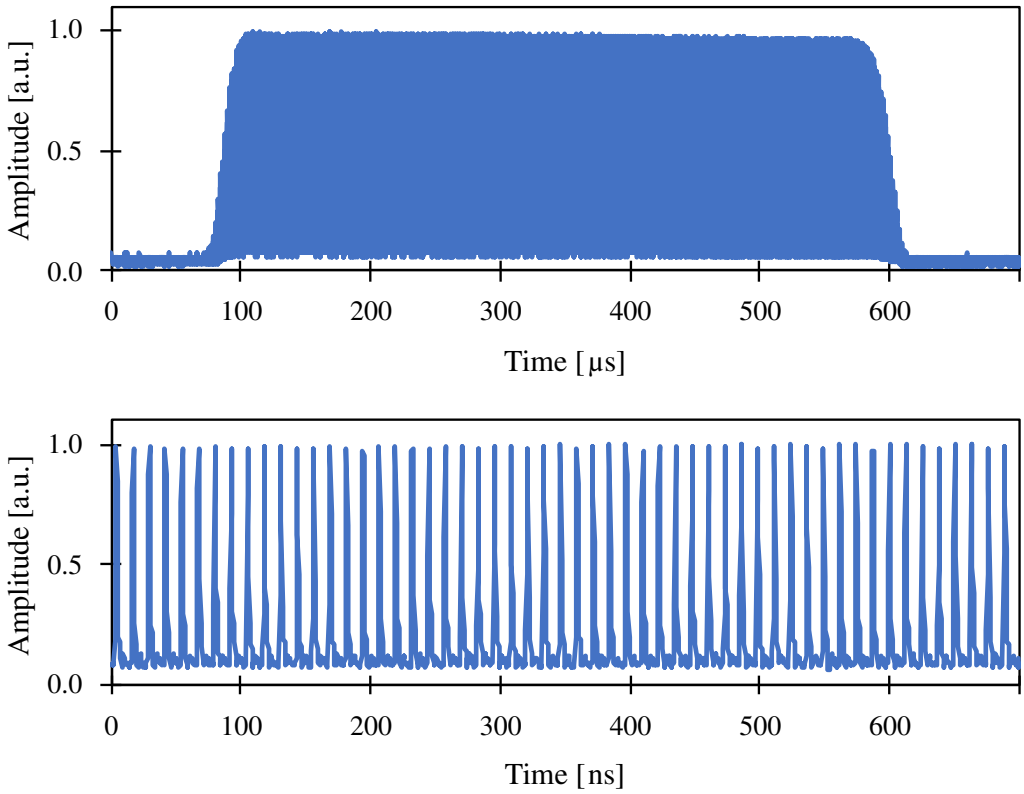

Figure 4.6: The 266 nm pump pulse train during the open chop cycle. Top trace: one complete chopper opening with approximately 40,000 pulses. Bottom trace: small pulse section showing relatively stability from pulse to pulse over 700 ns.

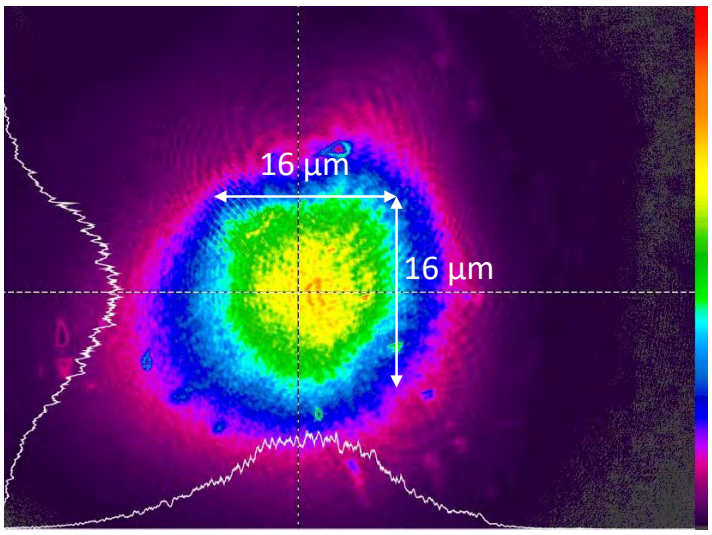

Figure 4.7: The 266 nm pump focal waist, imaged using a 35 mm plano-convex lens and a UV sensitive CCD detector, in the absence of the laser crystal. The $1/e^2$ beam diameter was calculated by the D4σ method.

Simulated Gain Modulation

The transverse spatial distribution of the gain is governed by the shape of the pump beam, which was a reasonably circular Gaussian (figure 4.7). However, in the axis of propagation, the gain is non-uniform. Firstly, the energy of the pump is depleted as it propagates through the Ce:LiCAF crystal, via absorption; the gain varies along the z-axis. Secondly, using synchronous pumping causes the gain profile to also vary with time. When the intra-cavity laser pulse drifts in time due to slight asynchronism, it encounters a different level of gain.

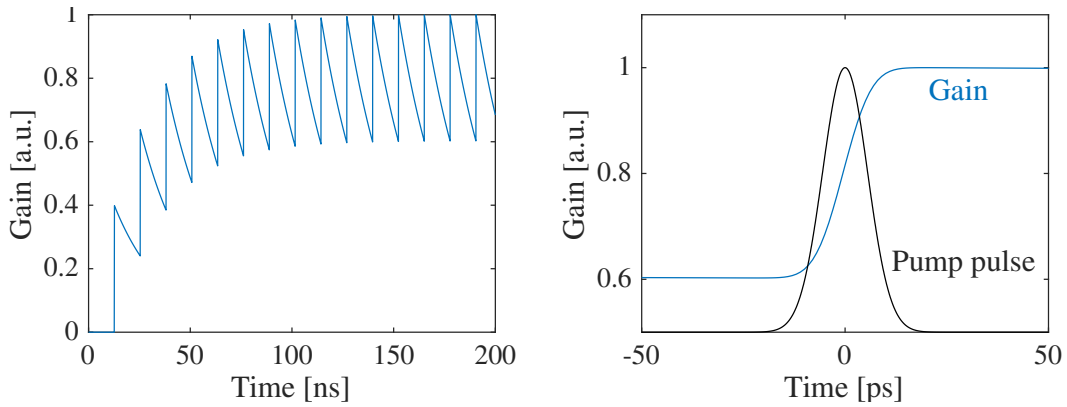

Figure 4.8: Left: theoretical gain modulation of our Ce:LiCAF laser towards the steady-state. Right: steady-state gain step used in modeling, centered on the peak of the arriving pump pulse. Depletion of gain due to lasing has not been included, only fluorescence.

The undepleted gain step that is introduced by pumping a Ce:LiCAF crystal, due to its short upper-state lifetime of 25 ns [172], was modelled simply for 13 ps pump pulses at a repetition rate of 78 MHz (inter-pulse period of 12.6 ns). The Ce:LiCAF crystal was treated as a point, as opposed to a medium with finite length. This is a reasonable assumption, since the crystal length is less than half the 4 mm physical length of the 13 ps pump pulse (FWHM). Therefore, while the longitudinal gain profile within the crystal is approximately an exponential due to absorption, the total gain can be represented by this simplified model, the results of which are shown in figure 4.8. While the calculation was performed numerically, this is essentially an analytical model that increases by integration of the Gaussian profile of the pump pulses, and decreases due to exponential decay. Once an equilibrium is reached, the gain has a modulation of 20%. It is also at a maximum after the pump pulse has been absorbed, which means that for a well-matched cavity length to the synchronous pump, the resonating pulse will likely encounter the pump pulse just outside the crystal, not within it. Note that if this were not the case, the interaction of the pump pulse and the resonating laser pulse could otherwise be a significant factor in Kerr-lensing, due to cross-phase modulation between the two pulses. For very slight detuning of cavity length (<10 µm) theory suggests that the resonating pulse will reform each round trip, as there is differential gain between its leading and trailing edge. Based on the temporal gain (right-hand side of figure 4.8) the pulse could encounter steep or shallow differential gain, depending on the direction of detuning.

4.3 Initial Characterisation

The evolution of characterisation for our Ce:LiCAF laser was discussed in chapter 3. Since the laser's initial construction and characterisation by Eduardo Granados Mateo [213], there have been several changes to the elements which comprise the cavity. Firstly, we used a slightly longer laser crystal (1.40 ± 0.01 mm instead of 1.25 mm) which slightly inceases the single pass absorption at the expense of scattering losses. Secondly, and more importantly, the three Melles-Griot cavity mirrors that Granados Mateo used (M_1, M_2, M_3) were replaced by Barbara Wellman [4]. The new mirrors were coated by Advanced Thin Films (ATF) and reduced the round-trip loss by almost 1%. The measurements presented in this chapter include a new plane output coupling mirror as M3 (instead of an HR mirror) in place of the near-Brewster's angle plate that was used as an output coupler in the experiments conducted by the aforementioned authors. This new OPC has two distinct advantages for an ultrafast oscillator. It consolidates the laser output into a single beam, compared to the four beams that are produced by a standard Brewster's plate. Additionally, it introduces significantly less chromatic dispersion to the cavity, which is also invariable; although the output coupling loss is adjustable using Brewster's plate, doing so also alters the dispersion, so our plane mirror OPC simplifies two contributing factors to the generation of ultrafast pulses: power and dispersion. The latter of these is discussed in depth in chapter 5.

Plane Mirror Output Coupler

We elected for an OPC transmission that was relatively low, 1-2% compared to 2.5% that generated optimal power output with a Brewster's plate [4]. This was done for two reasons; firstly to reduce the threshold, since it was unclear whether the lasing threshold could be reached with the additional losses of an intra-cavity prism pair, and secondly to maximise the intra-cavity power. Increasing the intra-cavity power allowed us to invoke the essential non-linear effects that comprise the soliton-like Kerr-lens mode-locking processes of femtosecond oscillators. The low threshold, in addition to surpassing threshold with an intra-cavity prism pair, allowed us to reduce pump power enough for the first demonstration of an un-chopped mode-locked Ce:LiCAF laser (section 4.5). The reflectivity curves for the plane mirror OPCs are shown in figure 4.9, and indicate less than 0.2% variation over the 285-295 nm region in which Ce:LiCAF has its primary gain peak.

The transmission loss of the OPC was measured using a Cary5000 UV-vis-NIR spectrophotometer, which is shown in figure 4.10. Each line represents the measurement of an individual mirror, and variation is primarily due to the alignment of the mirror to the probe beam within the spectrophotometer. Based on these results, $T = 1.5 \pm 0.1\%$. Knowledge of the transmission through this OPC allows us to accurately determine the average intra-cavity power, which is approximately a factor of 66× the power output measured from the laser. This can be used to calculate power and pulse energy inside the cavity.

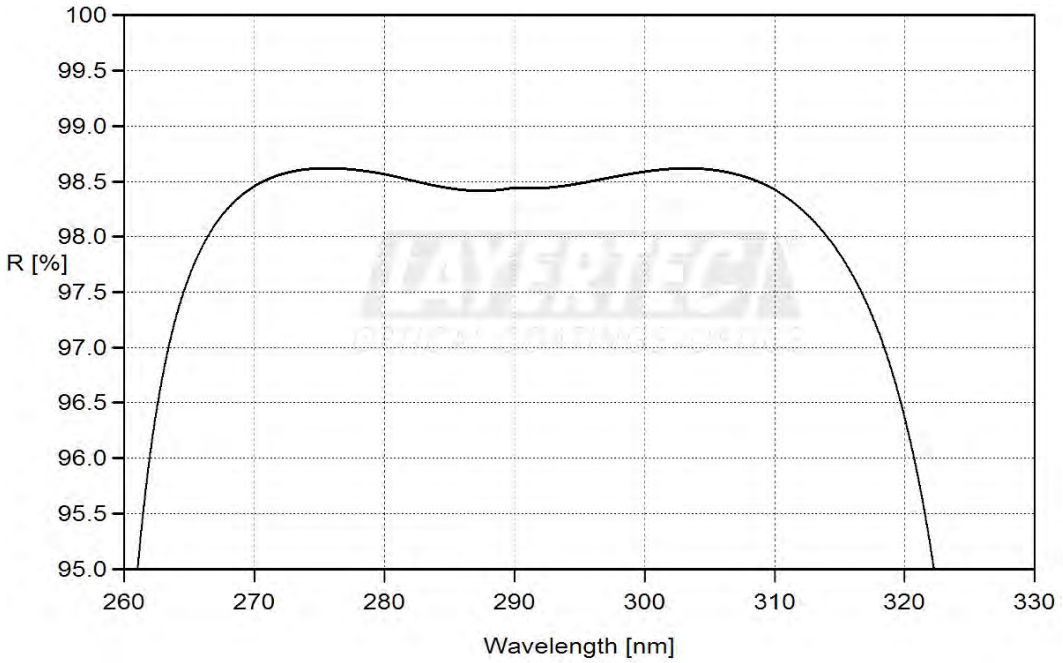

Figure 4.9: Calculated reflectivity of our output coupling plane mirror from Layertec, with respect to unpolarised light at 0° angle of incidence.

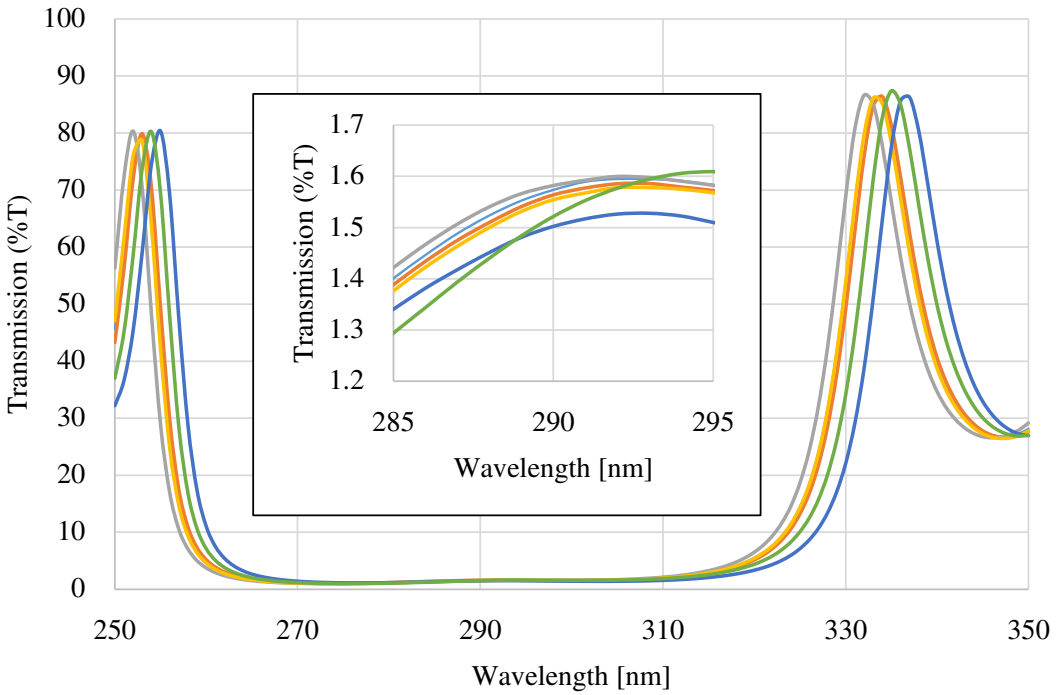

Figure 4.10: Transmission of plane mirror OPC, measured using a Cary5000 UV-vis-NIR spectrophotometer (each line represents the measurement of an individual mirror).

Alignment and Maintenance

Initial arrangement of the laser cavity was performed by setting the distance between the two curved mirrors (M_1 and M_2) to 101-102 mm, measured simply using a ruler, and angling the long arm of the cavity to 12.6° using lines marked out using a protractor. The longitudinal focal position of the pump beam was set to 50 mm from M_1 by translating the focussing lens, whilst observing ablation caused by the focal spot (significantly attenuated). The Ce:LiCAF crystal was positioned at the same location and set at Brewster's angle using the angle of the reflected pump beam. The transverse position of the pump beam on all three cavity mirrors was observable via scattering or transmission losses; fluorescence losses by propagation through the substrate of the input coupler M_1, transmission losses through M_2 (fluorescence was observed on a small piece of paper positioned behind M_2), and scattering losses on the cavity-side surface of M_3. It was important to position the pump beam at the centre of each cavity mirror for alignment without prisms, and then optimise the alignment of the cavity mirrors to match the position of the laser cavity mode to that of the pump. Coarse alignment was performed by observing the position of the laser cavity mode on M_1 and M_3 which was observable due to scatttering losses on the surface of each mirror. Fine alignment was performed using a photodiode and power meter to maximise power output, on both a fast and slow timescale.

The intra-cavity prisms were inserted into the cavity and aligned, after transverse translation of the end mirror M_3. Setting the prism angle was done in a similar fashion to the Brewster's-cut Ce:LiCAF crystal, by adjusting their rotation based on the angle of the reflected pump beam. The insertion of the second prism was increased to allow the pump beam to direct the pump beam to M_3, which was adjusted to overlap the input pump beam and return pump beam on M_1. Once the laser was operational, the approximate position of the laser beam through the prisms could be identified by observation of fluorescence within the material, and scattering on the surfaces. Fine adjustment of the prism pair rotation was then performed by monitoring the spectral output of the laser, which could be tuned via the horizontal angle of M_3. When misaligning M_3, optimal prism alignment resulted in minimal spectral tuning, while severe prism misalignment resulted in continuous tuning over a wide range of wavelengths. The output power was also monitored by a power meter, as it should be maximal for optimally aligned Brewster's-cut prisms.

Aside from alignment optimisation, maintaining the power and efficiency of both the laser and its pump system was necessary. Cleaning of the cavity mirrors and un-enclosed pump system elements was performed regularly, using ethanol as a solvent, by firmly wiping optical tissue over each mirror, followed by realignment (if necessary) and optimisation for power output. In order to minimise air flow and dust deposition, the optical table was partially covered. In addition to cleanliness, maintaining a consistent temperature for the pump laser was essential in maximising its output power. This required a fixed temperature for both

the chiller unit (22°) and the air conditioning system (22°), as the temperature affects the wavelength of the diode lasers that power the pump laser resonator itself (and thus absorption by the gain medium Nd:YVO_4). Finally, to isolate the system from noise vibration, a floating table was used, and the conduits between the chiller unit and the pump laser were surrounded by foam. Unfortunately, suppression of vibration through the conduits seemed to have only a marginal effect, suggesting that the most significant source of vibration that remained was from sound, air flow, or water flow.

Mode-Locking

The majority of experiments using our Ce:LiCAF laser were performed while a chopper was used to chop the infrared beam of the pump laser at approximately a 1:12 duty cycle; it was operated at a frequency of 150 Hz for which it had an opening time of approximately 500 µs. In this thesis, the values of power output are compensated for this duty cycle, multiplied by 13, except for section 4.5 in which the chopper was not used. A single opening of the chopper can be seen in figure 4.11, which was recorded during mode-locked operation as seen in the expanded view. The Ce:LiCAF laser power builds up quickly and is well stabilised after a short period of less than 25 µs, which corresponds to 2000 round-trips. This means that slow measurements (e.g. average power measured with a thermal power meter) accurately represent the performance of the laser during the burst.

The envelope of the open chop cycle sometimes had a slight decline or incline, which can be the result of various transient thermal effects occuring in the pump stage. The envelope was also affected by imperfect alignment of the laser cavity mode, which presents as a severe, albeit stable, decline or incline at any time during the open cycle. The variation in figure 4.11 is standard for a reasonably well-aligned cavity and pump arrangement. It was recorded for a cavity length position for which the Ce:LiCAF laser produces its maximum output power. However, this cavity length was not optimal for ultrashort pulses, in fact, it required slight detuning away from synchronicity between the laser and the pump. For maximum power output, the cavity was made approximately 20 µm longer than the defined $\Delta x = 0$, which was defined by the cavity length that resulted in synchronously pumped mode-locking and generated the shortest measured pulses at approximately 290 nm.

The power output and stability of our Ce:LiCAF laser output around $\Delta x = 0$ varied significantly, which is to say over a few µm of cavity length around the first harmonic of synchronous mode-locking. This is shown in figure 4.12, which shows the open chop-cycle, also recorded on a photodiode. Here, the downward slope may be the result of thermally affected pump power or pointing angle. This slope has negligible bearing on the presence of modulation, since the modulation occurs regardless of quality of alignment. The frequency of modulation tends to increase (bottom left in figure 4.12) for shorter cavity lengths in the mode-locking region. While this semi-stable power output of our Ce:LiCAF laser is an issue,

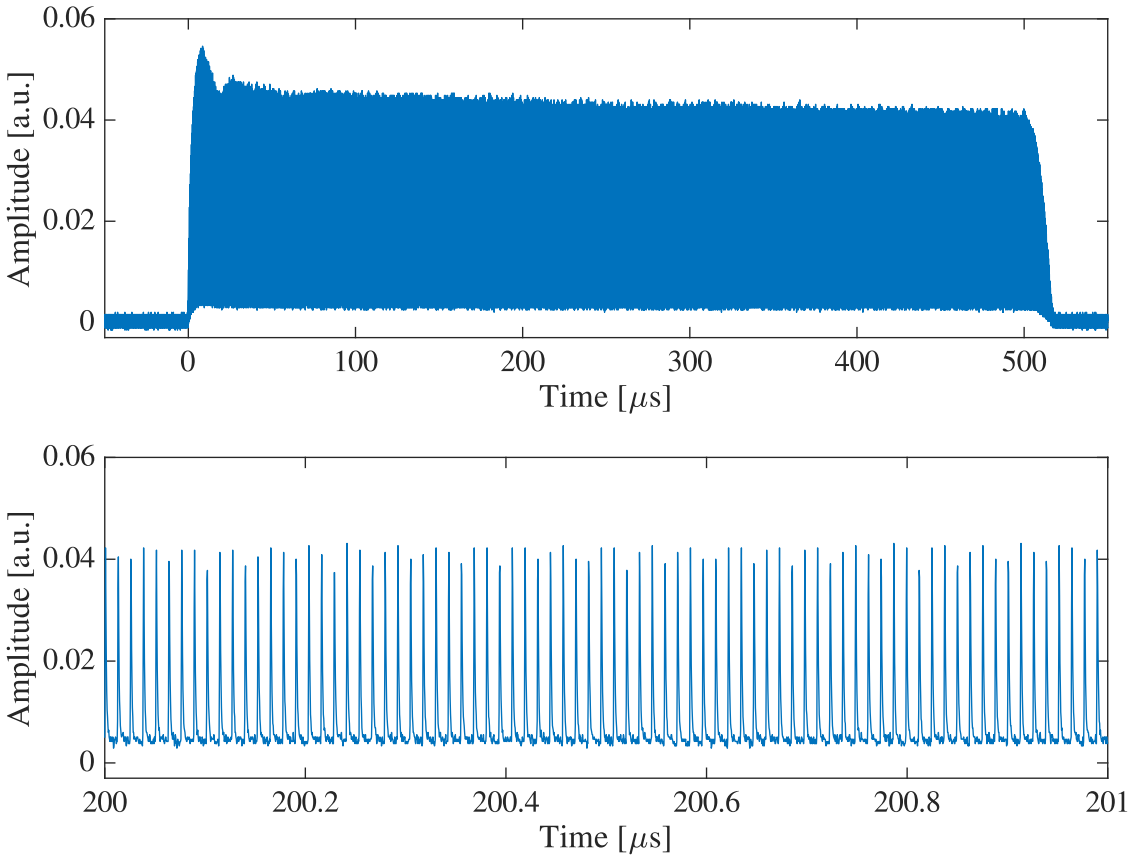

Figure 4.11: Ce:LiCAF laser mode-locked operation during one opening of the chopper, recorded on a photodiode.

the solution may simply require a more mechanically robust laser cavity and pump system to reduce variation in cavity length, or alternatively, active stabilisation of the Ce:LiCAF laser cavity length. While these are feasible, they are beyond the scope of this thesis. The modulation may correspond to mode-locking instability caused by synchronous pumping, which was also observed in dye lasers on a timescale of kHz to MHz. This frequency varied with cavity length, as does the wavelength due to dispersion tuning which is also present in synchronously pumped dye lasers. See chapter 2 for background regarding dispersion tuning, and chapter 5 for a detailed analysis of the dispersion tuning present in our Ce:LiCAF laser. Essentially, chromatic dispersion in an actively mode-locked laser resonator (such as ours) can translate a change in cavity length to a shift in wavelength to maintain synchronicity. Due tp dispersion tuning (the details of which are presented in chapter 5, the cavity length range that supports short pulses via synchronous mode-locking increases with the amount of dispersion, so reducing dispersion in our laser (which is necessary for KLM) reduces the acceptable cavity length for active mode-locking and exacerbates the sensitivity of cavity length to vibrations.

The semi-stable modulation of output power can be characterised more simply by a reduction of average power. This was measured using a standard thermal power meter, which has a slow response time. These results are shown in figure 4.13, for which the cavity length

position of $\Delta x = 0$ refers approximately to the centre of the dispersion tuning range; that is the cavity length of synchronicity between the pump and the Ce:LiCAF laser for the peak wavelength of Ce:LiCAF, and is therefore the optimal cavity length for generating ultrashort pulses.

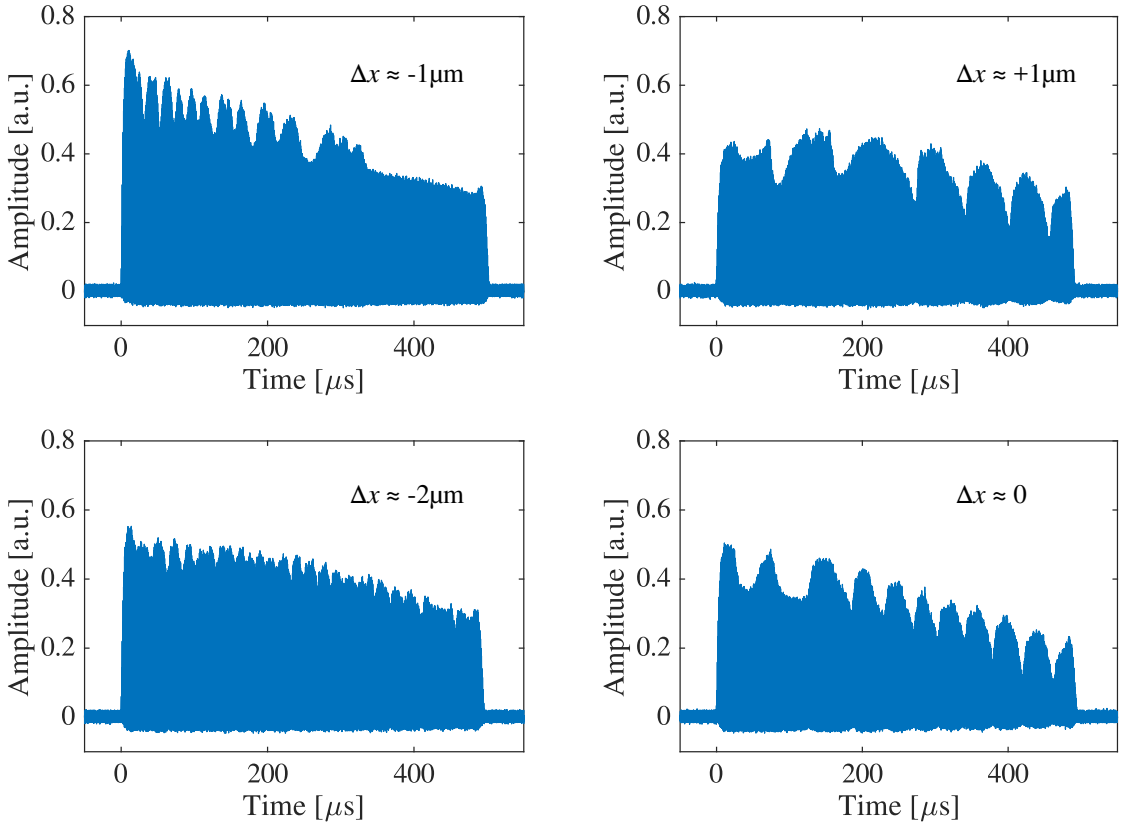

Figure 4.12: Modulation of Ce:LiCAF laser output, as measured on a photodiode.

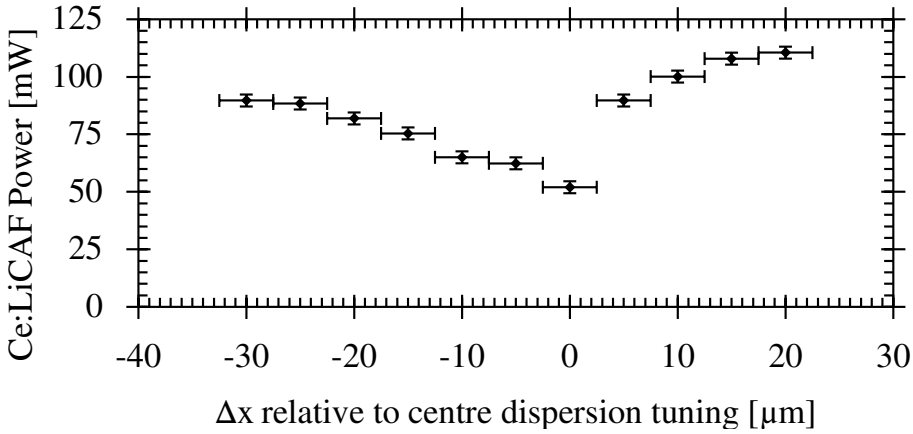

Figure 4.13: Power output (corrected for chopper duty cycle) over the range of negative dispersion tuning when using an intracavity prism pair.

4.4 Slope Efficiency

The slope efficiency of a laser is measured by varying the input pump power and measuring the laser's output power; it is defined by the slope of output power to input power, only in the region for which the laser is above threshold. The output power of the Ce:LiCAF laser was measured using a power meter placed immediately after the plane mirror OPC (M_3) and the pump power was measured using the same power meter, prior to being focussed into the gain medium. The pump power was varied with the combination of a HWP and thin-film Brewster's angle polariser, which acted as a continously variable attenuator. The recorded pump power does not account for intermediate losses from one HR mirror, an AR-coated focussing lens, and the dichroic cavity mirror M1; transmission loss from these elements is estimated to be 10%. The duty cycle of the chopper, on the other hand, has been accounted for, so these results a representative of power during the burst. The slope efficiency results are shown in figure 4.14 to compare the power output of operation with and without a pair of intra-cavity prisms that are utilised in the coming sections. These data were both recorded for a cavity length slightly longer than $\Delta x = 0$, to generate maximum power, as mentioned above.

Although the prisms were cut so that the intra-cavity beam would be incident at Brewster's angle, losses were still introduced due to slight misalignment, absorption, and primarily

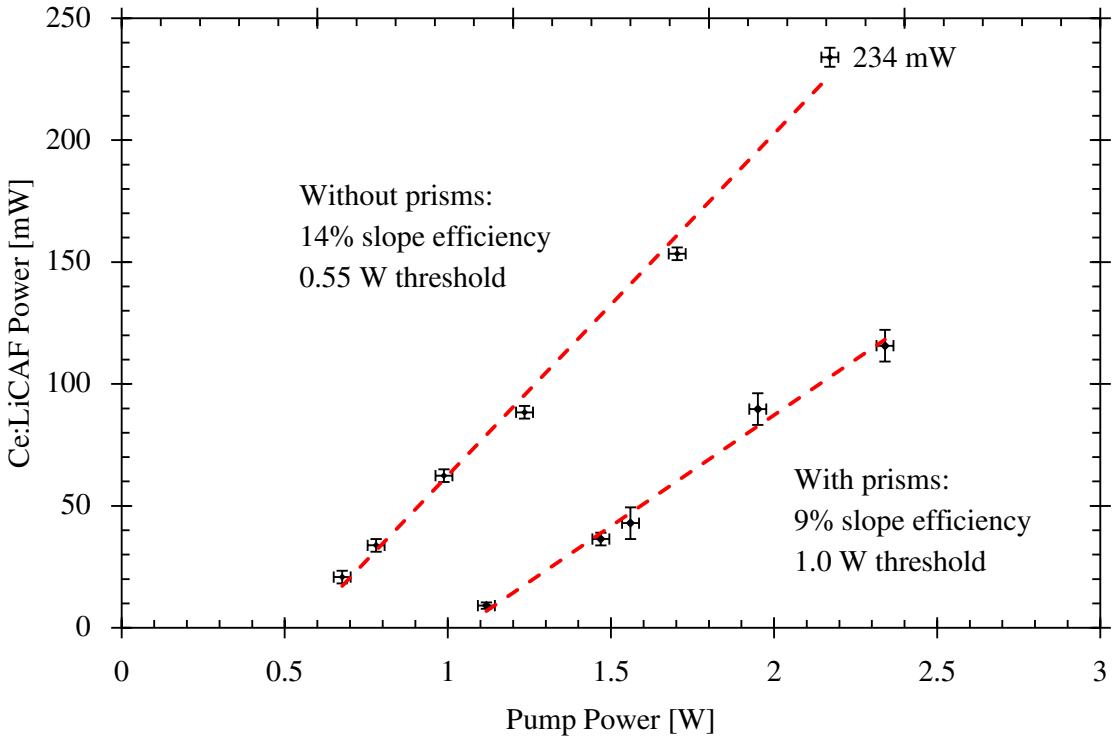

Figure 4.14: Comparison of slope efficiency and pump threshold for the Ce:LiCAF with and without an intracavity prism pair cut at Brewster's angle for 290 nm light, made from UV grade fused silica. A plane output coupler was used.

scattering; UV wavelengths are particularly prone to scattering. The total round-trip loss that the prisms introduce was calculated to be approximately 2.2% using the measured slope efficiency of the laser with and without prisms. The simplified equation for this calculation is shown in equation 4.10, adapted from [220]; η_Δ and η is the slope efficiency with and without prisms, respectively; L_{OPC} is the 1.5% transmission from the OPC; L_t is the 2.5% round-trip loss without prisms; and L_Δ is the round-trip loss introduced by the prism pair.

$$\frac{\eta}{\eta_\Delta} = \frac{L_{OPC} + L_t + L_\Delta}{L_{OPC} + L_t} = 1 + \frac{L_\Delta}{L_{OPC} + L_t} \tag{4.10}$$

The underlying assumption for this calculation is that all other variables remain fixed and the previously measured 2.5% round-trip loss has not increased. This is reasonably valid owing to the presence of a well-aligned HR mirror used to reflect the pump beam that misses the second intra-cavity prism (due to a larger angle of refraction from the first prism) and double-pass pump the Ce:LiCAF crystal, which matches the pumping arrangement of the prismless cavity. All other optical elements were identical between these measurements, and it is assumed that the scattering losses of the OPC are similar to that of the HR end-mirror.

4.5 Un-Chopped Operation

Operating our Ce:LiCAF laser un-chopped required a few key changes to the pump stage, but was made possible by the choice of a low transmission output coupler that resulted in a low threshold. In the first frequency doubling stage, the LBO temperature was reduced from 152.4 °C to 148.6 °C to compensate for the increased heat deposition from the 1064 nm IR beam. Since LBO is thermomechanically robust, this was the only alteration necessary to generate unchopped 532 nm green light. Thermal effects in the next frequency doubling stage, specifically in the BBO crystal, limit the 266 nm power that our pump stage is capable of. To reduce this issue, the 532 nm radiation was attenuated using a half-wave plate and thin film polariser at Brewster's angle. This allowed for continuous adjustment of input power to the BBO crystal, to establish a balance between power and stability; approximately 50% of the 16 W of 532 nm radiation was used, while the waste 8 W was monitored on a power meter for changes. Although our system can generate over 2 W of 266 nm radiation with more 532 nm power, operating well above the 50% mark caused the 266 nm power to drop to 1 W within 5 minutes. Additionally, the beam pointing angle of the 266 nm beam exhibited some walk-off due to thermal effects in the BBO. This limited the reliable 266 nm pump power to 1.2-1.3 W, whilst maintaining reasonably stable delivery of the pump radiaton.

The un-chopped Ce:LiCAF laser was initially operated without the use of the intra-cavity prism pair, since this increases the threshold. The slope efficiency in this case was recorded, and is shown in figure 4.15. While the gradient is neat and linear, the slope efficiency itself is 3% lower than in un-chopped case. Although unlikely to be the primary cause, this difference

could be affected by laser operation during the time it takes for the chopper to block and unblock the pump beam. However, the increased threshold indicates that it is more likely to be operating with lower efficiency; possibly due to slight misalignment, decreased stability of the pump, and increased thermal lensing within the Ce:LiCAF crystal. While it is not included in the figure (since it was achieved separately), over 80 mW was generated by the mode-locked Ce:LiCAF laser, but this declined in less than a minute. At a reduced pump power of 0.9 W, a power output of 40 mW could be maintained for tens of minutes, likely due to the improved pointing stability of the pump beam that was observed. The laser's poor power stability is almost certainly to be solely caused by thermal issues in the pump stage, specifically pointing angle stability of the pump beam, which were possibly combined with thermal lens effects in the Ce:LiCAF crystal itself. Although cooling the crystal mount to 22°C (from 27°C at thermal equilibrium) was tested, it had no noticeable effect on the power stability; however, the top and bottom surfaces of the crystal have a small contact area to the mount (or indeed any cooling element) so cooling may not have a significant effect on the gain volume.

Un-chopped operation was also demonstrated whilst the intra-cavity prisms were in the same position that recorded a minimum pulse duration previously. A slope efficiency was not recorded simply because the pump power was set to its stable limit of 1.2-1.3 W, and would therefore be unreliable (the laser was running just above threshold; an insufficient range of pump power was available to accurately determine a slope efficiency). A reasonably stable output power of 10-20 mW was achieved from the Ce:LiCAF laser in this configuration, which is consistent with the power recorded with the chopper runing; although, stability was much better with reduced pumping for the lower loss (prism-less) cavity. The output power also varied on a kHz time-scale in the same manner as presented in chapter 4, section 4.3, over the range of dispersion tuning, likely an effect of cavity length variation under our synchronous pumping regime.

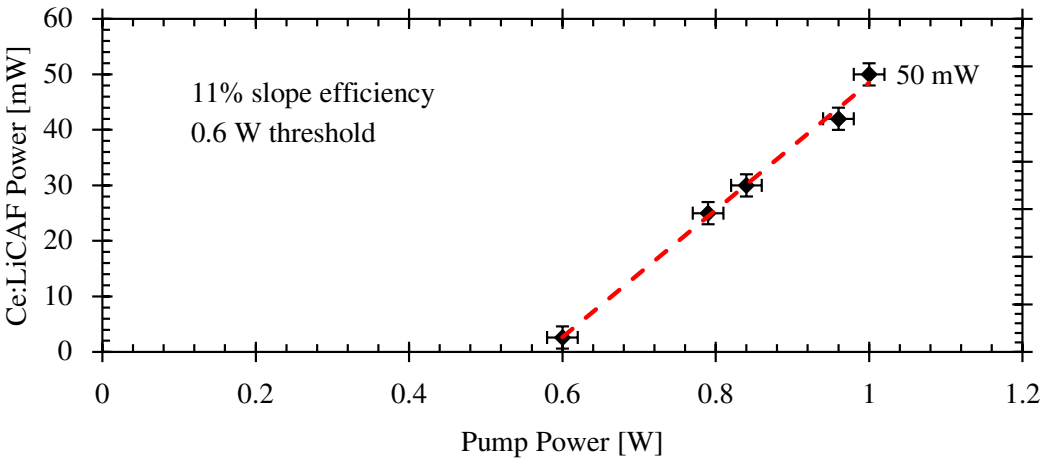

Figure 4.15: Slope efficiency of our Ce:LiCAF cavity, recorded during un-chopped operation.

4.6 Discussion

In this chapter, the first hybrid-mode-locked Ce:LiCAF laser was presented. This is the first time that Kerr-lensing has been utilised in the mode-locking of a Ce:LiCAF laser; KLM provided a passive contribution to mode-locking, while synchronous pumping provided the active contribution. In addition to hybrid-mode-locking, this is the first time that un-chopped operation of a mode-locked Ce:LiCAF laser has been demonstrated. This was the result of minimising thermal issues in the pump system by reducing the thermal load on the BBO crystal, and reducing the threshold of the laser cavity by replacing the near-Brewster's plate output coupler with a plane-mirror OPC. Owing to the new OPC, this is the first time that the mode-locked Ce:LiCAF laser has generated a single output beam, and the highest power within an individual beam ever recorded for such a laser. A portion of the findings within this chapter were published as conference proceedings and are presented in appendix A.

While this is a promising step forward for CW and mode-locked Ce:LiCAF lasers, several unresolved issues are still present in the current oscillator and pump configuration. These issues are mostly related to the cavity length requirement of synchronous pumping. The cavity length requirement is more sensitive when the dispersion is reduced, which is necessary for Kerr-lensing to take place; ergo, implementing KLM in a hybrid-mode-locking scheme can exacerbate issues associated with variation of the cavity length (i.e. vibration) unless active stabilisation of the cavity length is employed.

Stability

Technical issues limit the stability of the output power and pulse duration produced by the Ce:LiCAF laser. Modulation of the output power occurs on a kHz time-scale for cavity lengths that satisfy synchronicity, with a frequency that is lower for a cavity length that is central to this range. The dynamics here are not fully understood, and may simply be the result of vibrations within some component of the optical system, which includes elements internal to the pump laser which has vibrations from the water cooling system. However, the intra-cavity pulse duration likely plays a significant role in the dynamics of mode-locking within the synchronous-asynchronous transition. Longer pulses encounter a greater gain differential over their length than shorter pulses, which may cause sufficiently long pulses to shift in time more readily, while shorter ones decay as a new pulse is formed. In turn, this may be causing modulation of the pulse energy.

The maximum power of the Ce:LiCAF laser was recorded for a longer cavity length than precise synchronicity, but this longer cavity length produces pulses that are much longer, of order 100 ps [212]. The fact that there is no visible modulation is likely because the mode-locking becomes somewhat insensitive to slight variation of cavity length and are therefore more stable. For cavity lengths that satisfy synchronicity precisely (at which KLM can be invoked) there is considerable interplay between pulse duration and pulse energy, since they

both contribute to Kerr-lensing, which then affects the stability of the laser cavity mode. Ultimately, since all of these mechanisms are linked, they are simultaneously destabilised by cavity length drift and vibration.

Astigmatic Kerr-Lensing in a Gain Medium

The astigmatic nature of our Ce:LiCAF cavity may have a significant effect on Kerr-lensing, and the stability of the laser cavity mode. Relative to the axis of propagation, the sagittal and tangential focal positions are separated by approximately 0.4 mm. Also in this axis, the gain profile decays exponentially as the pump is absorbed according to $e^{-\alpha_L z}$. Hence, the pulse energy (and therefore peak power) at each of these positions is different, as it has encountered a different level of amplification. Travelling from M_2 to the crystal, the sagittal focus is present first, with the least pulse energy. Secondly, the tangential focus has a higher pulse energy. Thirdly, on the second pass through the crystal, the tangential focus occurs again with an even higher pulse energy. Fourthly, and lastly, the sagittal focus occurs with the highest pulse energy. Since the gain medium is also a significant contributor to dispersion, the pulse duration will also differ between these focal positions, in addition to the pulse energy.

The magnitude of lensing is inherently different in each direction of propagation. This is normal; Ti:sapphire lasers may operate with significantly different pulse energies with respect to each direction of propagation through the crystal. This means that the cavity mode has a transverse profile that is different depending on the direction of travel within the resonator. However, our cavity is also astigmatic, which means that instead of just two different lenses (forwards and backwards), there are effectively four lenses. Since the Kerr-lensing is governed by peak power density, the first lens in the Ce:LiCAF crystal (e.g. sagittal focal position) will affect the beam size (and therefore the magnitude of Kerr-lensing) at the second lens.

Normally, KLM cavities are symmetric and are therefore not inherently astigmatic. However, since these cavities usually have a gain medium at Brewster's angle, the elliptical focus results in astigmatism introduced by the Kerr-lens itself. In our cavity, the combination of astigmatic Kerr-lensing in combination with the pre-existing astigmatism may compound for even stronger self-focussing. This may affect cavity stability, hence the semi-stable operation in pulse duration and energy. From [221], "we believe symmetric resonators to be more suitable than asymmetric ones for KLM with a hard aperture". A possible solution to experimentally analyse astigmatism and Kerr-lensing in our hybrid-mode-locked Ce:LiCAF laser would be to assess the relative mode-clipping for the tangential and sagittal planes, in the region where the beam is most astigmatic. A slit may be more effective than a circular aperture, since lensing can increase the beam waist in one plane but not the other. Alternatively, using a CW pump laser and modifying the cavity geometry to be symmetric and minimally astigmatic would permit experiments that focus solely on KLM. In these experiments, it is estimated from equation 4.11 that the focal length of the generated Kerr-lens was on the order

of 1-10 mm (assuming an intra-cavity peak power of 100 kW) which is exceedingly short. For comparison, the Ti:sapphire presented later in this thesis (chapter 6) had a Kerr-lens focal length of approximately 15 cm. This indicates that the Kerr-lens is of a sufficient magnitude and may even be affecting the stability of the cavity mode.

$$f^{-1} = \frac{8n_2 d}{\pi w^4} P \tag{4.11}$$

Chapter Summary

In this chapter, the design and modelling of a 3-mirror hybrid-mode-locked Ce:LiCAF laser was presented, as well as the layout of the pump laser system required to power it; a mode-locked Nd:YVO_4 laser operating at 78 MHz with an external frequency quadrupling stage. The characteristics of the Ce:LiCAF laser's power output were documented, in terms of maximum output, efficiency, and stability at cavity lengths close to synchronicity to the pump laser. Without intra-cavity prisms, 234 mW output power and a 14% slope efficiency was achieved while introducing a prism pair into the cavity reduced this to 116 mW and a 9% slope efficiency (corrected for chopper duty cycle). However, these results correspond to a slightly longer cavity length than is synchronous to the pump laser. The output power was found to decrease by up to approximately 50% in the cavity length region of synchronicity and the pulse energy became unstable, oscillating on a kHz time-scale. Note that the details of the Ce:LiCAF laser's spectral output are presented in chapter 5 and the pulse characteristics in chapter 6, and are both relevant to the stability of the laser. The slope efficiency of 11% for un-chopped operation was also presented (without prisms) with a power output of 50 mW. For a mode-locked Ce:LiCAF laser, this is the first demonstration of stable operation without the use of a chopper and the highest average power output achieved in a single beam. Un-chopped operation was also achieved using the intra-cavity prisms, for output powers of 10-20 mW.

5

Intra-Cavity Dispersion Management

Chromatic dispersion often has a detrimental affect on mode-locked lasers and the pulses of light that they generate. To prevent significant broadening of pulses propagating outside the cavity, low or negative dispersion mirrors are used to compensate for normal dispersion from optics and air, to keep it around zero. However, management of the intra-cavity dispersion is slightly more complicated for passively mode-locked lasers that have the potential for Kerr-lensing because of the interplay between self-phase modulation (SPM) and anomalous dispersion. These mode-locked lasers require management of group delay dispersion (GDD) to generate pulses on the order of 100 fs. Shorter pulses, on the order of 10 fs and below, require a more rigorous analysis that compensates higher orders, most significantly third order dispersion (TOD), to sustain the broad bandwidth that is necessary to support such short pulses. A more detailed description of these mode-locking dynamics are presented in chapter 2. This chapter covers the tools and techniques that were used to manage the dispersion of the hybrid-mode-locked Ce:LiCAF laser that is the focus of this thesis.

5.1 Theoretical Intra-Cavity Dispersion

Every optical element in the Ce:LiCAF laser contributes some amount of dispersion, but the most significant contributors are air and the laser crystal itself. Therefore, even when the cavity is considered to be empty, without Brewster's windows or prisms, it has a significant amount of dispersion. To quantify this, the refractive indices of air [222] and undoped LiCAF [223] were calculated using their respective Sellmeier equations (as a function of wavelength).

From this, the GDD and TOD were determined as a function of wavelength. These values are likely to be reasonably valid, but high precision is not assumed, because of variable factors that affect these refractive indices, which include humidity of air, temperature, and dopants in the LiCAF crystal (such as Ce^{3+}). The theoretical background for calculating GDD and TOD from refractive index is presented in chapter 2. Their estimated values for the Ce:LiCAF laser are presented in figure 5.1. For comparison, the GDD of the plane mirror output coupler (OPC) is shown in figure 5.2; note that the positive gradient at 290 nm with respect to wavelength corresponds to an anomalous value of TOD $\approx -110\,\mathrm{fs}^3$.

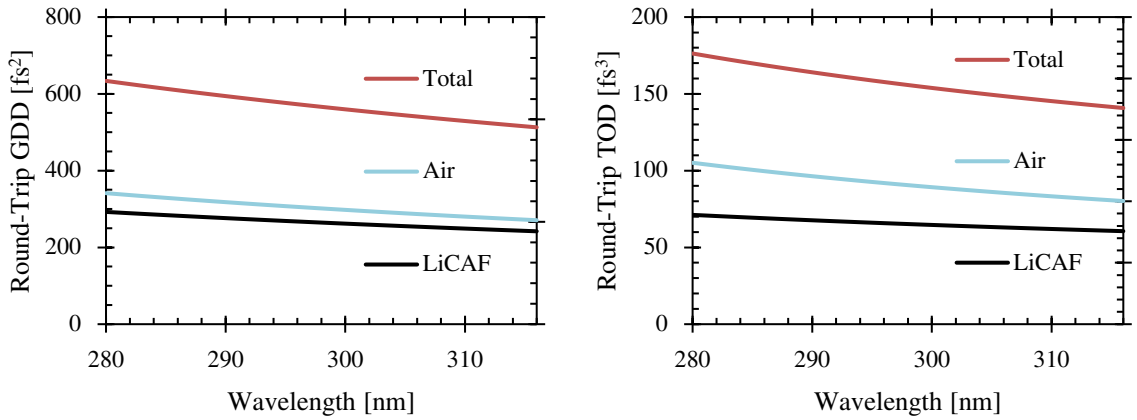

Figure 5.1: Theoretical round-trip dispersion contribution from air and LiCAF.

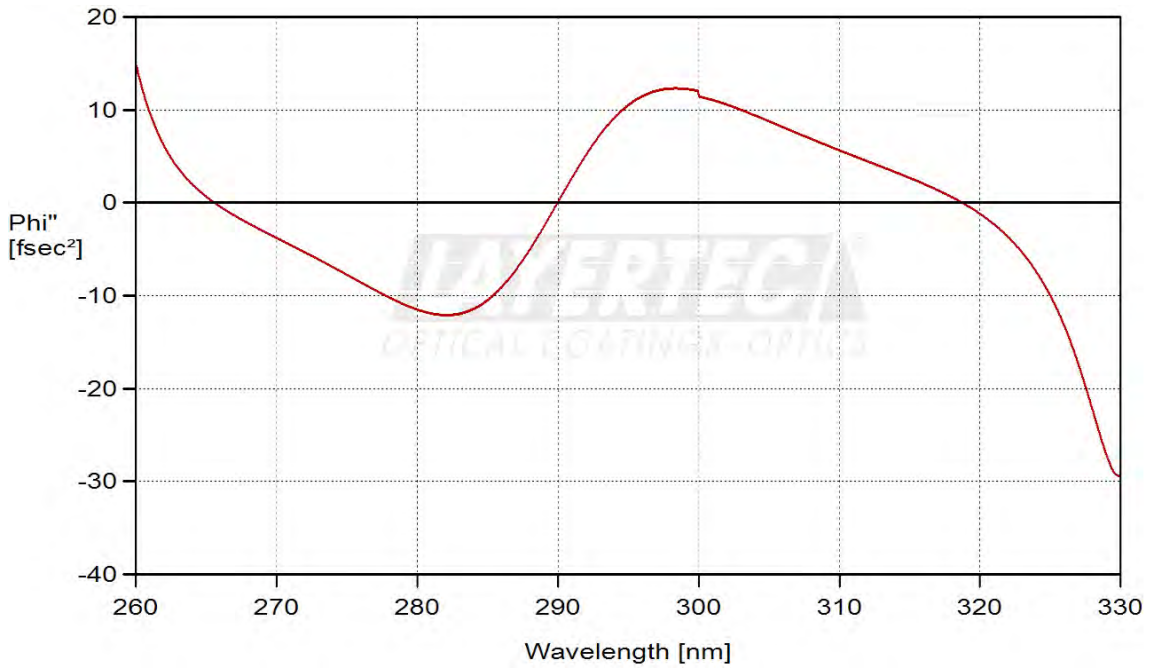

Figure 5.2: GDD of plane OPC, as calculated by Layertec.

Unfortunately the dispersion characteristics of the two curved mirrors, M_1 and M_2, were unavailable, and challenging to measure; however, they are likely to be similar to the OPC. The combined dispersion of air, LiCAF and the OPC is shown in figure 5.3. It was determined via tracing the theoretical plot, hence the slight wobble of the round-trip TOD near the wavelength of 302 nm. The dispersion contribution from the OPC almost flattens the GDD curve at 290 nm, which corresponds to the trough seen in the TOD. Despite this slight alteration to GDD, dispersion is still dominated by the contribution of Ce:LiCAF and a long propagation distance through air, which cannot be ignored for UV wavelengths. It is later shown that if the intra-cavity prism pair is arranged to reduce round-trip GDD to a negative value close to zero (required for KLM) there is a high amount of negative TOD. This compounds with the negative TOD contribution of the OPC, which is detrimental to generating ultrafast pulses with a broad bandwidth. Although the dispersion characteristics of M_1 and M_2 are unknown, they are HR mirrors so may have dispersion properties that are similar to the OPC, such as a relatively low contribution to GDD but a significant TOD contribution. The result would be a complex TOD curve, with respect to wavelength, and therefore challenging to compensate for accurately over the bandwidth of Ce:LiCAF.

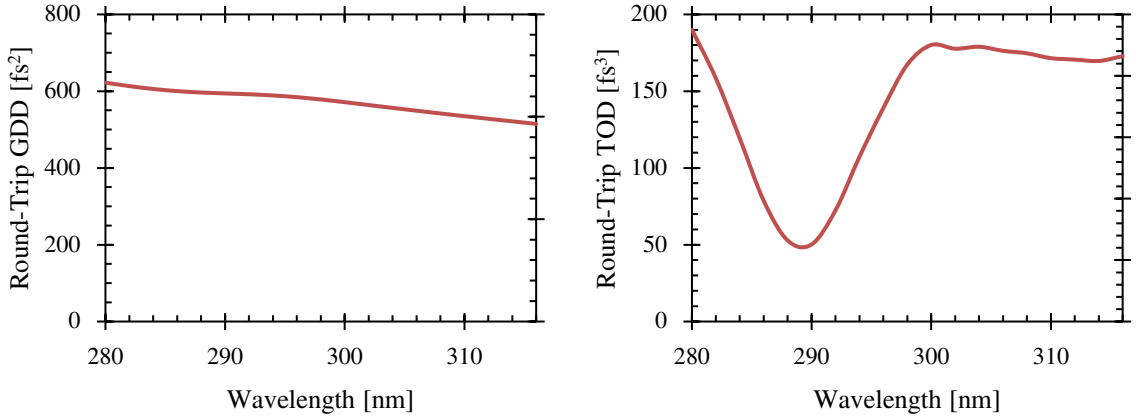

Figure 5.3: Combined theoretical round-trip dispersion of air, LiCAF, and the OPC.

5.2 Dispersion Tuning

Mode-locked lasers with significant chromatic dispersion and temporally modulated gain or loss can be wavelength-tuned by varying the cavity length. This occurs because synchronism between the modulation frequency and the cavity repetition rate must be maintained. For a fixed modulation frequency, changing the cavity length changes the group velocity that is necessary for synchronism. Due to the high chromatic dispersion, the lasing wavelength shifts to match the required group velocity for synchronism. Alternatively, the wavelength can be tuned by varying the modulation frequency of a fixed cavity length laser. This mechanism is known as dispersion tuning and was discovered in 1977 using a fibre Raman oscillator [224], which dispersion-tuned to maintain temporal overlap between the pump and Stokes

signal. It was further improved upon in 1996, using an erbium-doped fibre ring laser [225] to produce more stable pulses via dispersion, self-phase modulation, and amplitude modulation. Nowadays, lasers that are designed for dispersion tuning use a grating pair or similar optical element with immense chromatic dispersion, combined with the aforementioned modulation.

Dispersion-Tuned Ce:LiCAF Laser

Ultraviolet light typically encounters much higher chromatic dispersion in materials (including air) compared with longer wavelengths. In our Ce:LiCAF laser, the gain is also modulated because we are using a pump laser that is mode-locked with a fixed repetition rate, and Ce:LiCAF has a short upper-state lifetime of just 25 ns. This modulation and the high dispersion is sufficient to cause dispersion tuning. However, the modulation of gain does not prevent laser action that isn't synchronous with the pump laser; the Ce:LiCAF laser operates in the CW regime outside of the mode-locking region. Therefore, the range of wavelengths over which the laser may be dispersion-tuned is limited by the range over which synchronous mode-locking produces short pulses. This range is affected by several factors including gain, loss, modulation amplitude, chromatic dispersion, and non-linear effects. Modelling the tuning characteristics in a dispersion-tuned laser requires knowledge of all of these [226, 227]. In addition, these properties must be stable for modelling to be valid. While this is relatively simple to achieve for the commonly used fibre lasers, the performance in our Ce:LiCAF laser varies from day to day; most significantly due to changes in the ratio of gain:loss via pump power, crystal position, dust, and misalignment, but also non-linear effects under hybrid mode-locking, which is not insignificant. We also lack some dispersion information for the cavity, such as for the curved mirrors M_1 and M_2. All of this makes it challenging to compare a comprehensive model to experimental results. However, the amount of GDD can be calculated simply and approximately compared to the rate at which the laser tunes.

To characterise the nature of dispersion tuning in our Ce:LiCAF laser, its output spectrum was measured over the tuning range using an Ocean Optics HR4000 ultraviolet fibre-fed spectrometer, which has a wavelength resolution of 0.03 nm. The schematic for this is shown in figure 5.4. Four amounts of dispersion were tested. The spectrum for an empty cavity without an output coupler was measured via the reflected beam from the Ce:LiCAF crystal. By inserting two different thickness UV-grade fused silica Brewster's windows into the cavity, the dispersion was increased, using each of them and then both of them. They were approximately 4.0 mm and 7.2 mm in length when positioned at Brewster's angle (54.5°) thereby increasing the GDD inside the cavity by 1300 fs^2 and 2400 fs^2, respectively. Note that an HR plane mirror was used instead of the OPC in order to compensate for the additional losses of the Brewster's windows. In this case, the small reflection from the Brewster's window faces was used to monitor the laser performance.

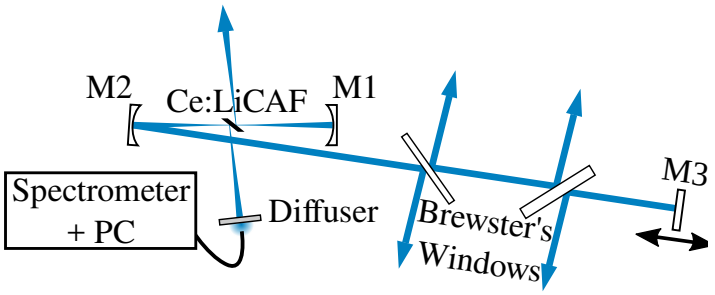

Figure 5.4: Schematic for measuring dispersion tuning with a fibre-fed spectrometer.

To measure the longitudinal position of the end mirror M_3 with a higher resolution than is indicated on the translation stage micrometer (10 µm) a rod was attached to the end of the micrometer, and a protractor placed behind it. Using this setup, increments of 0.5° on the protractor corresponded to approximately 0.7 µm of translation. These measurements were performed by hand, and required careful and fine adjustment of the micrometer to avoid backlash. Variation in the viewing angle for reading the rod position on the protractor may have also contributed a parallax error, which, if read at an angle, could introduce a slight curve in the results. Therefore, the uncertainty of the end mirror position is at least comparable to the 0.7 µm resolution of these measurements. In addition to the human element of uncertainty, variation in the cavity length due to drift of the translation stage and various other elements was an issue, which necessitated rapid data collection. On a faster timescale, vibration could also cause the cavity length to change and thus shift the wavelength. To reduce this effect, data were recorded by averaging 3-5 spectra, each of which was captured using an integration time of 40-200 ms, adjusted for signal-to-noise and to avoid saturation.

5.2.1 First Harmonic

Figures 5.5, 5.6, 5.7, and 5.8 show the dispersion tuning of our Ce:LiCAF laser operating at the first harmonic. The dispersion tuning covers 15-70 µm of cavity length range, which is affected by increased dispersion from the Brewster's windows. Just outside this range is a mode-locked state that is further detuned from synchronism to the pump, generating longer pulses with less stability. On the edge of the dispersion tuning region, both states appear to oscillate, since two spectral peaks are present: the dispersion-tuned peak and the peak at approximately 290 nm (the gain peak of Ce:LiCAF).

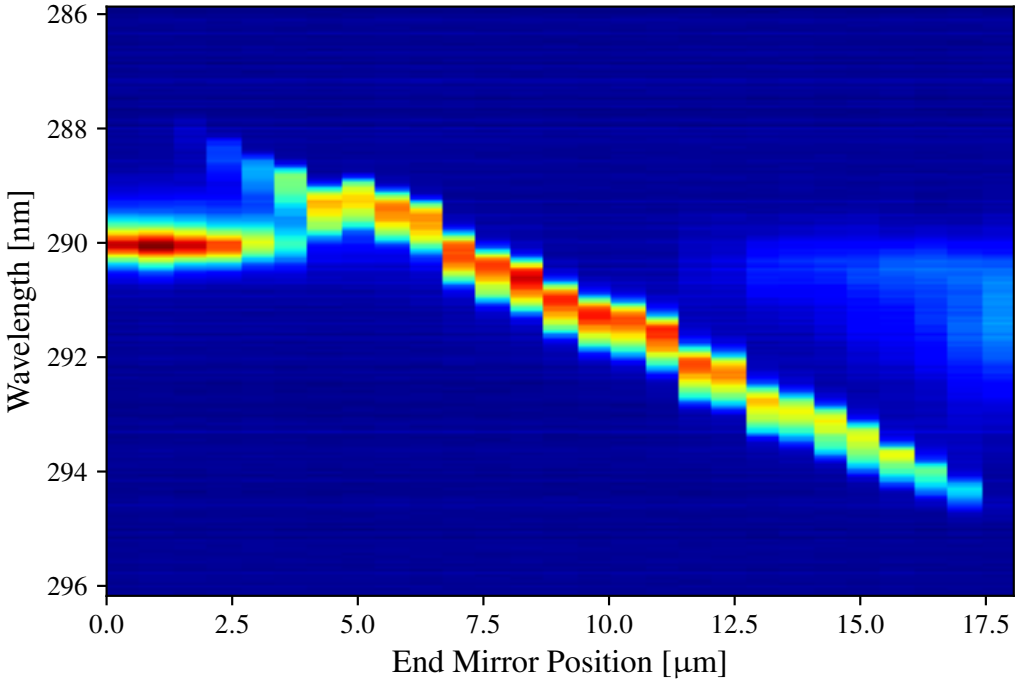

Figure 5.5: Dispersion tuning at the first harmonic without a Brewster's window. Increments of 0.7 μm.

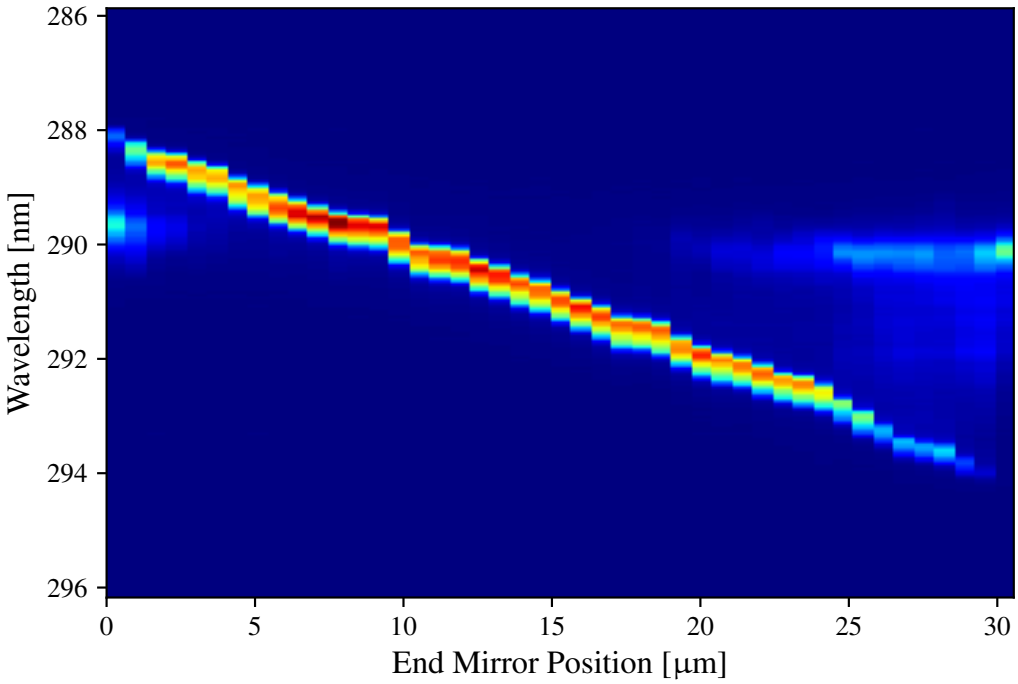

Figure 5.6: Dispersion tuning at the first harmonic using a 4 mm Brewster's plate to provide additional intra-cavity dispersion, GDD $\approx 1300\,\mathrm{fs}^2$. Increments of 0.7 μm.

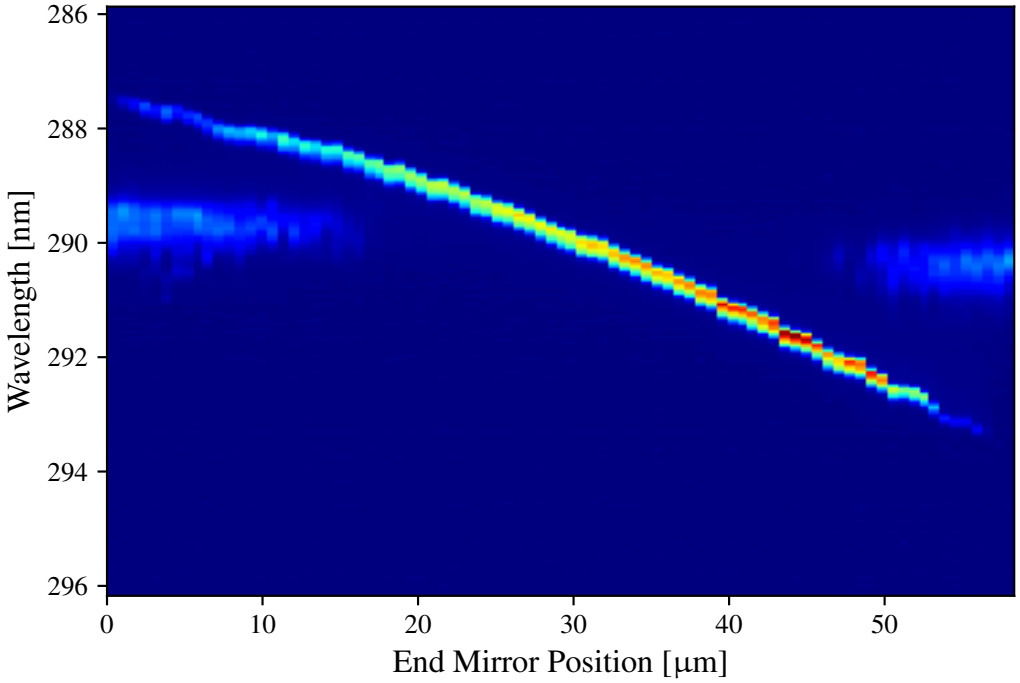

Figure 5.7: Dispersion tuning at the first harmonic using a 7 mm Brewster's plate to provide additional intra-cavity dispersion, GDD $\approx 2400\,\mathrm{fs}^2$. Note that the curve of this data is unlikely to be real, and could just be an artifact of the data collection method. Increments of 0.7 μm.

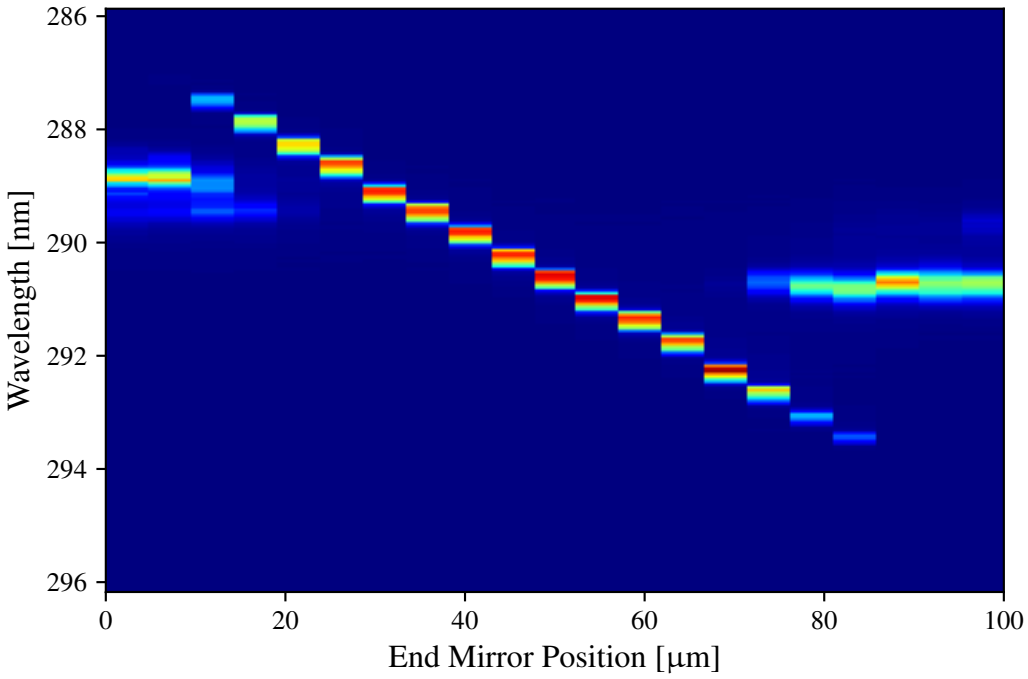

Figure 5.8: Dispersion tuning at the first harmonic using both 4 mm and 7 mm Brewster's plates to provide additional intra-cavity dispersion, GDD $\approx 3700\,\mathrm{fs}^2$. Note, increments of 5 μm were used for fast data collection.

5.2.2 Third Harmonic

Dispersion tuning was also characterised with the Ce:LiCAF cavity set to the third harmonic; the length of the cavity was reduced to one third of the pump laser cavity length by repositioning the end mirror M_3 and adjusting the position of the folding mirror M_2 to form a stable cavity. Compared to the first harmonic cavity arrangement, the round-trip dispersion contribution from air is one third but the mirrors and crystal are the same. The round-trip GDD without Brewster's windows is therefore reduced from approximately 600 fs^2 to 400 fs^2. This reduces the rate of tuning with respect to cavity length. The spectral data is shown in figures 5.9, 5.10, 5.11, and 5.12. There is approximately 3-30 µm of cavity length ranges over which dispersion tuning is present, which is lower than the ranges recorded for the first harmonic. This is partly due to the lower dispersion, which causes the wavelength shift of dispersion tuning to become more sensitive to cavity length changes. Another factor is the ratio of gain to loss; the loss is approximately the same, but the average available gain per round-trip is lower for the third harmonic than it is for the first, since gain has declined due to depletion and fluorescence on the two subsequent passes through the Ce:LiCAF crystal, before the next pump pulse arrives. This affects mode competition at the edge of dispersion tuning, at wavelengths which are detuned from the gain peak of Ce:LiCAF. This was confirmed by the increase and decrease of tuning range with variation of pump power. Due to day-to-day changes in pump power or cavity alignment, characterisation of cavity length range versus power would not be consistent, but would be an important aspect of a comprehensive model.

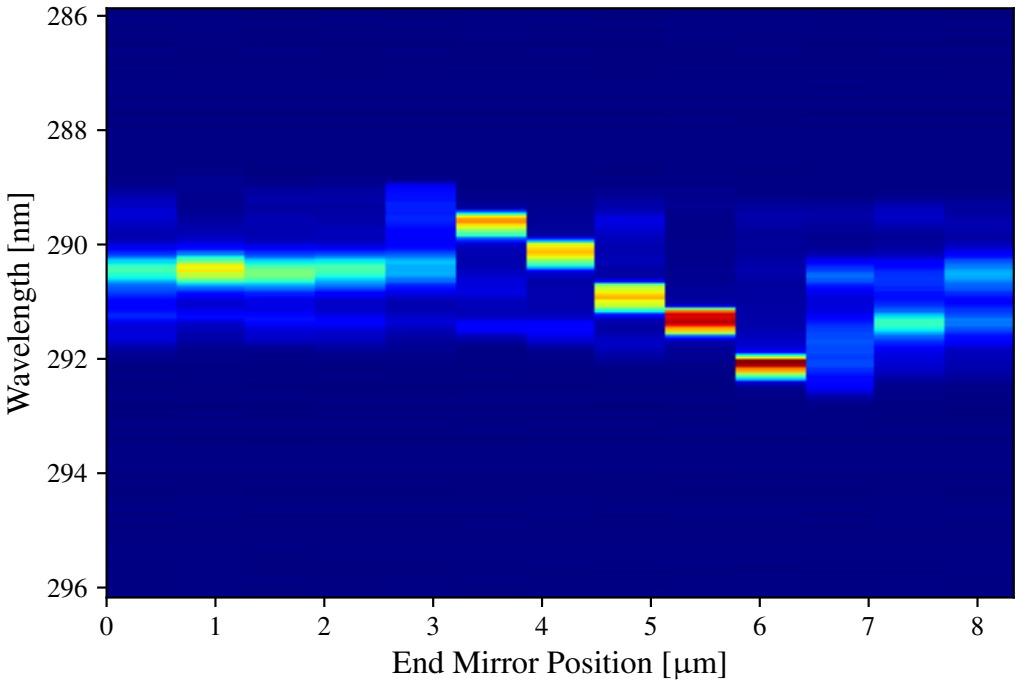

Figure 5.9: Dispersion tuning at the third harmonic without a Brewster's window. Increments of 0.7 µm.

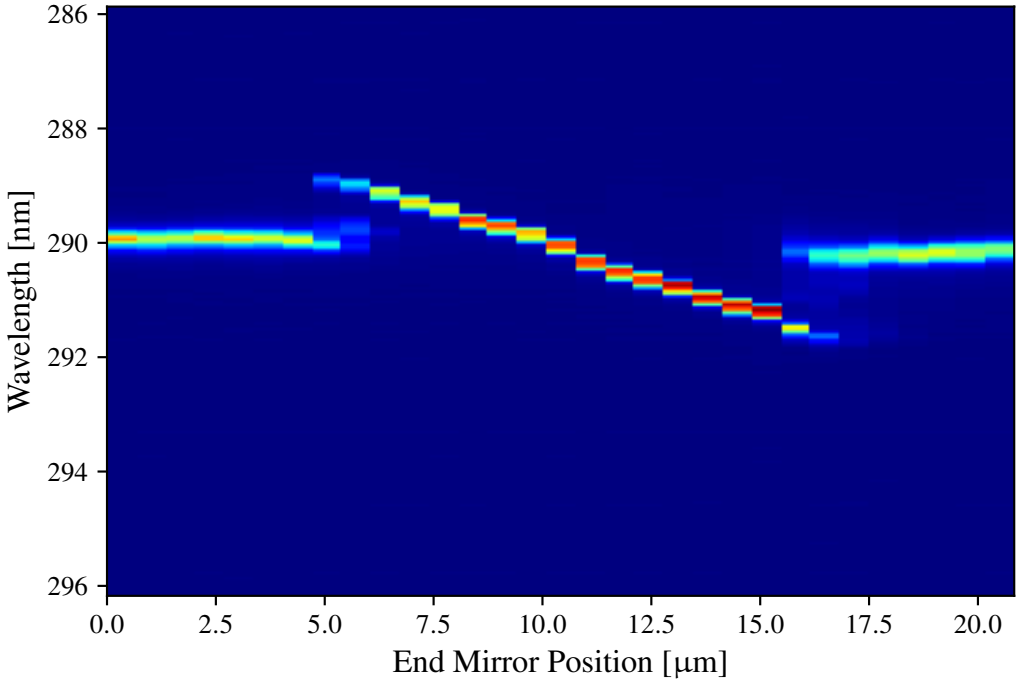

Figure 5.10: Dispersion tuning at the third harmonic using a 4 mm Brewster's plate to provide additional intra-cavity dispersion, GDD ≈ 1300 fs^2. Increments of 0.7 μm.

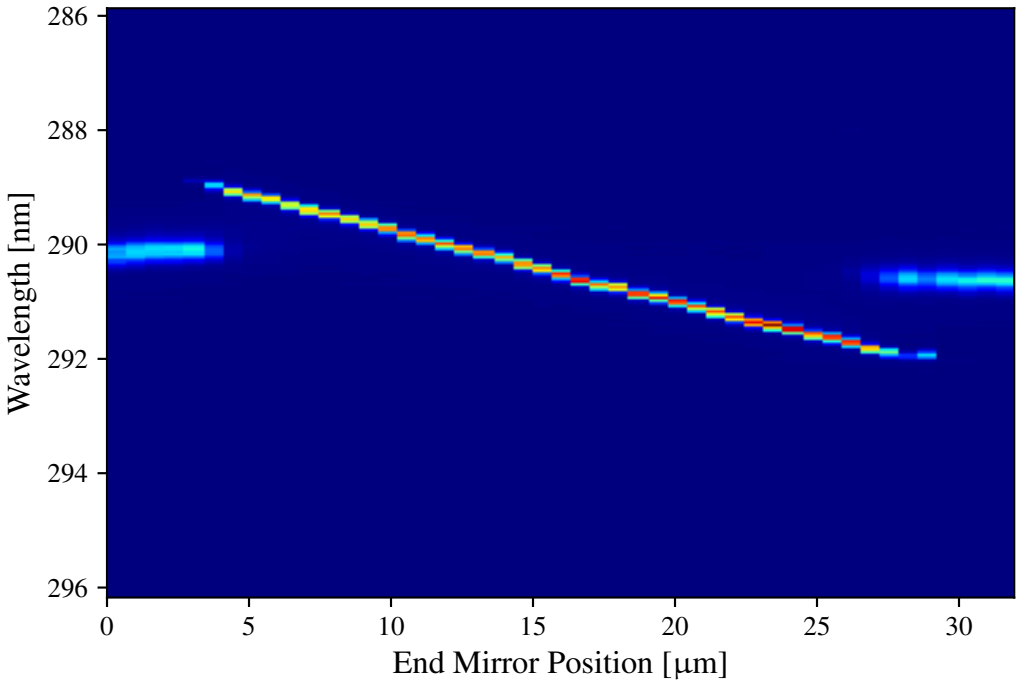

Figure 5.11: Dispersion tuning at the third harmonic using a 7 mm Brewster's plate to provide additional intra-cavity dispersion, GDD ≈ 2400 fs^2. Increments of 0.7 μm.

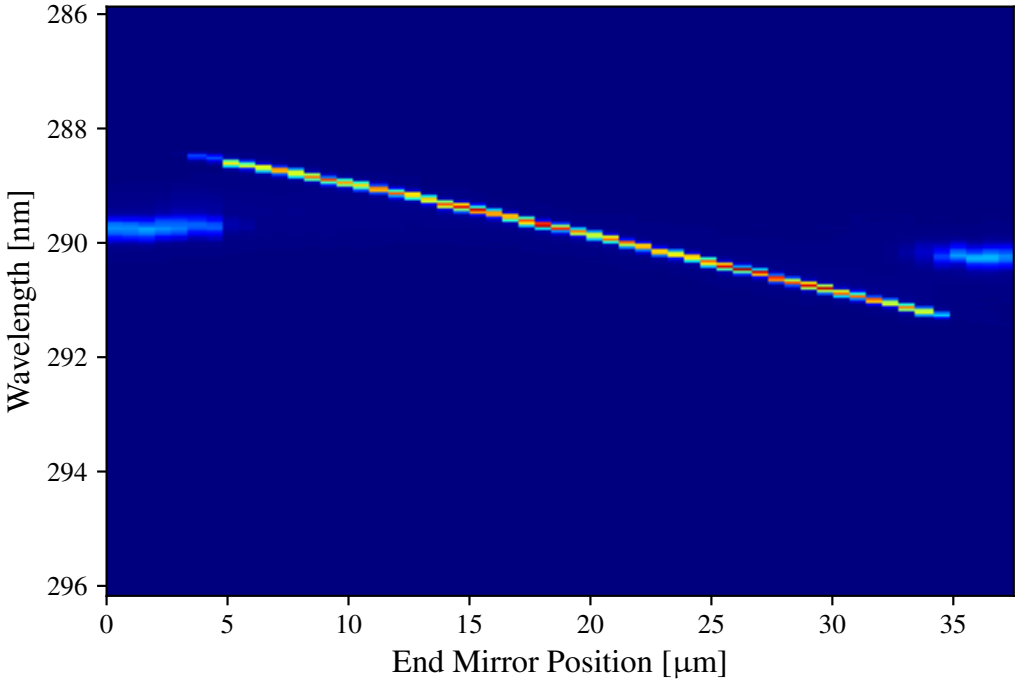

Figure 5.12: Dispersion tuning at the third harmonic using both 4 mm and 7 mm Brewster's plates to provide additional intra-cavity dispersion, GDD $\approx 3700\,\mathrm{fs}^2$. Increments of 0.7 μm.

Bandwidth

Aside from the cavity length range, the dispersion tuning in our Ce:LiCAF laser can be described by two features: bandwidth, and sensitivity of the wavelength tuning to change in cavity length. The bandwidth is governed by dispersion and power. Higher dispersion or lower power reduces the laser bandwidth. Conversely, the potential bandwidth can be increased by reducing the dispersion. The bandwidth for the centre of the dispersion tuning range in the first and third harmonic arrangements is shown in figures 5.13 and 5.14, and summarised in table 5.1. For both harmonics, increasing dispersion (with Brewster's plates) reduces the bandwidth; the gain profile narrows as synchronicity between longitudinal modes and the pump laser PRF decreases. However, the bandwidth for the third harmonic is also less than that for the first harmonic, despite the fact that there is less dispersion (less air) within the cavity at the third harmonic. The lower average available gain that is present for the third harmonic reduces the number of longitudinal modes that encounter net gain.

Table 5.1: Bandwidth at the centre of dispersion tuning (FWHM).

Brewster's Plate	First Harmonic [nm]	Third Harmonic [nm]
None	0.80	0.45
4 mm	0.46	0.23
7 mm	0.30	0.13
4 mm + 7 mm	0.27	0.11

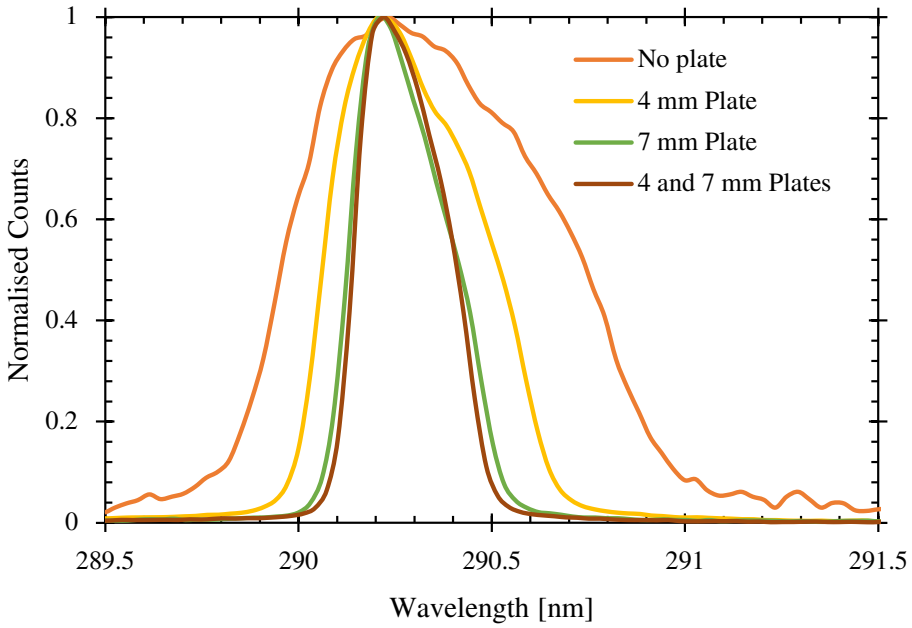

Figure 5.13: First harmonic bandwidth near the centre of dispersion tuning using Brewster's plates. The spectra position on the horizontal axis have been slightly shifted by <0.5 nm to improve the visual overlap.

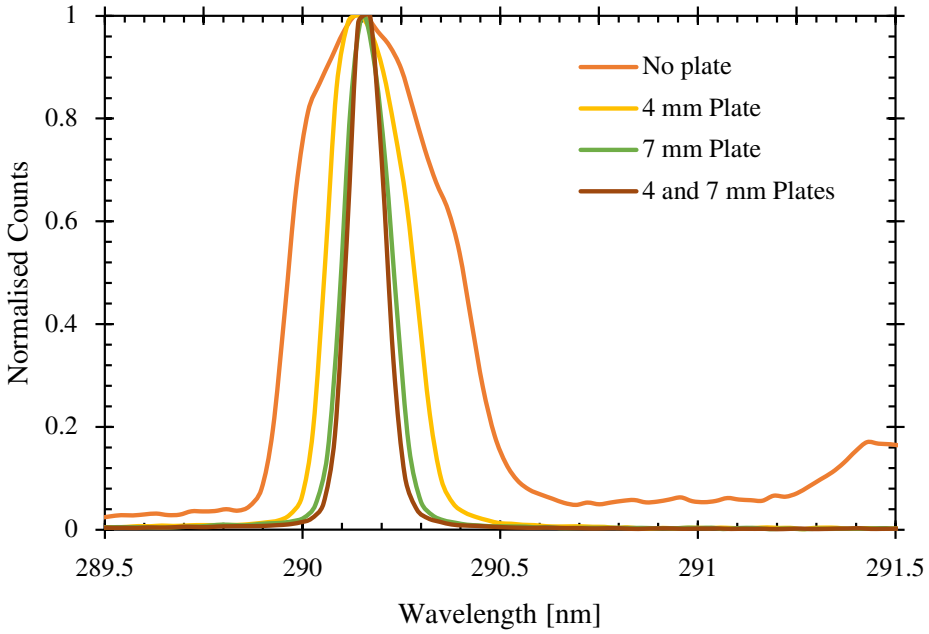

Figure 5.14: Third harmonic bandwidth near the centre of dispersion tuning using Brewster's plates. The spectra position on the horizontal axis have been slightly shifted by <0.6 nm to improve the visual overlap.

Group Delay Dispersion

The sensitivity of the laser wavelength to changes in cavity length is primarily governed by the GDD of the cavity. To compare the theoretical quantity of GDD within the cavity to the sensitivity of dispersion tuning, the gradient of wavelength versus cavity length detuning are first determined. These slopes are represented visually in figures 5.15 and 5.16, which show the peak wavelength within the dispersion tuning range and the corresponding line of best fit. The end mirror position was adjusted to centre on a wavelength near to the centre of the four tuning ranges. However, the absolute mirror position for each of these varied by up to 7 mm for the first harmonic, and 5 mm for the third; the addition of a Brewster's plate increases the optical path length of the cavity, and the length must be decreased to suite. Most of this data appears to closely fit a straight line which implies that the third order dispersion (TOD) is not a significant factor in dispersion tuning over this range, and it cannot be estimated accurately from these results.

The reduced tuning range of the third harmonic compared to the first harmonic is expected, as discussed above. However, there is also a degree of blue-shifting that appears with the added Brewster's plates; in most cases (particularly for the first harmonic) additional plates consistently shifts the tuning range to shorter wavelengths. This could be caused by the rotation of the inserted plates; when one or two of the Brewster's windows were used to increase dispersion, one of the windows was offset from Brewster's angle to generate sufficient output power for measuring the laser spectrum. Since Brewster's angle is dependent on wavelength (governed by refractive indices), loss introduced by rotation of the plates will also be dependent on wavelength. The two options for offsetting the rotation from Brewster's angle at 290 nm will result in higher losses for either shorter or longer wavelengths.

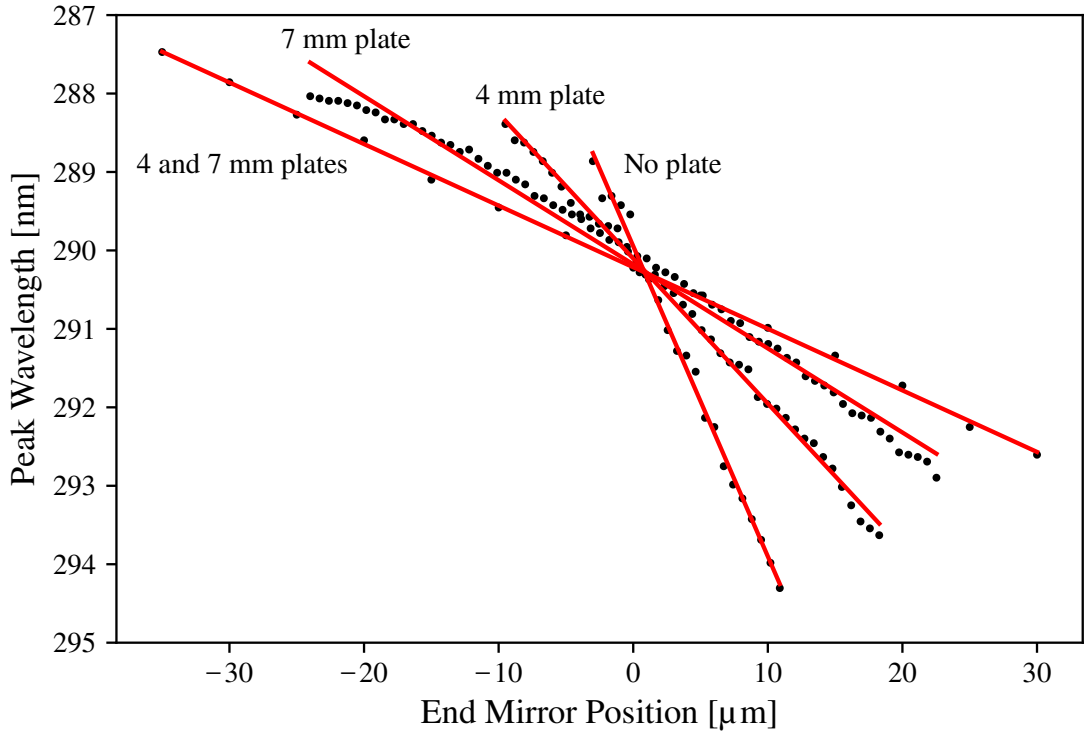

Figure 5.15: First harmonic dispersion tuning peak wavelengths, approximately relative to the centre of the range of tuning.

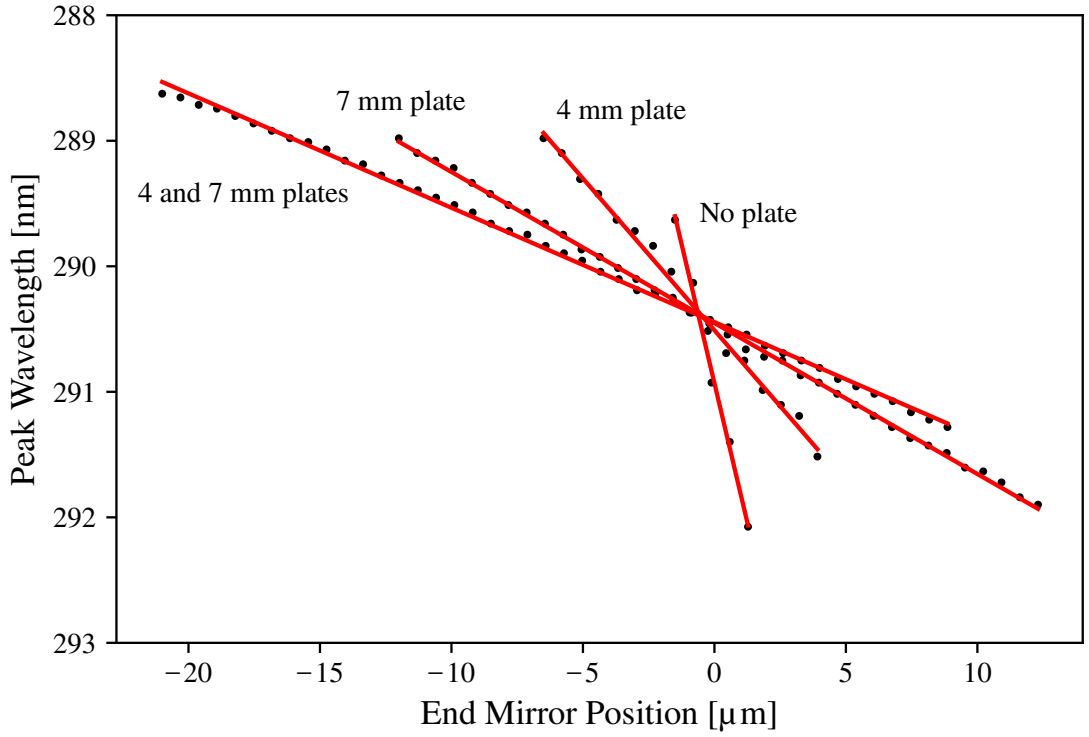

Figure 5.16: Third harmonic dispersion tuning peak wavelengths, approximately relative to the centre of the range of tuning.

5.2.3 Comparison to Theory

The theoretical GDD of air and LiCAF (section 5.1) were combined with the GDD of fused silica, which was similarly calculated using its Sellmeier equation, as determined by Malitson [228]. This produced a theoretical quantity of GDD without including the cavity mirrors; this is justified since the cavity mirrors are likely to have a negligible contribution to GDD compared to the additional Brewster's plates. The dispersion tuning slopes of wavelength versus end mirror position were converted from group delay per wavelength shift [µm/nm] or [fs/nm] to the commonly used unit of GDD [fs^2] for a centre wavelength of 290 nm. This was done using:

$$\mathrm{GDD} = \frac{\mathrm{d}t}{\mathrm{d}\lambda} \cdot \frac{\mathrm{d}\lambda}{\mathrm{d}\omega} = \frac{2}{\mathrm{c}} \cdot \frac{\mathrm{d}x}{\mathrm{d}\lambda} \cdot \frac{\lambda_0^2}{2\pi\mathrm{c}} \tag{5.1}$$

where c is the speed of light, λ_0 is the centre wavelength, dt is the group delay, and dλ/dx is the measured dispersion tuning slopes in figures 5.15 and 5.16. A comparison between the GDD determined from dispersion tuning and the theoretical value is summarised in figures 5.17 and 5.18.

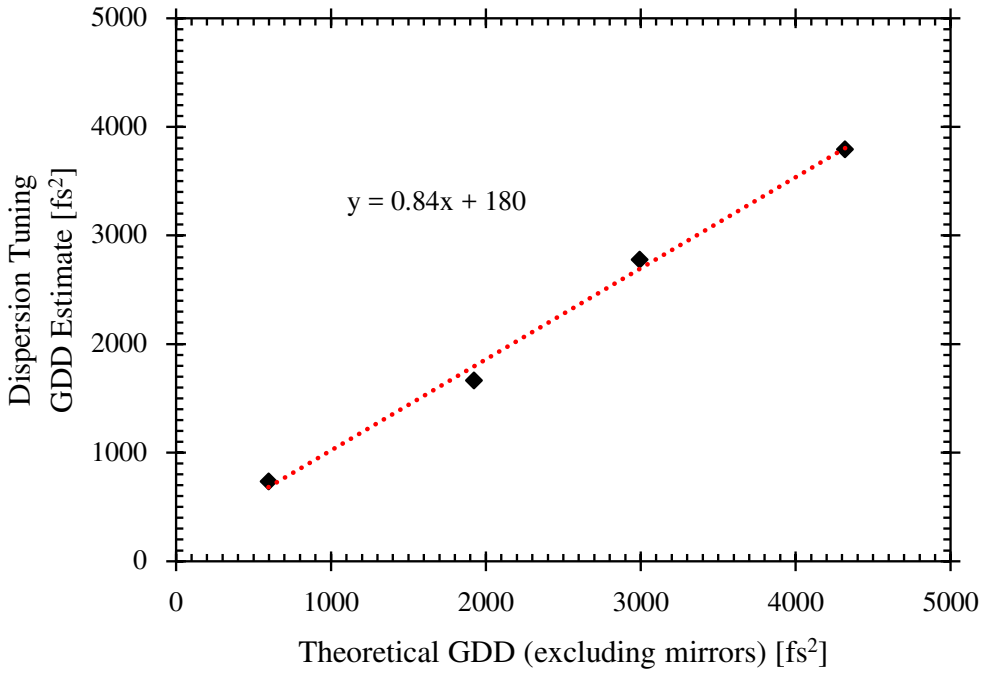

Figure 5.17: Comparison of intra-cavity GDD of the Ce:LiCAF laser at the first harmonic, estimated from dispersion tuning, compared to theoretical calculation of air and LiCAF (mirrors are neglected).

There is a clear difference between the theoretical and estimated GDD; the theoretical GDD is higher, with a gradient of 0.84 and 0.82 for the first and third harmonic, respectively. This could be the result of neglecting higher orders of dispersion and over-simplifying the

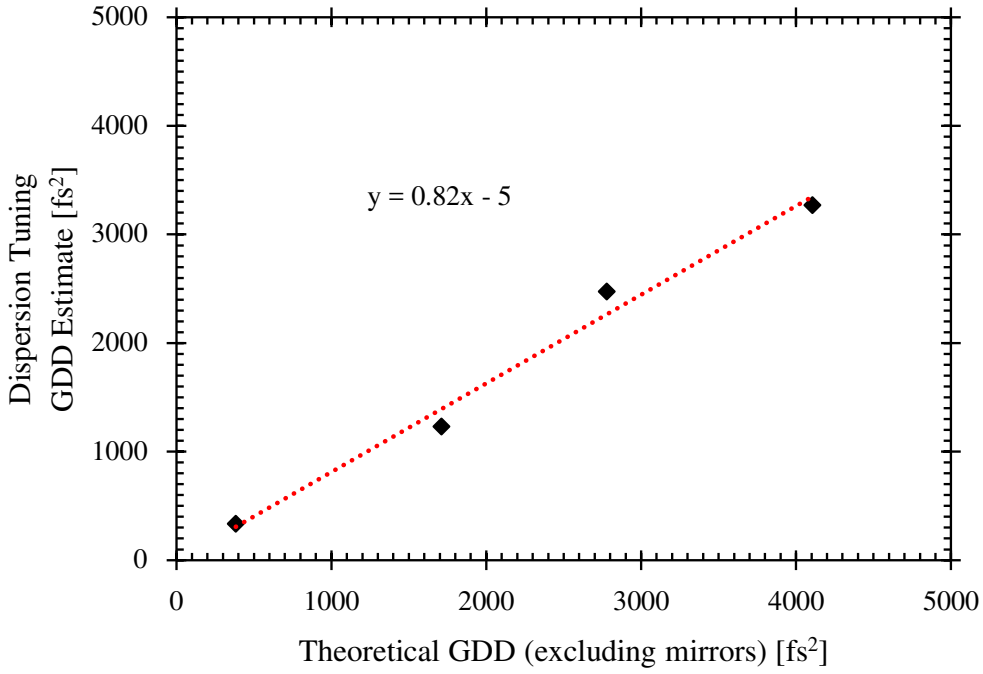

Figure 5.18: Comparison of intra-cavity GDD of the Ce:LiCAF laser at the third harmonic, estimated from dispersion tuning, compared to theoretical calculation of air and LiCAF (mirrors are neglected).

effect that GDD has on the sensitivity of dispersion tuning. The latter of these could be determined through a comprehensive model which may simply reveal that the oscillating wavelength is pulled towards the 290 nm peak of Ce:LiCAF; this would reduce the sensitivity of dispersion tuning and thus the estimated GDD. On the other hand, there is certainly some intra-cavity dispersion that has gone unaccounted for in the theoretical calculation of GDD presented here, due to the omission of the contribution from the cavity mirrors. More significantly, the Sellmeier equations that were used to calculate the contribution from air, LiCAF, and fused silica may not accurately match our experiment conditions. The refractive index of air varies with temperature and humidity; the cerium dopant in Ce:LiCAF may affect the refractive index of LiCAF; and the Malitson's Sellmeier equations for fused silica were developed 55 years ago - manufacturing differences between our fused silica samples and those used by Malitson may be significant in the UV. The grade of the fused silica is also unknown.

The individual GDD contribution from each Brewster's plate could also be different, due to manufacturing differences, or due to imprecise calculation of the path length, which is affected by the rotation of the plate itself (the plates were assumed to be at Brewster's angle). This is supported by the similar pattern that the data points follow in each figure. This pattern is less prominent for the first harmonic, since the contribution from air decreases the relative contribution from the fused silica. Based on this pattern, the GDD contribution from the

4 mm plate may have been underestimated, while the contribution from the 7 mm plate may have been overestimated. The last detail of these figures, the y-intercept, increases for the first harmonic data, yet it is expected to be zero. This may be indicative of more complicated mechanisms, or simply arise from inaccuracy, since the only experimental difference is the distance of air that contributes to cavity GDD. Increasing the theoretical GDD of air would horizontally shift the data in both figures, however each have a positive and negative intercept, so this alone does not explain the non-zero intercept. A more comprehensive model may explain the discrepencies in this data, but was not required in hybrid-mode-locking of our Ce:LiCAF laser, so the sensitivity of dispersion tuning was used only to estimate the GDD of the cavity.

5.3 Intra-Cavity Prism Pair

To generate the shortest possible pulses using the passive Kerr effects (lensing and SPM) that comprise the quasi-soliton KLM scheme (discussed in chapter 2), a slightly negative value of GDD is required. Since our empty Ce:LiCAF laser has a GDD in the range of 600-700 fs^2, additional elements would need to provide at least 700-800 fs^2 of anomalous dispersion to over-compensate for the GDD of the cavity and facilitate KLM. Ideally, the chosen elements would negate the TOD of the cavity as well, and not introduce a high amount of unnecessary TOD, whether it is normal or anomalous. Unfortunately, the optical components that are commonly used for precise dispersion management, such as chirped mirrors and gratings, have excessively high losses at the UV wavelengths that our laser operates. This prohibits their implementation in a mode-locked or CW Ce:LiCAF laser, which already has a high threshold, as they increase the pump power requirement. Until the ratio of loss to negative GDD is reduced (to provide dispersion compensation with minimal losses), these elements will only be useable external to the laser cavity. Hence, inside the cavity, dispersion compensation was only possible using the simple, low loss solution of a prism pair cut such that the laser cavity mode enters and exits at Brewster's angle, as is already the case with the Ce:LiCAF crystal itself.

In some cases, prism pairs can be used to compensate for TOD as well as GDD [229, 230], depending on the material and centre wavelength of light being used. If compensation of the intra-cavity TOD used a prism pair is impossible, it is still somewhat beneficial to choose a prism material that minimises it. In our Ce:LiCAF laser, we assumed a Brewster's angle geometry, so the only variable in choosing a prism pair was the material. The chosen material had to be highly transmissive in the 280-316 nm region, and within budget. From these criteria, three options arise: magnesium fluoride (MgF_2), calcium fluoride (CaF_2), and UV-grade fused silica (UVFS/fused quartz/amorphous silicon dioxide/SiO_2). We purchased a standard off-the-shelf UVFS prism pair from Lambda Research Optics, cut at Brewster's angle for 800 nm light (an apex angle of 69.1°) since it was the quickest and cheapest option

we found with the best surface quality. A surface flatness of $\lambda/8$@633 nm was specified for a scratch-dig of 10-5, compared to typical scratch-dig specifications of 40-20 or 60-40 for scientific research applications (lower is better). The surface quality is more significant in the ultraviolet region than the near-IR, as shorter wavelengths exhibit increased scattering losses. Therefore, minimising the scratch-dig rating of our intra-cavity prism pair was important to maintain low round-trip loss, and ensure the system was still capable of surpassing the lasing threshold. While the losses introduced by the off-the-shelf prism pair were sufficiently low, reducing them further was important to reduce the threshold lower, and achieve un-chopped operation of our entire system (presented in chapter 4). Hence, we elected to also purchase a custom pair of prisms from Uni Optics, cut for Brewster's angle at 290 nm (an apex angle of 67.7°) with a specified scratch-dig of 10-5. The previous prisms were still used in an extra-cavity role, to compensate for the chirp introduced by transmission through the OPC, and also the small spatial chirp that arises due to the position of the intra-cavity prism pair. The slight difference in their apex angle adds either temporal or spatial chirp, but this is likely to be negligible.

Assuming a prism pair that is cut for Brewster's angle is actually to be placed at the necessary angle (for minimal losses), the positioning of these prisms relies on only two variables. Firstly, the distance between the prisms; increasing only this factor introduces more anomalous dispersion (as long as the material is normally dispersive). Secondly, the propagation distance of the laser beam through the prism material, also referred to as the insertion of the prisms; the material will introduce normal dispersion for a standard prism pair. The theoretical equations for the GDD and TOD of such a prism pair are presented in chapter 2. These were used to calculate a map of the dispersion that is introduced via a double-pass through our custom-cut intra-cavity prism pair; the map is shown in figure 5.19. On the horizontal axis, L represents the prism separation, and on the vertical axis, L_g is the propagation distance through the prism material. Both the GDD and TOD are shown; the solid lines represent the zero value, and each dashed line (parallel with the solid lines) indicates a step of -1000 fs^2 or -1000 fs^3, respectively. Based on this information, and the previous estimates of the empty cavity's GDD (600 fs^2) and TOD (50 fs^2), there is no possible arrangement that can compensate for both GDD and TOD. Since achieving slightly anomalous GDD is a requirement, our solution necessarily introduces additional anomalous TOD. To minimise this, the least possible insertion (described by L_g) was used that still resulted in compensation of GDD. This resulted in a separation of approximately 7 cm for our fused silica prism pair.

Maps were also plotted to assess CaF_2 and MgF_2 as prospects for compensating TOD and GDD. Unfortunately at UV wavelengths, TOD is so severe that an excessive amount of anomalous TOD is still introduced; the only noteable difference for these two materials is that a larger prism separation would be required to compensate for GDD. These materials are also far more expensive than fused silica, and for these reasons, they were not chosen. Besides

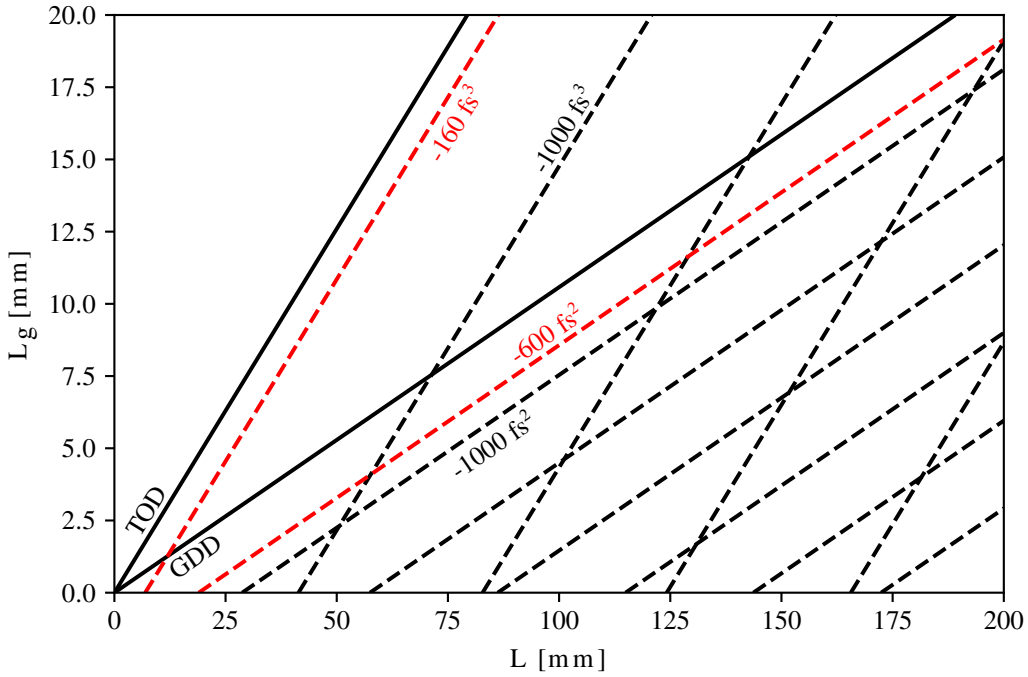

Figure 5.19: Parametric plot of theoretical intra-cavity GDD and TOD compensation for a range of prism pair geometries. Calculated for UV-grade fused silica prisms, cut at Brewster's angle for a wavelength of 290 nm.

choice of material, the only other variables of the theoretical equations presented previously are the apex angle of the prism, and the rotation of the prism pair. Similar to material choice, the TOD is too severe to gain anything significant from altering these, and doing so provides only the disadvantage of increasing loss by aligning the prisms away from Brewster's angle.

5.3.1 Optimisation

While the undesired anomalous TOD increases the minimum possible pulse duration of our Ce:LiCAF laser, it does not preclude KLM altogether; some anomalous GDD is sufficient. This GDD can be arranged by careful placement of the prism pair, inititially using the map of figure 5.19 - a minimum value of $L_g \approx 4$ mm was achieved by reducing insertion of the prisms until the laser power started to decline. For this level of insertion, the shortest prism separation that was used to compensate for the cavity GDD was 7 cm. This was arrived at experimentally by utilising the nature of dispersion tuning within our cavity. A positive value of GDD, which is the case without prisms (section 5.2), causes the laser to generate longer wavelengths for a longer cavity. In contrast to this, using the prism pair to overcompensate for normal GDD results in a net GDD that is negative. Dispersion tuning then operates in the opposite direction; the laser generates shorter wavelengths for a longer cavity. This is shown in figure 5.20, for which the prism pair was separated by L = 10 cm. This amount of anomalous GDD resulted in hybrid mode-locking of our Ce:LiCAF laser, and generated pulse durations of order 150-200 fs.

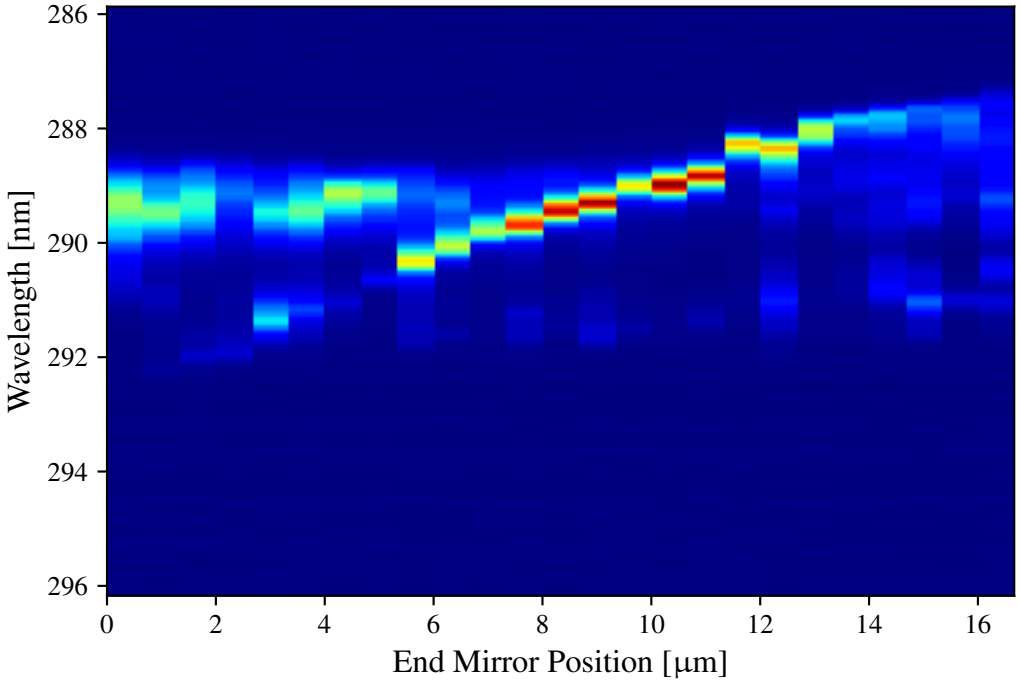

Figure 5.20: Dispersion tuning using an intra-cavity prism pair set up for negative GDD; overcompensating for intra-cavity dispersion. Estimated net GDD $\approx -1300\,\mathrm{fs}^2$.

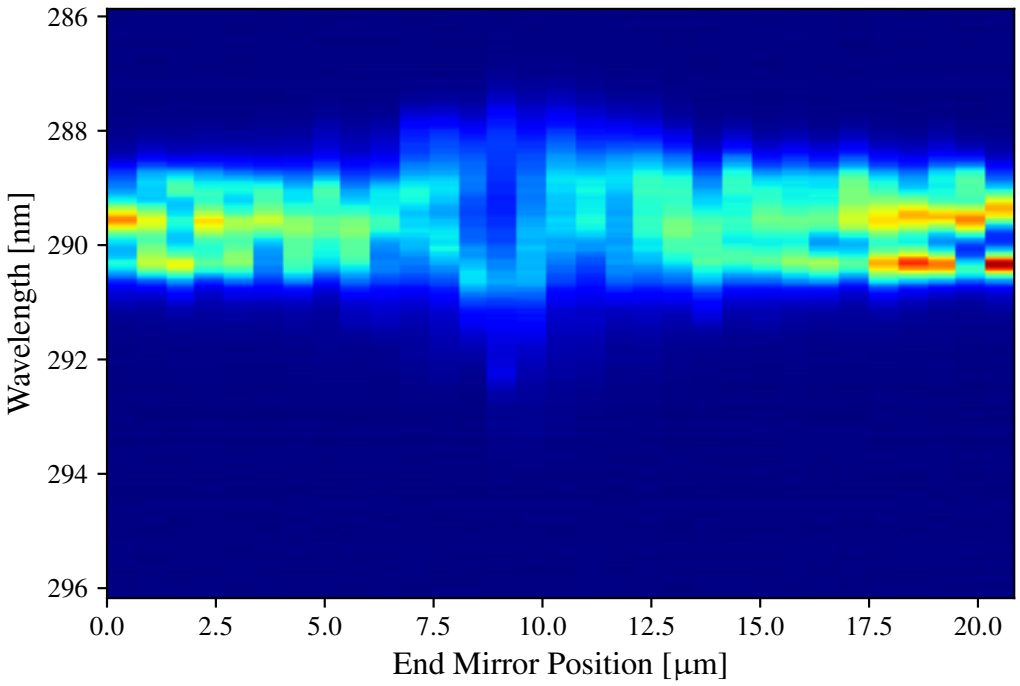

Figure 5.21: Dispersion tuning eliminated using intra-cavity prism pair. The estimated GDD is therefore zero.

Reducing dispersion to a value closer to zero was performed by reducing the separation of the prisms, or increasing their insertion for finer adjustments that avoid altering the transverse position of the output beam on the OPC. By monitoring the direction and sensitivity of dispersion tuning via regular cavity length adjustment (which was also necessary after adjusting the prism pair), the GDD was reduced to an anomalous amount closer to zero. This method was used to generate the shortest pulses, by simultaneous monitoring of the state of hybrid mode-locking. It was necessary to begin this process from the anomalous regime (more separation) as this is required for the passive aspect of our hybrid mode-locking scheme. When the net GDD of the cavity is close to zero, the direction of dispersion tuning becomes difficult to identify, as shown in figure 5.21, for which an end mirror position of approximately 9 µm corresponds to what was otherwise the centre of dispersion tuning (synchonicity to the pump laser). In this regime, via hybrid mode-locking, the cavity length requirement for synchronicity to the pump laser is more sensitive compared to operation with a significant amount of anomalous GDD. Changes on the order of 1 µm affect mode-locking more severely near to zero net GDD, since the laser can no longer simply shift wavelength via dispersion tuning to compensate.

The optimal cavity length of figure 5.21 that was for synchronous pumping, resulted in a laser bandwidth that was exceptionally broad. The broadest recorded spectrum that was achieved using this method is shown in figure 5.22, which shows a FWHM bandwidth of almost 5 nm around a centre wavelength of 290 nm. It was recorded with an integration time of 300 ms, with no averaging. The significant amount of noise is caused by a lack of averaging, combined with a reduced signal; the peak counts are reduced as the bandwidth is much wider at the synchronous cavity length.

Unfortunately, it is likely that the spectra was recorded with an integration time longer than fast time-scale variation of the wavelength, so does not represent the bandwidth of a single resonating pulse. This could be caused by rapid dispersion tuning that occurrs due to variation of the cavity via vibration of the cavity mirrors. Additionally, as the range of cavity lengths is reduced, mode competition may become more prevalent at the centre of what is (or was) the dispersion tuning region, so this broad bandwidth could be attributed to more than just a single dispersion tuning peak. In theory, a bandwidth of this magnitude is capable of supporting transform-limited pulse durations of less than 20 fs. In reality, higher orders of dispersion would increase the pulse duration, particularly TOD, but these were not controllable with the currently available equipment. Pulse durations this short (in the region of 100 fs) cannot be determined simply using a photodiode; a more complex measurement technique is required, such as cross-correlation, which is presented in the next chapter. Nevertheless, this method of monitoring dispersion tuning while adjusting prism insertion was used effectively to control the net intra-cavity GDD and generate the shortest ever pulses from a Ce:LiCAF laser.

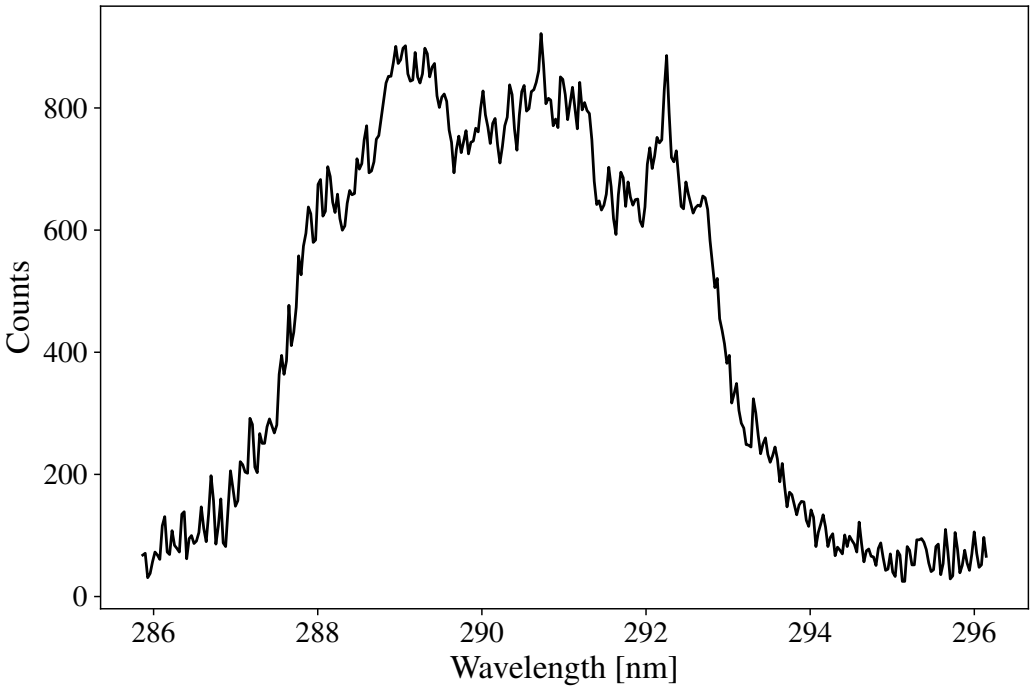

Figure 5.22: A broad free-running Ce:LiCAF bandwidth recorded using a prism pair for intra-cavity dispersion compensation.

Chapter Summary

In this chapter, the theoretical dispersion of our 3-mirror Ce:LiCAF laser cavity was calculated; air and the gain medium were assumed to be the most significant contributors to GDD, introducing approximately 600 fs^2 of round-trip GDD; and 150 fs^2 of TOD, but this was likely to be significantly affected by the mirrors, as indicated by the high TOD introduced by the OPC. The nature of dispersion tuning in the Ce:LiCAF laser was also characterised in detail at the first and third harmonic of the pump laser's PRF, with increasing amounts of dispersion introduced by Brewster's windows. The empty cavity was capable of over 5 nm of spectral tuning by a cavity length change of 10 µm. Experimental results were compared to theory to enable estimation of the cavity dispersion by measuring the sensitivity of dispersion tuning. To enable dispersion compensation, the theoretical anomalous dispersion that an intra-cavity fused silica prism pair provides was determined for a range of geometries. Fine tuning the level of dispersion compensation inside the cavity was shown to be experimentally achievable simply by monitoring the sensitivity of dispersion tuning while adjusting the geometry of the prism pair. A prism separation of 7 cm was found to be optimal, resulting in a net round-trip GDD close to zero and minimimal anomalous TOD (which was over-compensated for).

6

Femtosecond Ce:LiCAF Laser Operation and Characterisation

The performance of our hybrid-mode-locked Ce:LiCAF laser that was achieved in the previous chapters was characterised using multiple tools that include a power meter, photodiode, and spectrometer. These are basic tools for experimental laser physics so they are very common, and commercially available. To measure the pulse duration of an ultrafast laser requires different tools; a probe that is as short as the laser pulse itself, or ideally much shorter. A brief overview of the most common methods of ultrafast pulse characterisation were presented in chapter 2. However, the characterisation of our sub-100 fs UV pulses is more complicated because of their spectral region and low energy. Measuring the pulse duration of weak ultrafast ultraviolet pulses is challenging primarily because the most standard techniques are currently unusable; autocorrelation, FROG, and SPIDER commonly rely on SHG using a non-linear crystal. The transparency range of known nonlinear crystals is restrictive, and does not extend to the second harmonic (145 nm) of the deep ultraviolet region (290 nm) in which Ce:LiCAF lasers operate; the shortest transparency cut-off is KBBF at 160 nm. Phase matching these wavelengths is also a challenge. Therefore, since there are currently no crystals that are capable of generating the second harmonic of Ce:LiCAF laser light, which is necessary for the aforementioned standard autocorrelation methods, we must consider other methods.

Some ultrafast pulse characterisation techniques that do not rely on phase-matching, such as autocorrelation via two-photon absorption (TPA), polarisation-gating, self-diffraction,

transient-grating, and 3-photon fluorescence have the potential to measure the duration of ultrafast pulses in the UV [94, 231–233]. However, these require higher energy pulses compared with $\chi^{(2)}$ based methods, at least on the order of several tens of nJ, whereas our pulses are typically 3-4 nJ. These methods often exploit $\chi^{(3)}$ nonlinear interactions, which rely on more powerful electric fields than our laser is currently capable of generating, and are therefore unusable. Therefore, the low energy of our UV pulses limit the available techniques to $\chi^{(2)}$ based processes.

On the other hand, in recent years, TPA has been combined with the conduction of electrons (as opposed to attenuation of optical power) to provide a robust means of measuring pulse durations in the DUV, even for low energy pulses such as ours [234]. The characterisation device exploits TPA in sapphire to create a conductive channel between two electrodes, which is then detected as a voltage; the traditional autocorrelation technique is used to retrieve a pulse profile. Unfortunately, the TPA coefficient of sapphire declines severely at around 280 nm, which is the lower limit of the gain cross-section for Ce:LiCAF. Therefore, a different material would be necessary to utilise this simple autocorrelator.

The ideal technique to characterise our Ce:LiCAF laser pulses is X-FROG (see chapter 2) because it not only provides pulse duration, but also spectral phase; it is also highly effective at retrieving this information from extremely low energy pulses. The primary issue with X-FROG, with respect to our laser, is synchronisation to a probe laser. The pump laser, while somewhat synchronised to the Ce:LiCAF laser, generates pulses that are far too long (13-20 ps) for deconvolution to accurately retrieve the Ce:LiCAF laser pulse duration, and so they are unusable. Therefore, for X-FROG, the auxiliary reference laser would need to be synchronised to our test laser. To achieve this is non-trivial, because synchronisation of two lasers requires that both lasers are reasonably stable. As chapter 4 shows, the pulse energy of our Ce:LiCAF laser fluctuates over the cavity length range of synchronous mode-locking, and as we will see in this chapter, it is possible that the pulse duration is also semi-stable. The efficacy of synchronisation under these conditions is questionable, and if it were achieved, the timing stability could be affected. Regardless of these issues, the presence of the chopper in our system, reducing the Ce:LiCAF laser to 500 µs bursts every 6.7 ms, makes synchronisation impossible altogether. While synchronisation of the reference laser to an un-chopped portion of the pump laser was considered and has been performed previously [89], the timing jitter between the pump and the reference pulses was on the order of 100 fs, which does not include jitter between the pump and the Ce:LiCAF laser pulses, which would introduce significant uncertainty. To characterise our laser using standard X-FROG therefore relies on several system improvements to sychronise the reference laser to the Ce:LiCAF laser; most importantly: stability of un-chopped pump power and pointing angle, mechanically stable mounting of Ce:LiCAF cavity elements, and reduced environmental vibrations via a different chiller and fully enclosed table.

The characterisation method that was used previously, for measuring the pulse duration

of our Ce:LiCAF laser is asynchronous cross-correlation [214]. It employs a reference laser to operate freely with a pulse repetition frequency very close to the laser to be characterised. This method is capable of characterising weak pulses, as well as multipulsing, and unstable operation. Since our Ce:LiCAF laser was developed from a state of multiple, unstable, ultrafast pulses to semi-stable operation, this method was ideal; it did not require synchronisation, which would be impossible to implement with a laser exhibiting unstable operation or multipulsing, and the technique also allowed the pulse shape to be monitored whilst it was improved. Stability monitoring was a crucial aspect of adjusting the factors that contribute to KLM, so this technique was essential in establishing KLM in combination with synchronous pumping for our hybrid mode-locking scheme.

6.1 Asynchronous Cross-Correlation

Previous asynchronous cross-correlation experiments that measured the pulse duration of the first synchronously mode-locked Ce:LiCAF laser used the following probe laser; a KLM Ti:sapphire laser with an adjustable PRF which was capable of 15 fs pulse durations. This short duration is effectively a Dirac delta function compared to the 6 ps Ce:LiCAF pulse duration that was measured. The asynchronous cross-correlation principle is simple, and yields an effective cross-correlation trace, albeit without phase-retrieval; a probe laser frequency mixed with the test laser in a phase-matching material. The two lasers must be at a slightly different cavity length, and thus pulse repetition frequency (PRF) for effective results. As shown in figure 6.1, the frequency mixed signal pulses at the beat frequency between the two lasers. By detecting the mixed signal, and measuring the beat frequency, the time axis can be scaled to determine the pulse duration of the test pulse.

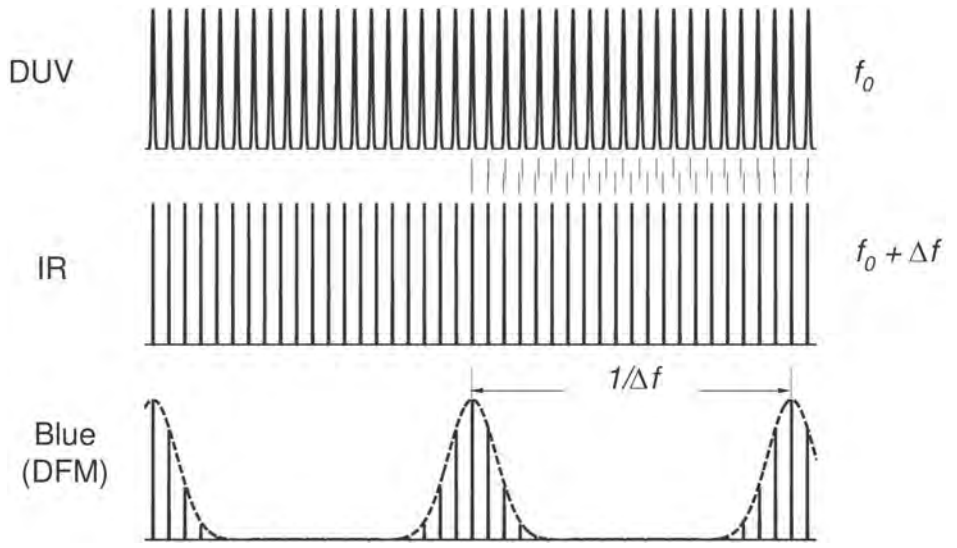

Figure 6.1: Asynchronous test and probe laser pulse trains, and the corresponding (expanded) cross-correlation, from [214].

The change in relative delay between the two pulse trains is given by equation 6.1, where the DUV laser PRF $f_0 >> \Delta f$ the difference in PRF of the two lasers (beat frequency). The change in relative delay corresponds to the sampling resolution of the cross-correlation. With blue pulses generated at time intervals of $1/f_0$, the measured cross-correlation is expanded with respect to the time axis by a factor of $f_0/\Delta f$. For example, for $f_0 = 78\,\text{MHz}$ and $\Delta f = 50\,\text{Hz}$, a time-scale magnification of 1.56×10^6 is obtained; individual blue pulses are generated every 12.7 ns, with a change in relative delay of $\Delta\tau = 8.2\,\text{fs}$ between each pulse. Using this calibration factor, we can convert the envelope of blue pulses to a cross-correlation, and from there retrieve the DUV pulse shape. The duration of the reference pulse and temporal walk off caused by GVD in the frequency mixing crystal may need to be accounted for when deconvolving the cross-correlation during the retrieval process.

$$\Delta\tau = \frac{\Delta f}{f_0\,(f_0 + \Delta f)} \approx \frac{\Delta f}{f_0^2} \tag{6.1}$$

The uncertainty of this method was optimal (±10%) for a beat frequency in the range of 200 Hz - 3 kHz in [214] when measuring pulses of approximately 20 ps duration. This range was high enough to prevent the slow fluctuation of Δf (±50 Hz) between the two lasers from affecting the measurement; reducing the beat frequency below this would dramatically increase the uncertainty of Δf and therefore the uncertainty of the measured pulse duration. On the other side of this range, increasing Δf higher than 3 kHz by detuning cavity length reduced the sampling, and so the measurement eventually succumbed to signal-to-noise at a beat frequency of 20 kHz. However, using this method to measure pulse durations on the order of 100 fs requires a low beat frequency (50-500 Hz) to even provide sufficient sampling from which a pulse duration is retrieved. Increasing sampling to even higher rates (lower Δf) is also valuable to resolve the temporal shape of the pulse, in addition to the duration itself. However, since lowering Δf increases its uncertainty exponentially, we used an alternative technique to determine Δf during the cross-correlation pulse. This used a simple microscope coverslip as a fixed time reference, which is detailed in the coming sections. This method provided a reliable time reference, and made direct measurement of the beat frequency redundant.

6.2 Experimental Setup

The setup is shown in figure 6.2. As a reference laser, we used a similar homebuilt Ti:sapphire system to generate 808 nm pulses that were 60-100 fs long (varied from day-to-day, usually at 75 fs) with a PRF of 78 MHz and an average power of 400 mW. The OPC of the Ti:sapphire laser was mounted on a high precision manual translation stage, to closely match its cavity length to the Ce:LiCAF laser. The generated 808 nm pulses were characterised by diverting a portion of power in the output beam into a Mesa Photonics FROGscan system operating at

1 Hz, and were found to be very close to transform limited. The pulse duration was monitored regularly, especially during measurement of the Ce:LiCAF pulses, as it is necessary for deconvolution of the cross-correlation trace.

The dispersion within the cavity was varied between approximately -100 fs^2 and -2000 fs^2, which is necessary for KLM; the shortest pulses were obtained for the lowest quantity of dispersion that still facilitated KLM. To compensate for chromatic dispersion that was encountered by the output pulse, such as the OPC material itself, and the spatial chirp that the intra-cavity prism pairs introduced in the beam due to their location with respect to the OPC, an extra-cavity prism pairs was used to mirror the intra-cavity ones. Their geometry was optimised, fine adjustments were made via the insertion of the second prism, until the shortest pulses were observed from asynchronous cross-correlation. A half-wave-plate (HWP) was positioned after this arrangement to rotate the polarisation of the 290 nm from horizontal to vertical, which was necessary for phase-matching in the frequency mixing stage.

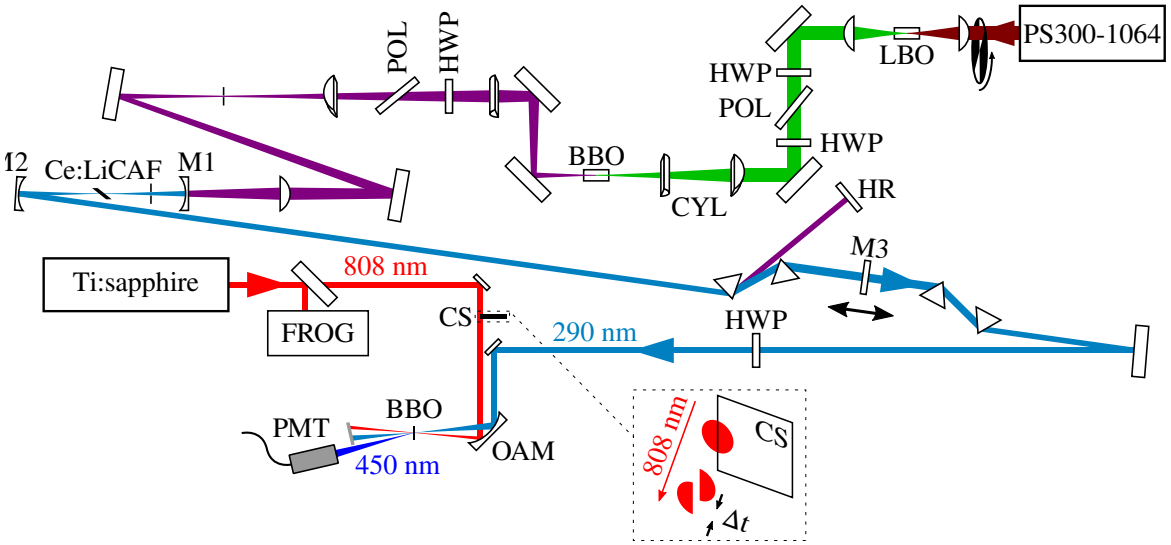

Figure 6.2: Schematic of split-beam asynchronous cross-correlation, including the test laser. The inset indicates how a cover slip that is partially inserted into the reference beam can be used to split it into two halves which have a fixed relative temporal delay.

The reference and test laser pulses were combined in a MesaPhotonics X-FROG system (switched off) which is simplified in figure 6.2 by two folding mirrors, an OAM, and a BBO. The X-FROG system was composed of several broad-band mirrors that had a reflectivity of 90% for 290 nm wavelengths, and 99% for 808 nm. The 290 nm beam was reflected five times before entering the BBO, which reduced the power of the inserted beam to 60%. This attenuated power was still more than adequate, since we used a highly sensitive photo-multiplier tube (PMT: Hamamatsu H10721-110) to detect the frequency mixed signal, in place of a high resolution spectrometer used for X-FROG. Its responsivity curve is shown in figure 6.3. In terms of group-delay dispersion (GDD), these broad-band mirrors typically contribute less than 100 fs^2 each. Five reflections of this order of magnitude, for a total of

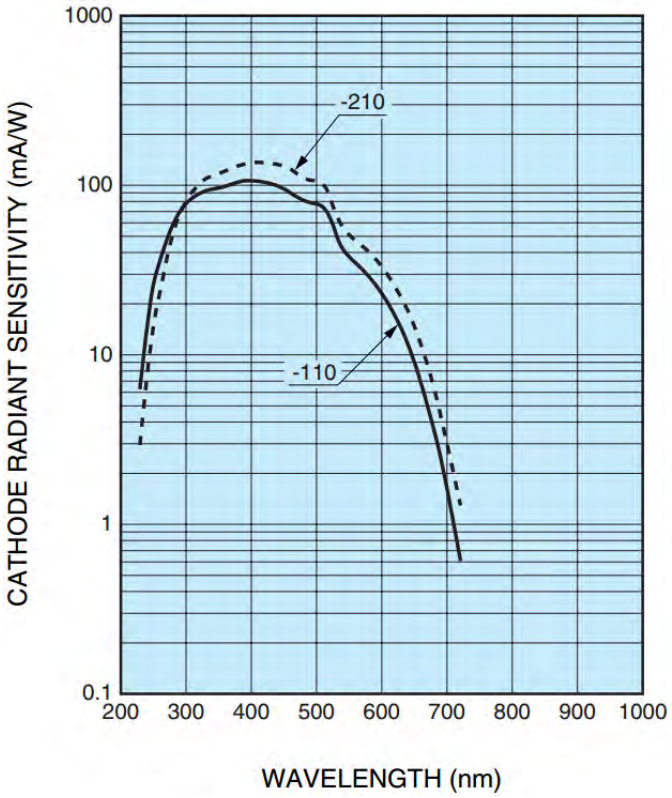

Figure 6.3: Responsivity of PMT used for detection; Hamamatsu H10721-110.

500 fs^2, would stretch a 100 fs bandwidth-limited pulse to 101 fs, or a 60 fs pulse to 64 fs. The FROG system that was used to characterise the 808 nm reference pulses used the same mirrors, so pulse stretching is accounted for. Stretching of the 290 nm pulses is minimised by the extra-cavity prism pair which compensates for all extra-cavity GDD, as they are optimised for minimum pulse duration. However, since the precise dispersion contribution of these mirrors is unknown, their effect on third-order dispersion (TOD) is also unknown.

The 808 nm and 290 nm beams were focussed non-collinearly at a small angle into a 30 μm long BBO crystal cut at 34.3°. Spatial overlap within the BBO was performed by eye and using a 50 micron pinhole (a component of the X-FROG system) while temporal overlap is not necessary due to our asynchronous approach. The phase matching conditions for difference frequency generation between 290 nm and 808 nm radiation in BBO are listed in appendix B. The difference frequency generation of these wavelengths produces 452 nm radiation, which is in proximity to the peak sensitivity of the PMT. The overlap of the two beams was optimised by maximising the PMT signal (set gain of 0.8 V) as monitored on a oscilloscope (LeCroy WaveMaster 8620A - 6 GHz @ 20GS/s). For a thin crystal such as ours, temporal walk-off during the frequency mixing process between the reference and test laser pulses only becomes significant for pulse durations on the order of 10 fs [235–237]. This is advantageous, as the walk-off could therefore be neglected in the deconvolution process.

To provide a time reference (details in section 6.3) a microscope cover slip was inserted into half of the reference beam. This is depicted in figure 6.2 by CS. The result is that

each reference pulse is split into two halves; one half is delayed by the additional optical path length that is introduced by propagation through the cover slip glass (commonly a borosilicate). While splitting the beam shape may pose an issue for characterisation of the spatial properties of the beam (across the transverse profile of the beam) these experiments serve only to characterise the longitudinal profile (pulse duration) so it may be neglected. Furthermore, since the 808 nm reference beam and 290 nm test beam encounter the same focussing mirror, the focal waist will be larger for the longer wavelength radiation, so even if any spatial chirp is present it should not significantly affect the measurement result.

6.3 Split-Beam Time Reference

The microscope cover slips that were used to delay approximately half of the Ti:sapphire reference pulse train can be defined by their relative time delay Δt, which depends on the material, as $\Delta t = d\Delta n_g/c$ where d is the coverslip thickness, Δn_g is the difference in group velocity between the coverslip material and air, and c is the phase velocity of light in vacuum. The split-beam technique allows a single pulse (from our Ce:LiCAF laser) to be asynchronously cross-correlated with a pair of reference pulses that are separated by a known time delay. The time delay introduced by the cover slip was measured using the autocorrelation measurement of a commercial MesaPhotonics FROG system. This is shown in figure 6.4 for a type 4 cover slip, manually using the software's cursors to measure the time interval between the two peaks. The calibration of the time-scale for this measurement was predefined by the FROG system.

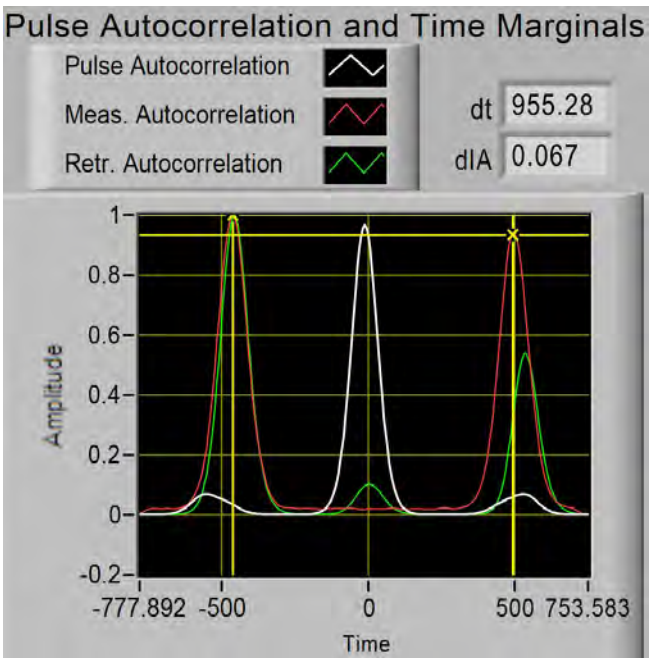

Figure 6.4: Autocorrelation measurement within MesaPhotonics software (red line) with a time delay dt measured using cursors. The units of time are in femtoseconds.

A summary of the three varieties of cover slips used to create a referenceable time delay is shown in table 6.1. Using several different delays allowed us to confirm the validity of this technique, and assess its accuracy.

Table 6.1: The three different cover slips used to create a relative time delay in approximately half of the Ti:sapphire reference beam, by splitting it into two. Note that the group index of borosilicate glass at 808 nm is approximately 1.526.

Type	Typical thickness [μm]	Time delay [fs]	Thickness [μm]
1	130 – 160	260 ± 10	150 ± 5
2	190 – 250	335 ± 10	190 ± 5
4	430 – 640	950 ± 30	550 ± 5

Curve Fitting

The measured autocorrelation in figure 6.4 shows a smooth temporal profile that is characteristic of this type of measurement. This trace is easily analysed to determine the time delay, which was performed using the software's built in cursors; the relative time delay of each cover slip is shown in table 6.1. Unlike the autocorrelation trace, the raw data (DFG) of our asynchronous cross-correlation is not smooth; it is composed of individual peaks (pulses) that vary in amplitude (energy). The envelope of these pulses are the cross-correlation on a magnified timescale. Using the split-beam time reference allows us to determine the level of magnification. The distance between the envelope's peaks is the time delay introduced by the microscope cover slip, but to process this data and accurately retrieve a measurement of pulse duration warrants the use of a fitted function to map out of the envelope and set the time scale. The raw data was initially smoothed using the Hilbert transform function in MATLAB. The fitted function that was then fitted to the envelope of the raw data, shown below in equation 6.2.

$$y = a_1 \exp\left[-\left(\frac{x - b_1}{c_1}\right)^2\right] + a_2 \exp\left[-\left(\frac{x - b_2}{c_2}\right)^2\right] \tag{6.2}$$

Where a, b, and c correspond to the amplitude, time offset, and width of each pulse envelope, respectively. The time axis can be calibrated by the distance between the two peaks:

$$\Delta\tau = \frac{\Delta t}{b_2 - b_1} \tag{6.3}$$

while the convolved duration of each pulse (FWHM from [238]) was determined from:

$$t_{1,2} = \Delta\tau \cdot 2\sqrt{\log 2} \cdot c_{1,2} \tag{6.4}$$

The deconvolution was then performed simply using $\tau_{1,2} = \sqrt{t_{1,2}^2 - \tau_r^2}$ and the final pulse duration was the average of this result. Two examples of the raw data, smoothed data (envelope), and fitted curve are shown in figures 6.5 and 6.6. The amplitudes of each cross-correlation peak typically are not equal, as their amplitudes are sensitive to the microscope cover-slip's insertion into the beam. The width of each peak is typically not equal either; in part, this is the result of variation in the beat frequency. Higher sampling than is shown in figure 6.5 would require a lower beat frequency, which is difficult to maintain due to drifts in alignment. For example, to achieve $\Delta f = 10 \pm 1$ Hz would require a cavity length stability of just 23 nm (for both lasers).

For efficiency in ascertaining the pulse duration using the fitted function, combined with a statistical approach that validates the measurement (which necessarily uses a large quantity of data) a script was written using MATLAB to process a number of individually recorded oscilloscope traces (see appendix C). Each trace included the double Gaussian-like envelope that is characteristic of the split-beam asynchronous cross-correlation method, composed of a number of individual cross-correlation pulse peaks.

The properties of each fit were stored in a data array, in order to concatenate groups of data that were recorded. However, a small percentage of traces contained less then three pulse peaks, did not match the expected envelope shape, or were captured in error due to a spike in electrical noise. To avoid removing these data manually, certain results were removed from the large data set used to obtain an accurate measurement. Those that yielded complex values for the fitted function were removed, and those that had a beat frequency that significantly deviated from the average, from a single run of measurements, were also removed. The threshold for removal by beat frequency was set to 3σ, thrice the standard deviation, to minimise the number of real data that may be removed by the automated selection process.

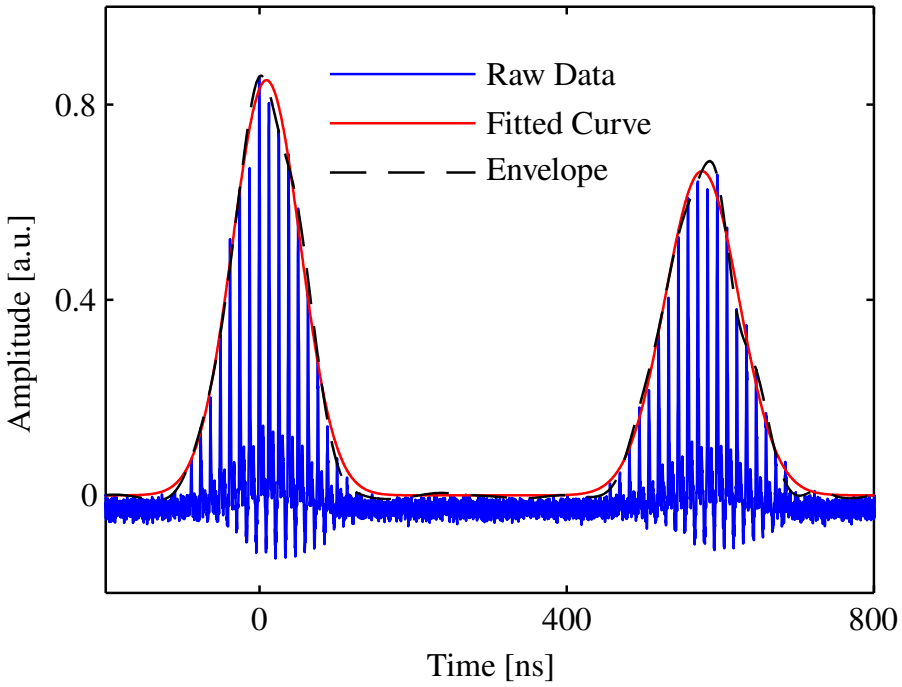

Figure 6.5: Asynchronous cross correlation using a type 4 cover slip as a time reference, where $\Delta t = 950 \pm 30$ fs; $\Delta f \approx 130$ Hz. The corresponding average deconvolved pulse duration is 150 fs.

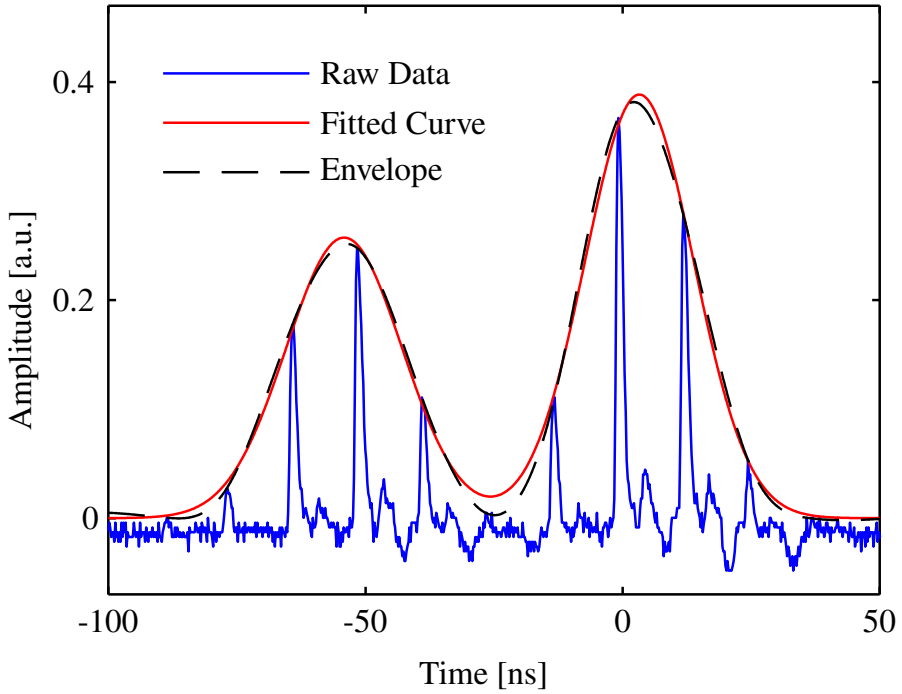

Figure 6.6: Asynchronous cross correlation using a type 1 cover slip as a time reference, where $\Delta t = 260 \pm 10$ fs; $\Delta f \approx 350$ Hz. The corresponding average deconvolved pulse duration is 89 fs.

6.4 Pulse Shape and Duration

The pulse duration of our Ce:LiCAF laser without dispersion compensation (i.e. no intra-cavity prisms) was previously characterised as a function of cavity length by Granados Mateo (details in chapter 3). The duration of those pulses were as low as 6 ps, for a well-matched, synchronous cavity. This increased only by a factor of 2 over the 30 µm cavity length range that yielded ultrashort pulses, with the shortest pulse duration at the centre of the matched cavity length range (the centre of dispersion tuning). While the pulse duration was recorded, the temporal profile of the pulse was not. Here we show that when synchronous pumping is the sole mechanism for mode-locking, the pulse's temporal shape is generally not smooth, even for well matched cavity lengths.

Apart from pulse duration, the spectral features of our Ce:LiCAF laser are also dependent on cavity length, which includes dispersion tuning over the synchronous mode-locking region. This feature was documented by Granados Mateo but not identified (chapter 3). More detailed analyses of this tuning mechanism were presented in chapter 5. Here, in terms of the output pulse's temporal profile, we examine the mode-locking characteristics of the Ce:LiCAF laser under three circumstances. Firstly, when there is no dispersion compensation present. Secondly, when there is a prism pair used to introduce anomalous dispersion in the cavity. Thirdly, when the prism pair is combined with a hard aperture to promote an intense pulse. Details of the dispersion management achieved using the prism pair is also presented in chapter 5.

6.4.1 Without Prisms

The pulse duration was measured over the dispersion tuning range, which exhibited the shortest pulse duration for the centre of this range, where the gain peak of Ce:LiCAF is a maximum. The pulses in this region are not temporally smooth, but consist of many random peaks that follow an overall Gaussian envelope. The individual peaks arise from noise in the cavity, which coincidentally resonate with the time varying gain provided by synchronous pumping. Therefore only the peaks that are synchronous with the pump laser are amplified.

There were two cavity lengths of interest. Firstly, the centre of dispersion tuning which was defined as $\Delta x = 0$, which resulted in a lower output power was lower over a few µm in the dispersion tuning region. Secondly, a longer cavity length (by approximately 20 µm) which produced the highest power output.

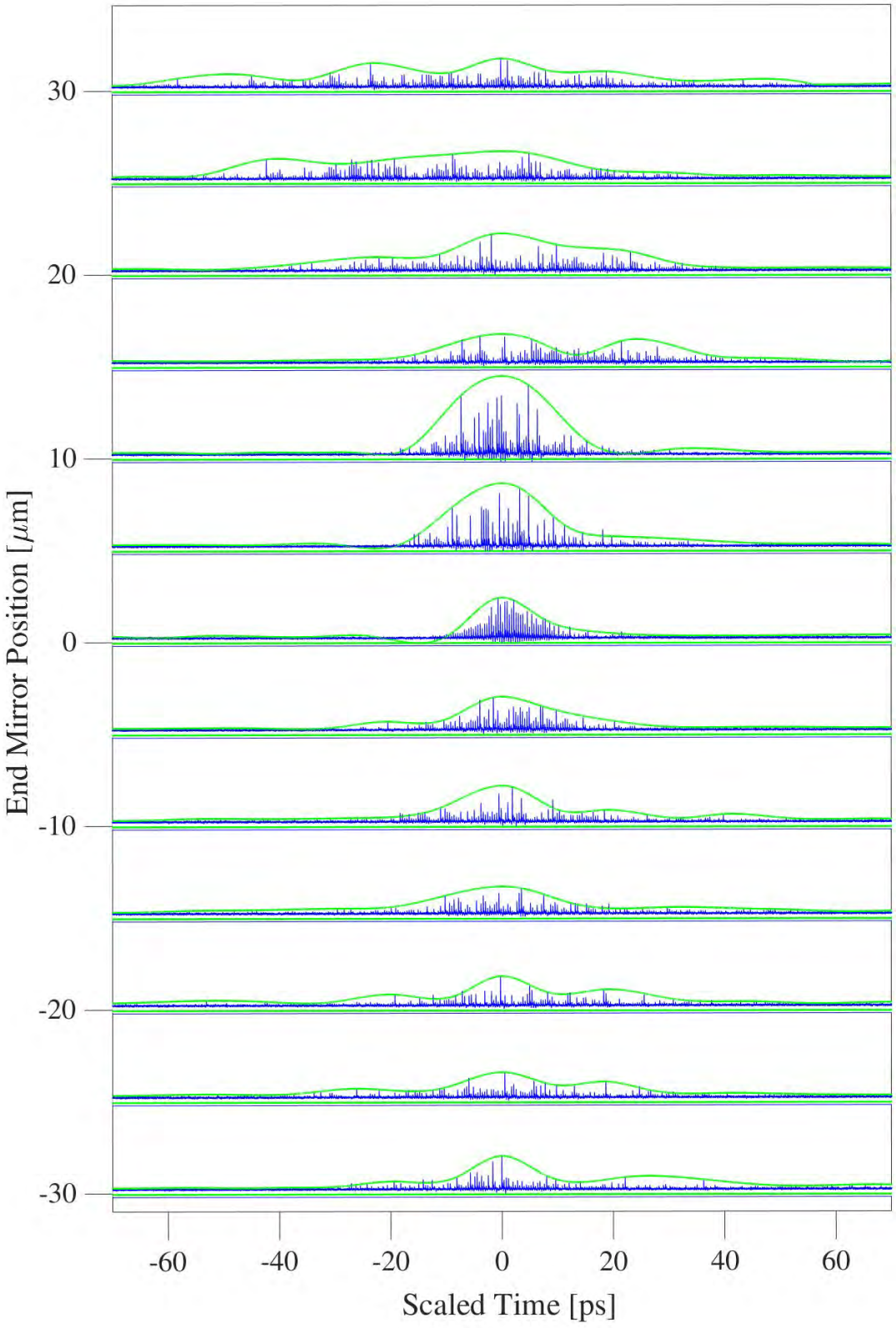

Figure 6.7: Visualisation of pulse duration and shape versus cavity length. Blue: raw cross-correlation data, green: smoothed data via Hilbert transform.

Figure 6.7 shows data recorded using cross-correlation with an auxiliary probe laser in increments of 5 µm (more detail in chapter 6). Note that the narrow peaks of the raw data (blue) represent individual pulses that are generated by frequency mixing, and the temporal profile of the measured pulse is defined by the envelope of these peaks. To visualise the measured pulse shape, the raw data was smoothed via Hilbert transform using the envelope function in MATLAB. This is shown in green, and is merely a visualisation, since the raw data represents a single measurement recorded in approximately 2 µs. Averaging multiple sweeps can excessively smooth the raw data, which hides the mode-locking behaviour of the laser over the <200 round-trips seen here. By considering both the raw data and the smooth data, it is clear that the pulse duration is shortest, on the order of <10 ps, at $\Delta x = 0$. A longer cavity length of $\Delta x = 10$ µm, the position at which maximum power is generated, results in a higher pulse energy but a longer pulse duration. The temporal profile at this cavity length is also affected, and exhibits more variation when compared with the data for $\Delta x = 0$. The $\Delta x = 10$ µm data were recorded just beyond the cavity length range that results in dispersion tuning, which is 10-15 µm long. Figure 6.8 shows a compressed view of the pulse shape at $\Delta x = 0$, which has a reasonably well-defined temporal profile, with some asymmetry and variation. The pulse duration is approximately 8 ps, which is reasonably consistent with previous measured conducted by Granados Mateo.

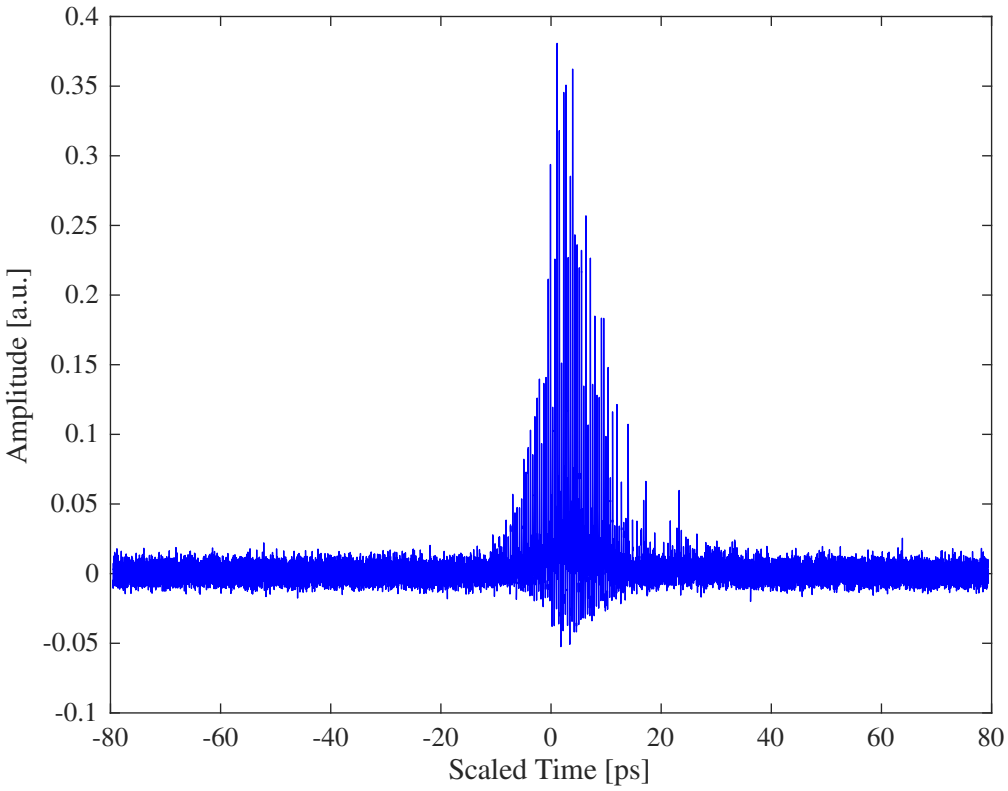

Figure 6.8: Pulse duration measurement of mode-locked Ce:LiCAF laser (via synchronous pumping only) for zero cavity length detuning, measured via asynchronous cross-correlation. This is the zero cavity length position of figure 6.7.

6.4.2 With Prisms

To evoke the passive Kerr-lensing effect in our Ce:LiCAF laser crystal, the dispersion inside the cavity must be reduced to an amount that is close to zero, but slightly anomalous. Intra-cavity prisms were used to achieve this, for which the basic dispersion theory was discussed in section 2.3. Chapter 5 provides a more detailed analysis of the dispersion for our Ce:LiCAF laser cavity, with and without prisms. The shortest pulse duration was recorded with a prism separation of only 7 cm; for reference, the long arm of the cavity is 180 cm long. Increasing the prism separation also increases the minimum pulse duration, but does not significantly alter the shape of the pulse itself, provided that the net dispersion of the cavity is anomalous and hybrid-mode-locking can be established. When this mode-locking scheme is used, the temporal pulse profile is well-defined, and closely matches a Gaussian envelope. This is indicated in figure 6.9, which includes an approximate timescale as a guideline (its uncertainty increases for these shorter timescales). The prism separation for this pulse was 12 cm, which corresponds to a GDD of approximately -1300 fs^2; the pulse duration was approximately 150 fs (FWHM). When the prisms were brought closer together to a separation of 7 cm, reducing the anomalous dispersion close to zero, the pulse duration decreased to approximately 100 fs.

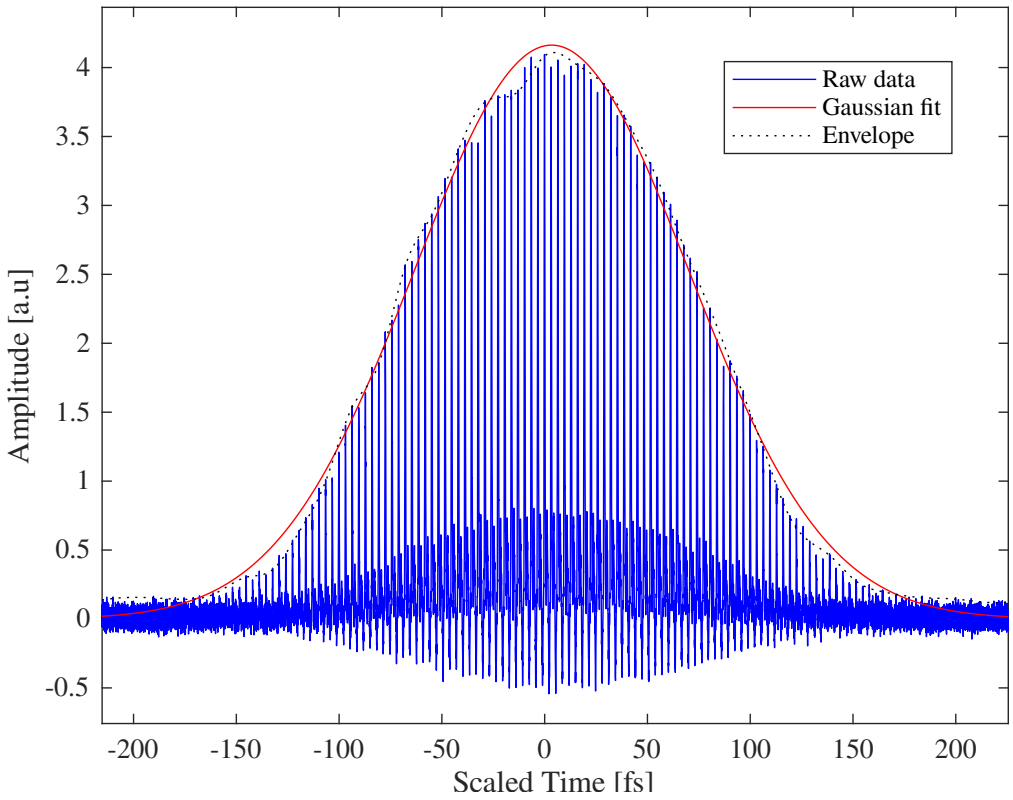

Figure 6.9: Hybrid mode-locking characteristics; a smooth temporal pulse profile, with an approximately Gaussian envelope.

Kerr-Lensing

The Kerr-lens within our Ce:LiCAF crystal is formed when an intense light pulse propagates through it. However, this effect can be insufficient to maintain passive mode-locking without an additional element. By introducing a variable aperture to an appropriate section of the laser cavity, usually near the position of a waist, the low-intensity light that does not evoke significant Kerr-lensing encounters increased loss; intense pulses encounter relatively higher gain. This is generally referred to as hard-aperture KLM, when the Kerr effect is the sole mode-locking mechanism. In our case, the aperture position was chosen to be between the Ce:LiCAF crystal and the input coupling mirror M_1, approximately 2 cm from the Ce:LiCAF crystal. The circular aperture was reduced to a diameter of 1-3 mm and its transverse position was adjusted until there was only one resonating pulse detected by cross-correlation with the probe laser. The regular operation of our Ce:LiCAF laser operating well above threshold in the anomalous regime is shown in figure 6.10. Each peak is Gaussian-shaped as seen previously in figure 6.9, and covers a time-scale that matches the pulse duration set by active mode-locking alone (synchronous pumping). The aperture was then closed and its positioning optimised; its effect on mode-locking is shown in figure 6.11, which shows a single, isolated pulse detected in the same time-scale of active mode-locking (i.e. when driven by the synchronous pump).

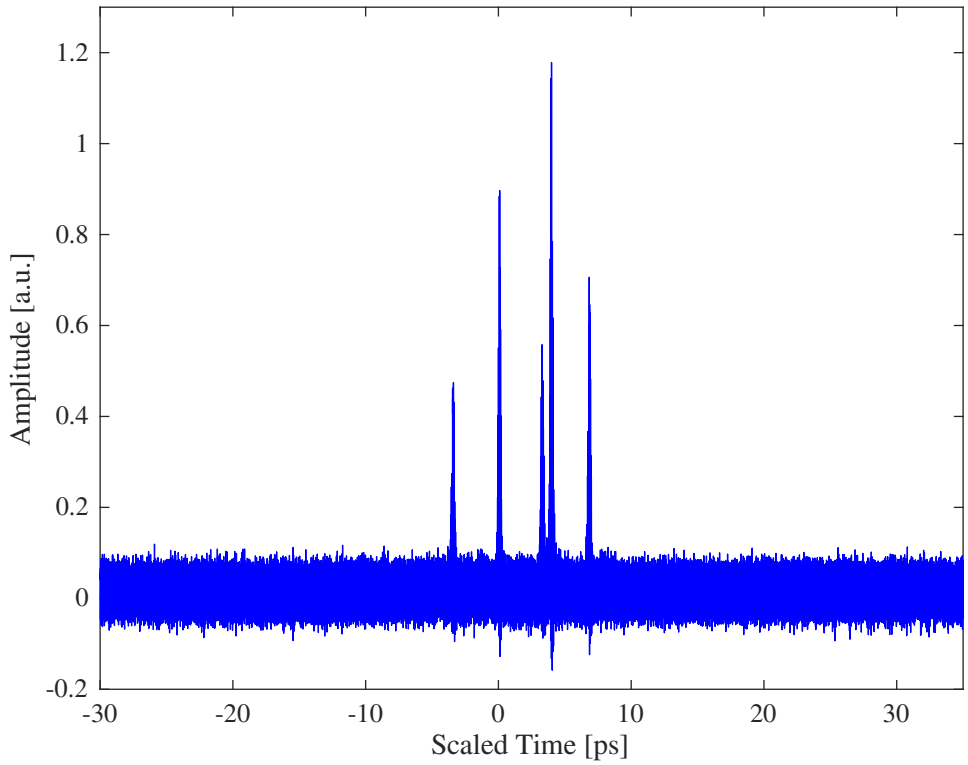

Figure 6.10: Mode-locking characteristics without a hard aperture; semi-stable multi-pulsing within the longer envelope of mode-locked operation without dispersion management.

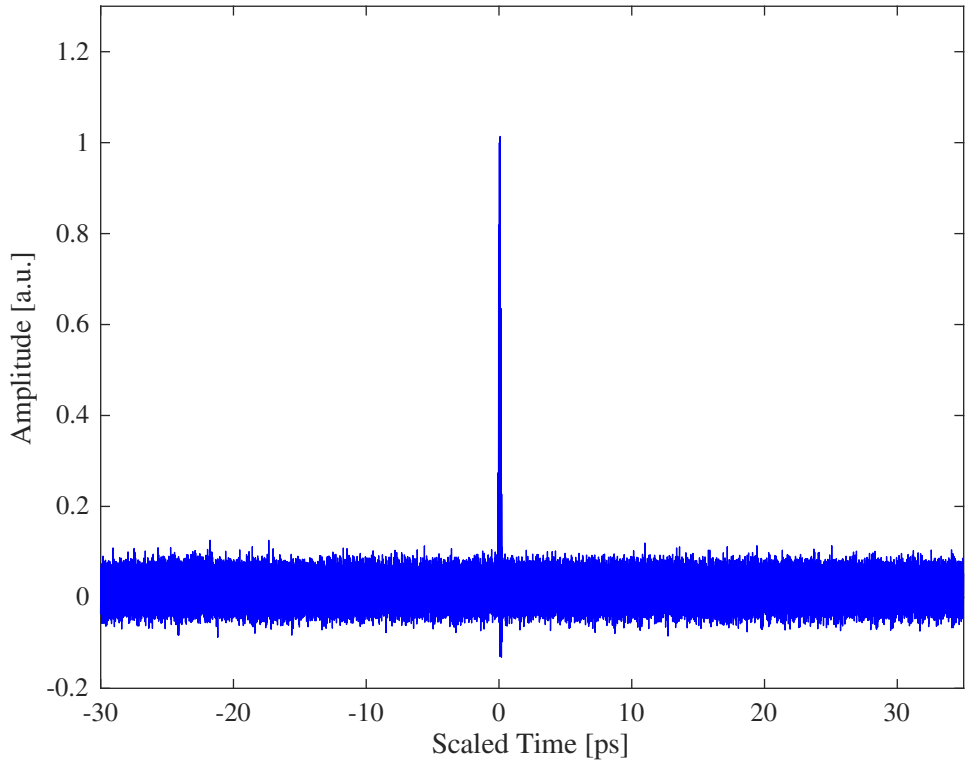

Figure 6.11: Mode-locking characteristics with a hard aperture; an isolated pulse with a duration less than 500 fs.

For characterisation, the Ce:LiCAF test laser was setup for minimum pulse duration, with the chopper in operation, and hybrid mode-locking in action. Within a 20 minute time-frame, over 600 asynchronous cross-correlation traces were recorded by saving data off each trigger event. Each coverslip was used in turn, and the beat frequency was allowed to drift freely below 500 Hz.

The efficacy of the hard-aperture in isolating a single resonating pulse within our laser cavity was sufficient for long term operation, which was mostly limited by the instability of the pump pointing angle, which affected pumping efficiency, as well as pump power as the pump beam was slightly clipped by the aperture itself. However, the single pulses were regular enough to peform hundreds of cross-correlation scans in quick succession, in order to ascertain the pulse duration. Only a few percent (always <10%) of these scans were not used for this measurement, as they were extreme outliers or the curve fitting routine did not converge. Figure 6.12 shows the simplified statistical result that was obtained from over 600 sweeps using this method, in which less than 3% of the data were deemed as outliers. The average and standard deviation of this data is 91±15 fs, which was the minimum pulse duration that was recorded, with a data set that was sufficiently large for a valid result. These data were recorded with the chopper in operation, so each sweep/count is from a separate chopper opening (≈40,000 round-trips).

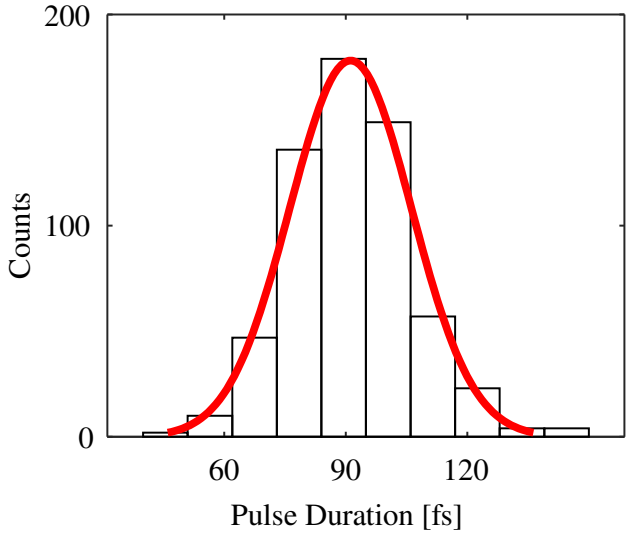

Figure 6.12: Histogram of more than 600 Ce:LiCAF laser pulse duration measurements, recorded during chopped operation.

The pulse duration was also recorded without the chopper in operation, in the same manner as above. The statistical result of over 200 measurements is shown in figure 6.13, which has an average and standard deviation of 106±13 fs. Interestingly, the pulse stability significantly improved during un-chopped operation, so much so, that the aperture was not necessary to isolate a single pulse to resonate. This may have been due to the combination of soft-aperture affects caused by the spatial properties of the pump (soft-aperture KLM), and the lower pump power (compared with un-chopped results) that reduces intra-cavity power and therefore the occurrence of secondary pulses.

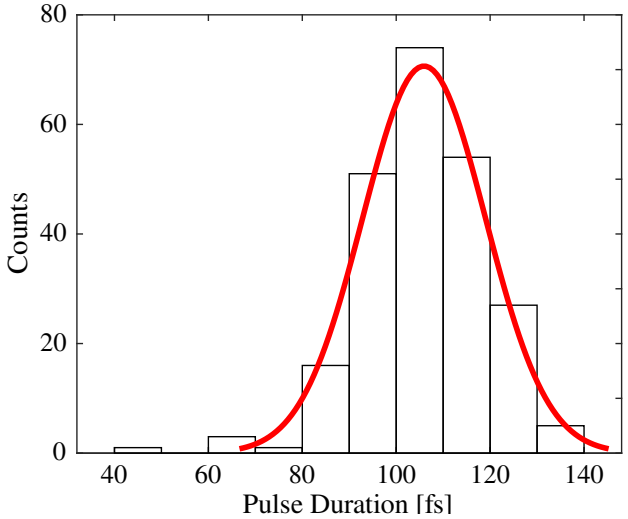

Figure 6.13: Histogram of more than 200 pulse duration measurements, conducted during un-chopped operation of the Ce:LiCAF laser.

6.5 Limitations and Uncertainty Analysis

Figure 6.14 shows the range of measurements that were recorded, which are coloured by the beat frequency that was determined by their individual fitted function according to:

$$\Delta f = \frac{f_0 \Delta t}{b_2 - b_1} \tag{6.5}$$

The average of these data was presented in chapter 4 to be 91 fs, in addition to a simplified histogram (with a standard deviation of 15 fs) that was determined by averaging the retrieved pulse duration of each asynchronous cross-correlation peak. The average and standard deviation of the results obtained using each cover slip were almost identical, and were all within a range of 3 fs, which supports the validity of our measurement technique. They are reasonable well clustered around the average, with a small percentage of outliers from the cluster. Less than 3% of the recorded data were rejected by the fitting routine. There appears to be no systematic variation of measured pulse duration with beat frequency, suggesting that even relatively undersampled measurements (such as in figure 6.6) appear to retrieve a valid pulse duration.

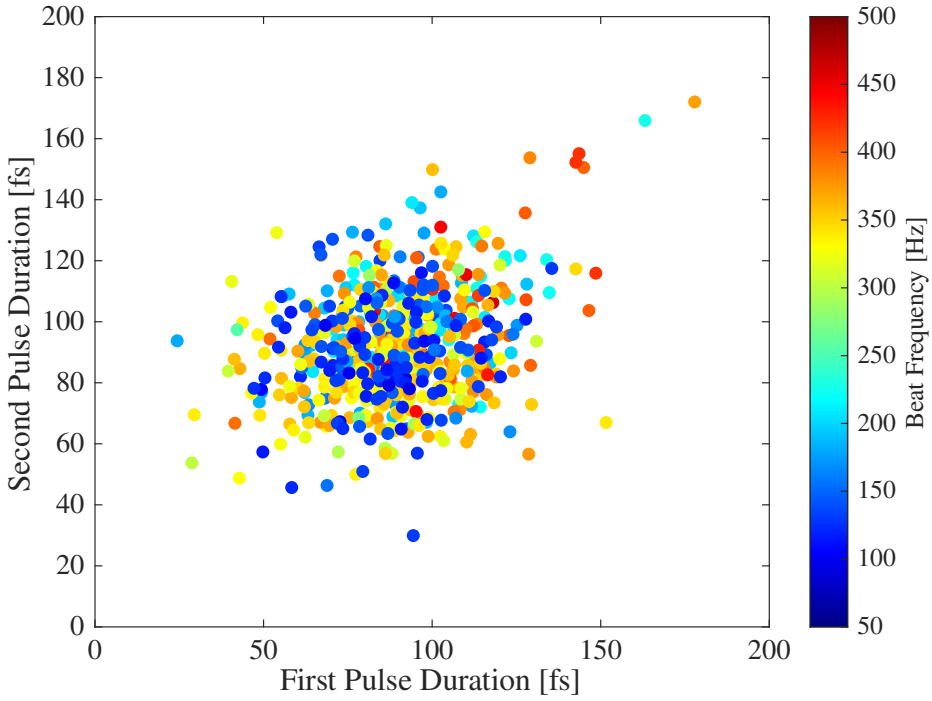

Figure 6.14: Deconvolved pulse duration of first and second pulses in asynchronous cross correlation using the double pulses from the Ti:sapphire laser as a time reference.

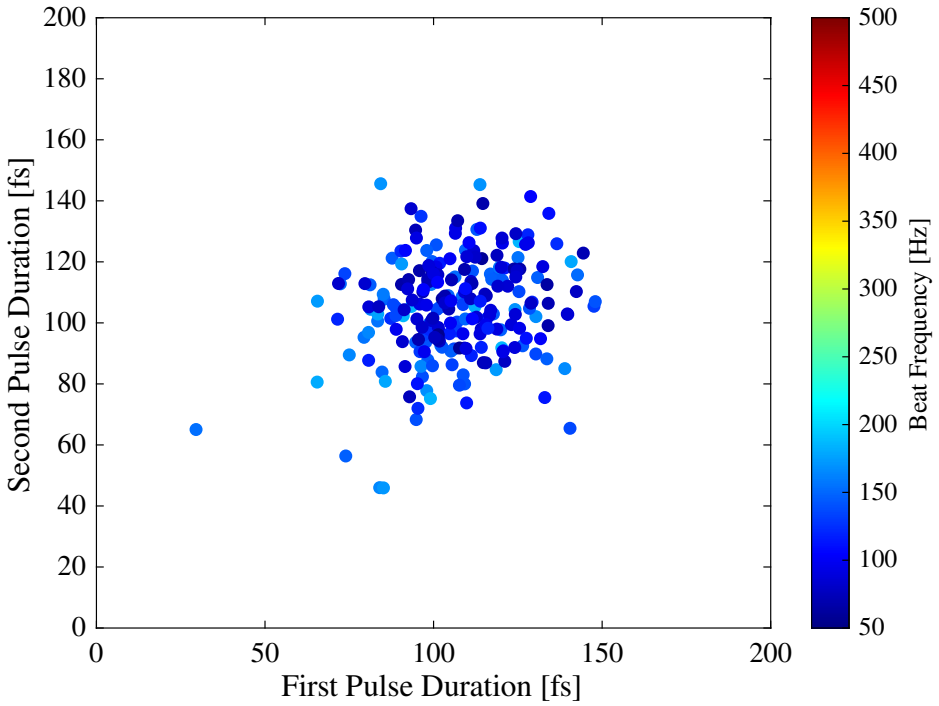

Figure 6.15: Deconvolved pulse duration of first and second pulses in asynchronous cross correlation using the double pulses from the Ti:sapphire laser as a time reference.

Figure 6.15 shows approximately 250 data that were collected while the chopper was not in use. A type 4 cover slip was used and a rejection rate of less than 10% was obtained for the fitted functions; these are both likely to be the result of reduced stability that is caused by issues related to the increased thermal load without the chopper. The average was determined to be 106 fs with a standard deviation of 13 fs. The increased average is unsurprising, as there were several alterations that had to be made before switching off the chopper, to counter the increased thermal effects. These include switching the pump laser off and on again, changing the temperature of the LBO crystal used to generate 532 nm radiation, adjusting the attenuation of the 532 nm beam via a HWP, optimising the angle of the BBO crystal used to generate 266 nm radiation, and realign this beam into the Ce:LiCAF cavity via two turning mirrors. As such, the chopped and un-chopped sets of data were recorded approximately 30 minutes apart. Compared to the data recorded with the chopper running, there is slightly tighter clustering around the average. However, this may simply be the result of a lower sample size.

The most useful advantage of the asynchronous cross-correlation method, in regard to characterisation of our hybrid mode-locked laser, was certainly the capability to determine the stability of the laser, and presence of multi-pulsing. This aspect was crucial to achieving and identifying the contribution of KLM to the mode-locking scheme. However, this technique is not without issue.

There are multiple sources of uncertainty that affect the measurement of pulse duration

by split-beam asynchronous cross correlation, aside from the quality of the fitting routine which was checked manually for several traces before parsing through several hundred. These errors are largely associated with the variation of properties of the test and reference pulses. In particular, their timing, their energy, and their duration. All of these influence the cross-correlation trace. The most likely causes of variation for these parameters are presented below, but to identify the most significant contributor may necessitate further experiments.

Firstly, the beat frequency is constantly varying. The cavity length of both the reference laser and the test laser are changing as a result of vibrations, and drift due to the translation stages, bending of the optical table, and ambient temperature changes. A linear change in the beat frequency on the timescale of 1 µs, which is comparable to the duration of a single dual-peak cross correlation trace can cause the width of each Gaussian envelope (peak) to differ from one another. If the beat frequency decreases ($\mathrm{d}\Delta f/\mathrm{d}t < 0$) then the second peak will appear to be wider, and conversely narrow if it increases. If there is a turning point in the beat frequency ($\mathrm{d}^2\Delta f/\mathrm{d}t^2 < 0$ or $\mathrm{d}^2\Delta f/\mathrm{d}t^2 > 0$) then both peaks will appear to be wider, or narrower, with respect to their separation. In other words, between the peaks that are separated by a known time reference, the two pulse trains are sweeping through each other faster or slower. This would ultimately affect the retrieved pulse duration, and may be the most significant factor in the variation of our pulse duration measurements. To ensure the time-base of the cross-correlation is linear, the Ti:sapphire and Ce:LiCAF laser cavity lengths would need stability on the order of tens of nanometres over a time-span on the order of microseconds.

Secondly, and similarly, timing jitter can originate from optical elements that are external to each laser cavity, which may also be vibrating in a significant manner. Timing jitter between the reference and test pulses affects the energy of the frequency mixed pulses generated by cross-correlation; the two pulses mix differently when they have an unexpected timing jitter, thereby altering the amplitude of the detected pulse peak and the corresponding envelope. This may also have an effect similar to the variation in beat frequency. In an attempt to reduce these issues, the system was isolated from vibration by using an air-floated table, moving the noisy chiller unit farther away, and adding coverings to the open-air laser cavities, but these did not have a measurable effect.

Finally, real variation and semi-stable operation of the reference and test laser pulse duration may be affecting the retrieved pulse duration, since they both affect the width of the Gaussian envelope. One possiblity for variation in the pulse duration, is a slightly unstable laser cavity, caused by the Kerr-lens; varying the distance between the curved mirrors may remedy this, but since this alters the cavity length (and thus synchronous mode-locking) fine-tuning the mirror separation to improve KLM is very time consuming. Alternatively, this could be caused by the semi-stable pulse energy that was detected from the Ce:LiCAF laser over the range of synchronous mode-locking. Stabilisation of timing jitter, power, pulse-to-pulse amplitude variation could be possible with active stabilisation of the Ce:LiCAF laser's

cavity length, or by switching to a CW pumping scheme, but the latter of these is currently a challenge.

The uncertainty that is associated with our asynchronous cross-correlation measurements is not necessarily a limitation, since it only arises because the cross-correlation traces are not time-integrated over several milliseconds (which standard autocorrelation techniques require). We may actually be characterising fast variation in the pulse duration, which would provide more insight, and is therefore not a limitation. On the other hand, if we are simply characterising the variation of beat frequency or timing jitter, an individual trace is insufficient to retrieve a pulse duration. In our case, accurate determination of the pulse duration required a statistically significant number of measurements to be accurate. Therefore, integration may or may not be a limitation, depending on the cause of variation in the pulse duration measurement. A more mechanically stable laser and characterisation system may significantly reduce uncertainty to an extent that a single trace is an accurate measurement.

Another limitation is complexity, since there are several components that need to be operated and aligned. Firstly, an auxiliary mode-locked laser with a known/measured pulse duration that can be operated close to a harmonic of the test laser. In our case, a commercial FROG system was used to determine the pulse duration. Secondly, a non-linear phase-matching crystal (ideally very short) in which the reference and test laser pulses are frequency mixed, which requires precise alignment. This crystal can also a more significant issue for pulses supported by much broader bandwidths that are comparable to the acceptance bandwidth for phase matching. Lastly, a highly sensitive PMT combined with a reasonably fast oscilloscope. The combination of all of these elements can be costly and challenging to align whilst maintaining stable operation.

The final limitation of our approach is that it does not include phase retreival, so the chirp of a pulse is not determined. This is due to the use of a single, high sensitivity PMT, which was the equipment available. Modifications to the method are detailed in the next chapter, and provide a simple arrangement for phase retrieval using split-beam asynchronous cross-correlation.

6.6 Pulse Timing & Semi-Synchronous Cross-Correlation

The presence of synchronous pumping imposes precise conditions of cavity length. Variation in the cavity length of the Ce:LiCAF laser or the pump laser affects the pulse duration and spectrum of the mode-locked operation. Without active cavity length stabilisation, synchronicity between the ultrashort intra-cavity pulse and the arriving pump will always drift or walk-off in time, since it is likely that the upper-state lifetime of Ce:LiCAF is too short for asynchronicity to be permitted, as is the case with synchronously pumped Ti:sapphire lasers. If the cavity length is detuned by 1 μm, each round trip causes the pulse to acquire an additional time offset from the pump of approximately 3.3 fs. After 15000 round trips

(200 µs) the pulse trains would have drifted apart by 50 ps. If the pulse reformation did not occur, and the Ce:LiCAF laser were capable of completely asynchronous mode-locked operation (like synchronously pumped Ti:sapphire lasers) the beat frequency between the intra-cavity pulses and the pump pulses would be 20 Hz. However, 3.3 fs of drift per round-trip is short for a 100 fs, pulse, so the pulse could quite easily reform on each round-trip, if the detuning is small enough. This may result in a small amount of dispersion tuning to accomodate for the different group velocity requirement of the changed PRF; in which case, the operating bandwidth may be restricited to accomodate the dispersion tuning, and the minimum achievable pulse duration is longer as a result.

In our Ce:LiCAF laser, the gain modulation is not temporally symmetric, as shown earlier in chapter 4, figure 4.8. The gain is higher for a slightly longer cavity length than a shorter one. This will result in behaviour that is different for a shorter cavity length than a longer one, which is often the case. However, this gain profile is a simplified presentation of the dynamics that may be occurring, since the pump pulse is counter-propagating. The pump pulse is effectively 4 mm long, more than double the length of the crystal. If the laser and pump pulses encounter each other inside the Ce:LiCAF crystal, this would mean that the resonating pulse would be on or near the steep slope of the simplified temporal gain profile. While this could influence Kerr-lensing as cross-phase modulation may become significant, the peak power of the pump pulse is only of the order of 1% of the resonating pulse (1 kW compared to 100 kW; note that this an estimate with significant uncertainty due to unstable pulse energies) so it seems unlikely. Therefore, the differential gain and cavity length stability may play the most significant roles in the timing walk-off of the two pulses.

In an actively mode-locked laser, like a synchronously pumped one, cavity length variation affects the steady-state properties of the resonating pulse. As shown in chapter 2, small variations <1 µm from the synchronous cavity length can simply cause the pulse to reform each round-trip; higher gain is encountered on either the leading or the trailing edge of the pulse, so it is constantly shifting. Larger variation causes the resonating pulse to drift away from the modulation of active mode-locking faster than pulse shifting can occur; a new pulse forms regularly, to maintain synchronicity. To determine the regime in which our laser is operating is challenging, and requires high temporal precision of the resonating pulse timing over a relatively long time-scale.

To measure the timing walk-off between the pump pulse and the resonating pulse, two photodiodes were used; one to monitor the 266 nm pulse train (THORLABS DET10A with a 1 ns rise/fall time) in place of the pump-recyling HR mirror after the prism pair (shown in figure 6.2) and one to monitor the output of the 290 nm pulse train (ALPHALAS UPD-50-UP with a 50 ps rise/fall time). The results are shown in figure 6.16. The red trace is the measurement uncertainty (pump-pump timing difference) which was determined by splitting the pump beam between the two photodiodes. This measurement uncertainty also closely matches measurements without the use of an intra-cavity aperture, for which a group of pulses

are resonating; individual pulses within the group are not resolved by the photodiode, but their envelope was stable to within the measurement uncertainty. The blue trace was measured when using an intra-cavity aperture for hybrid mode-locking. In this case there was only a single pulse resonating in the cavity, which was confirmed by simultaneous cross-correlation.

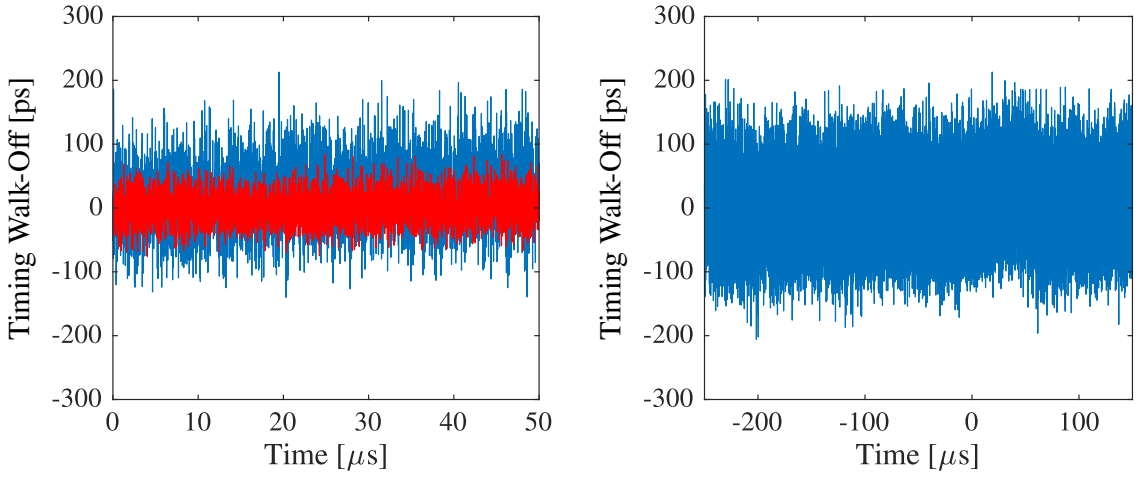

Figure 6.16: Timing walk-off between the laser and pump pulse. Red: measurement uncertainty, blue: walk-off of a single, resonating laser pulse. The figure on the right shows walk-off for approximately 30,000 round-trips (left and right are the same data on two different timescales).

Note that the timing difference shown in the figure has been centred on zero, to make the results visually comparable. The laser pulse actually propagates through the long arm of the cavity 300-500 ps behind the pump pulse; the average timing difference of several thousand pulses was measured to be 370±50 ps. This pulse delay is a combination of two things. Firstly, the laser pulse counter-propagates through the Ce:LiCAF crystal, so travels 100 mm (334 ps) before being reflected to travel in the same direction as the pump pulse. This occurs because there is higher gain for a pulse that returns to the gain medium quickly, rather than propagating through the long arm of the cavity first, at which point the population inversion has decayed more. Secondly, the undepleted gain reaches a maximum after the pump pulse has been completely absorbed, approximately 21 ps after the peak of the pump pulse. The combined delay of these two factors is 355 ps, which is in good agreement with the measured value.

The variation in timing difference depicted in figure 6.16 shows that the isolated laser pulse drifts more than a group of pulses. This implies that there is a larger temporal walk-off of the laser pulse when there is only one resonating pulse, as opposed to several bunched pulses. The fact there is a single pulse, confirmed by cross-correlation, indicates that the laser is likely to be operating in the regime in which the pulse is constantly shifting on each round-trip. In this case, the walk-off could be higher because there is no gain competition with a secondary pulse(s), since there is only one pulse. Conversely, if a group of short

pulses (≈100 fs) are resonating within an envelope (≈10 ps) then the unresolved pulse timing (i.e. figure 6.16) will be more consistent, since each short pulse is regularly drifting and competing for gain. When hybrid mode-locking is utilised, there is only a single pulse resonating, and it is less likely that drift of the pulse timing will result in a secondary pulse forming, because of the hard-aperture that increases loss for less intense pulses. Since cavity length variation effectively prevents laser oscillation that is truly steady-state, it is possible that the combination of timing walk-off and preferential gain laser pulse is causing this single laser pulse to drift forwards and backwards while constantly being reshaped.

To further characterise pulse timing, a semi-synchronous cross-correlation of the hybrid-mode-locked Ce:LiCAF laser was performed. The cavity length was set to the edge of the dispersion tuning range, for which the spectrum (as measured on a spectrometer with a 40 ms integration time) resembles a superposition of the dispersion tuning peak and the spectrum outside of the dispersion tuning range, which generally results in long pulses on the order of 50 ps. In figure 6.17, the peaks of the semi-synchronous cross-correlation represent every time the Ce:LiCAF laser pulse is overlapped with the reference pulse (which is synchronised to the timing of the pump pulse). There appears to be a correlation between the pulse timing in the Ce:LiCAF laser and the modulation of pulse energy, suggesting that pulse timing drift is a significant factor for modulation of pulse energy. Using the split-beam approach permitted measurement of a 150 Hz beat frequency, which corresponds to a cavity mismatch to the pump laser of +7.5 µm. The pulse duration was approximately 150 fs, as the cavity was set

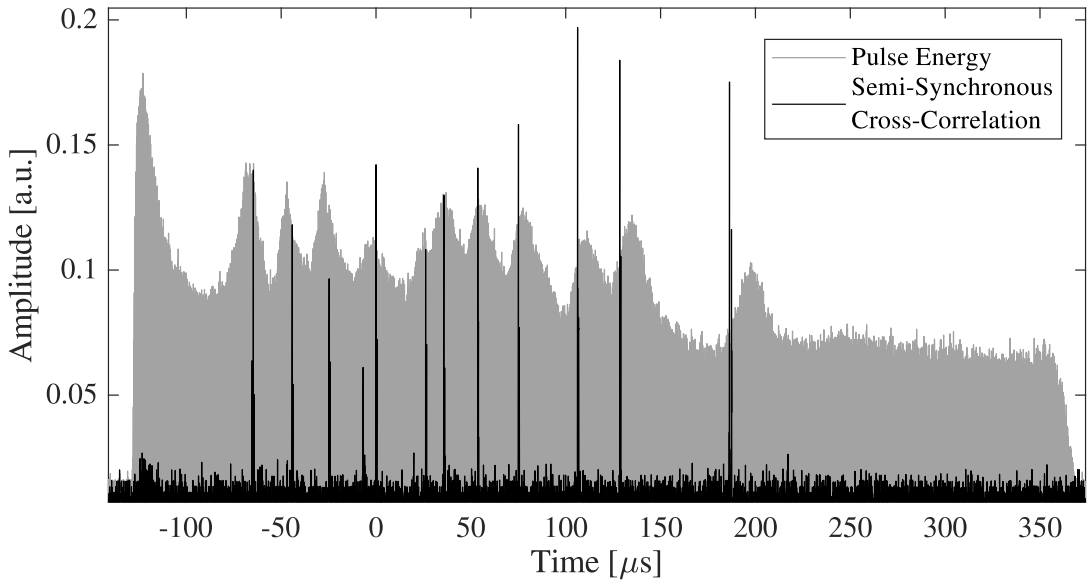

Figure 6.17: Comparison of Ce:LiCAF laser pulse energy during one chopper opening and relative timing to the arrival of pump pulses, measured via semi-synchronous cross-correlation (reference laser synchronised to pump laser). The Ce:LiCAF laser cavity length was approximately 7.5 µm longer than synchronicity to the pump. Note that the irregularity of semi-synchronous cross-correlation measurements is likely due to instability of the beat frequency.

up with additional anomalous dispersion to allow for dispersion tuning, so this mismatch is consistent with the expected amount. The polarity of the beat frequency did not change from peak to peak (determined by uneven peaks of split-beam cross-correlation) which confirms that the Ce:LiCAF laser pulses swept through the reference pulses in the same direction every time. These data therefore imply that the resonating pulse is reforming every few thousand round trips (for reference, 50 µs ≈ 4000 round trips) which is to be expected from hybrid-mode-locked lasers on the synchronous-asynchronous transition [81]. If we neglect pulse shifting (power shifting towards the leading side of the resonating pulse) then the resonating pulse is therefore limited to a timing offset of approximately 100 ps away from the optimum; encorporating shifting would reduce this value. This is in reasonable agreement with the timing walk-off measured via the unresolved pulse (using photodiodes).

As a comparison to laser behaviour on the synchronous-asynchronous transition, the cavity length of the Ce:LiCAF was shortened, to a length that was closer to the centre of dispersion tuning; the result is shown in figure 6.18. While there are clearly more occurrences of the pulse timing matching the pump laser, the beat frequency and its polarity was not consistent, but was generally below 100 Hz. It is possible that these particular data recorded fluctuation of pulse timing close to the synchronous cavity length, for which the polarity of beat frequency may change often. Alternatively, or additionally, new pulses could be forming more rapidly due to the steeper gain edge that is encountered for a negative cavity length mismatch.

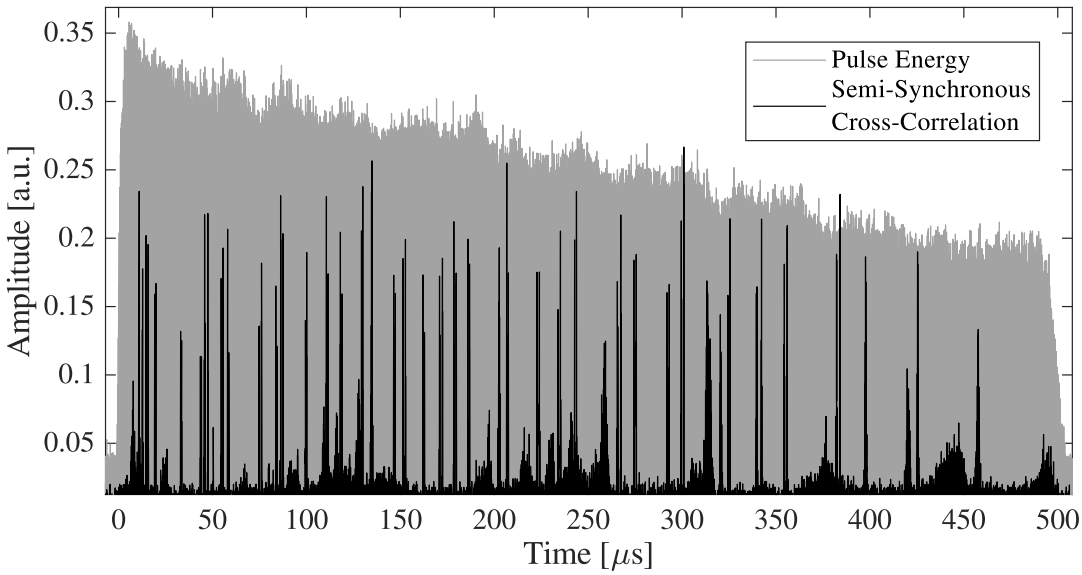

Figure 6.18: Comparison of Ce:LiCAF laser pulse energy during one chopper opening and relative timing to the arrival of pump pulses, measured via semi-synchronous cross-correlation (reference laser synchronised to pump laser). The Ce:LiCAF laser cavity length was set close to synchronicity to the pump. Note that the irregularity of semi-synchronous cross-correlation measurements is likely due to instability of the beat frequency.

Chapter Summary

In this chapter, the ultrafast pulse characterisation technique of asynchronous cross-correlation was introduced before presenting the modified version that was developed in this thesis, which includes a beam-splitting time reference in the form of a microscope cover slip. This enabled a time reference that was much faster than the beat frequency of the test and reference lasers; on the order of 1 µs compared to 1 ms. The curve fitting routine that is necessary to process the raw data from this technique was outlined, with visual examples of the collected data. A large set of data consisting of over 600 measurements were presented and analysed to assess sources of uncertainty using this technique. These measurements produced a new shortest pulse record for Ce:LiCAF lasers, at 91±15 fs for chopped operation and 106±13 fs for unchopped. The temporal shape of the Ce:LiCAF laser pulses for active mode-locking versus hybrid mode-locking were also compared and found to be significantly more consistent for the latter, more closely matching a Gaussian profile. Finally, the pulse timing between pump pulses and resonating laser pulses was measured using photodiodes, in addition to using a further modified form of asynchronous cross-correlation, semi-synchronous cross-correlation. The result of these measurements indicated that the pulse energy instability that is exhibited by the hybrid-mode-locked Ce:LiCAF is linked to pulse timing walk-off, and therefore cavity length variations and vibrations.

I know that I know nothing

Socrates

7

Conclusion

The aim of this research project originally titled "cerium lasers: ultraviolet, ultrafast, and ultracool" was the continued development of ultrafast Ce:LiCAF lasers by the MQ Photonics Research Centre. This was achieved experimentally by following a research pathway similar to that of the first Kerr-lens mode-locked (KLM) Ti:sapphire lasers, for which prism pairs were utilised to compensate for intra-cavity chromatic dispersion, and ultimately generate mode-locked pulses on the order of 60 fs. On the other hand, the development of mode-locked Ce:LiCAF lasers has been much more gradual than Ti:sapphire, despite the fact that they were discovered within a decade of each other, and have a comparable spectral bandwidth. This is primarily because of the short upper-state lifetime of Ce:LiCAF, the scarcity of high-powered pump sources, and the increased losses introduced by optical elements for UV wavelengths. Despite these issues, development of cerium lasers continues toward their ultimate ultrafast potential, alongside parallel progress in fields that are working to develop better pump sources, and UV optics with lower losses, that will enable research breakthroughs in the future.

The achievements presented in this thesis act as a stepping stone towards the prospect of Ce:LiCAF lasers replacing more complex frequency converted laser systems that initially generate radiation at IR wavelengths. Whether the Ce:LiCAF laser will be a viable tool for several industrial and scientific applications, instead of using more complex systems, is a question that will continue to be asked as Ce:LiCAF lasers, and the elements which support them, continue to improve.

7.1 Summary of Results

Plane Output Coupler & Un-chopped Operation

The success of the work presented in this thesis can be attributed to several alterations that were made to the original layout of the first mode-locked Ce:LiCAF laser. The first of these was the alteration of a simple but vital component: the output coupler (OPC). This part is not to be overlooked; without it, the most significant achievements presented in this thesis would have been more challenging or impossible. The switch from a near-Brewster's angle window acting as an OPC to a low transmission plane mirror made the prospect of KLM within the cavity simpler in two regards. Firstly, the intra-cavity group-delay dispersion (GDD) was decreased by a factor of 2; dispersion was also no longer a variable linked to the angle of the OPC. Secondly, the power generated by the laser cavity was consolidated from 4 beams into 1, thereby increasing the efficiency of power generation, which was useful for characterisation of the pulse duration. A relatively low transmission of 1.5% was measured, which reduced the threshold of the original power-optimised 3-mirror cavity (without prisms) from 1.37 W to 0.55 W.

This low threshold also enabled, to the best of our knowledge, the first stable operation of an un-chopped mode-locked Ce:LiCAF laser. Although output powers of over 80 mW from the Ce:LiCAF laser (at its first harmonic with the pump laser) were achieved by pushing the pump laser system to its thermal limits, this was not maintainable, owing primarily to thermal dephasing and lensing in the BBO crystal. During more stable operation of the pump system, a slope efficiency of 11% was achieved without prisms for a threshold of 0.6 W, similar to that of chopped operation. With the intra-cavity prism pair in place, a slope efficiency of 9% was measured (chopped) for a threshold of only 1.0 W, which allowed for un-chopped operation just above threshold.

Dispersion Tuning

The presence of dispersion tuning in our Ce:LiCAF laser was identified as a byproduct of a synchronous pumping scheme combined with the short upper-state lifetime of Ce:LiCAF. The nature of dispersion tuning was characterised by measuring the spectrum of the laser output as a function of cavity length. This was performed for the first and third harmonic (relative to the pump laser) with, and without, additional GDD introduced by Brewster's windows. For a higher GDD, it was found that the tuning sensitivity and bandwidth generally decrease. The gain within the laser was also found to generally increase the bandwidth and tuning range. At the first harmonic (which has higher gain than the third harmonic), over 5 nm of tuning range was demonstrated around the 290 nm gain peak. Using two Brewster's plates to increase dispersion, the bandwidth (FWHM) was reduced from 0.8 to 0.27 nm at the first harmonic and from 0.45 to 0.11 nm at the third harmonic. These were performed

in the regime of normal dispersion, with synchronous pumping as the only mode-locking mechanism.

The spectral characterisation of the Ce:LiCAF laser yielded a reasonably accurate relation between dispersion measured by tuning, and the theoretical intra-cavity dispersion, and therefore the means to estimate the intra-cavity dispersion based on the sensitivity dispersion tuning. When using an intra-cavity prism pair to reverse the polarity of dispersion, thus entering the anomalous regime, the presence of dispersion tuning was also used practically, to identify when the intra-cavity dispersion was close to zero. Approaching zero dispersion from the anomalous regime resulted in a significant increase in bandwidth; up to 5 nm of bandwidth was recorded using this method, which corresponds to a potential bandwidth-limited pulse duration of only 20 fs. However, this bandwidth may have been increased due to time-integration of a rapidly-shifting bandwidth that was actually narrower.

Hybrid Mode-Locking & Split-Beam Asynchronous Cross-Correlation

The pre-existing synchronous pumping scheme was combined with KLM to form a hybrid mode-locking scheme, which was used to generate sub-100 fs pulses from our Ce:LiCAF laser. To the best of the author's knowledge, these are the shortest pulses ever generated using the Ce:LiCAF gain medium. Since KLM relies on a slightly anomalous net round-trip dispersion, the practical approach of estimating GDD (particularly the zero-value) using dispersion tuning was a vital tool to achieving this result. However, even more vital was the measurement technique that was used to stabilise KLM as well as measure the pulse duration, which has been termed as split-beam asynchronous cross-correlation. This new approach to asynchronous sampling, which splits the probe pulses in half with a fixed time delay, suffers significantly less from uncertainty than the standard approach, since the time reference occurs much faster, on the order of 10^4 (e.g. 500 ns compared with 10 ms); less time elapses between the two points that comprise a time reference, so the beat frequency has less time to fluctuate, and the uncertainty that arises from it is lower. Using a sample size of over 600 and 200, respectively, a shortest pulse duration of 91 ± 15 fs (chopped) and 106 ± 13 fs (un-chopped) was measured using this technique and a tailored curve-fitting script. Stabilisation of hybrid mode-locking was essential in reaching this stage, for which almost every oscilloscope trace that was triggered resulted in a measurement. Asynchronous cross-correlation was used to monitor stability and the presence of multi-pulsing from our Ce:LiCAF laser, while multiple variables were adjusted to optimise it; these include pump power, cavity length, and intra-cavity aperture diameter. Fine adjustment of the synchronous cavity length was also performed whilst monitoring the output spectrum that was affected by dispersion tuning. It was only through these controls that the combination of active and passive mode-locking schemes reached a stable solution.

Table 7.1: Summary of laser parameters for our Ce:LiCAF laser. Note that the peak power has been estimated under the hybrid-mode-locking conditions of the shortest pulse durations; it has significant uncertainty due to unstable pulse energies that were measured for this case.

Parameter	Chopped	Un-chopped
Threshold [W]	1.0	1.0
Slope efficiency [%]	9	N/A
Maximum power output [mW]	116	10-20 (limited by pump power)
Minimum pulse duration [fs]	91	106
Estimated peak power [kW]	1.5	1.5

7.2 Implications of the Work

The bandwidth of Ce:LiCAF has the potential to support sub-5 fs pulses, and since the carrier frequency at its maximum gain peak 290 nm is approximately three times higher compared with Ti:sapphire lasers, the single cycle limit (970 as) is correspondingly three times shorter. The results of this thesis have shown that hybrid-mode-locked Ce:LiCAF lasers are capable of sub-100 fs pulse durations using only a prism pair to manage dispersion. In order to unlock the full potential of the gain medium and generate the shortest possible pulses, higher orders of dispersion must be controlled precisely. However, these pulse durations may already suffice for some applications, such as ultrafast spectroscopy and direct-write waveguides. The presence of dispersion tuning in our Ce:LiCAF laser could also be utilised for simple and rapid wavelength tuning, which may be useful for applications such as spectral optical coherence tomography that can be performed with a wavelength-swept laser. Amplifying the output of our laser could also enable applications that demand more intense pulses. The introduction described how high-harmonic generation (HHG) is more efficient when driven by radiation of a shorter wavelength. Since Ce:LiCAF lasers generate the shortest wavelength of any optically-pumped solid-state laser medium, a multi-pass amplification system following a hybrid-mode-locked Ce:LiCAF laser could be an efficient starting point for HHG at multi-MHz PRFs.

The performance of the Ce:LiCAF laser running continuously was limited by the pump laser system, specifically thermal effects in the BBO crystal that restricted power. Increasing the power of the Ce:LiCAF laser therefore relies on either modifying the frequency doubling stage (532 nm to 266 nm) or choosing a different pump source entirely. The ideal pump source for a KLM Ce:LiCAF laser would generate CW radiation, thus making KLM the sole mode-locking mechanism. Replacing the mode-locked pump source with a CW alternative would not only remove the cavity length requirement of the Ce:LiCAF laser, but it may also reduce the minimum pulse duration that can be achieved with the current resonator design, since the presence of dispersion tuning restricts the spectral bandwidth. The advantages of CW pumping are therefore the potential for shorter pulses and a less restrictive cavity length,

but these are accompanied by the disadvantages of a higher threshold (since the intra-cavity pulse is no longer matched to a gain peak) and a more complex pump system; frequency conversion of CW radiation to 266 nm is not feasible without additional elements such as an optical parametric oscillator (OPO) or multiple phase-matching crystals. On the other hand, OPOs that are used for frequency conversion of CW Ti:sapphire lasers require the added complexity of tuning, so the overall system may be simpler than Ti:sapphire-based alternatives in regards to active elements. In addition to KLM, the use of a robust CW pumping scheme would also be beneficial for CW output from the Ce:LiCAF laser and its potential for single longitudinal mode operation. Recent advances in DUV diode lasers indicate that generating pump radiation may even be possible without any frequency conversion at all; the development of a diode laser at 271.8 nm is close to the same peak in absorption cross-section that the 266 nm sources utilise.

7.3 Future Work

The work in this thesis and the resultant hybrid-mode-locked Ce:LiCAF laser enable a variety of potential avenues for research and development. Firstly, the effect of active stabilisation could be explored; directly synchronising the generated Ce:LiCAF laser pulses to the pump pulses, or locking the spectral output from the Ce:LiCAF laser are two viable options to perform this task. Combining this with improved characterisation of the pulse timing (in relation to shift, drift, and new pulses forming) could be used to determine the requirement for cavity length stability; whether or not active stabilisation of the cavity length significantly improves the stability of pulse energy is an important question. Secondly, a standard X-FROG measurement would necessitate direct synchronisation between the Ce:LiCAF laser and the Ti:sapphire reference laser; the effect of pulse timing between pump pulses and the resonating pulse inside the Ce:LiCAF laser could also be explored if all three lasers were synchronised. For example, synchronising the Ce:LiCAF laser to the Ti:sapphire laser to the Nd:YVO_4 pump laser, with a delay line to manipulate the time offset between the Ce:LiCAF and pump laser pulses. Thirdly, as an alternative approach to measuring pulse chirp, the asynchronous cross-correlation approach developed in this thesis could be adapted to include phase retrieval. Fourthly, and perhaps most importantly in regards to the viability of CW and mode-locked Ce:LiCAF lasers, both the pump system and Ce:LiCAF laser cavity would benefit from several redesigns to accomodate higher average powers for stable operation without the use of a chopper. Lastly, the management of higher orders of intra-cavity dispersion is essential to reach the shortest pulse duration that Ce:LiCAF is capable of; it is also the most challenging at the time of writing, since common approaches to this task are accompanied by high losses in the UV region.

Measuring Pulse Timing

In regards to measuring the relative pulse timing between the Ce:LiCAF and pump laser, improving the resolution of data can be achieved using a faster photodiode and oscilloscope. The data presented in this thesis (figure 6.16) was recorded using a photodiode with a 50 ps rise time (ALPHALAS UPD-50-UP) attached to a 6 GHz oscilloscope (LeCroy WaveMaster 8620A) which has a sampling rate of 20GS/s. However, photodiodes with faster responses are available, with rise times as low as 10 ps. Additionally, oscilloscopes as fast as 110 GHz, with sampling rates of 256GS/s are also available (the Keysight Technologies Infiniium UXR-Series). Improving resolution beyond this is challenging without alternative methods. Cross-correlation between the Ce:LiCAF and pump laser, for example, may provide resolution on the order of 1 ps using the variation of pulse energy in the frequency mixed signal. However, recording reliable data using this approach may necessitate a significantly more stable laser output (specifically pulse energy) which could require stabilisation of several elements; for example, pump beam point angle, and Ce:LiCAF laser cavity length.

Spectral Stabilisation of Cavity Length

Active stabilisation of cavity length relies on locking the output power, spectrum, or pulse duration/timing. Of these, the pulse timing and spectrum are the most sensitive to cavity length variation and are therefore the best choice. Locking the spectral output of the Ce:LiCAF laser to the centre of the dispersion tuning range results in a relatively simple arrangement for this task, and is depicted in figure 7.1. The output beam from the laser is spectrally dispersed using a prism or grating, and incident upon two photodiodes (PD) that are positioned to detect two different wavelengths. As the cavity length changes and the spectrum shifts, the signal that each PD receives becomes unbalanced. A standard feedback loop using a PID locking box (e.g. LaseLock) can be used to counter changes in the cavity length by controlling the displacement of a mirror-mounted piezoelectric crystal. The advantage of this approach is that it only requires the output of the Ce:LiCAF laser; it also locks the wavelength which may be useful. A potential disadvantage is the response time, since it takes more time for the wavelength to shift than it does for the pulse timing to drift (the latter governs the former) but this may not be a significant issue.

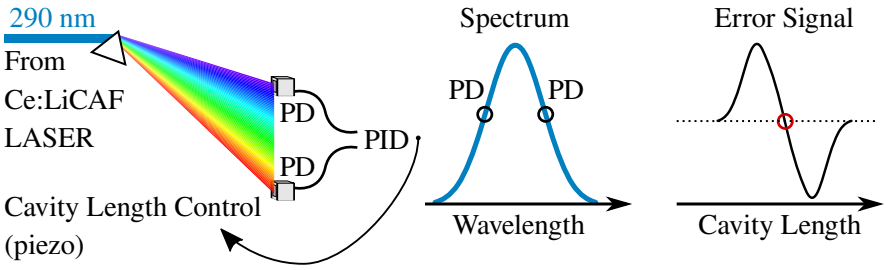

Figure 7.1: Active stabilisation of synchronously pumped Ce:LiCAF laser, utilising dispersion tuning. PD: photodiode; PID: stabilisation regulator, e.g. LaseLock.

Balanced Cross-Correlation

A potentially more precise method of active cavity length stabilisation may be synchronisation of the intracavity pulse to the pump pulse. With this aim in mind, the simplest concept to perform exactly this task is a balanced cross-correlation system to synchronise the intracavity 290 nm pulses to the 266 nm pulses via a feedback loop to the Ce:LiCAF laser cavity length. This would necessarily utilise DFG between the two pulses (since SFG is not feasible) and detecting the DFG signal in the feedback loop. However, this can prove to be an expensive method of stabilisation via synchronisation, due to the wavelength of the DFG signal. Detectors would need to be responsive in the 1.7-5.3µm. There are also very few nonlinear frequency conversion crystals that are transmissive for all three of the mixed wavelengths; BBO declines significantly for wavelengths past 3 µm. The peak power of both the Ce:LiCAF and pump laser pulses are also both lower than the reference laser, so the resulting DFG signal would be relatively weak. One way to mitigate these issues is to synchronise the 290 nm pulses to the 532 nm, or 1064 nm pulses from the pump system. This would generate 640 nm, or 400 nm light, respectively, for which there are highly sensitive detectors. Additionally, the 532 nm, or 1064 nm waste light from the two single pass SHG stages that comprise the pump system is significantly more powerful than the 266 nm stage, so this approach may be feasible.

While synchronisation of the Ce:LiCAF laser to the pump laser may stabilise the laser system somewhat, it would be more beneficial to synchronise the reference laser and the Ce:LiCAF laser, which would enable a standard X-FROG measurement to retrieve the phase profile of the UV pulses. Given that the peak power of the Ti:sapphire reference pulses (at 808 nm) are higher than either of the other lasers, one option may be to synchronise the Ti:sapphire laser to the Nd:YVO_4 pump laser (using a mostly pre-existing system described in [89]) and then to synchronise the Ce:LiCAF laser to the Ti:sapphire laser. This could provide stabilisation between Ce:LiCAF and Nd:YVO_4 lasers, in addition to enabling X-FROG between Ce:LiCAF and Ti:sapphire lasers.

On the other hand, a potential issue with simply synchronising the timing of Ce:LiCAF pulses to pump pulses is the lack of spectral control; a change in pulse timing may still cause a shift in wavelength of the resonating pulse. It remains to be seen if this would have a significantly detrimental effect on the efficacy of this method of cavity length stabilisation. If it proves to be an issue, the best arrangement may be to stabilise the Ce:LiCAF laser cavity length via its spectral output, and synchronise the Ti:sapphire laser to the Ce:LiCAF laser. The necessary balanced cross-correlation system for this task is depicted in figure 7.2. One arm introduces a relative delay between the pulse trains that is ideally equal to the FWHM of the longer pulse duration; a relative delay of approximately 100 fs would position the Ti:sapphire pulses on either side of the Ce:LiCAF pulses in each arm. This could be performed simply using fused silica with a thickness of approximately 250 µm, the equivalent

of a type 2 microscope coverslip. The balanced cross-correlation system produces a standard error signal, synchronising the reference laser to the Ce:LiCAF laser for X-FROG.

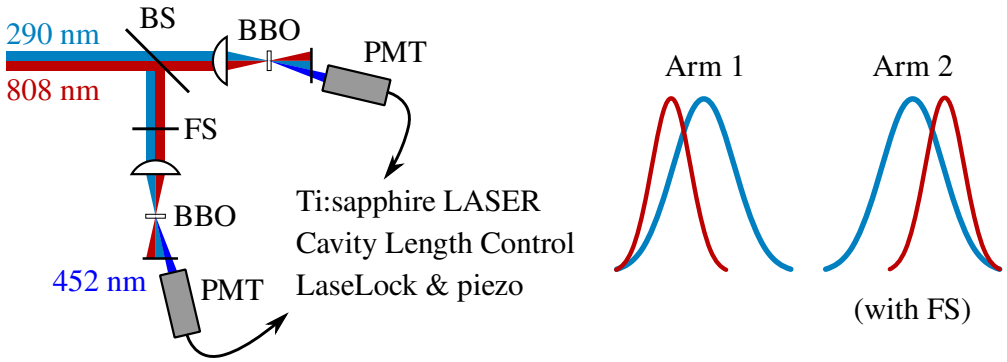

Figure 7.2: Synchronisation via balanced cross-correlation. BS: beam splitter; FS: fused silica cover slip; PMT: photomultiplier tube.

Asynchronous Cross-Correlation Frequency Resolved Optical Gating

To avoid the array of challenges that synchronisation entails, the asynchronous approach in this thesis could be modified to make it capable of determining the chirp of a pulse, by replacing the single PMT with a spectrally dispersive element and PMT array. The basic arrangement of this is shown in figure 7.3. Using a high dispersion spectrograph grating to spatially separate the DFG signal into its spectral components, and a PMT array to detect the individual DFG pulses. For example, a 32-channel Hamamatsu H11460-200, which is highly sensitive to blue light, would be ideally suited to detection of our DFG pulses which are in the 450 nm region. A fast oscilloscope with the same number of channels would also be needed, such as the Tektronix 6-Series mixed signal oscilloscope. Using a PMT array with fewer elements would simply reduce the resolution of the phase profile. An example of traces that could be captured for a chirped pulse is depicted in figure 7.4; processing these would necessitate an original algorithm for this method.

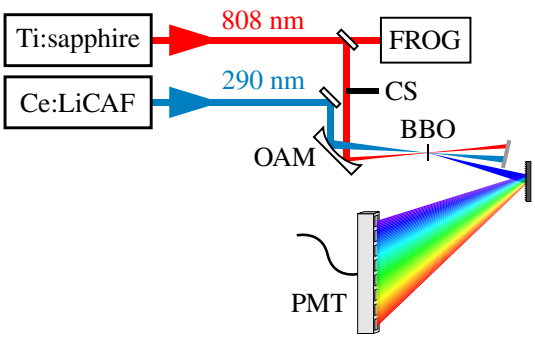

Figure 7.3: Schematic for split-beam asynchronous X-FROG. OAM: off-axis mirror; CS: microscope cover slip; PMT: photo-multiplier tube array.

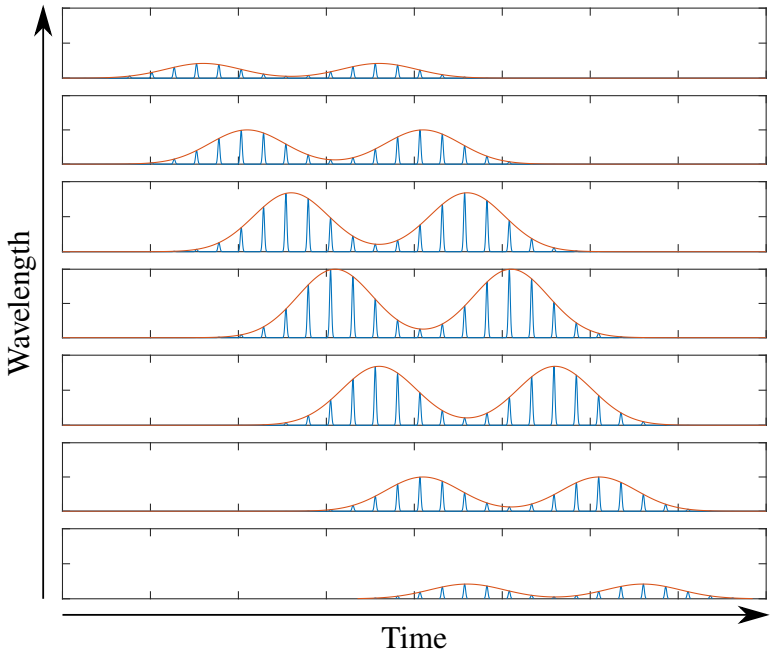

Figure 7.4: Split-beam asynchronous X-FROG trace using a PMT array.

Pump Laser System

The route to a standard X-FROG for phase retrieval of our Ce:LiCAF laser pulses is complex and has several challenging requirements before characterisation can even be performed. Synchronisation to the reference laser requires that the Ce:LiCAF laser is operated with high stability without the chopper in use. This task necessitates stabilisation of the pump power, and would also benefit from improved pointing angle stability; these are important improvements for our laser system, regardless of enabling high resolution phase retrieval from a standard X-FROG measurement. Although a viable pump laser is commercially available from Photonics Industries (266 nm, 3 W, 100 MHz) it would be possible to modify the current scheme to handle higher un-chopped powers. The simplest way to achieve this may be to change the focussing scheme within the BBO crystal. Swapping from a horizontal line focus to a vertical one has been shown to be more stable at high power [113], since it reduces the overlap between the input and generated beams, such that the generated 266 nm light quickly shifts away from the 532 nm pump to distribute heat accumulation as well as reduce two photon absorption that contributes to it. This was attempted simply by rotating the polarisation and BBO in our system by 90° resulting in a sufficient and stable power of 1.7 W during un-chopped operation; therefore this is the simplest viable option, requiring only modification of the cylindrical lenses to recollimate the beam for good mode-matching within the Ce:LiCAF crystal. An alternative approach is to switch to a different phase matching crystal, such as those that are described in chapter 3; however, this choice either reduces conversion efficiency or introduces additional challenges, such as increased hygroscopy. If pointing stability is still problematic, an active system could be added, composed of two

quadrant photodiodes to measure beam positioning, and two motorised mirrors that weakly transmit the beam to the photodiodes behind them.

Gain-switched Ce:LiCAF lasers are attractive because they are simple and the pump scheme (a Q-switched laser) can be relatively cheap and simple, compared to high-powered mode-locked lasers such as the pump laser used during the course of this thesis. Ideally, an electrically pumped diode laser would be used to pump any CW or CW mode-locked Ce:LiCAF laser. Diode laser action at a wavelength capable of pumping Ce:LiCAF has only recently been demonstrated for pulsed operation [133]. If these diodes advance significantly over the coming decade, to operate continuously at high powers, CW and CW mode-locked Ce:LiCAF lasers may no longer require a frequency quadrupled pump laser. This would reduce the cost of such a UV laser system immensely, making Ce:LiCAF an even more viable choice for UV generation. Indeed, the pulsed operation of the diode laser may allow them to be used in gain-switched Ce:LiCAF lasers, to reduce system cost and complexity. Since these diodes are still in development, this prospect remains a prospect. For now, a CW pump scheme composed of an OPO or multiple phase-matching crystals in a cascaded geometry could be implemented to potentially result in shorter pulses via KLM.

Laser Cavity Design

While the LiCAF host medium of our laser is robust, average powers of over 0.5 W for CW and mode-locked operation may be challenging. Although average powers of around 1 W have been demonstrated in gain-switched operation, the PRF was in the kHz range so the period between laser action was on the order of 100 µs. Deposited heat is therefore given significantly more time to diffuse; the crystal has more time to thermally recover. The pumped volume was also larger than in our Ce:LiCAF laser; thermal issues may be a significant hurdle to overcome in our system.

Power scaling of other colquiriite lasers, such as CW and mode-locked Cr-doped LiCAF lasers has become difficult due to the relatively poor thermal properties of the LiCAF host compared with, for example, YAG, Alexandrite, or Ti:sapphire [2]. In the 100 MHz range, the power of Cr:LiCAF is limited to about 1 W, with 0.75 W actually being achieved [239]. The prospect of thin-disk geometry is attractive for CW powers in excess of 10 W and has been suggested as the logical direction for Cr-doped colquiriite lasers as a way of alleviating thermal effects [240]. Since the thin disk cavity geometry is being considered as a solution to the thermal limitations of Cr-doped colquiriites such as Cr:LiCAF, it may also be the future path of mode-locked and CW Ce:LiCAF lasers, especially when pump power can be increased. A proposed cavity geometry for a mode-locked Ce:LiCAF laser is shown in figure 7.5 and indicates the crystal mounted onto a heat sink. The c-axis of the Ce:LiCAF crystal would need to be oriented in the tangential plane and perpendicular to the polarisation of 266 nm radiation, in order to minimise ESA. Although there are reflection losses introduced

because of the pump beam's angle of incidence, these are likely to be slightly less than the transmission losses (T = 91%) from an input coupling mirror. A Brewster's angle geometry is ideally avoided (although may be feasible) in order to ensure that the 266 and 290 nm radiation is as close as possible to being π polarised relative to the c-axis, in each direction of propagation (both arms of the cavity) thereby minimising ESA at 266 nm and maximising the gain cross section at 290 nm. To account for increased reflection losses at 290 nm from avoiding Brewster's angle, an AR coating would need to be applied to the front face of the crystal (with an HR coating on the back face). This is challenging in the UV, and exacerbated by high powers, but may be feasible with high transmission (>99%) and durability.

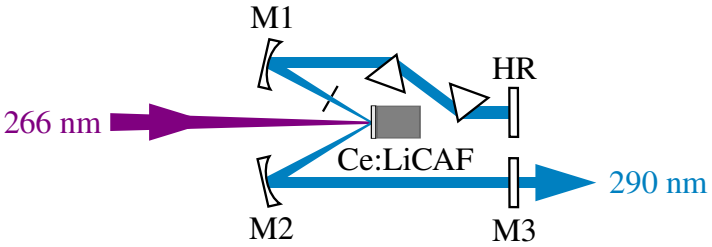

Figure 7.5: Thin disk arrangement of a symmetrical Ce:LiCAF cavity.

Higher Order Dispersion Compensation

To further reduce the minimum pulse duration of our hybrid-mode-locked Ce:LiCAF, higher orders of dispersion need to be compensated for inside the laser cavity. Two options for improving the dispersion management are as follows. Firstly, compensating the residual anomalous TOD and higher orders introduced by the prism pair arrangement could result in the desired shorter pulse durations, while retaining the flexibility of the prism pair for varying dispersion. A large amount of normal TOD would be necessary for this approach, on the order of +1000 fs^3. The second option is dispersion compensation using dispersive mirrors only, totalling approximately -700 fs^2 of GDD and -300 fs^3 TOD, as well as higher orders. In both cases, the design of dispersive mirrors require accurate modelling that takes into account every dispersive element for as many orders of dispersion as is reasonable. This can be measured by interferometric techniques to characterise the group delay of light over a broad bandwidth [241]. After the appropriate amount of dispersion is determined, the next logical step is to review the capabilities of the manufacturing methods that are currently available. The types of dispersive mirrors that may be used for dispersion compensation inside our Ce:LiCAF cavity are restricted due to losses, but we will discuss the most prospective two: chirped mirrors, and Gires-Tournois interferometer (GTI) type mirrors.

Chirped mirrors are fabricated using alternating layers of high and low refractive index material, depicted in figure 7.6. In the UV, hafnium dioxide (HfO_2) and silicon dioxide (SiO_2) are potential high and low refractive index coatings, respectively [242]. These are manufactured by electron beam sputtering and are likely still too lossy to use intra-cavity due

to imperfections, scattering and absorption. For example, 92% average reflectance has been achieved for the 290-350 nm region, providing a GDD of -75 fs^2 [87]. It is conceivable that targeting a narrower wavelength range (i.e. part of the 280-316 nm region) could result in a higher average refelectance, in excess of 95%. However, pairs of chirped mirrors are usually necessary, so that ripples in the GDD errors from each mirror partially cancel each other, which further increases loss.

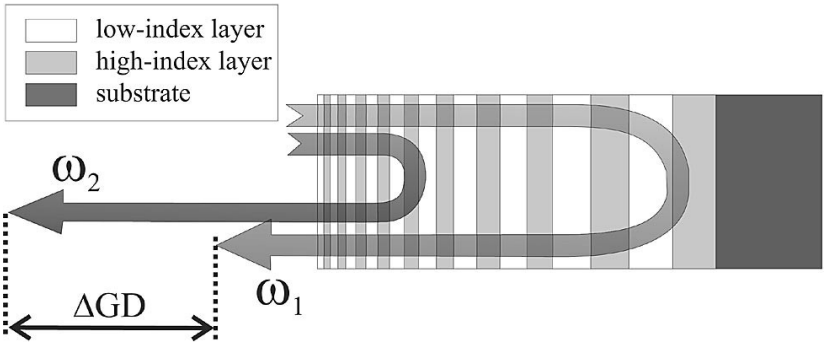

Figure 7.6: Chirped mirror design using alternating layers of low- and high-index dielectrica, from [243]. An anti-reflective coating may also be present on the surface.

Like chirped mirrors, GTI mirrors are composed of multiple layers, except there are fewer of them with much less variation in thickness compared with chirped mirrors. The layers comprise two sections; the surface section which has a low reflectance, and the back section which ideally has 100% reflectance (quarter-wave stack). These sections make up the interferometer type of arrangement. The reduced number of layers that comprise GTI mirrors result in a higher reflectance. They have also been demonstrated in the UV [244], for compressing a pulse between 266 and 271 nm to 30 fs. The mirrors were designed to have a GDD of -50 fs^2 and a reflectance of 99%. The disadvantage of these mirrors is the reduced control over higher orders of dispersion, and the limited spectral range that can be controlled; although increasing the amount of GDD that these mirrors can provide may reduce the required number of reflections to compensate for dispersion, this also reduces the range of reflectivity range.

Low losses are more challenging to achieve in the UV region, for all optical coatings, since short wavelength radiation is more prone to scattering. Although chirped mirrors may not yet exhibit low enough losses to be used within a Ce:LiCAF cavity, other optics such as lenses, prisms, and crystals may still benefit from the high transmission that AR-coatings provide. Recent developments in AR-coatings push peak transmission past 99.9% in the DUV by using ultrasmall silica nanoparticles [245]. Reducing the size of the nanoparticles that were used to dip-coat optics was found to be a crucial stage of preparing these types of AR-coatings for high transmission, while coating thickness was found to shift the peak wavelength; therefore coatings could be designed to have a peak transmission at 290 nm. Silica nanoparticle coatings have been shown to have a high damage threshold >100 J/cm^2

[246], so these coatings could be tailored for Ce:LiCAF and potentially implemented intracavity, possibly as part of dispersive mirrors.

In conclusion, a holistic approach to further development of mode-locked Ce:LiCAF lasers may be the best strategy. It may be necessary to implement the combination of improved pump systems, a thin disk cavity geometry, and the best available dispersion control elements. The thin disk geometry not only allows for higher powers, but can also reduce dispersion contributed by Ce:LiCAF, which alleviates the requirement of the dispersive elements, such as chirped mirrors. One option to reduce this further is to enclose the system in a vacuum (or use helium gas, which has approximately 3% of the dispersion of air at 290 nm) to remove the contribution from air. Both alterations may even reduce round-trip GDD to a level that is manageable using only a pair of chirped mirrors; the coating could even be applied to back face of the Ce:LiCAF crystal itself to reduce the number of reflections in the cavity (combined with a chirped output coupler). While a vacuum enclosure may create more issues than it solves, it is also practically essential for HHG; dispersion of attosecond pulses generated by HHG is far more severe. Since this is one of the primary prospects for applications of ultrafast Ce:LiCAF lasers, it should not be overlooked.

A

Publications Arising from this Thesis

Two posters were presented during the course of this thesis, the first is titled “Short UV Pulses: Cerium Lasers Adam Sharp” by David W. Coutts, and David J. Spence. The second was part of the Conference on Lasers and Electro-Optics Pacific Rim (CLEO-PR 2020), titled “Asynchronous Cross-Correlation Using a Time Reference”, matching the paper that was published for this conference. For the same conference, a conference paper was written and presented, titled “Femtosecond Ultraviolet Pulses Generated Directly From a Mode-Locked Ce:LiCAF Laser. The authors for both CLEO-PR publications were Adam Sharp, Ondrej Kitzler, Alex Fuerbach, David J. Spence, and David W. Coutts. Both articles were published as proceedings and are shown below.

Pages 154-155 of this thesis have been removed as they contain published material. Please refer to the following citation for details of the article contained in these pages.

Sharp, A., Kitzler, O., Fuerbach, A., Spence, D. J., & Coutts, D. W. (2020). Femtosecond ultraviolet pulses generated directly from a mode-locked Ce:LiCAF laser. In CLEO-PR 2020: 14th Pacific Rim Conference on Lasers and Electro-Optics [C7A_2] Institute of Electrical and Electronics Engineers (IEEE).

DOI: 10.1364/CLEOPR.2020.C7A_2

Pages 156-157 of this thesis have been removed as they contain published material. Please refer to the following citation for details of the article contained in these pages.

Sharp, A., Kitzler, O., Fuerbach, A., Spence, D. J., & Coutts, D. W. (2020). Asynchronous cross-correlation using a time reference. In CLEO-PR 2020: Proceedings of the 14th Pacific Rim Conference on Lasers and Electro-Optics [P1_20] OSA Publishing.

DOI: 10.1364/CLEOPR.2020.P1_20

B

Phase Matching Non-Linear Crystals

The phase matching angles that were determined during the course of this thesis were all calculated using SNLO nonlinear optics code, available from A. V. Smith, AS-Photonics, Alburquerque, NM.

Table B.1: The type 1 phase-matching parameters in LBO (T≈148 °C) for SHG of light from a Nd:YVO_4 laser, as generated by SNLO.

Parameter	1064 nm (o)	1064 nm (o)	532 nm (e)
Walkoff [mrad]	0.00	0.00	0.27
Phase velocities [c/]	1.605	1.605	1.605
Group velocities [c/]	1.626	1.626	1.639
GDD [fs^2/mm]	16.6	16.6	87.7
θ, ϕ [°]	90.0, 0.4		
d_{eff} [pm/V]	0.85		
Angle tolerance×L [mrad · cm]	123.94		
Temperature range×L [K · cm]	5.36		
Mix accep. angle×L [mrad · cm]	247.88	247.88	
Mix accep. bandwidth×L [GHz · cm]	2287.04	2287.04	

Table B.2: The type 1 phase-matching parameters in BBO (T≈90 °C) for FHG of light from a Nd:YVO_4 laser, as generated by SNLO.

Parameter	532 nm (o)	532 nm (o)	266 nm (e)
Walkoff [mrad]	0.00	0.00	85.01
Phase velocities [c/]	1.673	1.673	1.673
Group velocities [c/]	1.721	1.721	1.893
GDD [fs^2/mm]	136.0	136.0	429.0
θ [°]	47.8		
d_{eff} [pm/V]	1.75		
Angle tolerance×L [mrad · cm]	0.19		
Temperature range×L [K · cm]	6.00		
Mix accep. angle×L [mrad · cm]	0.37	0.37	
Mix accep. bandwidth×L [GHz · cm]	174.23	174.23	

Table B.3: The type 1 phase-matching parameters in BBO for SFG of light from Nd:YVO_4 and Ti:sapphire lasers, as generated by SNLO.

Parameter	1064 nm (o)	808 nm (o)	459.2 nm (e)
Walkoff [mrad]	0.00	0.00	61.24
Phase velocities [c/]	1.654	1.660	1.658
Group velocities [c/]	1.674	1.684	1.719
GDD [fs^2/mm]	44.0	73.9	158.6
θ [°]	25.5		
d_{eff} [pm/V]	2.02		
Angle tolerance×L [mrad · cm]	0.45		
Temperature range×L [K · cm]	28.77		
Mix accep. angle×L [mrad · cm]	1.05	0.79	
Mix accep. bandwidth×L [GHz · cm]	670.93	864.66	

Table B.4: The type 1 phase-matching parameters in BBO for SHG of Ti:sapphire, as generated by SNLO.

Parameter	808 nm (o)	808 nm (o)	404 nm (e)
Walkoff [mrad]	0.00	0.00	67.55
Phase velocities [c/]	1.660	1.660	1.660
Group velocities [c/]	1.684	1.684	1.740
GDD [fs^2/mm]	73.9	73.9	192.8
θ [°]	28.9		
d_{eff} [pm/V]	2.00		
Angle tolerance×L [mrad · cm]	0.36		
Temperature range×L [K · cm]	20.15		
Mix accep. angle×L [mrad · cm]	0.72	0.72	
Mix accep. bandwidth×L [GHz · cm]	531.11	531.11	

Table B.5: The type 1 phase-matching parameters in BBO for DFG between a Ti:sapphire laser and the fourth harmonic of a Nd:YVO_4 laser.

Parameter	808 nm (o)	396.5 nm (o)	266 nm (e)
Walkoff [mrad]	0.00	0.00	86.53
Phase velocities [c/]	1.660	1.694	1.683
Group velocities [c/]	1.684	1.785	1.908
GDD [fs^2/mm]	73.9	218.5	440.3
θ [°]	44.3		
d_{eff} [pm/V]	1.87		
Angle tolerance×L [mrad · cm]	0.18		
Temperature range×L [K · cm]	6.66		
Mix accep. angle×L [mrad · cm]	0.56	0.27	
Mix accep. bandwidth×L [GHz · cm]	133.96	244.56	

Table B.6: The type 1 phase-matching parameters in BBO for DFG between a Ti:sapphire laser and a Ce:LiCAF laser.

Parameter	808 nm (o)	452.4 nm (o)	290 nm (e)
Walkoff [mrad]	0.00	0.00	83.29
Phase velocities [c/]	1.660	1.683	1.675
Group velocities [c/]	1.684	1.751	1.853
GDD [fs^2/mm]	73.9	174.7	358.1
θ [°]	40.4		
d_{eff} [pm/V]	1.91		
Angle tolerance×L [mrad · cm]	0.21		
Temperature range×L [K · cm]	8.32		
Mix accep. angle×L [mrad · cm]	0.58	0.32	
Mix accep. bandwidth×L [GHz · cm]	177.50	293.54	

C

Curve Fitting Script

```
%%%%%%%%%%%%%%%%%%%%%%%%%%%%%%%%%%%%%%%%%%%%%%%%%%%%%%%%%%%%%%%%%%%%%%%%%%%%
% This script processes an asynchronous cross-correlation for retreiving
% the pulse duration of the probe pulse, accounting for pump pulse
% duration when there is a small optical delay in half the probe beam
%%%%%%%%%%%%%%%%%%%%%%%%%%%%%%%%%%%%%%%%%%%%%%%%%%%%%%%%%%%%%%%%%%%%%%%%%%%%

% STEP 1 - IMPORT
% The data are imported as either a single file OR a folder of
% sequentially numbered files to be plotted in 3D.

% STEP 2 - SMOOTHING
% An envelope of the pulses is recorded as a new data set which should
% look like two offset Gaussian curves, roughly equal
% The background is also subtracted, and the timescale is centered.

% STEP 3 - FITTING
% Two Gaussian curves are fitted to the smoothed data. The separation and
% FWHM of the two curves are recored: optical delay and pulse duration

% STEP 4 - TEMPORAL CORRECTION
% The optical delay (entered manually) is used to correct the timescale
% and retreive the real FWHM of both pulses (which should be similar)
```

```
%%%%%%%%%%%%%%%%%%%%%%%%%%%%%%%%%%%%%%%%%%%%%%%%%%%%%%%%%%%%%%%%%%%%%%%%%%%%
%% PARAMETERS

% Laser repetition rate
freq = 78000000;

% Reference pulse duration in fs
reference = 75e-15;

% Optical delay
%delay = 260e-15;    % type 1 cover slip
%delay = 335e-15;    % type 2 cover slip
%delay = 950e-15;    % type 4 cover slip
delay = 1035e-15;    % type 4 cover slip at external angle 8 degrees

% Raw data Smoothing: higher = more, lower = less
smooth_factor = 20;

% Import and process data? (temporal correction, data removal)
import_data = true;

% Single parse = false, additive parse = true
add_data = true;

% Plot data?
plot_data = false;

% Export data?

%%%%%%%%%%%%%%%%%%%%%%%%%%%%%%%%%%%%%%%%%%%%%%%%%%%%%%%%%%%%%%%%%%%%%%%%%%%%
%% IMPORT

if import_data==true

% Choose files
[file, path] = uigetfile('.txt', 'Multiselect', 'on');
files_cell = strcat(path, file);

% Create delay list
delay_list = delay * ones(length(files_cell),1);

% Create empty fit list
fit_list = cell(length(files_cell),1);

% Create empty arrays for pulse duration and beat frequency
tau_1 = zeros(length(fit_list),1);
tau_2 = zeros(length(fit_list),1);
```

```
del_f = zeros(length(fit_list),1);

% A for loop version of "cross_correlation_satellite.m"
for i = 1:length(files_cell)

% Import individual file into a matrix
raw_import = readmatrix(files_cell{i});

% Remove headers
raw = raw_import(3:end, 1:2);

%%%%%%%%%%%%%%%%%%%%%%%%%%%%%%%%%%%%%%%%%%%%%%%%%%%%%%%%%%%%%%%%%%%%%%%%%%%%%%%
%% SMOOTHING

% Envelope of data
[env, env_low] = envelope(raw, smooth_factor, 'peak');

% Background Subtraction
raw(:,2) = raw(:,2) - mean(env(:,2));
env(:,2) = env(:,2) - mean(env(:,2));

%%%%%%%%%%%%%%%%%%%%%%%%%%%%%%%%%%%%%%%%%%%%%%%%%%%%%%%%%%%%%%%%%%%%%%%%%%%%%%%
%% FITTING

% Timescale as viewed on oscilloscope
time = env(:,1);
ampl = env(:,2);

% Find all the peaks (only need 2)
[pks,locs]=findpeaks(ampl);

% Find maximum peak
[max1, loc1] = max(pks);
time1 = time(locs(loc1));

% 'Remove' peak
pks(loc1) = -Inf;

% Find second maxima peak
[max2, loc2] = max(pks);
time2 = time(locs(loc2));

% Double Gaussian fit, if statement for chronology
if time1<time2
    [f,gof] = fit(time, ampl, 'gauss2', 'Lower', [0,-Inf,0,0,-Inf,0], ...
    'StartPoint', [max1, time1, 4e-8, max2, time2, 4e-8]);
else
```

```
    [f,gof] = fit(time, ampl, 'gauss2', 'Lower', [0,-Inf,0,0,-Inf,0], ...
    'StartPoint', [max2, time2, 4e-8, max1, time1, 4e-8]);
end

% Save fit to array
fit_list{i} = f;

%%%%%%%%%%%%%%%%%%%%%%%%%%%%%%%%%%%%%%%%%%%%%%%%%%%%%%%%%%%%%%%%%%%%%%%%%%%%
%% TEMPORAL CORRECTION

% Calculate magnification
t_scale = delay/abs(f.b1-f.b2);

% Calculate deconvolved pulse durations FWHM
fwhm_1 = t_scale * (f.c1 * 2 * sqrt(log(2)));    % Convolved FWHM 1
fwhm_2 = t_scale * (f.c2 * 2 * sqrt(log(2)));    % Convolved FWHM 2
tau_1(i) = sqrt(fwhm_1^2 - reference^2);         % Deconvolved FWHM 1
tau_2(i) = sqrt(fwhm_2^2 - reference^2);         % Deconvolved FWHM 2

% Calculate beat frequency
del_f(i) = delay * freq / abs(f.b2-f.b1);

end

% Calculate deconvolved pulse durations FWHM mean
tau_m = (tau_1 + tau_2)/2;

%%%%%%%%%%%%%%%%%%%%%%%%%%%%%%%%%%%%%%%%%%%%%%%%%%%%%%%%%%%%%%%%%%%%%%%%%%%%
%% DATA REMOVAL

% Remove complex results (failed fit)
real_boolean = zeros(length(tau_m), 1);
real_index = [];
for i = 1:length(tau_m)
    real_boolean(i, 1) = isreal(tau_m(i, 1));
    if real_boolean(i, 1)==0
        real_index = [real_index;i];
    end
end
tau_1 = nonzeros(tau_1.*real_boolean);
tau_2 = nonzeros(tau_2.*real_boolean);
tau_m = nonzeros(tau_m.*real_boolean);
del_f = nonzeros(del_f.*real_boolean);
fit_list(real_index) = [];
delay_list(real_index) = [];
files_cell(real_index) = [];
```

```
% Remove extreme outliers via beat frequency (max 3 standard devs away)
for k = 1:3
max_del_f = median(del_f) + 3*std(del_f);
outlier_boolean = zeros(length(tau_m), 1);
outlier_index = [];
for i = 1:length(del_f)
    outlier_boolean(i, 1) = del_f(i, 1) < max_del_f;
    if outlier_boolean(i, 1)==0
        outlier_index = [outlier_index;i];
    end
end
tau_1 = nonzeros(tau_1.*outlier_boolean);
tau_2 = nonzeros(tau_2.*outlier_boolean);
tau_m = nonzeros(tau_m.*outlier_boolean);
del_f = nonzeros(del_f.*outlier_boolean);
fit_list(outlier_index) = [];
delay_list(outlier_index) = [];
files_cell(outlier_index) = [];
end


end

%%%%%%%%%%%%%%%%%%%%%%%%%%%%%%%%%%%%%%%%%%%%%%%%%%%%%%%%%%%%%%%%%%%%%%%%%%%%%%%
%% ADDITIVE PARSE

% Adds data to current list, or doesn't
if add_data==true
    all_tau_1 = [all_tau_1; tau_1];
    all_tau_2 = [all_tau_2; tau_2];
    all_tau_m = [all_tau_m; tau_m];
    all_del_f = [all_del_f; del_f];
    all_fit_list = [all_fit_list; fit_list];
    all_delay_list = [all_delay_list; delay_list];
    all_files_cell = [all_files_cell, files_cell];
else
    all_tau_1 = tau_1;
    all_tau_2 = tau_2;
    all_tau_m = tau_m;
    all_del_f = del_f;
    all_fit_list = fit_list;
    all_delay_list = delay_list;
    all_files_cell = files_cell;
end

%%%%%%%%%%%%%%%%%%%%%%%%%%%%%%%%%%%%%%%%%%%%%%%%%%%%%%%%%%%%%%%%%%%%%%%%%%%%%%%
%% PLOT HISTOGRAM
```

```
if plot_data==true

stat_mean = mean(all_tau_m);

tiledlayout(1, 2, 'Padding', 'compact')
nexttile

hold on
histfit(all_tau_m * 1e15)

xlabel('Pulse Duration [fs]')
ylabel('Counts')

hold off

%%%%%%%%%%%%%%%%%%%%%%%%%%%%%%%%%%%%%%%%%%%%%%%%%%%%%%%%%%%%%%%%%%%%%%%%%%%%
%% PLOT tau_1 vs tau_2 vs del_f (colour)

nexttile

hold on
scatter(all_tau_1 * 1e15, all_tau_2 * 1e15, 30, all_del_f, 'filled')

xlim([0 200])
ylim([0 200])

xlabel('First Pulse Duration [fs]')
ylabel('Second Pulse Duration [fs]')

colormap(jet)
cb = colorbar('eastoutside');
cb.Label.String = 'Beat Frequency [Hz]';

box on

hold off


end
```

List of Figures

List of Tables

List of Symbols and Abbreviations

α . . . . . angle

α_L . . . . . absorption coefficient

α_{UV} . . . . . absorption coefficient

β . . . . . angle

θ . . . . . angle

λ . . . . . wavelength

λ_{L} . . . . . driving laser wavelength

$\Delta\nu$ . . . . . laser cavity mode spacing

ρ . . . . . walk-off angle

τ_p . . . . . pulse duration

$\Delta\tau$ . . . . . time delay

$\chi^{(2)}$ . . . . . second-order non-linear susceptibility

$\chi^{(3)}$ . . . . . third-order non-linear susceptibility

Ψ . . . . . optical phase

ω . . . . . angular frequency

A . . . . . amplitude

b . . . . . curve-fitting coefficient

c . . . . . speed of light

d . . . . . distance

$\mathrm{d_{eff}}$ . . . . . non-linear coefficient

df . . . . . modulation frequency detuning

E_c . . . . . photon energy

f . . . . . focal length

f_0 . . . . . base pulse repetition frequency (≈78.6 MHz)

Δf . . . . . beat frequency

I . . . . . optical intensity

I_{L} . . . . . driving laser intensity

I_{p} . . . . . atomic ionisation potential

k . . . . . angular wavenumber

L . . . . . distance

L_c . . . . . crystal thickness

$\mathrm{L_g}$ . . . . . distance

L_{OPC} . . . . . output coupler transmission

L_t . . . . . round-trip loss

L_Δ . . . . . double-pass prism loss

n . . . . . refractive index

n_2 . . . . . non-linear refractive index

Δn . . . . . change in refractive index

Δn_g . . . . . difference in group refractive index

M . . . . . modulation strength

N . . . . . number of laser cavity modes

q . . . . . complex beam parameter

R . . . . . radius of curvature

s . . . . . distance

t . . . . . time; distance (prism theory)

Δt . . . . . time delay

U_p . . . . . average quiver energy/ponderomotive energy

v_g . . . . . group velocity

w . . . . . Gaussian beam waist size (radius)

Δx . . . . . path length difference

z . . . . . propagation distance

ADP . . . . . $(NH_4)H_2PO_4$ - ammonium dihydrogen phosphate

AP . . . . . aperture

AR . . . . . anti-reflection

ASM . . . . . asynchronous mode-locking

ATF . . . . . Advanced Thin Films

BBO . . . . . β-BaB_2O_4 - beta barium borate

BS . . . . . beam splitter

CC . . . . . colour centre

CCD . . . . . charge-coupled device

Ce:LAF . . . . . Ce^{3+}:LaF_3 - cerium doped lanthanum fluoride

Ce:LiCAF . . . Ce^{3+}:$LiCaAlF_6$ - cerium doped lithium calcium aluminium fluoride

Ce:LiSAF . . . Ce^{3+}:$LiSrAlF_6$ - cerium doped lithium strontium aluminium fluoride

Ce:LiSCAF . . Ce^{3+}:$LiSrAlF_6$ - cerium doped lithium strontium calcium aluminium fluoride

Ce:LiLuF . . . Ce^{3+}:$LiLuF_4$ - cerium doped lithium lutetium fluoride

Ce:YAG . . . . . Ce^{3+}:$Y_3Al_5O_{12}$ - cerium doped yttrium aluminium garnet

Ce:YLF . . . . . Ce^{3+}:$YLiF_4$ - cerium doped yttrium lithium fluoride

CLBO . . . . . $CsLiB_6O_10$ - cesium lithium borate

Cr:YAG . . . . . Cr^{4+}:$Y_3Al_5O_{12}$ - chromium doped ytterium aluminium garnet

CS . . . . . microscope cover slip

CVL . . . . . copper vapour laser

CW . . . . . continuous wave

CYL . . . . . cylindrical lens

DFG . . . . . difference frequency generation

DFM . . . . . difference frequency mixing

DKDP . . . . . KD_2PO_4 - deuterated potassium dihydrogen phosphate

DM . . . . . dichroic mirror

DNA . . . . . deoxyribonucleic acid

DPSS . . . . . diode-pumped solid-state

DUV . . . . . deep ultraviolet

ESA . . . . . excited state absorption

FROG . . . . . frequency resolved optical gating

FS . . . . . fused silica

FWHM . . . . . full width at half maximum

GDD . . . . . group delay dispersion

GTI . . . . . Gires-Tournois interferometer

GVD . . . . . group velocity dispersion

HHG . . . . . high harmonic generation

HR . . . . . high reflectance

HWP . . . . . half-wave plate

IR . . . . . infrared

KABO . . . . . $K_2Al_2B_2O_7$ - potassium aluminium borate

KBBF . . . . . $KBe_2BO_3F_2$ - potassium fluoroboratoberyllate

KDP . . . . . KH_2PO_4 - potassium dihydrogen phosphate

KLM . . . . . Kerr-lens mode-locking/Kerr-lens mode-locked

LBO . . . . . LiB_3O_5 - lithium triborate

M . . . . . mirror

MOPA . . . . . master oscillator power amplifier

Nd:YAG . . . . Nd^{3+}:$Y_3Al_5O_{12}$ - neodymium doped ytterium aluminium garnet

Nd:YVO_4 . . . Nd^{3+}:YVO_4 - neodymium doped yttrium orthonovanadate

NIR. . . . . near infra-red

NOPA . . . . . non-collinear optical parametric amplifier

NSBBF . . . . . $NaSr_3Be_3B_3O_9F_4$ - fluorine strontium boroberyllate sodium

OAM . . . . . off-axis mirror

OFC . . . . . optical frequency comb

OC . . . . . output coupler

OPC . . . . . output coupler

OPO . . . . . optical parametric oscillator

PCF . . . . . photonic crystal fibre

PD. . . . . photodiode

PG-FROG . . . polarisation-gated frequency resolved optical gating

PID . . . . . proportional integral derivative (controller)

PMT . . . . . photo-multiplier tube

POL . . . . . thin-film polariser

PRF . . . . . pulse repetition frequency

Q. . . . . quality factor

RBBF. . . . . $RbBe_2BO_3F_2$ - rubidium fluoroberyllium borate

RNA. . . . . ribonucleic acid

ROC . . . . . radius of curvature

SESAM . . . . . semi-conductor saturable absorber mirror

SFG . . . . . sum frequency generation

SFM . . . . . sum frequency mixing

SHG . . . . . second harmonic generation

SLM . . . . . single longitudinal mode

SPIDER . . . . . spectral phase interferometry for direct electric field reconstruction

SPM . . . . . self-phase modulation

TIR . . . . . total internal reflection

Ti:sapphire . . $Ti^{3+}:Al_2O_3$ - titanium doped sapphire

TPA . . . . . two photon absorption

TOD . . . . . third-order dispersion

TOGVD . . . . . third-order group velocity dispersion

UV . . . . . ultraviolet

UV . . . . . ultraviolet-grade fused silica

VUV . . . . . vacuum ultraviolet

X-FROG . . . . cross-correlation frequency resolved optical gating

XUV . . . . . extreme ultraviolet

References

[1] T. H. Maiman. *Stimulated optical radiation in ruby*. Nature **187**(4736), 493 (1960).

[2] U. Demirbas. *Cr:colquiriite lasers: Current status and challenges for further progress*. Progress in Quantum Electronics **68**(100227) (2019).

[3] S. Ono, Y. Suzuki, T. Kozeki, H. Murakami, H. Ohtake, N. Sarukura, H. Sato, S. Machida, K. Shimamura, and T. Fukuda. *High-energy, all-solid-state, ultraviolet laser power-amplifier module design and its output-energy scaling principle*. Applied Optics **41**(36), 7556 (2002).

[4] B. Wellmann. *Mode-locked pumped continuous wave Ce:LiCAF lasers*. Macquarie University, Faculty of Science, Department of Physics and Astronomy (2016).

[5] J. Cheng, C. S. Liu, S. Shang, D. Liu, W. Perrie, G. Dearden, and K. Watkins. *A review of ultrafast laser materials micromachining*. Optics and Laser Technology **46**, 88 (2013).

[6] X. Liu, D. Du, and G. Mourou. *Laser ablation and micromachining with ultrashort laser pulses*. IEEE Journal of Quantum Electronics **33**(10), 1706 (1997).

[7] K. C. Phillips, H. H. Gandhi, E. Mazur, and S. K. Sundaram. *Ultrafast laser processing of materials: A review*. Advances in Optics and Photonics **7**(4), 684 (2015).

[8] C.-M. Inc. *Machining with long pulse lasers* (2011). URL http://www.cmxr.com/Education/Long.html.

[9] C.-M. Inc. *Machining with ultrafast pulses* (2011). URL http://www.cmxr.com/Education/Short.html.

[10] C. Kerse, H. Kalaycioglu, P. Elahi, B. Cetin, D. K. Kesim, O. Akcaalan, S. Yavas, M. D. Asik, B. Oktem, H. Hoogland, R. Holzwarth, and F. O. Ilday. *Ablation-cooled material removal with ultrafast bursts of pulses*. Nature **537**(7618), 84 (2016).

[11] D. Von Der Linde and K. Sokolowski-Tinten. *Physical mechanisms of short-pulse laser ablation*. The Symposium A on Photo-Excited Processes, Diagnostics and Applications of the 1999 E-MRS Spring Conference (ICPEPA-3) **154**, 1 (2000).

[12] B. Wellmann, D. J. Spence, and D. W. Coutts. *Dynamics of solid-state lasers pumped by mode-locked lasers*. Optics Express (2015).

[13] K. M. Davis, K. Miura, N. Sugimoto, and K. Hirao. *Writing waveguides in glass with a femtosecond laser*. Optics Letters **21**(21), 1729 (1996).

[14] R. Gattass and E. Mazur. *Femtosecond laser micromachining in transparent materials*. Nature Photonics **2**(4), 219 (2008).

[15] V. De Michele, M. Royon, E. Marin, A. Alessi, G. Zhang, G. Cheng, R. Stoian, M. Cannas, and Y. Ouerdane. *Laser wavelength effects on the refractive index change of waveguides written by femtosecond pulses in silica glasses*. In *Bragg Gratings, Photosensitivity and Poling in Glass Waveguides and Materials, BGPPM 2018*, vol. Part F98-BGPPM 2018 (OSA - The Optical Society, 2018).

[16] V. D. Michele, M. Royon, E. Marin, A. Alessi, A. Morana, A. Boukenter, M. Cannas, S. Girard, and Y. Ouerdane. *Near-IR- and UV-femtosecond laser waveguide inscription in silica glasses*. Optical Materials Express **9**(12), 4624 (2019).

[17] T. Kobayashi and Y. Kida. *Ultrafast spectroscopy with sub-10 fs deep-ultraviolet pulses*. Physical Chemistry Chemical Physics **14**(18), 6200 (2012).

[18] B. Xue, A. Yabushita, and T. Kobayashi. *Ultrafast dynamics of uracil and thymine studied using a sub-10 fs deep ultraviolet laser*. Physical Chemistry Chemical Physics **18**(25), 17044 (2016).

[19] T. Kobayashi, A. Yabushita, and Y. Kida. *Development of sub 10 fs visible-NIR, UV, and DUV pulses and their applications to ultrafast spectroscopy*. Photonics **3**(4), 15 (2016).

[20] S. H. Shi and H. Rabitz. *Quantum-mechanical optimal-control of physical observables in microsystems*. Journal of Chemical Physics **92**(1), 364 (1990).

[21] E. D. Potter, J. L. Herek, S. Pedersen, Q. Liu, and A. H. Zewail. *Femtosecond laser control of a chemical-reaction*. Nature **355**(6355), 66 (1992).

[22] R. S. Judson and H. Rabitz. *Teaching lasers to control molecules*. Physical Review Letters **68**(10), 1500 (1992).

[23] C. Brif, R. Chakrabarti, and H. Rabitz. *Control of quantum phenomena: Past, present and future*. New Journal of Physics **12** (2010).

[24] A. Assion, T. Baumert, M. Bergt, T. Brixner, B. Kiefer, V. Seyfried, M. Strehle, and G. Gerber. *Control of chemical reactions by feedback-optimized phase-shaped femtosecond laser pulses*. Science **282**(5390), 919 (1998).

[25] A. M. Weiner. *Femtosecond pulse shaping using spatial light modulators*. Review of Scientific Instruments **71**(5), 1929 (2000).

[26] R. Junjuri and M. K. Gundawar. *Femtosecond laser-induced breakdown spectroscopy studies for the identification of plastics*. Journal of Analytical Atomic Spectrometry **34**(8), 1683 (2019).

[27] T. M. Fortier, M. S. Kirchner, F. Quinlan, J. Taylor, J. C. Bergquist, T. Rosenband, N. Lemke, A. Ludlow, Y. Jiang, C. W. Oates, and S. A. Diddams. *Generation of ultrastable microwaves via optical frequency division*. Nature Photonics **5**(7), 425 (2011).

[28] C. Gohle, T. Udem, M. Herrmann, J. Rauschenberger, R. Holzwarth, H. A. Schuessler, F. Krausz, and T. W. Hänsen. *A frequency comb in the extreme ultraviolet*. Nature **436**(7048), 234 (2005).

[29] T. Fortier and E. Baumann. *20 years of developments in optical frequency comb technology and applications*. Communications Physics **2**(1), 153 (2019).

[30] T. Kanai, E. J. Takahashi, Y. Nabekawa, and K. Midorikawa. *Observing molecular structures by using high-order harmonic generation in mixed gases*. Physical Review A **77**(4), 4 (2008).

[31] R. A. Ganeev. *Harmonic generation in laser-produced plasmas containing atoms, ions and clusters: A review*. Journal of Modern Optics **59**(5), 409 (2012).

[32] R. A. Ganeev. *High-order harmonic generation in laser surface ablation: Current trends*. Physics-Uspekhi **56**(8), 772 (2013).

[33] J. Hecht. *High harmonic generation pushes spectroscopy to the cutting edge*. Laser Focus World **48**(2), 44 (2012).

[34] J. F. Ward and G. H. C. New. *Optical third harmonic generation in gases by a focused laser beam*. Physical Review **185**(1), 57 (1969).

[35] J. Bokor, P. H. Bucksbaum, and R. R. Freeman. *Generation of 35.5-nm coherent radiation*. Optics Letters **8**(4), 217 (1983).

[36] A. Mc Pherson, G. Gibson, H. Jara, U. Johann, T. S. Luk, I. A. Mc Intyre, K. Boyer, and C. K. Rhodes. *Studies of multiphoton production of vacuum-ultraviolet radiation*

in the rare gases. Journal of the Optical Society of America B: Optical Physics **4**(4), 595 (1987).

[37] J. L. Krause, K. J. Schafer, and K. C. Kulander. *High-order harmonic generation from atoms and ions in the high intensity regime*. Physical Review Letters **68**(24), 3535 (1992).

[38] P. Antoine, A. Lhuillier, and M. Lewenstein. *Attosecond pulse trains using high-order harmonics*. Physical Review Letters **77**(7), 1234 (1996).

[39] I. P. Christov, J. Zhou, J. Peatross, A. Rundquist, M. M. Murnane, and H. C. Kapteyn. *Nonadiabatic effects in high-harmonic generation with ultrashort pulses*. Physical Review Letters **77**(9), 1743 (1996).

[40] I. P. Christov, M. M. Murnane, and H. C. Kapteyn. *High-harmonic generation of attosecond pulses in the "single-cycle" regime*. Physical Review Letters **78**(7), 1251 (1997).

[41] H. S. Chakraborty, M. B. Gaarde, and A. Couairon. *Single attosecond pulses from high harmonics driven by self-compressed filaments*. Optics Letters **31**(24), 3662 (2006).

[42] S. Kim, J. H. Jin, Y. J. Kim, I. Y. Park, Y. Kim, and S. W. Kim. *High-harmonic generation by resonant plasmon field enhancement*. Nature **453**(7196), 757 (2008).

[43] A. D. Shiner, C. Trallero-Herrero, N. Kajumba, H. C. Bandulet, D. Comtois, F. Legare, M. Giguere, J. C. Kieffer, P. B. Corkum, and D. M. Villeneuve. *Wavelength scaling of high harmonic generation efficiency*. Physical Review Letters **103**(7), 4 (2009).

[44] M. Lewenstein, P. Balcou, M. Y. Ivanov, A. L'Huillier, and P. B. Corkum. *Theory of high-harmonic generation by low-frequency laser fields*. Physical Review A **49**(3), 2117 (1994).

[45] D. Popmintchev, C. Hernández-García, F. Dollar, C. Mancuso, J. A. Pérez-Hernández, M. C. Chen, A. Hankla, X. Gao, B. Shim, A. L. Gaeta, M. Tarazkar, D. A. Romanov, R. J. Levis, J. A. Gaffney, M. Foord, S. B. Libby, A. Jaron-Becker, A. Becker, L. Plaja, M. M. Murnane, H. C. Kapteyn, and T. Popmintchev. *Ultraviolet surprise: Efficient soft X-ray high-harmonic generation in multiply ionized plasmas*. Science **350**(6265), 1225 (2015).

[46] C. Bourassin-Bouchet, S. De Rossi, J. Wang, E. Meltchakov, A. Giglia, N. Mahne, S. Nannarone, and F. Delmotte. *Shaping of single-cycle sub-50-attosecond pulses with multilayer mirrors*. New Journal of Physics **14** (2012).

[47] Z. Diveki, C. Bourassin-Bouchet, S. De Rossi, E. English, E. Meltchakov, O. Gobert, D. Guénot, B. Carré, P. Salières, T. Ruchon, and F. Delmotte. *Theoretical and experimental studies of broadband phase-controlled attosecond mirrors*. Journal of Modern Optics **61**(2), 122 (2014).

[48] F. Frassetto, P. Miotti, and L. Poletto. *Compression of extreme-ultraviolet ultrashort pulses by grating configurations*. Journal of Spectroscopy **2015** (2015).

[49] M. Mero, F. Frassetto, P. Villoresi, L. Poletto, and K. Varjú. *Compression methods for XUV attosecond pulses*. Optics Express **19**(23), 23420 (2011).

[50] H. Igarashi, A. Makida, M. Ito, and T. Sekikawa. *Pulse compression of phase-matched high harmonic pulses from a time-delay compensated monochromator*. Optics Express **20**(4), 3725 (2012).

[51] L. Poletto, F. Frassetto, and P. Villoresi. *Attosecond pulse compression in the extreme ultraviolet region by conical diffraction*. In *Conference on Lasers and Electro-Optics, CLEO 2007* (Optical Society of America, 2007).

[52] L. Young, K. Ueda, M. Gühr, P. H. Bucksbaum, M. Simon, S. Mukamel, N. Rohringer, K. C. Prince, C. Masciovecchio, M. Meyer, A. Rudenko, D. Rolles, C. Bostedt, M. Fuchs, D. A. Reis, R. Santra, H. Kapteyn, M. Murnane, H. Ibrahim, F. Légaré, M. Vrakking, M. Isinger, D. Kroon, M. Gisselbrecht, A. L'Huillier, H. J. Wörner, and S. R. Leone. *Roadmap of ultrafast X-ray atomic and molecular physics*. Journal of Physics B: Atomic, Molecular and Optical Physics **51**(3) (2018).

[53] W. G. Wagner and B. A. Lengyel. *Evolution of the giant pulse in a laser*. Journal of Applied Physics **34**(7), 2040 (1963).

[54] F. J. McClung and R. W. Hellwarth. *Giant optical pulsations from ruby*. Journal of Applied Physics **33**(3), 828 (1962).

[55] A. C. Butler, D. J. Spence, and D. W. Coutts. *Scaling Q-switched microchip lasers for shortest pulses*. Applied Physics B **109**(1), 81 (2012).

[56] A. Siegman. *Lasers* (University Science Books, 1986).

[57] R. W. Diels J. *Ultrashort Laser Pulse Phenomena 2nd Edition* (Academic Press, 2006).

[58] U. Keller. *Recent developments in compact ultrafast lasers*. Nature **424**(6950), 831 (2003).

[59] C. V. Shank and E. P. Ippen. *Subpicosecond kilowatt pulses from a mode-locked CW dye laser*. Applied Physics Letters **24**(8), 373 (1974).

[60] A. J. De Maria, D. A. Stetser, and H. Heynau. *Self mode-locking of lasers with saturable absorbers*. Applied Physics Letters **8**(7), 174 (1966).

[61] H. A. Haus. *Theory of mode locking with a fast saturable absorber*. Journal of Applied Physics **46**(7), 3049 (1975).

[62] H. A. Haus. *Theory of mode locking with a slow saturable absorber*. IEEE Journal of Quantum Electronics **11**(9), 736 (1975).

[63] U. Keller, K. J. Weingarten, F. X. Kärtner, D. Kopf, B. Braun, I. D. Jung, R. Fluck, C. Hönninger, N. Matuschek, and J. Aus Der Au. *Semiconductor saturable absorber mirrors (SESAM's) for femtosecond to nanosecond pulse generation in solid-state lasers*. IEEE Journal on Selected Topics in Quantum Electronics **2**(3), 435 (1996).

[64] J. C. Comly, A. Yariv, and E. M. Garmire. *Stable, chirped, ultrashort pulses in lasers using the optical Kerr effect*. Applied Physics Letters **15**(5), 148 (1969).

[65] D. E. Spence, P. N. Kean, and W. Sibbett. *60-fsec pulse generation from a self-mode-locked Ti:sapphire laser*. Optics Letters **16**(1), 42 (1991).

[66] U. Keller, G. W. ̀tHooft, W. H. Knox, and J. E. Cunningham. *Femtosecond pulses from a continuously self-starting passively mode-locked Ti:sapphire laser*. Optics Letters **16**(13), 1022 (1991).

[67] F. Salin, M. Piché, and J. Squier. *Mode locking of Ti:Al_2O_3 lasers and self-focusing: A Gaussian approximation*. Optics Letters **16**(21), 1674 (1991).

[68] J. Squier, F. Salin, G. Mourou, and D. Harter. *100-fs pulse generation and amplification in Ti:Al_2O_3*. Optics Letters **16**(5), 324 (1991).

[69] C. K. Chan and S. O. Sari. *Tunable dye laser pulse converter for production of picosecond pulses*. Applied Physics Letters **25**(7), 403 (1974).

[70] J. Herrmann and U. Motschmann. *Theory of the synchronously pumped picosecond dye-laser*. Applied Physics B-Photophysics and Laser Chemistry **27**(1), 27 (1982).

[71] H. Kobayashi, S. Tanaka, A. Watanabe, T. Kuwata, H. Tabuchi, and M. Ueoka. *Tunable near-infrared picosecond pulses from a mode-locked dye laser synchronously pumped by second harmonic of a Nd:YAG laser*. Japanese Journal of Applied Physics **23**(1), 40 (1984).

[72] C. W. Siders, E. W. Gaul, M. C. Downer, A. Babine, and A. Stepanov. *Self-starting femtosecond pulse generation from a Ti:sapphire laser synchronously pumped by a pointing-stabilized mode-locked Nd:YAG laser*. Review of Scientific Instruments **65**(10), 3140 (1994).

[73] U. Morgner and F. Mitschke. *Drift instabilities in the pulses from CW mode-locked lasers*. Physical Review E - Statistical Physics, Plasmas, Fluids, and Related Interdisciplinary Topics **58**(1), 187 (1998).

[74] J. Chesnoy and L. Fini. *Stabilization of a femtosecond dye laser synchronously pumped by a frequency-doubled mode-locked YAG laser*. Optics Letters **11**(10), 635 (1986).

[75] M. D. Dawson, D. Maxson, T. F. Boggess, and A. L. Smirl. *Cavity-length detuning effects and stabilization of a synchronously pumped femtosecond linear dye laser*. Optics Letters **13**(2), 126 (1988).

[76] D. S. Butterworth, S. Girard, and D. C. Hanna. *A simple technique to achieve active cavity-length stabilisation in a synchronously pumped optical parametric oscillator*. Optics Communications **123**(4-6), 577 (1996).

[77] P. Beaud, J. Q. Bi, W. Hodel, and H. P. Weber. *Experimental observation of the self-stabilization of a synchronously pumped dye laser*. Optics Communications **80**(1), 31 (1990).

[78] G. H. C. New. *Self-stabilization of synchronously mode-locked lasers*. Optics Letters **15**(22), 1306 (1990).

[79] D. S. Peter, P. Beaud, W. Hodel, and H. P. Weber. *Passive stabilization of a synchronously pumped mode-locked dye laser with the use of a modified outcoupling mirror*. Optics Letters **16**(6), 405 (1991).

[80] C. Spielmann, F. Krausz, T. Brabec, E. Wintner, and A. J. Schmidt. *Femtosecond pulse generation from a synchronously pumped Ti-sapphire laser*. Optics Letters **16**(15), 1180 (1991).

[81] S. Y. Wu, W. W. Hsiang, and Y. Lai. *Synchronous-asynchronous laser mode-locking transition*. Physical Review A **92**(1), 8 (2015).

[82] U. Keller. *Advances in lasers and applications*. Proceedings of the 52nd Scottish Universities Summer School in Physics, IOP Pub, Bristol p. 83 (1999).

[83] R. L. Fork, O. E. Martinez, and J. P. Gordon. *Negative dispersion using pairs of prisms*. Optics Letters **9**(5), 150 (1984).

[84] J. D. Kafka and T. Baer. *Prism-pair dispersive delay-lines in optical pulse-compression*. Optics Letters **12**(6), 401 (1987).

[85] F. Salin and A. Brun. *Dispersion compensation for femtosecond pulses using high-index prisms*. Journal of Applied Physics **61**(10), 4736 (1987).

[86] C. Y. Ramirez-Corral, M. Rosete-Aguilar, and J. Garduno-Mejia. *Third-order dispersion in a pair of prisms*. Journal of Modern Optics **56**(15), 1659 (2009).

[87] O. Razskazovskaya, M. T. Hassan, T. T. Luu, E. Goulielmakis, and V. Pervak. *Efficient broadband highly dispersive HfO_2/SiO_2 multilayer mirror for pulse compression in near ultraviolet*. Optics Express **24**(12), 13628 (2016).

[88] J. I. Dadap, G. B. Focht, D. H. Reitze, and M. C. Downer. *Two-photon absorption in diamond and its application to ultraviolet femtosecond pulse-width measurement*. Optics Letters **16**(7), 499 (1991).

[89] A. Sharp. *The characterisation of deep-ultraviolet ultrafast pulses by active synchronisation via balanced cross-correlation*. Macquarie University, Faculty of Science, Department of Physics and Astronomy (2015).

[90] D. J. Kane and R. Trebino. *Characterization of arbitrary femtosecond pulses using frequency-resolved optical gating*. IEEE Journal of Quantum Electronics **29**(2), 571 (1993).

[91] P. Hannaford. *Femtosecond Laser Spectroscopy* (Springer US: Boston, MA, Boston, MA, 2005).

[92] A. Baltuska, M. S. Pshenichnikov, and D. A. Wiersma. *Amplitude and phase characterization of 4.5-fs pulses by frequency-resolved optical gating*. Optics Letters **23**(18), 1474 (1998).

[93] S. Linden, J. Kuhl, and H. Giessen. *Amplitude and phase characterization of weak blue ultrashort pulses by downconversion*. Optics Letters **24**(8), 569 (1999).

[94] A. Monmayrant, S. Weber, and B. Chatel. *A newcomer's guide to ultrashort pulse shaping and characterization*. Journal of Physics B-Atomic Molecular and Optical Physics **43**(10), 34 (2010).

[95] M. Rhodes, Z. Guang, and R. Trebino. *Unstable and multiple pulsing can be invisible to ultrashort pulse measurement techniques*. Applied Sciences (Switzerland) **7**(1) (2017).

[96] M. Rhodes, G. Steinmeyer, J. Ratner, and R. Trebino. *Pulse-shape instabilities and their measurement*. Laser and Photonics Reviews **7**(4), 557 (2013).

[97] K. Jain and C. G. Willson. *Ultrafast deep UV lithography with excimer lasers*. IEEE Electron Device Letters **3**(3), 53 (1982).

[98] P. A. Franken, A. E. Hill, C. W. Peters, and G. Weinreich. *Generation of optical harmonics*. Physical Review Letters **7**(4), 118 (1961).

[99] L. G. Nair. *Dye lasers*. Progress in Quantum Electronics **7**(3-4), 153 (1982).

[100] D. J. Bradley, J. V. Nicholas, and J. R. D. Shaw. *Megawatt tunable second harmonic and sum frequency generation at 280 nm from a dye laser*. Applied Physics Letters **19**(6), 172 (1971).

[101] F. Laermer, J. Dobler, and T. Elsaesser. *Generation of femtosecond UV pulses by intracavity frequency doubling in a modelocked dye laser*. Optics Communications **67**(1), 58 (1988).

[102] M. E. Fermann and I. Hartl. *Ultrafast fibre lasers*. Nature Photonics **7**(11), 868 (2013).

[103] X. Y. Zhou, D. Yoshitomi, Y. Kobayashi, and K. Torizuka. *1 W average-power 100 MHz repetition-rate 259 nm femtosecond deep ultraviolet pulse generation from ytterbium fiber amplifier*. Optics Letters **35**(10), 1713 (2010).

[104] F. Kottig, F. Tani, C. M. Biersach, J. C. Travers, and P. S. Russell. *Generation of microjoule pulses in the deep ultraviolet at megahertz repetition rates*. Optica **4**(10), 1272 (2017).

[105] M. Müller, A. Klenke, T. Gottschall, R. Klas, C. Rothhardt, S. Demmler, J. Rothhardt, J. Limpert, and A. Tünnermann. *High-average-power femtosecond laser at 258 nm*. Optics Letters **42**(14), 2826 (2017).

[106] S. T. Yang, M. A. Henesian, T. L. Weiland, J. L. Vickers, R. L. Luthi, J. P. Bielecki, and P. J. Wegner. *Noncritically phase-matched fourth harmonic generation of Nd:glass lasers in partially deuterated KDP crystals*. Optics Letters **36**(10), 1824 (2011).

[107] S. H. Ji, F. Wang, L. L. Zhu, X. G. Xu, Z. P. Wang, and X. Sun. *Non-critical phase-matching fourth harmonic generation of a 1053-nm laser in an ADP crystal*. Scientific Reports **3**, 8 (2013).

[108] S. C. Kumar, J. C. Casals, J. Wei, and M. Ebrahim-Zadeh. *High-power, high-repetition-rate performance characteristics of β-BaB_2O_4 for single-pass picosecond ultraviolet generation at 266 nm*. Optics Express **23**(21), 28091 (2015).

[109] D. N. Nikogosyan. *Nonlinear optical crystals: A complete survey*. Nonlinear Optical Crystals: A Complete Survey (Springer New York, 2005).

[110] Q. Liu, X. P. Yan, X. Fu, M. Gong, and D. S. Wang. *High power all-solid-state fourth harmonic generation of 266 nm at the pulse repetition rate of 100 kHz*. Laser Physics Letters **6**(3), 203 (2009).

[111] M. Takahashi, A. Osada, A. Dergachev, P. F. Moulton, M. Cadatal-Raduban, T. Shimizu, and N. Sarukura. *Effects of pulse rate and temperature on nonlinear absorption of pulsed 262-nm laser light in β-BaB_2O_4*. Japanese Journal of Applied Physics **49**(8 PART 1) (2010).

[112] D. Kiefer, D. Preißler, T. Führer, and T. Walther. *Non-degrading CW UV generation in β-barium borate at 257 nm using an elliptical focusing enhancement cavity*. Laser Physics Letters **16**(7) (2019).

[113] M. Takahashi, A. Osada, A. Dergachev, P. F. Moulton, M. Cadatal-Raduban, T. Shimizu, and N. Sarukura. *Improved fourth harmonic generation in β-BaB_2O_4 by tight elliptical focusing perpendicular to walk-off plane*. Journal of Crystal Growth **318**(1), 606 (2011).

[114] G. L. Wang, A. C. Geng, Y. Bo, H. Q. Li, Z. P. Sun, Y. Bi, D. F. Cui, Z. Y. Xu, X. Yuan, X. Q. Wang, G. Q. Shen, and D. Z. Shen. *28.4 W 266 nm ultraviolet-beam generation by fourth-harmonic generation of an all-solid-state laser*. Optics Communications **259**(2), 820 (2006).

[115] Z. Fang, Z. Y. Hou, F. Yang, L. J. Liu, X. Y. Wang, Z. Y. Xu, and C. T. Chen. *High-efficiency UV generation at 266 nm in a new nonlinear optical crystal $NaSr_3Be_3B_3O_9F_4$*. Optics Express **25**(22), 26500 (2017).

[116] Z. Jia, N. Zhang, Y. Ma, L. Zhao, M. Xia, and R. Li. *Top-seeded solution growth and optical properties of deep-UV birefringent crystal $Ba_2Ca(B_3O_6)_2$*. Crystal Growth and Design **17**(2), 558 (2017).

[117] H. Yu, J. Young, H. Wu, W. Zhang, J. M. Rondinelli, and S. Halasyamani. *The next-generation of nonlinear optical materials: $Rb_3Ba_3Li_2Al_4B_6O_{20}F$-synthesis, characterization, and crystal growth*. Advanced Optical Materials **5**(23) (2017).

[118] V. Petrov, M. Ghotbi, O. Kokabee, A. Esteban-Martin, F. Noack, A. Gaydardzhiev, I. Nikolov, P. Tzankov, I. Buchvarov, K. Miyata, A. Majchrowski, I. V. Kityk, F. Rotermund, E. Michalski, and M. Ebrahim-Zadeh. *Femtosecond nonlinear frequency conversion based on BiB_3O_6*. Laser & Photonics Reviews **4**(1), 53 (2010).

[119] P. Baum, S. Lochbrunner, and E. Riedle. *Generation of tunable 7-fs ultraviolet pulses: achromatic phase matching and chirp management*. Applied Physics B-Lasers and Optics **79**(8), 1027 (2004).

[120] Z. Baozhen, J. Yongliang, K. Sueda, N. Miyanaga, and T. Kobayashi. *Sub-15fs ultraviolet pulses generated by achromatic phase-matching sum-frequency mixing*. Optics Express **17**(20), 17711 (2009).

[121] P. Baum, S. Lochbrunner, and E. Riedle. *Tunable sub-10-fs ultraviolet pulses generated by achromatic frequency doubling*. Optics Letters **29**(14), 1686 (2004).

[122] M. Galli, V. Wanie, D. P. Lopes, E. P. Mansson, A. Trabattoni, L. Colaizzi, K. Saraswathula, A. Cartella, F. Frassetto, L. Poletto, F. Legare, S. Stagira, M. Nisoli, R. M. Vazquez, R. Osellame, and F. Calegari. *Generation of deep ultraviolet sub-2-fs pulses*. Optics Letters **44**(6), 1308 (2019).

[123] N. Y. Joly, J. Nold, W. Chang, P. Hölzer, A. Nazarkin, G. K. L. Wong, F. Biancalana, and P. S. J. Russell. *Bright spatially coherent wavelength-tunable deep-UV laser source using an Ar-filled photonic crystal fiber*. Physical Review Letters **106**(20) (2011).

[124] Z. Sun and A. C. Ferrari. *Nonlinear optics: Fibre sources in the deep ultraviolet*. Nature Photonics **5**(8), 446 (2011).

[125] P. S. J. Russell, P. Hölzer, W. Chang, A. Abdolvand, and J. C. Travers. *Hollow-core photonic crystal fibres for gas-based nonlinear optics*. Nature Photonics **8**(4), 278 (2014).

[126] J. C. Travers, T. F. Grigorova, C. Brahms, and F. Belli. *High-energy pulse self-compression and ultraviolet generation through soliton dynamics in hollow capillary fibres*. Nature Photonics **13**(8), 547 (2019).

[127] P. W. Roth, A. J. Maclean, D. Burns, and A. J. Kemp. *Directly diode-laser-pumped Ti:sapphire laser*. Optics Letters **34**(21), 3334 (2009).

[128] K. Gürel, M. Hoffmann, C. J. Saraceno, V. J. Wittwer, S. Hakobyan, B. Resan, A. Rohrbacher, K. Weingarten, S. Schilt, and T. Südmeyer. *Ultrafast diode-pumped Ti:sapphire laser generating 200-mW average power in 68-fs pulses*. In *CLEO: Science and Innovations, CLEO-SI 2015*, p. 2267 (Optical Society of America (OSA), 2015).

[129] K. Gürel, V. J. Wittwer, M. Hoffmann, S. Schilt, and T. Südmeyer. *Diode-pumped Kerr-lens modelocked Ti:sapphire laser generating 450 mW in 58 fs pulses and 350 mW in 39 fs pulses*. In *Advanced Solid State Lasers, ASSL 2015* (Optical Society of America (OSA), 2015).

[130] A. Muti, A. Kocabas, and A. Sennaroglu. *5-nJ femtosecond Ti^{3+}:sapphire laser pumped with a single 1 W green diode*. Laser Physics Letters **15**(5) (2018).

[131] N. Sugiyama, H. Tanaka, and F. Kannari. *Mode-locked Ti:sapphire laser oscillators pumped by wavelength-multiplexed laser diodes*. Japanese Journal of Applied Physics **57**(5) (2018).

[132] J. C. E. Coyle, J. M. Hopkins, A. A. Lagatsky, and A. J. Kemp. *Titanium sapphire: A decade of diode-laser pumping*. In *2019 Conference on Lasers and Electro-Optics Europe and European Quantum Electronics Conference, CLEO/Europe-EQEC 2019* (Institute of Electrical and Electronics Engineers Inc., 2019).

[133] Z. Zhang, M. Kushimoto, T. Sakai, N. Sugiyama, L. J. Schowalter, C. Sasaoka, and H. Amano. *A 271.8 nm deep-ultraviolet laser diode for room temperature operation*. Applied Physics Express **12**(12) (2019).

[134] M. A. Dubinskii. *Spectroscopy of a new active medium of a solid-state UV laser with broadband single-pass gain*. Laser Phys. **3**, 216 (1993).

[135] P. Albers, E. Stark, and G. Huber. *Continuous-wave laser operation and quantum efficiency of titanium-doped sapphire*. Journal of the Optical Society of America B **3**(1), 134 (1986).

[136] L. R. Elias, W. S. Heaps, and W. M. Yen. *Excitation of UV fluorescence in LaF_3 doped with trivalent cerium and praseodymium*. Physical Review B (Solid State) **8**(11), 4989 (1973).

[137] C. M. Combes, P. Dorenbos, C. W. E. Van Eijk, C. Pedrini, H. W. Den Hartog, J. Y. Gesland, and P. A. Rodnyi. *Optical and scintillation properties of Ce^{3+} doped $LiYF_4$ and $LiLuF_4$ crystals*. Journal of Luminescence **71**(1), 65 (1997).

[138] T. Yanagida, Y. Fujimoto, N. Kawaguchi, Y. Yokota, K. Kamada, D. Totsuka, S. I. Hatamoto, A. Yoshikawa, and V. Chani. *Scintillation properties of Ce-doped $LuLiF_4$ and $LuScBO_3$*. Nuclear Instruments and Methods in Physics Research, Section A: Accelerators, Spectrometers, Detectors and Associated Equipment **652**(1), 251 (2011).

[139] T. Yanagida, Y. Fujimoto, K. Fukuda, and V. Chani. *Optical and scintillation properties of Ce-doped $LuLiF_4$ with different Ce concentrations*. Nuclear Instruments and Methods in Physics Research, Section A: Accelerators, Spectrometers, Detectors and Associated Equipment **729**, 58 (2013).

[140] K. H. Yang and J. A. Deluca. *UV fluorescence of cerium-doped lutetium and lanthanum trifluorides, potential tunable coherent sources from 2760 to 3220* Å. Applied Physics Letters **31**(9), 594 (1977).

[141] K. H. Yang and J. A. Deluca. *VUV fluorescence of Nd^{3+}-, Er^{3+}, and Tm^{3+}-doped trifluorides and tunable coherent sources from 1650 to 2600* Å. Applied Physics Letters **29**(8), 499 (1976).

[142] W. S. Heaps, L. R. Elias, and W. M. Yen. *Vacuum-ultraviolet absorption bands of trivalent lanthanides in LaF_3*. Physical Review B **13**(1), 94 (1976).

[143] R. W. Waynant and P. H. Klein. *Vacuum ultraviolet laser emission from Nd^{3+}:LaF_3*. Applied Physics Letters **46**(1), 14 (1985).

[144] M. A. Dubinskii, A. C. Cefalas, E. Sarantopoulou, S. M. Spyrou, C. A. Nicolaides, R. Y. Abdulsabirov, S. L. Korableva, and V. V. Semashko. *Efficient LaF_3:Nd^{3+}-based vacuum-ultraviolet laser at 172 nm*. Journal of the Optical Society of America B: Optical Physics **9**(7), 1148 (1992).

[145] J. S. Cashmore, S. M. Hooker, and C. E. Webb. *Vacuum ultraviolet gain measurements in optically pumped $LiYF_4$:Nd^{3+}*. Applied Physics B: Lasers and Optics **64**(3), 293 (1997).

[146] Y. Minami, R. Arita, M. Cadatal-Raduban, M. H. Pham, M. J. F. Empizo, M. V. Luong, T. Hori, M. Takabatake, K. Fukuda, K. Mori, K. Yamanoi, T. Shimizu, N. Sarukura, K. Fukuda, N. Kawaguchi, Y. Yokota, and A. Yoshikawa. *Temperature-dependent evaluation of Nd:LiCAF optical properties as potential vacuum ultraviolet laser material*. Optical Materials **58**, 5 (2016).

[147] M. V. Luong, M. J. F. Empizo, M. Cadatal-Raduban, R. Arita, Y. Minami, T. Shimizu, N. Sarukura, H. Azechi, M. H. Pham, H. D. Nguyen, Y. Kawazoe, K. G. Steenbergen, and P. Schwerdtferger. *First-principles calculations of electronic and optical properties of $LiCaAlF_6$ and $LiSrAlF_6$ crystals as VUV to UV solid-state laser materials*. Optical Materials **65**, 15 (2017).

[148] D. S. Hamilton. *Trivalent cerium doped crystals as tunable laser systems: Two bad apples*. In *Tunable Solid State Lasers, Proceedings of the First International Conference.*, pp. 80–90 (Springer-Verlag, 1985).

[149] R. J. Lang. *Spectrum of trebly ionised cerium*. Canadian Journal of Research **14**, 127 (1936).

[150] M. J. Weber. *Nonradiative decay from 5d states of rare earths in crystals*. Solid State Communications **12**(7), 741 (1973).

[151] D. W. Coutts and A. J. S. McGonigle. *Cerium-doped fluoride lasers*. IEEE Journal of Quantum Electronics **40**(10), 1430 (2004).

[152] A. S. Nizamutdinov, V. V. Semashko, A. K. Naumov, S. L. Korableva, R. Y. Abdulsabirov, A. N. Polivin, and M. A. Marisov. *Optical and gain properties of series of crystals LiF-YF_3-LuF_3 doped with Ce^{3+} and Yb^{3+} ions*. Journal of Luminescence **127**(1), 71 (2007).

[153] A. J. Bayramian, C. D. Marshall, J. H. Wu, J. A. Speth, S. A. Payne, G. J. Quarles, and V. K. Castillo. *Ce:LiSrAlF$_6$ laser performance with antisolarant pump beam*. Journal of Luminescence **69**(2), 85 (1996).

[154] D. J. Ehrlich, P. F. Moulton, and J. Osgood, R. M. *Ultraviolet solid-state Ce:YLF laser at 325 nm*. Optics Letters **4**(6), 184 (1979).

[155] D. J. Ehrlich, P. F. Moulton, and J. Osgood, R. M. *Optically pumped Ce:LaF$_3$ laser at 286 nm*. Optics Letters **5**(8), 339 (1980).

[156] J. F. Owen, P. B. Dorain, and T. Kobayasi. *Excited-state absorption in Eu^{+2}:CaF$_2$ and Ce^{+3}:YAG single crystals at 298 and 77 K*. Journal of Applied Physics **52**(3), 1216 (1981).

[157] C. Pedrini, F. Rogemond, and D. S. McClure. *Photoionization thresholds of rare-earth impurity ions. Eu^{2+}:CaF$_2$, Ce^{3+}:YAG, and Sm^{2+}:CaF$_2$*. Journal of Applied Physics **59**(4), 1196 (1986).

[158] G. J. Pogatshnik and D. S. Hamilton. *Excited-state photoionization of Ce^{3+} ions in Ce^{3+}:CaF$_2$*. Physical Review B **36**(16), 8251 (1987).

[159] K. S. Lim and D. S. Hamilton. *UV-induced loss mechanisms in a Ce^{3+}:YLiF$_4$ laser*. Journal of Luminescence **40-41**(C), 319 (1988).

[160] K. S. Lim and D. S. Hamilton. *Optical gain and loss studies in Ce^{3+}:YLiF$_4$*. Journal of the Optical Society of America B: Optical Physics **6**(7), 1401 (1989).

[161] D. S. Hamilton, S. K. Gayen, G. J. Pogatshnik, R. D. Ghen, and W. J. Miniscalco. *Optical-absorption and photoionization measurements from the excited states of Ce^{3+}:$Y_3Al_5O_{12}$*. Physical Review B **39**(13), 8807 (1989).

[162] P. Fabeni, G. P. Pazzi, and L. Salvini. *Impurity centers for tunable lasers in the ultraviolet and visible regions*. Journal of Physics and Chemistry of Solids **52**(1), 299 (1991).

[163] H. W. H. Lee, S. A. Payne, and L. L. Chase. *Excited-state absorption of Cr^{3+} in LiCaAlF$_6$: Effects of asymmetric distortions and intensity selection rules*. Physical Review B **39**(13), 8907 (1989).

[164] S. A. Payne, L. L. Chase, L. K. Smith, W. L. Kway, and H. W. Newkirk. *Laser performance of LiSrAlF$_6$-Cr^{3+}*. Journal of Applied Physics **66**(3), 1051 (1989).

[165] P. Beaud, M. C. Richardson, Y. F. Chen, and B. H. T. Chai. *Optical amplification characteristics of Cr:LiSAF and Cr:LiCAF under flashlamp-pumping*. IEEE Journal of Quantum Electronics **30**(5), 1259 (1994).

[166] P. Wagenblast, R. Ell, U. Morgner, F. Grawert, and F. X. Kärtner. *Diode-pumped 10-fs Cr^{3+}:LiCAF laser*. Optics Letters **28**(18), 1713 (2003).

[167] S. Sakadžić, U. Demirbas, T. R. Mempel, A. Moore, S. Ruvinskaya, D. A. Boas, A. Sennaroglu, F. X. Kartner, and J. G. Fujimoto. *Multi-photon microscopy with a low-cost and highly efficient Cr:LiCAF laser*. Optics Express **16**(25), 20848 (2008).

[168] U. Demirbas, D. Li, J. R. Birge, A. Sennaroglu, G. S. Petrich, L. A. Kolodziejski, F. X. Kärtner, and J. G. Fujimoto. *Low-cost, single-mode diode-pumped Cr:colquiriite lasers*. Optics Express **17**(16), 14374 (2009).

[169] P. C. Wagenblast, U. Morgner, F. Grawert, T. R. Schibli, F. X. Kartner, V. Scheuer, G. Angelow, and M. J. Lederer. *Generation of sub-10-fs pulses from a Kerr-lens mode-locked Cr^{3+}:LiCAF laser oscillator by use of third-order dispersion-compensating double-chirped mirrors*. Optics Letters **27**(19), 1726 (2002).

[170] M. A. Dubinskii, V. V. Semashko, A. K. Naumov, R. Y. Abdulsabirov, and S. L. Korableva. *Ce^{3+}-doped colquiriite - a new concept of all-solid-state tunable ultraviolet-laser*. Journal of Modern Optics **40**(1), 1 (1993).

[171] A. A. Shavelev, A. S. Nizamutdinov, M. A. Marisov, I. I. Farukhshin, O. A. Morozov, N. F. Rakhimov, E. V. Lukinova, S. L. Korableva, and V. V. Semashko. *Single crystals with advanced laser properties $LiCaAlF_6$:Ce^{3+} grown by Bridgman technique*. Journal of Crystal Growth **485**, 73 (2018).

[172] C. D. Marshall, J. A. Speth, S. A. Payne, W. F. Krupke, G. J. Quarles, V. Castillo, and B. H. T. Chai. *Ultraviolet-laser emission properties of Ce^{3+}-doped $LiSrAlF_6$ and $LiCaAlF_6$*. Journal of the Optical Society of America B-Optical Physics **11**(10), 2054 (1994).

[173] F. Okada, S. Togawa, K. Ohta, and S. Koda. *Solid-state ultraviolet tunable laser: A Ce^{3+} doped $LiYF_4$ crystal*. Journal of Applied Physics **75**(1), 49 (1994).

[174] M. A. Dubinskii, V. V. Semashko, A. K. Naumov, R. Y. Abdulsabirov, and S. L. Korableva. *A new active medium for a tunable solid-state UV laser with an excimer pump*. Laser Physics **4**(3), 480 (1994).

[175] M. A. Dubinskii and P. Misra. *Rare-earth doped all-solid-state lasers for ultraviolet free radical spectroscopy*. Spectroscopy (Santa Monica) **13**(6), 33 (1998).

[176] R. De Young, W. Carrion, R. Ganoe, D. Pliutau, G. Gronoff, T. Berkoff, and S. Kuang. *Langley mobile ozone lidar: Ozone and aerosol atmospheric profiling for air quality research*. Applied Optics **56**(3), 721 (2017).

[177] A. J. S. McGonigle, D. W. Coutts, and C. E. Webb. *A 380-mW 7-kHz cerium LiLuF laser pumped by the frequency doubled yellow output of a copper-vapor-laser*. Ieee Journal of Selected Topics in Quantum Electronics **5**(6), 1526 (1999).

[178] A. J. S. McGonigle, D. W. Coutts, and C. E. Webb. *530-mW 7-kHz cerium LiCAF laser pumped by the sum-frequency-mixed output of a copper-vapor laser*. Optics Letters **24**(4), 232 (1999).

[179] S. A. Payne and W. F. Krupke. *Glimpse into the laser-crystal ball*. Optics and Photonics News **7**(8), 31 (1996).

[180] M. Laroche, S. Girard, R. Moncorgé, M. Bettinelli, R. Abdulsabirov, and V. Semashko. *Beneficial effect of Lu^{3+} and Yb^{3+} ions in UV laser materials*. GDR 1148 CNRS **22**(2), 147 (2003).

[181] I. I. Farukhshin, A. S. Nizamutdinov, V. V. Semashko, and S. L. Korableva. *Laser characteristics of active medium $LiLu_{0.7}Y_{0.3}F_4$:Ce^{3+} in ultra-short pulse mode*. In V. V. Semashko, A. S. Nizamutdinov, and M. S. Tagirov, eds., *17th International Youth Scientific School on Actual Problems of Magnetic Resonance and Its Applications*, vol. 560 (Institute of Physics Publishing, 2014).

[182] V. V. Semashko, M. A. Dubinskii, R. Y. Abdulsabirov, S. L. Korableva, and A. K. Naumov. *Photodynamic processes in Ce-activated solid-state active media: anti-solarant co-doping and new tunable UV-blue laser materials*, vol. 68 of *Osa Trends in Optics and Photonics*, pp. 251–253 (Optical Soc America, Washington, 2002).

[183] A. A. Shavelev, A. S. Nizamutdinov, V. V. Semashko, and M. A. Marisov. *Growth of solid solutions with colquiriite structure $LiCa_{0.2}Sr_{0.8}AlF_6$:Ce^{3+}*. 17th International Youth Scientific School on Actual Problems of Magnetic Resonance and Its Applications **560**(1) (2014).

[184] A. S. Nizamutdinov, A. A. Shavelev, M. A. Marisov, and V. V. Semashko. *Spectroscopic properties of UV active medium Ce^{3+}:$LiSr_{0.8}Ca_{0.2}AlF_6$*. Optical Materials **52**, 157 (2016).

[185] S. Nicolas, E. Descroix, M. F. Joubert, Y. Guyot, M. Laroche, R. Moncorgé, R. Y. Abdulsabirov, A. K. Naumov, V. V. Semashko, A. M. Tkachuk, and M. Malinowski. *Potentiality of Pr^{3+}- and Pr^{3+} + Ce^{3+} -doped crystals for tunable UV upconversion lasers*. GDR 1148 CNRS **22**(2), 139 (2003).

[186] V. G. Gorieva, S. L. Korableva, M. A. Marisov, V. V. Pavlov, and V. V. Semashko. *First observation of optical gain on 5d-4f transitions of Ce^{3+} ions in up-conversionally pumped Ce^{3+}, Pr^{3+}:$LiY_{0.3}Lu_{0.7}F_4$ mixed crystals*. Laser Physics Letters **13**(2) (2016).

[187] A. A. Pushkar, T. V. Uvarova, and V. N. Molchanov. *BaY_2F_8 single crystals doped with rare-earth ions as promising up-conversion media for UV and VUV lasers*. Quantum Electronics **38**(4), 333 (2008).

[188] A. A. Pushkar, T. V. Uvarova, N. S. Kozlova, S. Y. Kuznetsov, and A. G. Uvarova. *The laser-diode-excited 5d-4f luminescence of Ce^{3+} and Pr^{3+} ions embedded into a BaR_2F_8 matrix*. Optics and Spectroscopy **114**(6), 809 (2013).

[189] M. V. Luong, M. Cadatal-Raduban, M. J. F. Empizo, R. Arita, Y. Minami, T. Shimizu, N. Sarukura, H. Azechi, M. H. Pham, H. D. Nguyen, and Y. Kawazoe. *Comparison of the electronic band structures of $LiCaAlF_6$ and $LiSrAlF_6$ ultraviolet laser host media from ab initio calculations*. Japanese Journal of Applied Physics **54**(12), 6 (2015).

[190] M. C. Richardson, M. J. Soileau, P. Beaud, R. J. DeSalvo, S. V. Garnov, D. J. Hagan, S. M. Klimentov, K. C. Richardson, M. Sheik-Bahae, A. A. Said, E. W. Van Stryland, and B. H. Chai. *Self-focusing and optical damage in Cr:LiSAF and Cr:LiCAF*. In E. Bennett Harold, L. Chase Lloyd, H. Guenther Arthur, B. Newman, and M. J. Soileau, eds., *Proceedings of the 24th Annual Boulder Damage Symposium Laser-Induced Damage in Optical Materials: 1992*, vol. 1848, pp. 392–402 (Publ by Society of Photo-Optical Instrumentation Engineers).

[191] G. Toci, M. Vannini, R. Salimbeni, M. A. Dubinskii, and E. Giorgetti. *First z-scan n(2) measurements on crystal hosts for ultraviolet laser systems*. Applied Physics B-Lasers and Optics **71**(6), 907 (2000).

[192] G. Toci, M. Vannini, R. Salimbeni, M. A. Dubinskii, and E. Giorgetti. *Multi-wavelengths Z-scan n(2) measurements on crystal hosts for ultraviolet laser systems*, vol. 4184 of *Proceedings of SPIE*, pp. 377–380 (Spie-Int Soc Optical Engineering, Bellingham, 2000).

[193] N. Sarukura, M. A. Dubinskii, Z. L. Liu, V. V. Semashko, A. K. Naumov, S. L. Korableva, R. Y. Abdulsabirov, K. Edamatsu, Y. Suzuki, T. Itoh, and Y. Segawa. *Ce^{3+}-activated fluoride-crystals as prospective active media for widely tunable ultraviolet ultrafast lasers with direct 10-ns pumping*. IEEE Journal of Selected Topics in Quantum Electronics **1**(3), 792 (1995).

[194] A. B. Petersen. *Diode-pumped tunable cerium UV lasers*. Conference Proceedings. LEOS '96 9th Annual Meeting. IEEE Lasers and Electro-Optics Society 1996 Annual Meeting (Cat. No.96CH35895) pp. 92–3 vol.1 (1996).

[195] Z. L. Liu, N. Sarukura, M. A. Dubinskii, R. Y. Abdulsabirov, and S. L. Korableva. *All-solid-state subnanosecond tunable ultraviolet laser sources based on Ce^{3+}-activated fluoride crystals*. Journal of Nonlinear Optical Physics & Materials **8**(1), 41 (1999).

[196] M. H. Pham, M. Cadatal-Raduban, M. V. Luong, H. H. Le, K. Yamanoi, T. Nakazato, T. Shimizu, N. Sarukura, and H. D. Nguyen. *Numerical simulation of ultraviolet picosecond Ce:LiCAF laser emission by optimized resonator transients*. Japanese Journal of Applied Physics **53**(6), 9 (2014).

[197] P. Cordelier, R. Moncorge, R. Abdulsabirov, V. Semashko, S. Korableva, M. Laroche, and S. Girard. *A Ce:LiCAF UV laser pumped by an intracavity frequency-doubled radiation at 532 nm*, vol. 5460 of *Proceedings of the Society of Photo-Optical Instrumentation Engineers (Spie)*, pp. 35–43 (Spie-Int Soc Optical Engineering, Bellingham, 2004).

[198] L. Hua, D. J. Spence, and D. W. Coutts. *Highly efficient ultra-low threshold miniature cerium fluoride lasers generating sub-nanosecond pulses at 287 nm and 311 nm*. Proceedings of the SPIE - The International Society for Optical Engineering **6100**, 610007 (2006).

[199] H. Liu, D. J. Spence, K. Johnson, D. W. Coutts, H. Sato, and T. Fukuda. *UV picosecond microchip cerium lasers*. In *Advanced Solid-State Photonics, ASSP 2007* (Optical Society of America).

[200] D. J. Spence, H. Liu, and D. W. Coutts. *Low-threshold miniature Ce:LiCAF lasers*. Optics Communications **262**(2), 238 (2006).

[201] T. Le, S. J. Schowalter, W. Rellergert, J. Jeet, G. P. Lin, N. Yu, and E. R. Hudson. *Low-threshold ultraviolet solid-state laser based on a Ce^{3+}:$LiCaAlF_6$ crystal resonator*. Optics Letters **37**(23), 4961 (2012).

[202] M. H. Pham, M. Cadatal-Raduban, D. V. Pham, T. X. Nguyen, M. V. Luong, K. Yamanoi, T. Shimizu, N. Sarukura, and H. D. Nguyen. *Tunable narrow linewidth picosecond pulses from a single grating gain-switched Ce:LiCAF laser*. Laser Physics **28**(8), 5 (2018).

[203] Z. L. Liu, N. Sarukura, M. A. Dubinskii, V. V. Semashko, A. K. Naumov, S. L. Korableva, and R. Y. Abdulsabirov. *Tunable ultraviolet short-pulse generation from a Ce:LiCAF laser amplifier system and its sum-frequency mixing with an Nd:YAG laser*. Japanese Journal of Applied Physics Part 2-Letters & Express Letters (1998).

[204] Z. L. Liu, T. Kozeki, Y. Suzuki, N. Sarukura, K. Shimamura, T. Fukuda, M. Hirano, and H. Hosono. *Chirped-pulse amplification of ultraviolet femtosecond pulses by use of Ce^{3+}:$LiCaAlF_6$ as a broadband, solid-state gain medium*. Optics Letters **26**(5), 301 (2001).

[205] Z. Liu, S. Izumida, H. Ohtake, N. Sarukura, K. Shimamura, N. Mujilatu, S. L. Baldochi, and T. Fukuda. *High-pulse-energy, all-solid-state, ultraviolet laser oscillator using large Czochralski-grown Ce:LiCAF crystal*. Japanese Journal of Applied Physics Part 2-Letters **37**(11A), L1318 (1998).

[206] A. Bensalah, K. Shimamura, Z. L. Liu, N. Sarukura, and T. Fukuda. *Growth and laser performance of Ce-doped $LiCaAlF_6$ and $LiSr_{0.8}Ca_{0.2}AlF_6$ single crystals for UV laser applications*, vol. 4268 of *Proceedings of the Society of Photo-Optical Instrumentation Engineers (Spie)*, pp. 167–174 (Spie-Int Soc Optical Engineering, Bellingham, 2001).

[207] K. Shimamura, S. L. Baldochi, N. Mujilatu, K. Nakano, Z. Liu, N. Sarukura, and T. Fukuda. *Growth of Ce-doped $LiCaAlF_6$ and $LiSrAlF_6$ single crystals by the Czochralski technique under CF_4 atmosphere*. The 11th American Conference on Crystal Growth and Epitaxy **211**(1), 302 (2000).

[208] Z. L. Liu, K. Shimamura, T. Fukuda, T. Kozeki, Y. Suzuki, and N. Sarukura. *High-energy pulse generation from solid-state ultraviolet lasers using large Ce:fluoride crystals*. Optical Materials **19**(1), 123 (2002).

[209] Z. L. Liu, T. Kozeki, Y. Suzuki, N. Sarukura, K. Shimamura, T. Fukuda, M. Hirano, and H. Hosono. *Ultraviolet femtosecond pulse amplification with high gain using solid-state, broad-band gain medium Ce^{3+}:$LiCaAlF_6$*. Japanese Journal of Applied Physics Part 1-Regular Papers Short Notes & Review Papers **40**(4A), 2308 (2001).

[210] J. L. Gabayno, M. Cadatal-Raduban, M. Pham, K. Yamanoi, E. Estacio, W. Garcia, T. Nakazato, T. Shimizu, N. Sarukura, T. Suyama, K. Fukuda, K. J. Kim, A. Yoshikawa, and F. Saito. *Amplification of ultraviolet femtosecond pulse by a micro-pulling down method-grown Ce:LiCAF crystal in a prismatic cell-type, side-pumping configuration*. Japanese Journal of Applied Physics **48**(12), 3 (2009).

[211] M. Cadatal-Raduban, M. H. Pham, J. L. Gabayno, K. Yamanoi, M. J. F. Empizo, T. Shimizu, N. Sarukura, H. D. Nguyen, A. Yoshikawa, and T. Fukuda. *Optimized Ce:LiCAF amplifier pumping configurations*, vol. 10511 of *Proceedings of SPIE* (Spie-Int Soc Optical Engineering, Bellingham, 2018).

[212] E. Granados, D. W. Coutts, and D. J. Spence. *Mode-locked deep ultraviolet Ce:LiCAF laser*. Optics Letters **34**(11), 1660 (2009).

[213] E. Granados Mateo. *Mode-locked lasers in the deep ultraviolet and the visible*. Macquarie University, Faculty of Science, Department of Physics and Astronomy (2010).

[214] E. Granados, A. Fuerbach, D. W. Coutts, and D. J. Spence. *Asynchronous cross-correlation for weak ultrafast deep ultraviolet laser pulses*. Applied Physics B-Lasers and Optics **97**(4), 759 (2009).

[215] B. Wellmann, D. J. Spence, and D. W. Coutts. *Tunable continuous-wave deep-ultraviolet laser based on Ce:LiCAF*. Optics Letters **39**(5), 1306 (2014).

[216] B. Wellmann, O. Kitzler, D. J. Spence, and D. W. Coutts. *Linewidth narrowing of a tunable mode-locked pumped continuous-wave Ce:LiCAF laser*. Optics Letters **40**(13), 3065 (2015).

[217] O. Kitzler, D. J. Spence, and D. W. Coutts. *Continuous-wave ultraviolet Ce:LiCAF laser*. In *Advanced Solid State Lasers, ASSL 2015* (Optical Society of America (OSA)).

[218] D. C. Hanna. *Astigmatic gaussian beams produced by axially asymmetric laser cavities*. IEEE Journal of Quantum Electronics **5**(10), 483 (1969).

[219] H. Kogelnik, E. Ippen, A. Dienes, and C. Shank. *Astigmatically compensated cavities for CW dye lasers*. IEEE Journal of Quantum Electronics **8**(3), 373 (1972).

[220] D. Alderighi, G. Toci, M. Vannini, D. Parisi, and M. Tonelli. *Experimental evaluation of the CW lasing threshold for a Ce:LiCaAlF$_6$ laser*. Optics Express **13**(19) (2005).

[221] V. Magni, G. Cerullo, S. De Silvestri, and A. Monguzzi. *Astigmatism in Gaussian-beam self-focusing and in resonators for Kerr-lens mode locking*. Journal of the Optical Society of America B: Optical Physics **12**(3), 476 (1995).

[222] P. E. Ciddor. *Refractive index of air: New equations for the visible and near infrared*. Applied Optics **35**(9), 1566 (1996).

[223] K. Shimamura, H. Sato, A. Bensalah, H. Machida, N. Sarukura, and T. Fukuda. *Growth of LiCaAlF$_6$ single crystals with an extended diameter and their optical characterizations*. Journal of Alloys and Compounds **343**(1-2), 204 (2002).

[224] R. H. Stolen, C. Lin, and R. K. Jain. *A time-dispersion-tuned fiber Raman oscillator*. Applied Physics Letters **30**(7), 340 (1977).

[225] K. Tamura and M. Nakazawa. *Dispersion-tuned harmonically mode-locked fiber ring laser for self-synchronization to an external clock*. Optics Letters **21**(24), 1984 (1996).

[226] B. Burgoyne, A. Dupuis, and A. Villeneuve. *An experimentally validated discrete model for dispersion-tuned actively mode-locked lasers*. IEEE Journal on Selected Topics in Quantum Electronics **20**(5) (2014).

[227] B. Metherall and S. Bohun. *A Nonlinear Model for Dispersion-Tuned Actively Mode-Locked Lasers* (2018).

[228] I. H. Malitson. *Interspecimen comparison of the refractive index of fused silica*. JOSA **55**(10), 1205 (1965).

[229] R. L. Fork, C. H. Brito Cruz, P. C. Becker, and C. V. Shank. *Compression of optical pulses to six femtoseconds by using cubic phase compensation*. Optics Letters **12**(7), 483 (1987).

[230] S. Uemura. *Dispersion compensation for a femtosecond Cr:LiSAF laser*. Japanese Journal of Applied Physics Part 1-Regular Papers Short Notes & Review Papers **37**(1), 133 (1998).

[231] M. Valadan, D. D'Ambrosio, F. Gesuele, R. Velotta, and C. Altucci. *Temporal and spectral characterization of femtosecond deep-UV chirped pulses*. Laser Physics Letters **12**(2), 7 (2015).

[232] K. Michelmann, T. Feurer, R. Fernsler, and R. Sauerbrey. *Frequency resolved optical gating in the UV using the electronic kerr effect*. Applied Physics B: Lasers and Optics **63**(5), 485 (1996).

[233] N. Sarukura, M. Watanabe, A. Endoh, and S. Watanabe. *Single-shot measurement of subpicosecond KrF pulse width by three-photon fluorescence of the XeF visible transition*. Optics Letters **13**(11), 996 (1988).

[234] K. J. Leedle, K. E. Urbanek, and R. L. Byer. *Simple, picojoule-sensitive ultraviolet autocorrelator based on two-photon conductivity in sapphire*. Applied Optics **56**(8), 2226 (2017).

[235] D. C. Edelstein, E. S. Wachman, L. K. Cheng, W. R. Bosenberg, and C. L. Tang. *Femtosecond ultraviolet pulse generation in β-BaB_2O_4*. Applied Physics Letters **52**(26), 2211 (1988).

[236] A. P. Baronavski, H. D. Ladouceur, and J. K. Shaw. *Analysis of cross correlation, phase velocity mismatch, and group velocity mismatches in sum-frequency generation*. IEEE Journal of Quantum Electronics **29**(2), 580 (1993).

[237] A. Fürbach, T. Le, C. Spielmann, and F. Krausz. *Generation of 8-fs pulses at 390 nm*. Applied Physics B: Lasers and Optics **70**(SUPPL. 1), S37 (2000).

[238] E. W. Weisstein. *Full width at half maximum*. From Mathworld - A Wolfram Web Resource URL https://mathworld.wolfram.com/FullWidthatHalfMaximum.html.

[239] U. Demirbas, I. Baali, D. A. E. Acar, and A. Leitenstorfer. *Diode-pumped continuous-wave and femtosecond Cr:LiCAF lasers with high average power in the near infrared, visible and near ultraviolet*. Optics Express **23**(7), 8901 (2015).

[240] U. Demirbas. *Power scaling potential of continuous-wave Cr:LiSAF and Cr:LiCAF lasers in thin-disk geometry*. Applied Optics **57**(35), 10207 (2018).

[241] S. Diddams and J.-C. Diels. *Dispersion measurements with white-light interferometry*. JOSA B **13**(6), 1120 (1996).

[242] V. Pervak, O. Razskazovskaya, I. B. Angelov, K. L. Vodopyanov, and M. Trubetskov. *Dispersive mirror technology for ultrafast lasers in the range 220-4500 nm*. Advanced Optical Technologies **3**(1), 55 (2014).

[243] G. Steinmeyer. *Femtosecond dispersion compensation with multilayer coatings: toward the optical octave*. Applied Optics **45**(7), 1484 (2006).

[244] C. A. Rivera, S. E. Bradforth, and G. Tempea. *Gires-Tournois interferometer type negative dispersion mirrors for deep ultraviolet pulse compression*. Optics Express **18**(18), 18615 (2010).

[245] X. Liu, X. Lu, P. Wen, X. Shu, and F. Chi. *Synthesis of ultrasmall silica nanoparticles for application as deep-ultraviolet antireflection coatings*. Applied Surface Science **420**, 180 (2017).

[246] F. Chi, N. Pan, C. Ding, X. Wang, F. Yi, X. Li, and J. Lei. *Ultraviolet laser-induced damage of freestanding silica nanoparticle films*. Applied Surface Science **463**, 566 (2019).